FEM based soil stress and strain analyses aimed at plant growth factors

FEM based soil stress and strain analyses aimed at plant growth factors

Albert Barneveld

The research described in this dissertation was carried out at the Department of Agricultural, Environmental and Systems Technology of Wageningen University.

Cover : Illuminated Cube
         Eefke de Graaf / Albert Barneveld [©]

BIBLIOTHEEK
LANDBOUWUNIVERSITEIT
WAGENINGEN

Keywords

Soil-load process, finite element method, Plaxis, interface, Mohr-Coulomb, soil model parameters, stress and strain analyses, three-dimensional visualisation, principal directions, kneading

Stellingen

1. Het niveau van de hoofdspanningen direct onder een landbouwband is hoger dan het niveau van normaalspanningen berekend op basis van principe [wiellast/contactoppervlak].

   - Klubertanz, G., L. Vulliet, M. Gysi and A. Ott, 1999. A study on soil compaction due to agricultural traffic: Computational results and field data. Numerical Models in Geomechanics - NUMOG VII, Pande, Pietruszczak & Schweiger (eds), pp. 621-626
   - Perdok, U.D. en W.B.M Arts, 1986. Het landbouw bandenboek
   - Tijink, F.G.J., A.J. Koolen en W.B.M Arts, 1990. Banden tussen voertuig en grond. In: Themadag Management bodemstructuur

2. Beheerst modelleren van een belastingsproces van grond door een band aan de hand van begrijpelijke modellen, met goed toegankelijke en te meten parameters, biedt perspectieven voor visualisering en analyse van een zeer ingewikkeld fysisch proces.

3. Bestaande modellen voor bepaling van spanningen in de bodem variëren van zeer eenvoudig tot uiterst complex; in de praktijk toegepaste modellen vallen niet onder deze extremen.

4. Het determineren van het kneedproces van grond is te vergelijken met het roeien door een amorfe massa; grondige en noeste arbeid dus.

5. Een continuüm-mechanica benadering impliceert niet dat het verloop van daaruit voortvloeiende grootheden continu is.

6. Filosoferen is mentaal metaboliseren; nodig dus.

7. Lage verkiezingsopkomsten geven blijk van het feit dat burgers hun betrokkenheid laten varen; hierdoor verliest de democratie haar wortels.

8. Het is nog altijd beter om zwemmend ten onder te gaan, dan zwammend op de (voor)grond te staan.

9. Door de mens te typeren als een genen-plaatje wordt de kwalitatieve waarde van de mens naar de marge gedrukt.

10. Het is een verdrietige constatering dat de arbeidsvreugde omgekeerd evenredig is met het aantal zogenaamde managers.

11. Het is onmogelijk om veel kennis te vergaren en inzicht te verkrijgen, wanneer men enkel datgene leest waarin men behagen schept.

12. Milieuheffing, een heffing die te pas en te onpas wordt gevorderd om niet adequaat functionerende politici financieel in een zeker milieu te houden.

13. Voorafgaande aan het maken van de economie tot het centrum van het leven gaat de ontkenning dat de innerlijke bronnen van de mens de fonteinen van het geluk wel eens zouden kunnen zijn.

14. Zonder spontaniteit geen humaniteit.

15. De nacht eindigt wanneer men in het gelaat van de medemens broeders en zusters ontwaart.

16. Ons bestaan wordt ontsloten door de tijd; maar ondanks alle wetenschappelijk gesnuffel, wat is nu eigenlijk de ons toegemeten tijd ?

Stellingen behorend bij het proefschrift

FEM based soil stress and strain analyses aimed at plant growth factors

Albert Barneveld

Wageningen, 2 mei 2000

Aan Gerline

Abstract

During vehicular traffic on agricultural soils, the soil is subjected to a loading process which finally results into a change of micro-factors, such as the amount and distribution of water, solid parts or bounds, not arising from the soil water, between these solid parts in the soil. Derivations of the micro-factors are the so-called soil qualities like coefficient of oxygen diffusion and water permeability, moisture characteristic, root penetration resistance and the coefficient of heat conductivity. Seeds and plants need a specific set of values of these soil qualities to grow properly.

The loading process of the soil is simulated through an impression of a strip into the soil with the help of a finite element method. Description is given of stress and strain theories with respect to a cubical soil body, the elastic-perfectly-plastic Mohr-Coulomb model, the soil-material interface and finite and interface elements of the used finite element program Plaxis. Derivation of soil model parameters for the finite element program Plaxis is given in case of a presented reference soil, a wet moderately heavy river clay with an entrapped air percentage of 5 %. Beside soil model parameters of the Mohr-Coulomb model, attention is given to soil model parameters of the elastic region of the Plaxis-Cap model.

A reference soil-load system is presented with corresponding finite element input. For handling the large amount of finite element output results, the stress and strain analysis program Trestana is developed. Characteristic of the program is that three-dimensional plots of quantities can be presented against the deformed mesh as ground surface, without loosing information through the use of smoothing procedures.

Finally, single and composite quantities are presented which can serve as building blocks for constructing so-called kneading numbers of soil. This all in view of the idea that changes of kneading numbers correlate reasonably with the changes of the soil qualities.

Contents

1 Introduction

When vehicular traffic, even in the case of trampling animals, takes place on agricultural soils, the soil is subjected to a loading process which finally results into a change of micro-factors of the soil. By micro-factors is meant the amount and distribution of water, solid parts or bounds, not arising from the soil water, between these solid parts in the soil. Derivatives of the micro-factors are the so-called soil qualities. Soil qualities are understood to mean properties like :
- coefficient of oxygen diffusion
- coefficient of water permeability
- moisture characteristic
- root penetration resistance
- coefficient of heat conductivity.

Seeds and plants need a specific set of values of these soil qualities to grow properly. Seeds and plants react immediately on the slightest change of one of the values of the soil qualities. Most of the time the reaction is a decrease of the growth of the seeds and plants. For example, sugar beet harvesting with a heavy wheel-equipped harvester in autumn on wet clayey soil might cause structure degradation. In the worst case the coefficient of oxygen diffusion and water permeability decrease so dramatically that in the following year(s) no plant growth is possible at all. It is obvious that this must be avoided anytime. Therefore there will be searched at relations between loading processes of the agricultural soil and the effect on the change of soil qualities, to create the possibility of predicting the change of soil qualities on base of an expected loading process of the soil under consideration.

Mostly all of the loading processes in agriculture are dynamic processes, i.c. soil under a moving tyre. Because of the must of managing, confining and simplifying the loading process, this research is based on a special case of a general three-dimensional state, the plane strain situation, with the loading process simulated as a strip impression into the soil. Simulation calculations of the strip impression into the soil are made on basis of a finite element method. The finite element program Plaxis is finally selected. Characteristics of Plaxis are :
- finite element code for modelling soil and rock behaviour of geotechnical problems
- scientific underpinning through verification, validation and publication in well-known scientific journals
- user-friendly powerful tool through robust and automatic calculation procedures and interactive menus combined with direct graphical checks
- good technical support
- possibility to extend the basic program with a special module on request.

On basis of the finite element results of the simulated strip impression into the soil, deformation and stress analyses can be made to help enlighten the complex field of agricultural tyre-soil interaction.

1.1   Aims of the research

The aims of the research are given below :
- simulation of an agricultural loading process with a finite element method
- development of a deformation and stress analysis program with the finite element results as input
- development of a program to visualise large amounts of stress and strain analysis data
- investigation of relevant quantities being useful to construct composite quantities, so-called kneading numbers.

1.2   Contents of this dissertation

In chapter 2 stresses and strains with respect to a cubical soil body are described. Here also the term treatment field under consideration is introduced, which can be subdivided into a displacement field, i.c. translation and rotation, and deformation field, i.c. distortion and volume change.

Chapter 3 deals with non-hardening models. Emphasis lies on the elastic-perfectly-plastic Mohr-Coulomb model, because this model is the base of the finite element simulations.

Chapter 4 deals with the interface between soil and material, because this interface is playing a key role in agriculture.

In chapter 5 the finite and interface elements of the used finite element program Plaxis are described.

Chapter 6 deals with the derivation of soil model parameters for the finite element program Plaxis in case of a presented reference soil. Beside soil model parameters of the Mohr-Coulomb model, attention is given to a specific soil model parameter of the elastic region of the Plaxis- Cap model.

In chapter 7 the used extended Plaxis version and the treatment and stress analysis program Trestana are examined.

In chapter 8 a reference soil-load system is presented with corresponding Plaxis finite element input. Subsequently, a detailed treatment and stress analysis is given based on the program Trestana. Furthermore, a three-dimensional visualisation of the results is described and presented. At last composite quantities, so-called kneading numbers, are presented.

Chapter 9 contains some general considerations on the dissertation subjects and recommendations for future research.

2   Stress and deformation analysis

In the context of this dissertation knowledge of stress and strain of a soil body is essential, but also complex. Therefore attention will initially be focussed on the stress of the soil body. Afterwards attention will be focussed on strain because it is the strain that is directly related to the stress. The description of the change in distance between a few adjacent points of the soil body that is being considered is the key to the analysis of deformation and will therefore be discussed in detail. The text is making use of parts of Atkinson & Bransby, 1978, Ford, 1963 and Fung, 1965. The beginning of this chapter is devoted to basics with respect to the material soil required throughout this dissertation.

2.1   Basics with respect to soil

Let's take a closer look at the deformation of agricultural soil under a moving tyre in a soil-vehicle system as given in figure 2.1. Undisturbed soil that is being approached by a tyre may be considered to be composed of small elemental volumes, cubes, arranged in such a way that their angular points form a 3-dimensional cubic grid of horizontal layers of cube rows parallel to the direction of wheel travel. Deformation of a volume element starts as soon as it enters the zone influenced by the tyre and deformation stops as soon as the element leaves the zone of influence. Looking at all the cubes under the tyre in figure 2.1, the soil deformation field at a particular time t is non-homogeneous. Choosing the soil cube size sufficiently small so that the state of deformation is not varying from point to point and the strains are infinitesimal, the deformation field in this cube is a homogeneous deformation field.
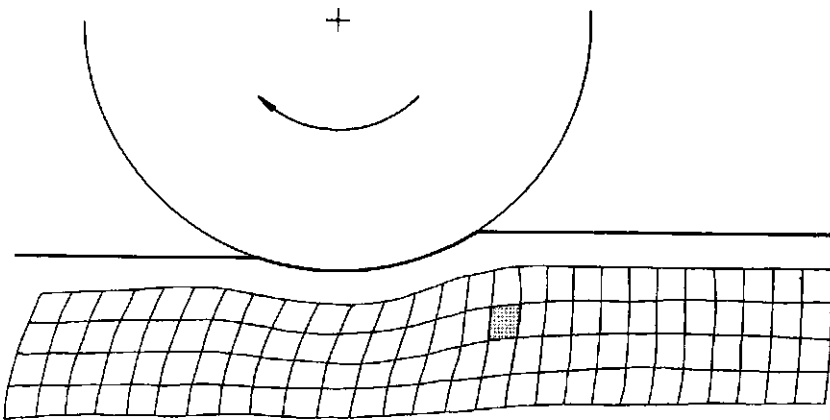

Figure 2.1   Soil deformation pattern under a moving tyre at time t.

Consider one cube of the undisturbed part of the soil. This soil cube, in its general form, is composed of a complex conglomeration of discrete particles, in a complete array of varying shapes and orientations. However, these micro-level structures are ignored and there is assumed that the discontinuous structure of the soil cube may be replaced by a smoothed out hypothetical continuum. Every portion of this continuum, however small, is assumed to exhibit macroscopic physical properties which are essentially properties of the bulk material.
In particular, the physical characteristics of material contained within an infinitesimal volume element, e.g. a soil cube, are assumed to be the same as those determined experimentally from measurements on a soil body with finite dimensions.
Assumptions that have been made underlying this concept are :
- material is continuously distributed in the region of space under consideration; soil cubes merge continuously into their neighbouring soil cubes
- homogeneity of the material; same equations apply throughout the material or material layer
- isotropy of the material; material properties in an arbitrary configuration of the material show no directional effect.
These assumptions bring into conformity the continuous space of mathematical analysis and the material points of the soil cube.

2.2 Stress analysis

Considering sufficiently small elemental volumes, in which the strain can be considered as homogeneous, the stress acting on any arbitrary plane in this volume can be considered as constant. The intensity of the stress on any arbitrary plane depends upon the orientation of the plane in space. This means that, to define a stress completely, it is not only necessary to know the intensity and direction of the stress, but also the direction of the plane on which it acts. This brings into conformity that stress is a tensor quantity.

Theoretically, there can be two types of force systems acting on a soil cube :
- body forces   : these develop without the agency of physical contact, for example a rotary cultivator where an acceleration force is caused by rotating the tine at high speed
- surface forces   : these exist only by virtue of the pressure between soil bodies and act over a surface; they are also called surface tractions.

Surface forces can be resolved into :
- normal stresses : stresses acting in the normal direction of a particular plane of the body on which the surface forces act (direct stresses)
- shear stresses   : stresses acting tangentially in the plane (indirect stresses).

According to mechanics body forces and surface forces must be in equilibrium. In soil mechanics body forces other than gravity are generally not taken into account. In this

discussion the elements are always relatively small. Then the gravity is small compared with stresses (surface tractions) arising from externally applied forces and has been ignored therefore.

Before the discussion of the analysis of stress starts, the sign convention for stress and rotation is given in figure 2.2. A Cartesian *xyz*-coordinate system is used. Tensile stresses and anticlockwise rotation are taken as positive. For normal and shear stresses the first subscript denotes the direction of a normal to the plane on which its acts. The second subscript refers to the direction in which the stress acts.
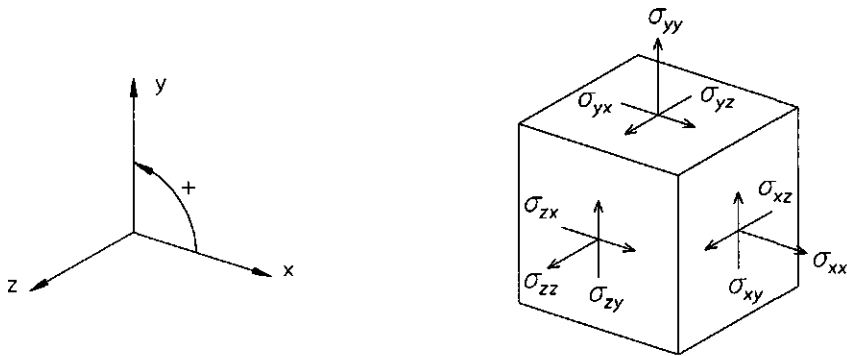
Figure 2.2 Positive coordinate system and sign convention for
rotation and stresses.

There is assumed that imaginary sections can be made in a soil specimen for which the forces over the sections, to maintain the material in equilibrium, can be equated and that it is possible to cut out an imaginary cube of the material and the surrounding material is replaced by surface tractions to maintain it in equilibrium; such surface tractions are the same as those existing between the cube and surrounding material when in position within the material. Furthermore, the elemental cube must be imagined to be of infinitesimal dimensions, so that the stresses can be taken constant over the very small areas of the faces of the cube. This is the base of the stress analysis.

Especially the following discussion concerns with the resolution of stresses into their components in certain directions in space, so that the resultant stress corresponds in magnitude and direction with that required for equilibrium of this cubical element.

Explanation of the analysis of stress will be given by establishing the general relationships between the stress parameters and the stresses on any plane oblique to the coordinate directions. Consider the cubical element in figure 2.3 to be in equilibrium under the stresses σ_{xx}, σ_{yy}, σ_{zz}, σ_{xy}, σ_{yz} and σ_{zx} and sufficiently small to represent stress at a point. Using the equilibrium conditions it can be shown that $\sigma_{xy} = \sigma_{yx}$, $\sigma_{yz} = \sigma_{zy}$ and $\sigma_{zx} = \sigma_{xz}$.
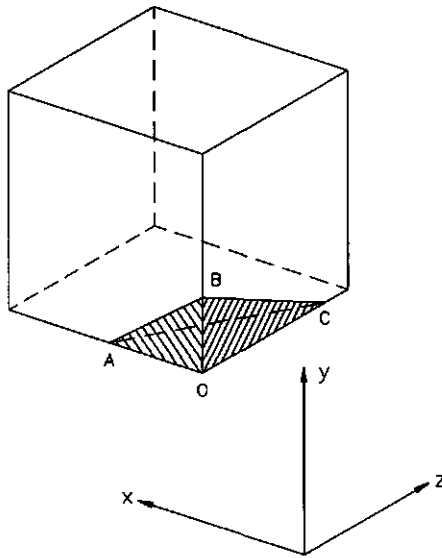
Figure 2.3 Cubical element with an imaginary tetrahedron cut off.

A plane oblique to the coordinate directions with corresponding triangular coordinate planes is given by the hatched part of the cubical element. Because the cubical element is in equilibrium, the tetrahedron cut off between this plane and the coordinate planes AOB, BOC and COA is also in equilibrium. Therefore it can be separated from the cubical element, as in figure 2.4, and the stress components on ABC required for equilibrium can be determined.
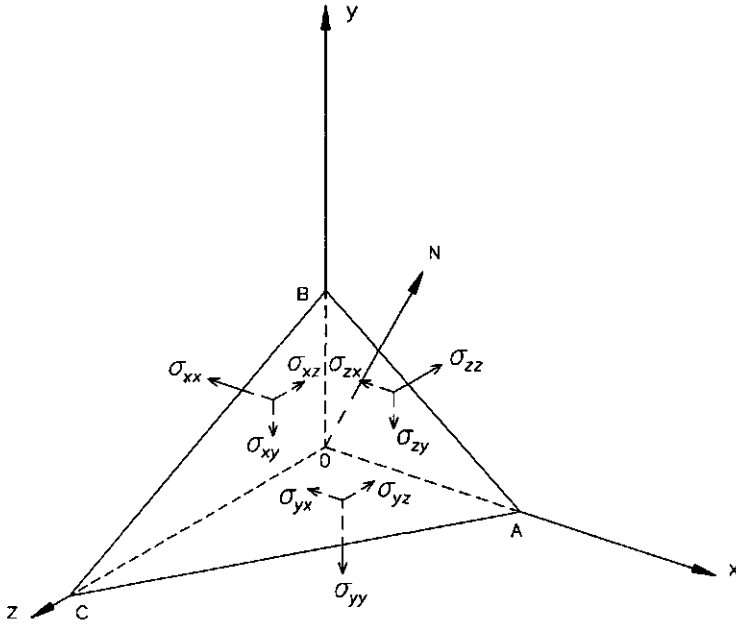
Figure 2.4   Tetrahedron with corresponding stresses for equilibrium on
the triangular coordinate planes.

The line ON in figure 2.4 is the normal to the plane ABC. Its direction is given if the three
angles α, β and γ, made with the coordinate axis x, y and z, are given.
These angles, represented by l, m and n, are called the direction cosines of line ON

$$
\begin{aligned}
l &= \cos \alpha \\
m &= \cos \beta \\
n &= \cos \gamma
\end{aligned}
\tag{2.1}
$$

Any point P on line ON with distance r from the origin, can be expressed in terms of its
coordinates

$$
\begin{aligned}
x &= r \cos \alpha &= r\,l \\
y &= r \cos \beta &= r\,m \\
z &= r \cos \gamma &= r\,n
\end{aligned}
\tag{2.2}
$$

The stress components in figure 2.4, acting on the triangular coordinate planes, will have a
resultant stress σ on the plane ABC, figure 2.5. This resultant stress will not, in general, be
normal to the plane. It can therefore be resolved into a stress normal to and one tangential to

the plane *ABC*. Let the normal component of the resultant stress σ be σ_n (direct stress) and the tangential component be σ_s (shear stress). Then

$$\sigma^2 = \sigma_n^2 + \sigma_s^2 \tag{2.3}$$

and σ_n will have the same direction cosines as the plane *ABC*.
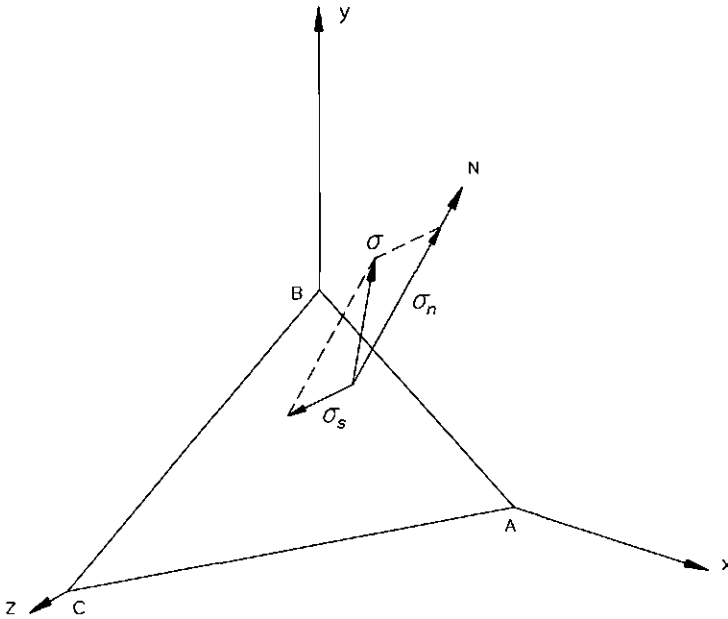
Figure 2.5 Resultant stress σ on the plane *ABC* resolved into a normal
and tangential component.

The stress σ can also be resolved in the coordinate directions *x, y* and *z* (figure 2.6), with the corresponding stresses σ_x, σ_y and σ_z

$$\sigma^2 = \sigma_x^2 + \sigma_y^2 + \sigma_z^2 \tag{2.4}$$
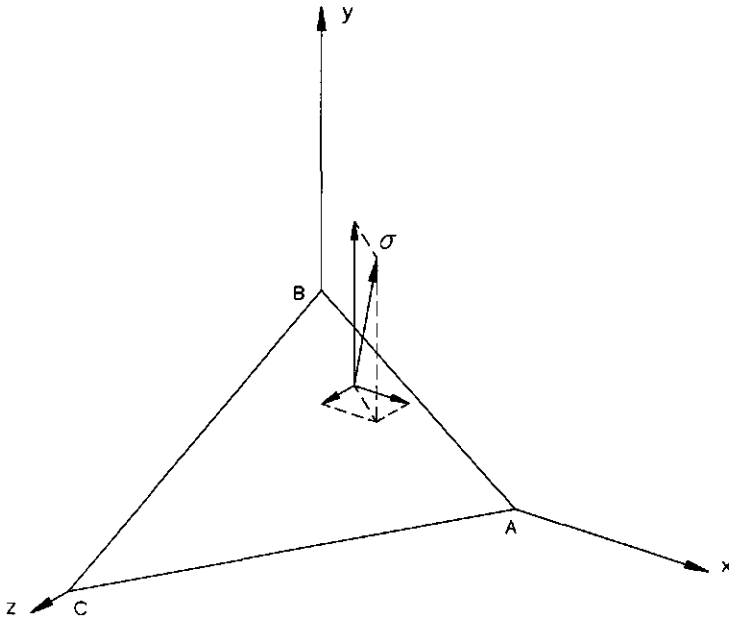
Figure 2.6 Resultant stress resolved into coordinate directions x, y and z.

Consider the equilibrium in the x-direction, where δA is the very small area of plane ABC

$$\sigma_x \times \delta A = \sigma_{xx} \left(\delta A \times l \right) + \sigma_{xy} \left(\delta A \times m \right) + \sigma_{xz} \left(\delta A \times n \right) \tag{2.5}$$

which results into

$$\sigma_x = \sigma_{xx} \, l + \sigma_{xy} \, m + \sigma_{xz} \, n \tag{2.6}$$

Similarly

$$\sigma_y = \sigma_{yx} \, l + \sigma_{yy} \, m + \sigma_{xz} \, n$$
$$\sigma_z = \sigma_{zx} \, l + \sigma_{zy} \, m + \sigma_{zz} \, n$$

Normal stress σ_n can be expressed in terms of σ_x, σ_y and σ_z

$$\sigma_n \times \delta A = \left(\sigma_x \, l + \sigma_y \, m + \sigma_z \, n \right) \delta A \tag{2.7}$$

i.e.

$$\sigma_n = \sigma_x \, l + \sigma_y \, m + \sigma_z \, n \tag{2.8}$$

Using equations 2.6 and 2.8 finally results into

$$\sigma_n = \sigma_{xx} \, l^2 + \sigma_{yy} \, m^2 + \sigma_{zz} \, n^2 + 2\,\sigma_{xy} \, lm + 2\,\sigma_{zy} \, mn + 2\,\sigma_{zx} \, nl \tag{2.9}$$

Finally, the shear stress σ_s on the plane ABC can be calculated by

$$\sigma_s^2 = \sigma_x^2 + \sigma_y^2 + \sigma_z^2 - \sigma_n^2 \tag{2.10}$$

Note that the resultant stress σ is not in fact the state of stress at a point, it is the resultant stress needed for equilibrium on a particular plane with direction cosines l, m and n.

Concept of principal stresses and principal directions

Of particular interest are the so-called principal stresses. A principal stress is defined as the normal stress on a plane in which the shear stress has vanished. Such a plane is called principal plane, its normal a principal direction. In three dimensions it is always possible to rotate the coordinate system in such a way that there are three mutually perpendicular planes found, such that all three shear stresses are simultaneously zero and there only remain three principal stresses with their principal directions. Consider the special stress state of an infinitesimal cube of figure 2.7a.

a]

b]
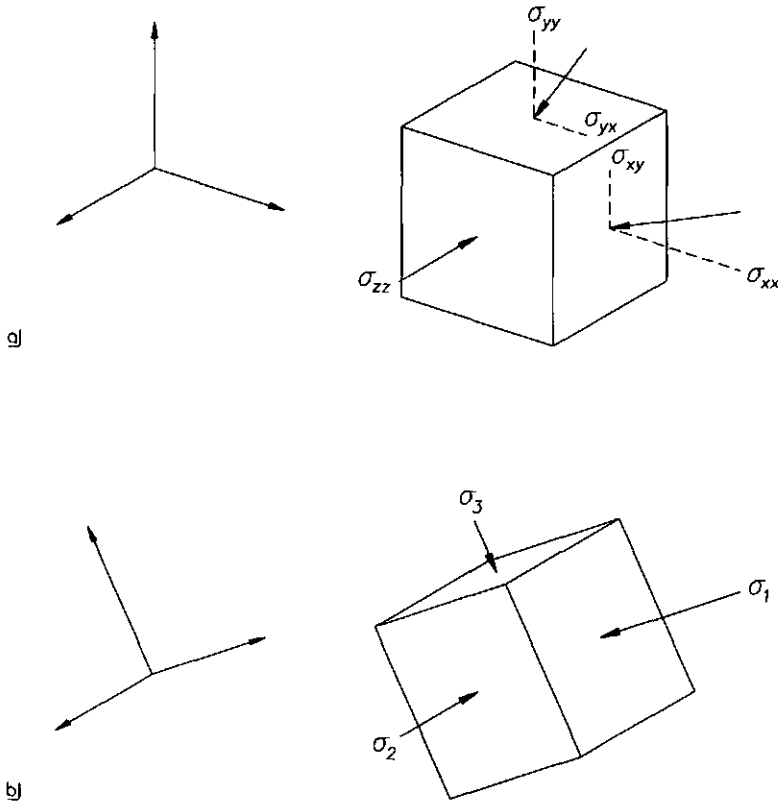
Figure 2.7 Infinitesimal small soil cube : arbitrary state of stress (a),
principal state of stress (b).

In this situation there is only a shear stress parallel to the xy-plane. Therefore the stress in the in the z-direction is already a principal stress. To let the remaining shear stress vanish in the xy-plane it is only necessary to rotate the coordinate system round the z-axis. The result of this rotation, three principal planes with their corresponding principal stresses and principal directions, is shown in figure 2.7b.

In figure 2.7a one principal direction is known with a matching principal stress σ_2. Generally for a principal stress σ on a principal plane states

$$
\begin{aligned}
\sigma_x &= \sigma_n\, l &= \sigma l \\
\sigma_y &= \sigma_n\, m &= \sigma m \\
\sigma_z &= \sigma_n\, n &= \sigma n
\end{aligned}
\qquad (2.11)
$$

from which results

$$\begin{aligned}
\sigma_x \ - \ \sigma l \ &= \ 0 \\
\sigma_y \ - \ \sigma m \ &= \ 0 \\
\sigma_z \ - \ \sigma n \ &= \ 0
\end{aligned} \qquad (2.12)$$

where σ_x is a part of the resolution of the principal stress into the x-direction etceteras.

According to 2.6 the stresses σ_x, σ_y and σ_z can also be expressed in stress components acting on the coordinate planes. Combining the equations of 2.6 with 2.12 results into

$$\begin{aligned}
\left(\sigma_{xx} - \sigma\right) l \ + \ \sigma_{xy} \ m \ + \ \sigma_{xz} \ n \ &= \ 0 \\
\sigma_{yx} \ l \ + \ \left(\sigma_{yy} - \sigma\right) m \ + \ \sigma_{yz} \ n \ &= \ 0 \\
\sigma_{zx} \ l \ + \ \sigma_{zy} \ m \ + \ \left(\sigma_{zz} - \sigma\right) n \ &= \ 0
\end{aligned} \qquad (2.13)$$

To calculate the principal stresses, these three linear equations in the direction cosines can be solved with Cramer's rule

$$\begin{vmatrix}
\sigma_{xx} - \sigma & \sigma_{xy} & \sigma_{xz} \\
\sigma_{yx} & \sigma_{yy} - \sigma & \sigma_{yz} \\
\sigma_{zx} & \sigma_{zy} & \sigma_{zz} - \sigma
\end{vmatrix} = 0 \qquad (2.14)$$

Expanding this symmetrical determinant gives three real values for σ, the principal stresses σ_1, σ_2 and σ_3. The principal directions of σ_1, σ_2 and σ_3 with respect to the space axes x, y and z, are obtained from 2.13 by substituting for σ the values σ_1, σ_2 and σ_3 in turn. Three sets of principal stress direction cosines are obtained : l_1, m_1, n_1 for σ_1; l_2, m_2, n_2 for σ_2 and l_3, m_3, n_3 for σ_3.
The three principal directions are mutually perpendicular which will be demonstrated for two principal stress directions corresponding to σ_1 and σ_2.
Substituting 2.13 with σ_1, l_1, m_1 and n_1 and multiply 2.13a by l_2, 2.13b by m_2 and 2.13c by n_2 gives the equations

$$\begin{aligned}
\left(\sigma_{xx} - \sigma_1\right) l_1 l_2 \ + \ \sigma_{xy} \ l_2 m_1 \ + \ \sigma_{xz} \ l_2 n_1 \ &= \ 0 \\
\sigma_{yx} \ l_1 m_2 \ + \ \left(\sigma_{yy} - \sigma\right) m_1 m_2 \ + \ \sigma_{yz} \ m_2 n_1 \ &= \ 0 \\
\sigma_{zx} \ l_1 n_2 \ + \ \sigma_{zy} \ m_1 n_2 \ + \ \left(\sigma_{zz} - \sigma\right) n_1 n_2 \ &= \ 0
\end{aligned} \qquad (2.15)$$

The same equations are constructed through substituting 2.13 with σ_2, l_2, m_2 and n_2, and multiplying 2.13a by l_1, 2.13b by m_1 and 2.13c by n_1. The first set of equations (2.15) are now subtracted from the second set, and after rearranging the terms this gives :

$$\left(\sigma_1 - \sigma_2\right)\left\{l_1 l_2 + m_1 m_2 + n_1 n_2\right\} = 0 \tag{2.16}$$

Mostly σ_1 is not equal to σ_2 (unless the state of hydrostatic stress) and accordingly

$$l_1 l_2 + m_1 m_2 + n_1 n_2 = 0 \tag{2.17}$$

indicating the directions of σ_1 and σ_2 are perpendicular. Similar results are obtained for σ_2 and σ_3 and for σ_3 and σ_1.

2.3 Deformation analysis

Going back to the deformation pattern under the moving tyre at time t of figure 2.1 and taking a close look at the hatched soil cube in this figure. A vertical plane of this soil cube, in the direction of travel, before and after deformation is shown in figure 2.8.
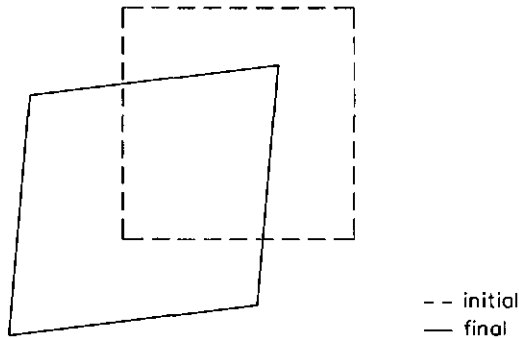
Figure 2.8 Soil cube before and after deformation.

The dashed object of figure 2.8 depicts the initial rectangular parallelepiped of the undisturbed soil. The solid object depicts a possible effect of an approaching tyre; the initial rectangular deforms into a rhomboid. When such a continuous soil body changes its configuration under some physical action, the assumption will be imposed that the change is continuous. During the deformation of the rectangular into the rhomboid, under the assumption of a homogeneous deformation field, three phenomena attract attention :
- opposite sides stay parallel to each other
- straightness of each side is conserved
- conservation of proportionality between parts of any side, figure 2.9.
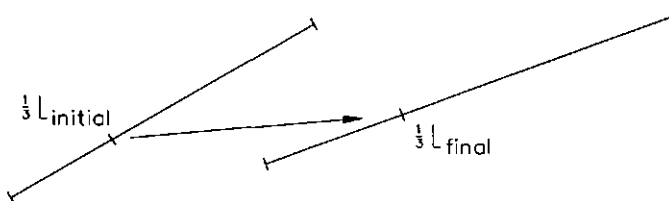
Figure 2.9 Proportionality of a line element.

In 2-dimensional representation the deformation of the soil cube can be completely recorded by recording the path of three angular points, not all lying in one plane.

At this stage it is useful to give the sign convention for strain and rotation, figure 2.10. In this Cartesian *xyz*-coordinate system tensile strain and anticlockwise rotation are taken as positive. For normal and shear strain the first subscript denotes the direction of a normal to the plane on which it acts. The second subscript refers to the direction in which the strain acts.
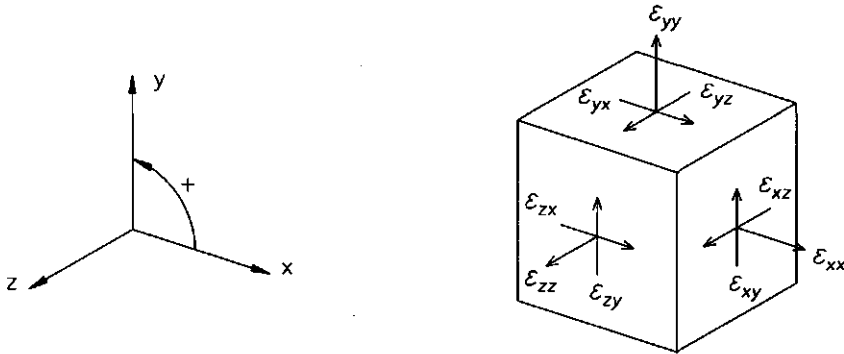
Figure 2.10 Positive coordinate system and sign convention for rotation and strains.

2.3.1 Strain in a displacement field

To get a theoretical approach of what is happening between the initial state and the final state of a soil cube, the change of state of the cube is divided into four elemental reactions : translation, rotation, distortion and volume change. Definitions of these elemental reactions, which will be used from now on, are :
- translation   : linear displacement of the element
- rotation   : angular displacement of the element
- distortion   : change of shape of the element without volume change
- volume change : change in length in all directions of the element without change of shape.

The term displacement is defined as a combination of translation and rotation, whereas the term deformation is defined as a combination of distortion and volume change. The change of state between the initial and final state of a soil element is defined as treatment, which represents the combination of all the four elemental reaction components to come to the final state of the element. Consequence of above subdivision is that it is better to speak about a treatment field under a subject of consideration, for example the tyre, and that this treatment field can be split up into a displacement and a deformation field, figure 2.11.
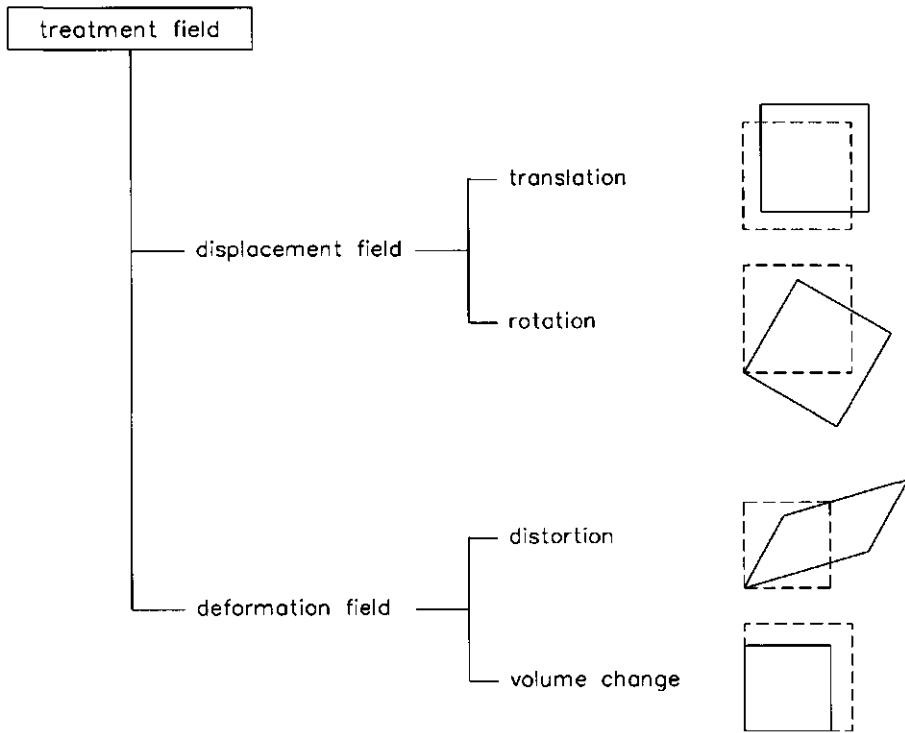
Figure 2.11 Diagram of the subdivision of a treatment field into elemental reactions.

The fact that there is homogeneous strain assumed with infinitesimal strains within the soil element, makes that the sequence of division of the treatment into elemental reactions can be arbitrarily.

Consider the 2-dimensional representation of a soil cube before and after treatment of a tyre. Because of dealing with homogeneous strain within this soil cube, which means that straight lines remain straight and parallel lines remain parallel after straining, only the left and bottom side of the cube are represented. These two sides and their position to each other are described by P, S and Q, figure 2.12.
Before treatment these three corners form two orthogonal fibres PS and PQ. After treatment the two fibres $P'S'$ and $P'Q'$ form one half of a rhomboid.
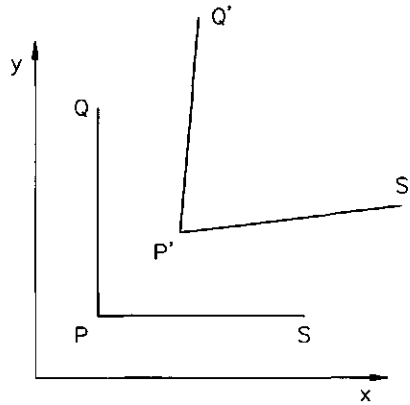
Figure 2.12 Schematic representation of one half of a soil cube before
and after treatment.

2.3.2 Definition of *u* and *v*

Consider a point P with initial coordinates (x, y), figure 2.12. Subsequently point P moves to
P' and by definition the coordinates of P' are $(x + u)$ and $(y + v)$, since the displacements of P
are u and v. Both u and v are continuous functions of x and y.

2.3.3 Translation

Translation of the rectangular parallelepiped of figure 2.12 is represented by the imaginary
vector PP'.

2.3.4 Distortion

The length of fibre PS is δx. The fibre PS is supposed to be very small so that the changes in
displacement over the length δx can be considered proportional to δx. Projecting line $P'S'$
on to a line parallel to PS, the length $P'S^*$ is, figure 2.13,

$$\delta x + \left(\frac{\partial u}{\partial x} \right) \delta x \tag{2.18}$$

where ∂ is the partial differentiation sign.

This means the change in length of δx is the rate of change of the displacement u with respect to x times the initial length being considered, δx.
However, the length $P'S'$ is slightly longer than $\delta x + (\partial u/\partial x)\,\delta x$ because v changes with movement in the x direction; v is not only a function of its own coordinate direction y, but will also depend upon x.
Moving a distance δx in the x direction and knowing that v may be a function of x, S' may move in the y direction by $(\partial v/\partial x)\,\delta x$.

Therefore

$$(P'S') = \left(\delta x + \left(\frac{\partial u}{\partial x}\right)\delta x\right)^2 + \left(\frac{\partial v}{\partial x}\,\delta x\right)^2$$

$$= \left(\delta x\right)^2\left(1 + 2\frac{\partial u}{\partial x} + \left(\frac{\partial u}{\partial x}\right)^2 + \left(\frac{\partial v}{\partial x}\right)^2\right) \tag{2.19}$$

Defining

$$e_{xx} = \frac{\partial u}{\partial x} + 0.5\left(\left(\frac{\partial u}{\partial x}\right)^2 + \left(\frac{\partial v}{\partial x}\right)^2\right) \tag{2.20}$$

then, by the usual definition of strain

$$\text{strain in } PS = \frac{P'S' - PS}{PS} = \frac{P'S'}{PS} - 1 = \sqrt{1 + 2\,e_{xx}} - 1 \tag{2.21}$$

Expanding $\left(\sqrt{1 + 2\,e_{xx}} - 1\right)$ results into

$$\frac{P'S'}{PS} - 1 = 1 + e_{xx} + \text{ higher order terms} \ldots - 1$$

$$= e_{xx} + \text{ higher order terms} \tag{2.22}$$

If strains are small, the higher order terms can be neglected and strain in PS equals 2.20.

If strains are infinitesimal, which is the case in this dissertation, the squares of terms of 2.20 can also be neglected. Thus the extension of $P'S'$ can be taken equal to the extension of $P'S^*$ and strain in PS is

$$e_{xx} = \frac{P'S^* - PS}{PS} = \frac{\delta x + (\partial u / \partial x)\,\delta x - \delta x}{\delta x}$$

$$= \frac{\partial u}{\partial x} \tag{2.23}$$

For the y coordinate a similar expression can be obtained

$$e_{yy} = \frac{\partial v}{\partial y} \tag{2.24}$$

The strains e_{xx} and e_{yy} are called direct strains.

A shear strain is the distortion corresponding to the sliding of plane layers over each other. Thus, in figure 2.8 shear strain distorts the rectangular parallelepiped into the rhomboid. Shear strain is measured as the tangential displacement of layers unit distance apart. Consider the shear in the xy-plane of figure 2.13.
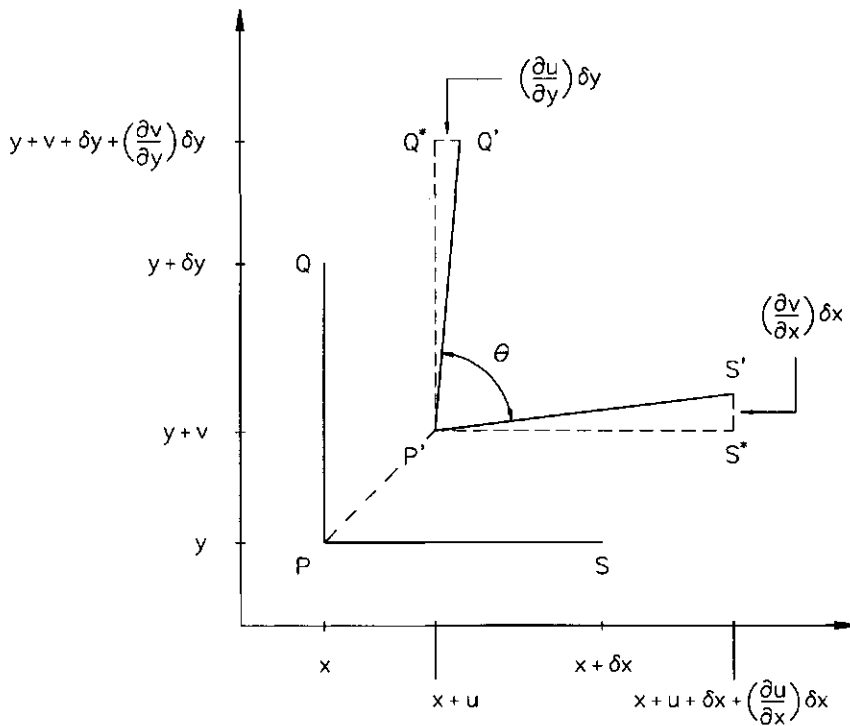
Figure 2.13 Derivation of the strain components.

The change in right angle QPS on straining is defined as follows. Calling the angular change γ means $\gamma = (\pi/2) - \theta$ where θ is the angle between $P'Q'$ and $P'S'$. If l and m are the direction cosines of $P'Q'$ and l' and m' those of $P'S'$, then

$$\cos \theta = ll' + mm' \tag{2.25}$$

In terms of figure 2.13

$$l = \frac{P'S^*}{P'S'} = \frac{\delta x + (\partial u/\partial x)\, \delta x}{P'S'} \tag{2.26}$$

$$m = \frac{(\partial v/\partial x)\, \delta x}{P'S'} \tag{2.27}$$

$$l' = \frac{(\partial u/\partial y)\, \delta y}{P'Q'} \tag{2.28}$$

$$m' = \frac{\delta y + (\partial v/\partial y)\, \delta y}{P'Q'} \tag{2.29}$$

But

$$P'S' = \delta x \sqrt{1 + 2\, e_{xx}}$$
$$= \text{the strained length of } \delta x \tag{2.30}$$

and

$$P'Q' = \delta y \sqrt{1 + 2\, e_{yy}} \tag{2.31}$$

Thus

$$\cos \theta = \frac{1}{\sqrt{1 + 2\, e_{xx}}\ \sqrt{1 + 2\, e_{yy}}}\left\{\frac{\partial u}{\partial y} + \frac{\partial v}{\partial x} + \frac{\partial^2 u}{\partial x \partial y} + \frac{\partial^2 v}{\partial x \partial y}\right\} \tag{2.32}$$

Using $\cos \theta = \cos\left((\pi/2) - \gamma\right) = \sin \gamma$, one finally gets

$$\frac{\sin \gamma}{\cos \gamma} * \left(\sqrt{1 + 2\, e_{xx}}\ \sqrt{1 + 2\, e_{yy}}\right) \cos \gamma = \frac{\partial u}{\partial y} + \frac{\partial v}{\partial x} + \frac{\partial^2 u}{\partial x \partial y} + \frac{\partial^2 v}{\partial x \partial y} \tag{2.33}$$

Physically, this equation can be interpreted as the shear strain *tan γ* * [area of the strained surface *P'Q'R'S'*]. Since small displacements are considered *tan γ* ≈ *γ* , figure 2.14.
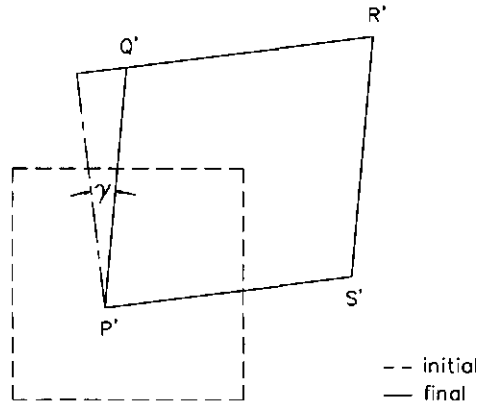
Figure 2.14 Distortion of a soil cube, initial and final state.

So the expression *tan γ* * [area of the strained surface *P'Q'R'S'*] is defined by

$$ e_{xy} = \left(\frac{\partial u}{\partial y} + \frac{\partial v}{\partial x} + \frac{\partial^2 u}{\partial x \partial y} + \frac{\partial^2 v}{\partial x \partial y} \right) \tag{2.34} $$

For infinitesimal strain the squares of terms can here also be neglected

$$ e_{xy} = \left(\frac{\partial u}{\partial y} + \frac{\partial v}{\partial x} \right) \tag{2.35} $$

Comparing strain equation 2.35 with the corresponding stress equation 2.9 there is a difference in the shear terms. In equation 2.9 the term is $(2\,\sigma_{xy})$, whereas in equation 2.35 the term is e_{xy}. It is a matter of definition of both shear stress and shear strain. Because of making use of matrix algebra throughout this dissertation, the mathematical expression for the shear strain is defined by

$$ e_{xy} = 0.5 \left(\frac{\partial u}{\partial y} + \frac{\partial v}{\partial x} \right) \tag{2.36} $$

and in this case the analogy is complete.

2.3.5 Rotation

It was shown in figure 2.13 that the rotation of the fibre *PS* was $\partial v/\partial x$ and the rotation of fibre *PQ* was $\partial u/\partial y$.

The rotation of the element *QPS* is defined as

$$\omega_{xy} = 0.5\left(\frac{\partial v}{\partial x} - \frac{\partial u}{\partial y}\right)$$
                                                                                                    (2.37)

and is shown in figure 2.15.
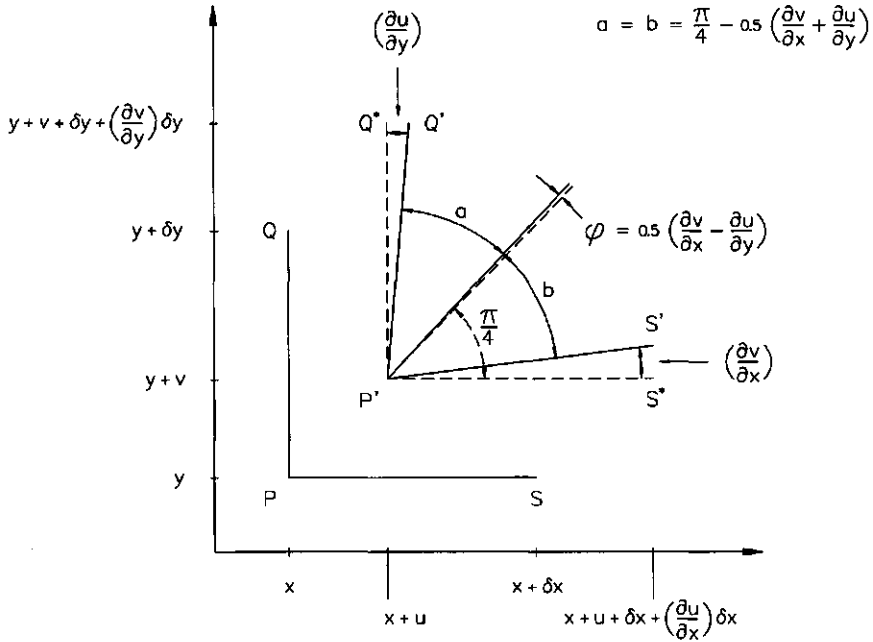
Figure 2.15 Derivation of the rotation components.

The suffix *xy* indicates that the rotation is in the *xy*-plane around the *z*-axis. The quantity ω_{xy} is in fact the rotation of the bisector of the angle *Q'P'S'* and this can be taken as defining the amount the element rotates as a rigid body.

Distinction between shear strain and rigid body rotation

The coordinates of P' are $(x+u)$ and $(y+v)$. Those of R' will be $(x+\delta x+u+\delta u)$ and $(y+\delta y+v+\delta v)$, where δu and δv are the increments in u and v over the lengths δx and δy. The term δu then represents the total displacement in the x-direction of point R' relative to P'

$$\delta u = \frac{\partial u}{\partial x} \delta x + \frac{\partial u}{\partial y} \delta y \tag{2.38}$$

Similarly, in the y-direction prevails

$$\delta v = \frac{\partial v}{\partial x} \delta x + \frac{\partial v}{\partial y} \delta y \tag{2.39}$$

Looking again at the displacement in the x-direction of figure 2.13. Not all of the two angles $Q^*P'Q'$ and $S^*P'S'$ are shear strains, because the general displacements δu and δv by definition, contain also displacement corresponding to a rigid body rotation, which does not contribute to shear. Looking only at the displacement in the x-direction of Q owing to shear, thus the displacement of Q^* to Q' in figure 2.13,

$$\text{distance } Q^*Q' \cong \frac{\partial u}{\partial y} \delta y \tag{2.40}$$

This last term can be split up into a shear strain part and a rigid body rotation part :

$$\left(\frac{\partial u}{\partial y}\right) \partial y = \left\{ 0.5 \left(\frac{\partial u}{\partial y} + \frac{\partial v}{\partial x}\right) + 0.5 \left(\frac{\partial u}{\partial y} - \frac{\partial v}{\partial x}\right) \right\} \partial y$$
$$= \left(e_{xy} - \omega_{xy} \right) \partial y \tag{2.41}$$

Finally, equation 2.38 is rewritten

$$\delta u = e_{xx} \delta x - \omega_{xy} \delta y + e_{xy} \delta y \tag{2.42}$$

The term $-\omega_{xy} \delta y$ is the rigid body displacement of the bisector PR in the x-direction owing to rotation, so that the only part of the displacement which corresponds to material deformation is

$$e_{xx} \delta x + e_{xy} \delta y \tag{2.43}$$

Similarly, it can be found that

$$\left(\frac{\partial v}{\partial x}\right)\partial x = \left\{0.5\left(\frac{\partial v}{\partial x} + \frac{\partial u}{\partial y}\right) + 0.5\left(\frac{\partial v}{\partial x} - \frac{\partial u}{\partial y}\right)\right\}\partial x$$

$$= \left(e_{xy} + \omega_{xy}\right)\partial x \tag{2.44}$$

$$\delta v = e_{yy}\,\delta y + e_{xy}\,\delta x + \omega_{xy}\,\delta x \tag{2.45}$$

and the part of the displacement which corresponds to material deformation is

$$e_{yy}\,\delta y + e_{xy}\,\delta x$$

2.3.6 Volume change

Distortion does not cause a change of volume in three dimensions or change of area in two dimensions, only a change of shape. Responsible for the change of area are the direct strains. The direct strains are described by e_{xx} and e_{yy}. Initial lengths of a small element are δx and δy. After a treatment the final lengths become $(1 + e_{xx})\,\delta x$ and $(1 + e_{yy})\,\delta y$. The initial area is $\delta x\,\delta y$, whereas the final area is described by

$$\left(1 + e_{xx}\right)\left(1 + e_{yy}\right)\delta x\,\delta y \tag{2.46}$$

The area change, indicated by Δ is defined as the change of area per unit area

$$\Delta = \frac{\left(1 + e_{xx}\right)\left(1 + e_{yy}\right)\delta x\,\delta y - \delta x\,\delta y}{\delta x\,\delta y}$$

$$= e_{xx} + e_{yy} + e_{xx}e_{yy} \tag{2.47}$$

If strains are infinitesimal, the second order term can be neglected, which gives

$$\Delta = e_{xx} + e_{yy} \tag{2.48}$$

2.3.7 General remarks

Remarks and definitions in relation to distortion and rigid body rotation

Attention should be made if

$$\frac{\partial v}{\partial x} = -\frac{\partial u}{\partial y} \tag{2.49}$$

then distortion $e_{xy} = 0$ and ω_{xy} is indeed the angle in which the element is rotated as a rigid body.

Pure shear is a distortion, thus without volume change, that is equivalent to equal tensile and compressive principal strains on planes at 45° to the planes of shear (figure 2.16). If prevails

$$\frac{\partial v}{\partial x} = \frac{\partial u}{\partial y} \tag{2.50}$$

means that there is no rigid body rotation.
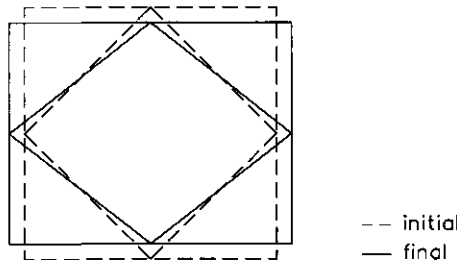
- - initial
— final

Figure 2.16 Pure shear, initial and final state.

It must be emphasised that, dependent of the orientation of the grid on an area element, the visual impression sometimes is completely different. Consider the inscribed and outscribed rectangular in the area element before and after treatment, figure 2.17. After treatment the inscribed rectangular parallelepiped gives the impression of only elongation and shortening, whereas the change of the outscribed rectangular parallelepiped into a rhomboid gives the impression of shear. This lack of clarity is not occurring by using the concept of principal directions.
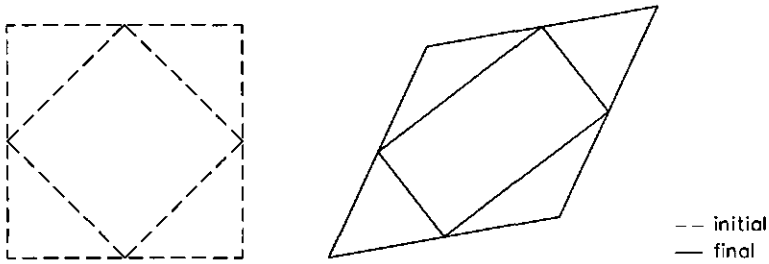
Figure 2.17 Grid effect on visual impression, initial and final state.

Simple shear is a special case of shear where

$$\frac{\partial v}{\partial x} = 0 \quad \text{or} \quad \frac{\partial u}{\partial y} = 0$$

The amount of distortion is the same as in the case of pure shear, different is the rigid body rotation which is not zero anymore, figure 2.18.
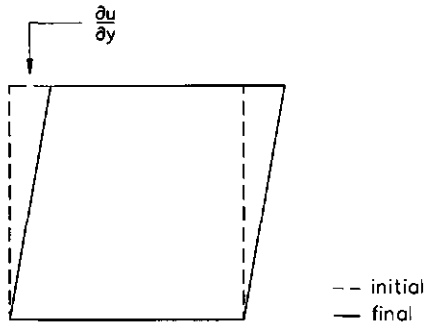
Figure 2.18 Simple shear, initial and final state.

Consequences of infinitesimal strains

The assumptions made before, e.g. the piece of soil is sufficiently small and the strains are infinitesimal, lead to considerable important consequences :
- *linear theory*
  Strains are described by linear expressions

$$e_{xx} = \frac{\partial u}{\partial x} \quad e_{yy} = \frac{\partial v}{\partial y}$$

$$e_{xy} = 0.5 \left(\frac{\partial u}{\partial y} + \frac{\partial v}{\partial x} \right)$$

- *principle of superposition*
  b_1 is the effect of a_1 and b_2 is the effect of a_2, the combined effect of $a_1 + a_2$ (in either order) will be $b_1 + b_2$

- *principal strains and directions*
  Also in the analysis of strain the so-called principal strains and principal directions are of particular interest. Four quantities are required to define a state of strain in two dimensions according to two coordinate axes fixed in space. During a very small deformation it is always possible to find two orthogonal axes passing through material points at time t which pass through the same material points and remain orthogonal after straining at time $t + \Delta t$. The principal axes of straining are defined as being this set of orthogonal axes. These axes are also the directions in which the strains have stationary values (maximum or minimum). The stationary values are called the principal strains, the corresponding directions principal directions

- *generalisation to three dimensions*
  Extension of the described analysis of strain to three dimensions is straightforward, although it is more complicated. In analogy to the stresses (section 2.2) it can be shown that $e_{xy} = e_{yx}$, $e_{yz} = e_{zy}$ and $e_{zx} = e_{xz}$.

Remarks with respect to treatment path

When soil is treated treatment-induced structural changes that make the physical properties of the considered soil cube change are expected. Consider a soil cube in a soil-vehicle system of figure 2.1. The initial shape of a soil cube is rectangular and a possible shape of the soil cube in the zone of influence of the tyre is given by the hatched soil cube in the already mentioned figure 2.1 (see also figure 2.8). The soil physical effect of the treatment endured by the soil cube cannot be determined uniquely by merely comparing its final shape with its initial shape, because the final shape can be obtained from the initial shape via an infinite number of different treatment paths.

Theoretically, there is always a unique shortest path to arrive at a given shape from another given shape before. When two shapes are compared and the occurred treatment is very small, it may be stated that the true path corresponds with the shortest path. Therefore, a relatively large treatment can be dealt with by dividing this treatment into a number of small steps in which the treatment in each step is sufficiently small. The relevant soil quantities of the whole treatment, found by adding up the calculated soil quantities for each small step on the basis of the shortest path assumption, is independent of the step number chosen, provided the steps are sufficiently small.

There are two principles of calculating strain in a treatment analysis. The true or natural vertical strain is defined by

$$\bar{e}_l = -\int_{l_f}^{l_i} \frac{dl}{l} = \ln\left(\frac{l_i}{l_f}\right) \tag{2.51}$$

wherein

$$i = \text{initial}$$
$$f = \text{final}$$

However, in this dissertation the treatment is split up into a finite number of small steps (n) in which during each step the treatment is small. This results in

$$\bar{e}_l = \sum_{j=1}^{n} \left(\Delta e_l\right)_j \tag{2.52}$$

wherein

$$\left(\Delta e_l\right)_j \text{ is the vertical strain of line } l \text{ in step } j$$

The technical vertical strain is defined by

$$e_l = \frac{l_i - l_f}{l_i} \tag{2.53}$$

Relation between the natural vertical and technical vertical strain, $\bar{e}_l$ and e_l respectively, is

$$\bar{e}_l = -\ln\left(1 - e_l\right) \tag{2.54}$$

3 Non-hardening models

In this chapter non-hardening models are described. The emphasis lies on the elastic-perfectly-plastic Mohr-Coulomb model (Vermeer & de Borst, 1984). This because stress and deformation analyses of which new quantities will be derived are based on finite element simulations with the constitutive Mohr-Coulomb model as foundation.

The Mohr-Coulomb model involves five elementary soil-model parameters, namely

Poisson's ratio	υ	} elasticity parameters
Young's modulus	E	
cohesion	c	} strength parameters
angle of internal friction	φ	
angle of dilatancy	ψ	} plastic volume change parameter

At last, the yielding criteria of Von Mises and Drucker-Prager are described.

3.1 Mohr-Coulomb

During a triaxial compression test, deformation of the soil sample occurs and there exist strains within the soil sample. In an arbitrary small step of the deformation, the total strain can be elastic or can be divided into an elastic and a plastic part. The last subdivision, total strain is the sum of an elastic and a plastic contribution, is the basic assumption in plasticity theory

$$\underline{\dot{\varepsilon}} = \underline{\dot{\varepsilon}}^e + \underline{\dot{\varepsilon}}^p \qquad\qquad (3:1)$$

wherein e and p denote elastic and plastic quantities respectively, an underlined symbol means a column vector while a dot implies that it all took place in a small step.

Hooke's law, a one-to-one relation between stress and strain, is used to calculate the elastic strains. For plane strain and axi-symmetric cases this gives

$$\begin{bmatrix} \dot{\sigma}_{xx} \\ \dot{\sigma}_{yy} \\ \dot{\sigma}_{xy} \\ \dot{\sigma}_{zz} \end{bmatrix} = \frac{E}{(1-2\upsilon)(1+\upsilon)} \begin{bmatrix} 1-\upsilon & \upsilon & 0 & \upsilon \\ \upsilon & 1-\upsilon & 0 & \upsilon \\ 0 & 0 & \frac{1}{2}-\upsilon & 0 \\ \upsilon & \upsilon & 0 & 1-\upsilon \end{bmatrix} \begin{bmatrix} \dot{\varepsilon}^e_{xx} \\ \dot{\varepsilon}^e_{yy} \\ \dot{\varepsilon}^e_{xy} \\ \dot{\varepsilon}^e_{zz} \end{bmatrix} \qquad (3.2)$$

abbreviated

$$\underline{\dot{\sigma}} = D\,\underline{\dot{\varepsilon}}^e \qquad\qquad (3.3)$$

wherein

$$\dot{\underline{\sigma}} = (\dot{\sigma}_{xx} \ \dot{\sigma}_{yy} \ \dot{\sigma}_{xy} \ \dot{\sigma}_{zz})^T$$

$$\dot{\underline{\varepsilon}}^e = (\dot{\varepsilon}^e_{xx} \ \dot{\varepsilon}^e_{yy} \ \dot{\varepsilon}^e_{xy} \ \dot{\varepsilon}^e_{zz})^T$$

$$D = \text{incremental elastic stress-strain matrix}$$

Combining equations 3.3 and 3.1 results into

$$\dot{\underline{\sigma}} = D\left(\dot{\underline{\varepsilon}} - \dot{\underline{\varepsilon}}^p\right) \tag{3.4}$$

An expression for the plastic strain increment $\dot{\underline{\varepsilon}}^p$ will be derived later in this chapter.

The Mohr-Coulomb strength criterion is given by

$$|\tau_\alpha| \leq c - \sigma_\alpha \tan\varphi \tag{3.5}$$

in which α denotes the angle between the considered surface and the x-axis.

This strength criterion can also be expressed in stress-tensor components

$$\tau^* - \sigma^* \sin\varphi - c \cos\varphi \leq 0 \tag{3.6}$$

where τ^* represents the radius and σ^* represents the centre of the stress circle

$$\tau^* = \sqrt{\tfrac{1}{4}\left(\sigma_{xx} - \sigma_{yy}\right)^2 + \sigma_{xy}^2} \tag{3.7}$$

$$\sigma^* = -\tfrac{1}{2}\left(\sigma_{xx} + \sigma_{yy}\right) \tag{3.8}$$

According to the earlier given sign convention in section 2.2 tensile stresses (and strains) are treated as positive.

To distinguish elastic from plastic states, a Mohr-Coulomb's yield function f is defined

$$f = \tau^* - \sigma^* \sin\varphi - c \cos\varphi \tag{3.9}$$

Therefore, equation 3.6 can be abbreviated as

$$f \leq 0 \tag{3.10}$$

Looking at figure 3.1 with respect to yield function f, three states can be deduced :
$f < 0$ - the stress circle makes no contact with the envelope; the material is in elastic state
$f = 0$ - the stress circle touches the envelope; the material is in plastic state
$f > 0$ - the stress circle intersects the envelope, which the material cannot sustain.
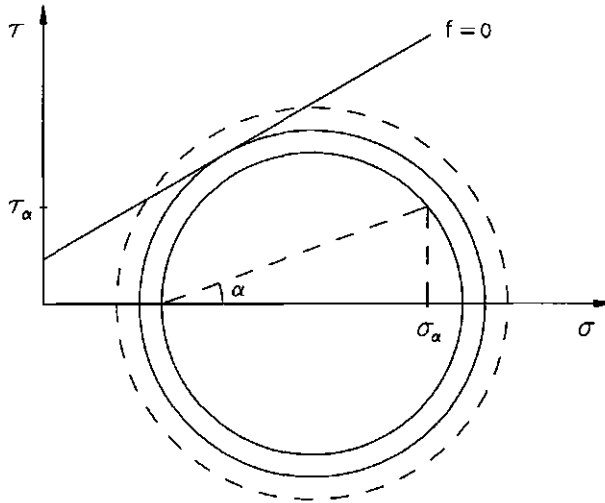
Figure 3.1 Three circles of Mohr combined with Coulomb's yield
function $f = 0$ in σ, τ -space.

For plastic yielding a material needs to be in a plastic state and must remain in a plastic state,
i.e. $f = 0$ and $\dot{f} = 0$.
Only under above-mentioned conditions $\underline{\dot{\varepsilon}}^p$ is nonzero. The plastic strain increment $\underline{\dot{\varepsilon}}^p$
remains zero for : - elastic state $f < 0$
                    - unloading $f = 0$ and $\dot{f} < 0$.

The two principles by which $\underline{\dot{\varepsilon}}^p$ can be calculated are :
- associated plasticity
- non-associated plasticity.

3.1.1 Associated plasticity

The yield function f is used to calculate the plastic strain increments

$$\underline{\dot{\varepsilon}}^{p} = \lambda \frac{\partial f}{\partial \underline{\sigma}} \tag{3.11}$$

wherein λ is a non-negative multiplier if plastic yielding occurs and is zero for elastic and unloading states. Multiplier λ has no further physical meaning.

During plastic straining the soil material flows in an associated manner, i.e. the plastic strain increment vector is normal to the yield surface f. A two-dimensional example is illustrated in figure 3.2a. Taken into account is an incompressible soil cube with $\varphi = 0$. Corresponding yield surface in σ_1, σ_3-space is shown in figure 3.2b. According to a certain $\dot{\sigma}_1$ and a smaller $\dot{\sigma}_3$, there exist a $\dot{\varepsilon}_1$ and $\dot{\varepsilon}_3$. Principal strain increment $\dot{\varepsilon}_3$ has the same magnitude as $\dot{\varepsilon}_1$ but is working in the opposite direction of the applied σ_3, figure 3.2. The plastic strain increment vector satisfies the condition

$$\dot{\varepsilon}_1^{p} + \dot{\varepsilon}_3^{p} = 0 \tag{3.12}$$

which represents no plastic volume change.

a)   -- initial
                          — final   b)
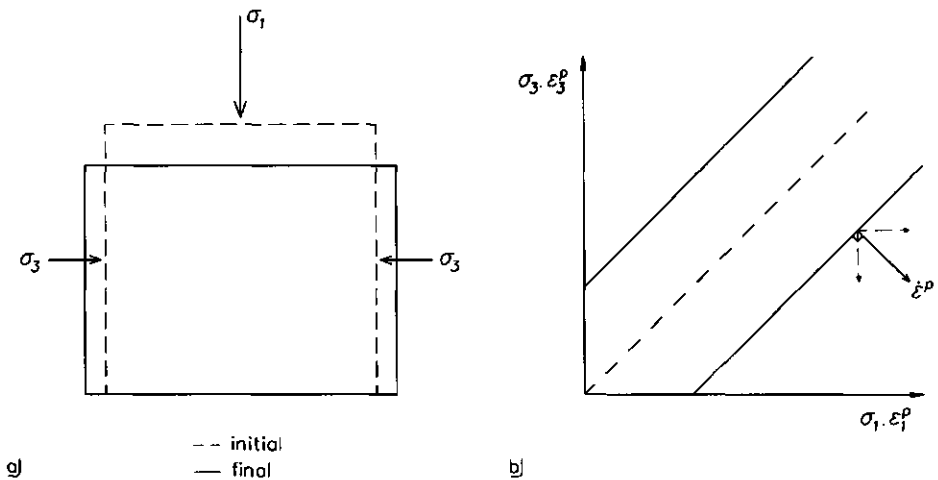
Figure 3.2 Plastic deformation of an incompressible frictionless soil
cube (a) in the case of associated flow (b).

For incompressible soil with $\varphi = 30°$, the corresponding yield surface in two dimensions is shown in figure 3.3. Again the plastic strain increment vector is normal to the yield surface. Decomposing $\dot{\underline{\varepsilon}}^p$ into $\dot{\varepsilon}_1^p$ and $\dot{\varepsilon}_3^p$ shows that $\dot{\varepsilon}_3^p$ is much more negative than $\dot{\varepsilon}_1^p$ is positive which results in dissatisfying equation 3.12.
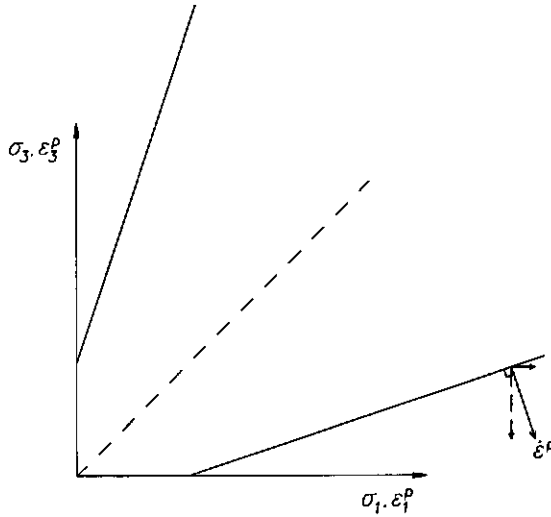
Figure 3.3   Plastic deformation of an incompressible soil cube with an
angle of internal friction φ of $30°$ in the case of associated
flow.

Because of above described shortcoming of the principle of associated plasticity for soils (Smith, 1982), the principle of non-associated plasticity is used for calculating $\dot{\underline{\varepsilon}}^p$.

3.1.2   Non-associated plasticity

In case of non-associated plasticity the yield function f is only used to distinguish elastic from plastic states. The plastic strain increments are derived from a plastic potential function g

$$\dot{\underline{\varepsilon}}^p = \lambda \, \frac{\partial g}{\partial \underline{\sigma}} \tag{3.13}$$

where g is defined as

$$g = \tau^* - \sigma^* \sin \psi + \text{constant} \tag{3.14}$$

The soil-model parameter ψ is the angle of dilatancy. Differentiating the plastic potential function g to each stress component, the so-called flow rule is obtained

$$
\begin{bmatrix} \dot{\varepsilon}_{xx}^p \\ \dot{\varepsilon}_{yy}^p \\ \dot{\varepsilon}_{xy}^p \\ \dot{\varepsilon}_{zz}^p \end{bmatrix} = \lambda \begin{bmatrix} \partial g/\partial \sigma_{xx} \\ \partial g/\partial \sigma_{yy} \\ \partial g/\partial \sigma_{xy} \\ \partial g/\partial \sigma_{zz} \end{bmatrix} = \frac{\lambda}{2} \begin{bmatrix} \left(\sigma_{xx} - \sigma_{yy}\right)/2\tau^* + \sin\psi \\ -\left(\sigma_{xx} - \sigma_{yy}\right)/2\tau^* + \sin\psi \\ 2\sigma_{xy}/\tau^* \\ 0 \end{bmatrix}
\tag{3.15}
$$

To understand the less well-known parameter ψ, the next equation is given

$$
\sin\psi = \frac{\dot{\varepsilon}_v^p}{\dot{\gamma}^p}
\tag{3.16}
$$

wherein

$$
\dot{\varepsilon}_v^p = \dot{\varepsilon}_{xx}^p + \dot{\varepsilon}_{yy}^p + \dot{\varepsilon}_{zz}^p
\tag{3.17}
$$

$$
\dot{\gamma}^p = \sqrt{\left(\dot{\varepsilon}_{xx}^p - \dot{\varepsilon}_{yy}^p\right)^2 + \left(\dot{\varepsilon}_{xy}^p\right)^2}
\tag{3.18}
$$

Comparing the shear stress τ^* (equation 3.7) with $\dot{\gamma}^p$, a certain similarity may be recognised. Therefore $\dot{\gamma}^p$ is referred to as the plastic distortion increment and the angle of dilatancy sets the ratio between the increments of plastic volumetric strain and plastic distortion.
In case of a plane strain condition ($\dot{\varepsilon}_2 = 0$), the following relation can be deduced with respect to the principal directions

$$
\sin\psi = \frac{\dot{\varepsilon}_v^p}{-2\dot{\varepsilon}_1^p + \dot{\varepsilon}_v^p}
\tag{3.19}
$$

$$
\dot{\varepsilon}_v^p = \dot{\varepsilon}_1^p + \dot{\varepsilon}_3^p
\tag{3.20}
$$

$$
\dot{\gamma}^p = \left| \dot{\varepsilon}_3^p - \dot{\varepsilon}_1^p \right|
\tag{3.21}
$$

Remarks with respect to the angle of dilatancy ψ :
- ψ is a measure of plastic volume change in the plastic state of a material :
    $\psi > 0$ volume increase
    $\psi = 0$ constant volume
    $\psi < 0$ volume decrease
- during soil deformation, the value of ψ runs to zero because the soil material cannot dilate infinitely
- in one small step of soil deformation ψ is constant

- normally consolidated clays show no dilatancy at all (Vermeer & de Borst, 1984); overconsolidated clays show a positive dilatancy angle (Vermeer, 1990)
- from graphs measured by Lebert et al. (1987) with a translational shearbox on unsaturated soils ψ -values are deduced and given in table 3.1.

Soil of Oberpfälzer Wald						
sample depth	dry density	clay content	water tension	preconsolidation stress	normal stress	ψ
[cm]	[gr/cm³]	[% by weight]	[kPa]	[kPa]	[kPa]	[°]
2-5	1.40	17.0	30	78	20	6.9
					30	7.4
					50	2.3
					70	3.6
25-29	1.58	23.5	30	145	10	7.7
					20	7.9
					30	6.7
					50	8.5
					70	8.4

Table 3.1   Values of ψ deduced from data of Lebert et al. (1987).

3.1.3 Three-dimensional stress states

Extension to three-dimensional stress states for the failure condition of Mohr-Coulomb is treated in this section. First the major and minor principal stresses are defined, respectively σ_1 and σ_3

$$\sigma_1 = -(\sigma^* + \tau^*) \tag{3.22}$$
$$\sigma_3 = -(\sigma^* - \tau^*) \tag{3.23}$$

Yield function f, equation 3.9, can be rewritten in terms of principal stresses

$$f = \tfrac{1}{2}(\sigma_3 - \sigma_1) + \tfrac{1}{2}(\sigma_3 + \sigma_1)\sin\varphi - c\,\cos\varphi \tag{3.24}$$

For yielding $f = 0$ and $\dot{f} = 0$ still prevails, which supply a six-angular yield surface in the three-dimensional stress space. Note that in case of a surface in principal stress space in combination with isotropic materials only, no order of magnitude need to be attached to the principal stresses. Thus, no more weight should be given to, say, σ_1 than σ_3. Also is σ_2 not necessarily the intermediate principal stress.

In case $\varphi = 0$ and $c \neq 0$ a special yield surface arises which is a hexagonal cylindrical prism in principal stress space, the so-called Tresca yield surface (figure 3.4).
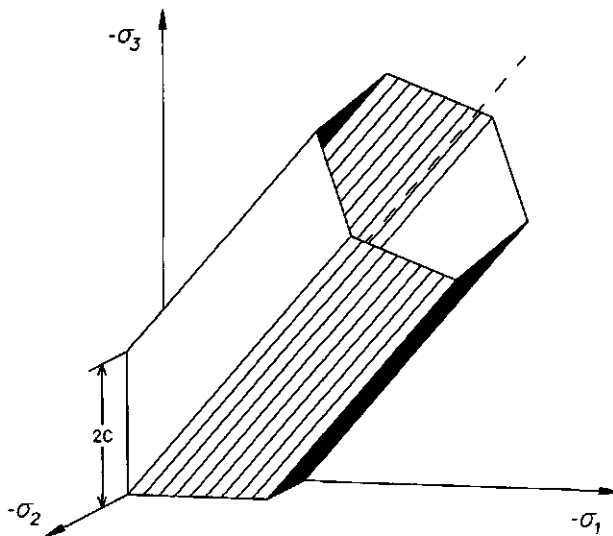

Figure 3.4 Tresca yield surface in principal stress space; only compressive stresses are considered (tension cut-off).

The Tresca yielding criterion states that yielding begins when the maximum shear stress reaches a certain value

$$\sigma_1 - \sigma_3 = 2c \tag{3.25}$$

where $\sigma_1 \geq \sigma_2 \geq \sigma_3$. This criterion closely approximates metal plasticity behaviour (Owen & Hinton, 1980). The axis of the cylindrical prism coincides with the space diagonal. The space diagonal is defined by points for which prevails

$$\sigma_1 = \sigma_2 = \sigma_3 \tag{3.26}$$

Each normal cross section of this cylindrical prism is identical, which is a consequence of the assumption that the yielding process is not influenced by the first stress invariant J_1

$$J_1 = \sigma_1 + \sigma_2 + \sigma_3 \tag{3.27}$$

Planes in principal stress space for which

$$\sigma_1 + \sigma_2 + \sigma_3 = \text{constant} \tag{3.28}$$

are called octahedral planes and are standing perpendicular to the space diagonal. A special octahedral plane is the so-called π-plane, a plane through the origin of the principal stress axes for which prevails

$$\sigma_1 + \sigma_2 + \sigma_3 = 0 \tag{3.29}$$

The line of intersection of the Tresca yield surface with arbitrary octahedral planes gives identical figures as shown in figure 3.5 because it is unaffected by the hydrostatic pressure.
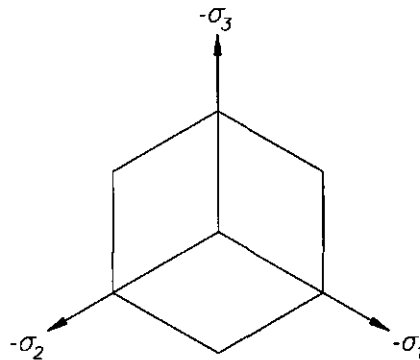
Figure 3.5   Line of intersection of the Tresca yield surface with the π-plane.

The Tresca yield surface can also be written in the form $f(\sigma_1 - \sigma_3, \, \sigma_2 - \sigma_3)$. Then a two-dimensional plot of the surface $f = 0$ is possible, with $\sigma_1 - \sigma_3$ and $\sigma_2 - \sigma_3$ as coordinate axes, figure 3.6.
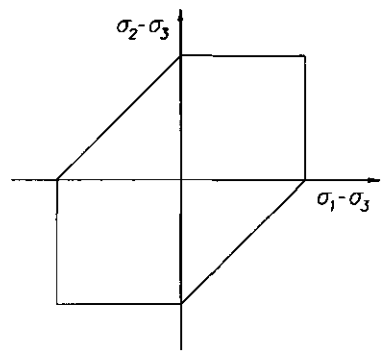
Figure 3.6 Line of intersection of the Tresca yield surface with the $(\sigma_1 - \sigma_3), (\sigma_2 - \sigma_3)$-plane.

In case $\varphi \neq 0$ the Mohr-Coulomb yield surface is a hexagonal cone, figure 3.7. In this case the yielding process is influenced by the first stress invariant J_1, which is applicable to soils.
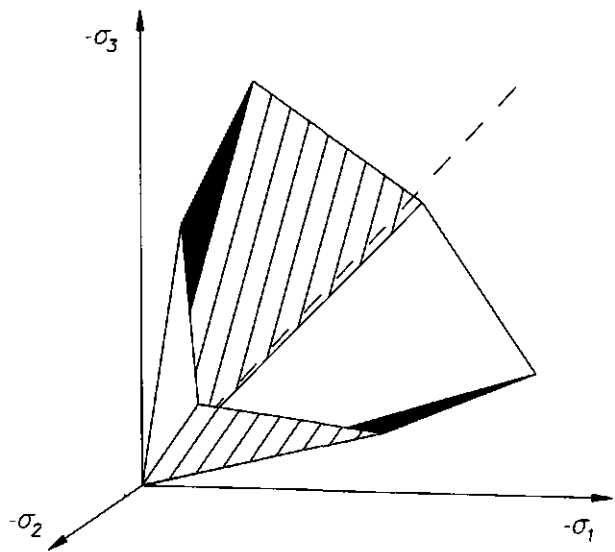
Figure 3.7 Mohr-Coulomb yield surface in principal stress space under the condition of $\varphi = 30°$ and $c = 0$.

Lines of intersections of the yield surface with arbitrary octahedral planes give symmetrical but not identical figures. One of such figures is presented in figure 3.8.
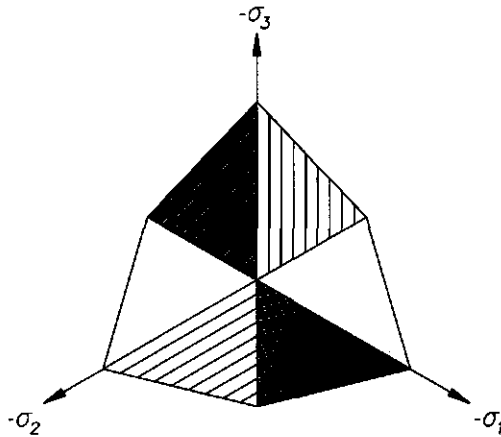
Figure 3.8 Line of intersection of the Mohr-Coulomb yield surface
with an octahedral plane for $\varphi = 30°$ and $c = 0$.

To leave no doubt, in the different figures 3.4 and 3.7, each plane through two principal axes is perpendicular to two sides of the yield surface. Such a pair of sides is indicated by the same hatch. For instance the left and right white surfaces who are standing perpendicular to σ_1, σ_2 - surface.

The plastic potential function g can also be rewritten in terms of principal stresses

$$g = \tfrac{1}{2}(\sigma_3 - \sigma_1) + \tfrac{1}{2}(\sigma_3 + \sigma_1)\sin\psi + \text{constant} \tag{3.30}$$

Applying the flow rule to g, i.e. differentiating g with respect to the principal stresses, the principal plastic strain increments are obtained

$$\begin{bmatrix} \dot{\varepsilon}_1^p \\ \dot{\varepsilon}_2^p \\ \dot{\varepsilon}_3^p \end{bmatrix} = \lambda \begin{bmatrix} -\tfrac{1}{2}(1-\sin\psi) \\ 0 \\ \tfrac{1}{2}(1+\sin\psi) \end{bmatrix} \tag{3.31}$$

From equation 3.24 it can be deduced that the intermediate principal stress does not influence the conditions for yielding. Also prevails that the flow rule for the Mohr-Coulomb criterion predicts no plastic straining in the direction of the intermediate principal stress, equation 3.31. Consider the left white surface of figure 3.7 and assume associated flow (then the figure also represents the plastic potential function g). An incremental plastic strain vector is perpendicular to this surface and this surface stands perpendicular to the σ_1, σ_2-surface and parallel to the σ_3-axis; therefore the incremental plastic strain vector has no component in the σ_3-direction.

This fact, that the intermediate principal stress does not influence the Mohr-Coulomb yield criterion, makes a generalisation to three-dimensional stress states straightforward.

However, in some situations two of the principal stresses are equal, either σ_1 and σ_2 or σ_2 and σ_3. This happens to be the case in triaxial tests at which $\sigma_2 = \sigma_3$. In this case the intersection of two planes of the six-angular yield surface is a line which is the result of two yield conditions

$$\begin{aligned} f_1 &= \tfrac{1}{2}(\sigma_3 - \sigma_1) + \tfrac{1}{2}(\sigma_3 + \sigma_1)\sin\varphi - c\,\cos\varphi = 0 \\ f_2 &= \tfrac{1}{2}(\sigma_2 - \sigma_1) + \tfrac{1}{2}(\sigma_2 + \sigma_1)\sin\varphi - c\,\cos\varphi = 0 \end{aligned} \tag{3.32}$$

At this point, where yielding occurs according to two yield conditions, the total plastic strain increment vector is the sum of the individual contributions of two flow rules

$$\underline{\dot{\varepsilon}}^p = \lambda_1 \frac{\partial g_1}{\partial \underline{\sigma}} + \lambda_2 \frac{\partial g_2}{\partial \underline{\sigma}} \tag{3.33}$$

By analogy with f_1 and f_2 the plastic potential functions g_1 and g_2 are defined

$$\begin{aligned} g_1 &= \tfrac{1}{2}(\sigma_3 - \sigma_1) + \tfrac{1}{2}(\sigma_3 + \sigma_1)\sin\psi + \text{constant} \\ g_2 &= \tfrac{1}{2}(\sigma_2 - \sigma_1) + \tfrac{1}{2}(\sigma_2 + \sigma_1)\sin\psi + \text{constant} \end{aligned} \tag{3.34}$$

The total plastic strain increment vector and the plastic volume strain increment become

$$\begin{bmatrix} \dot{\varepsilon}_1^p \\ \dot{\varepsilon}_2^p \\ \dot{\varepsilon}_3^p \end{bmatrix} = \frac{\lambda_1 + \lambda_2}{2} \begin{bmatrix} -\tfrac{1}{2}(1-\sin\psi) \\ 0 \\ \tfrac{1}{2}(1+\sin\psi) \end{bmatrix} \tag{3.35}$$

$$\dot{\varepsilon}_v^p = \left(\lambda_1 + \lambda_2\right)\sin\psi \tag{3.36}$$

from which can be deduced

$$\sin \psi = \frac{\dot{\varepsilon}_v^p}{-2\dot{\varepsilon}_1^p + \dot{\varepsilon}_v^p} \tag{3.37}$$

Comparing equation 3.19 for plane strain conditions with the derivation of above equation 3.37 for triaxial tests, it can be stated that this equation holds for plane strain conditions as well as for triaxial tests.

For the three-dimensional situation, matrix D of equation 3.3 forms a 6 by 6 matrix and the stress and strain vectors are described by

$$\dot{\underline{\sigma}} = (\dot{\sigma}_{xx} \ \dot{\sigma}_{yy} \ \dot{\sigma}_{zz} \ \dot{\sigma}_{xy} \dot{\sigma}_{yz} \ \dot{\sigma}_{zx})^T \tag{3.38}$$

$$\dot{\underline{\varepsilon}}^e = (\dot{\varepsilon}_{xx}^e \ \dot{\varepsilon}_{yy}^e \ \dot{\varepsilon}_{zz}^e \ \dot{\varepsilon}_{xy}^e \ \dot{\varepsilon}_{yz}^e \ \dot{\varepsilon}_{zx}^e)^T \tag{3.39}$$

To express the described constitutive model in this chapter in a matrix equation, equation 3.13 is substituted into equation 3.4

$$\dot{\underline{\sigma}} = D \ \dot{\underline{\varepsilon}} - \lambda \ \underline{a} \tag{3.40}$$

wherein

$$a = D \ \frac{\partial g}{\partial \underline{\sigma}} \tag{3.41}$$

The multiplier λ can be calculated from the condition that an element remains in a plastic state when it yields. For a non-hardening material in a plane strain condition this so-called consistency condition is written as

$$\dot{f} = \frac{\partial f}{\partial \sigma_{xx}} \ \dot{\sigma}_{xx} + \frac{\partial f}{\partial \sigma_{yy}} \ \dot{\sigma}_{yy} + \frac{\partial f}{\partial \sigma_{xy}} \ \dot{\sigma}_{xy} + \frac{\partial f}{\partial \sigma_{zz}} \ \dot{\sigma}_{zz} = 0 \tag{3.42}$$

or in abbreviated notation

$$\dot{f} = \frac{\partial f^T}{\partial \underline{\sigma}} \ \dot{\underline{\sigma}} = 0 \tag{3.43}$$

Substituting equation 3.40 into equation 3.43 the expression for λ is obtained

$$\dot{f} = \underline{b}^T \dot{\underline{\varepsilon}} - \lambda \ d = 0 \tag{3.44}$$

or

$$\lambda = \frac{\dot{\varepsilon}}{d} \, \underline{b}^T \tag{3.45}$$

where

$$\underline{b}^T = \frac{\partial f^T}{\partial \underline{\sigma}} \, D \tag{3.46}$$

$$d = \frac{\partial f^T}{\partial \underline{\sigma}} \, \underline{a} \tag{3.47}$$

The incremental stress-strain relation is finally obtained by substituting the expression for λ in equation 3.40

$$\underline{\dot{\sigma}} = \left[D - \frac{1}{d} \underline{a} \, \underline{b}^T \right] \underline{\dot{\varepsilon}} \tag{3.48}$$

With respect to principal stresses and making use of the elastic shear modulus G

$$G = \frac{E}{2(1+\upsilon)} \tag{3.49}$$

it can be deduced that for the Mohr-Coulomb yield criterion

$$D = \frac{G}{\left(\frac{1}{2} - \upsilon\right)} \begin{bmatrix} 1-\upsilon & \upsilon & \upsilon \\ \upsilon & 1-\upsilon & \upsilon \\ \upsilon & \upsilon & 1-\upsilon \end{bmatrix} \tag{3.50}$$

$$d = G \left(1 + \frac{\sin\varphi \, \sin\psi}{1 - 2\upsilon} \right) \tag{3.51}$$

$$\underline{a} = \frac{G}{(1-2\upsilon)} \begin{bmatrix} -1+2\upsilon+\sin\psi \\ 2\upsilon\sin\psi \\ 1-2\upsilon+\sin\psi \end{bmatrix} \tag{3.52}$$

$$\underline{b}^T = \frac{G}{(1-2\upsilon)} \begin{bmatrix} -1+2\upsilon+\sin\varphi & 2\upsilon\sin\varphi & 1-2\upsilon+\sin\varphi \end{bmatrix} \tag{3.53}$$

Substituting above-mentioned terms in incremental stress-strain equation 3.48 gives :

$$\underline{\dot{\sigma}} = \left[\frac{G}{\left(\frac{1}{2}-\upsilon\right)} \begin{bmatrix} 1-\upsilon & \upsilon & \upsilon \\ \upsilon & 1-\upsilon & \upsilon \\ \upsilon & \upsilon & 1-\upsilon \end{bmatrix} - \frac{G}{4\left(\upsilon-\frac{1}{2}\right)^2 + (1-2\upsilon)\sin\varphi\,\sin\psi} \begin{bmatrix} & Z & \end{bmatrix} \right] \underline{\dot{\varepsilon}}$$

(3.54)

where

$$Z = \begin{bmatrix} 4\left(\upsilon-\frac{1}{2}\right)^2 + (1-2\upsilon)(\sin\varphi+\sin\psi) & -4\left(\upsilon-\frac{1}{2}\right)^2 + (1-2\upsilon)(\sin\varphi-\sin\psi) & (1-2\upsilon)(2\upsilon\sin\varphi)+2\upsilon\sin\varphi\,\sin\psi \\ +\sin\varphi\,\sin\psi & +\sin\varphi\,\sin\psi & \\ & & \\ -4\left(\upsilon-\frac{1}{2}\right)^2 + (1-2\upsilon)(\sin\psi-\sin\varphi) & 4\left(\upsilon-\frac{1}{2}\right)^2 - (1-2\upsilon)(\sin\varphi+\sin\psi) & -(1-2\upsilon)(2\upsilon\sin\varphi)+2\upsilon\sin\varphi\,\sin\psi \\ +\sin\varphi\,\sin\psi & +\sin\varphi\,\sin\psi & \\ & & \\ (1-2\upsilon)(2\upsilon\sin\psi)+2\upsilon\sin\varphi\,\sin\psi & -(1-2\upsilon)(2\upsilon\sin\psi)+2\upsilon\sin\varphi\,\sin\psi & 4\upsilon^2\sin\varphi\,\sin\psi \end{bmatrix}$$

(3.55)

3.1.4 Striking difference between elastic and plastic strain increments

It is of major importance to know that there is a significant difference between the principal directions of the elastic strain increments and the principal directions of the plastic strain increments.

The elastic principal strain increments $\dot{\varepsilon}_i^e$ (i = 1,2,3) point in the direction of the principal stress increments, figure 3.9 and 3.10.

Figure 3.9 Two-dimensional reproduction of a loaded soil cube (a) under the influence of principal stress increments (b) that deforms elastically (c); $\dot{\varepsilon}_2^e = 0$ and $\dot{\varepsilon}_v^e = 0$.

Figure 3.10 Three-dimensional reproduction of a loaded soil cube (a)
under the influence of principal stress increments (b) that
deforms elastically (c); $\dot{\varepsilon}_2^e = 0$ and $\dot{\varepsilon}_v^e = 0$.

The two non-zero plastic principal strain increments $\dot{\varepsilon}_i^p$ (i = 1,3) point in the direction of the
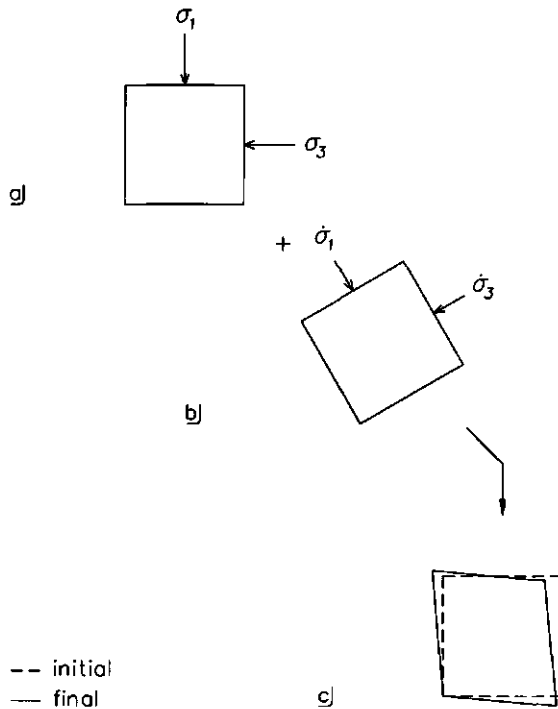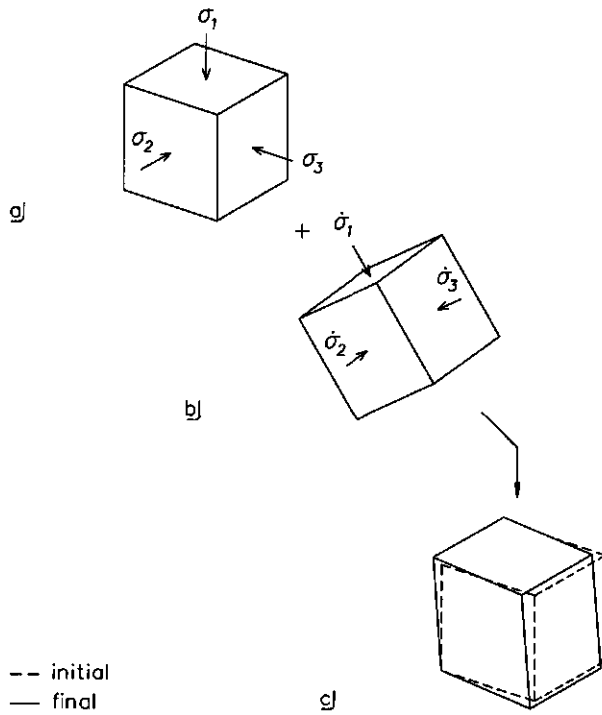extreme principal stresses, figure 3.11.
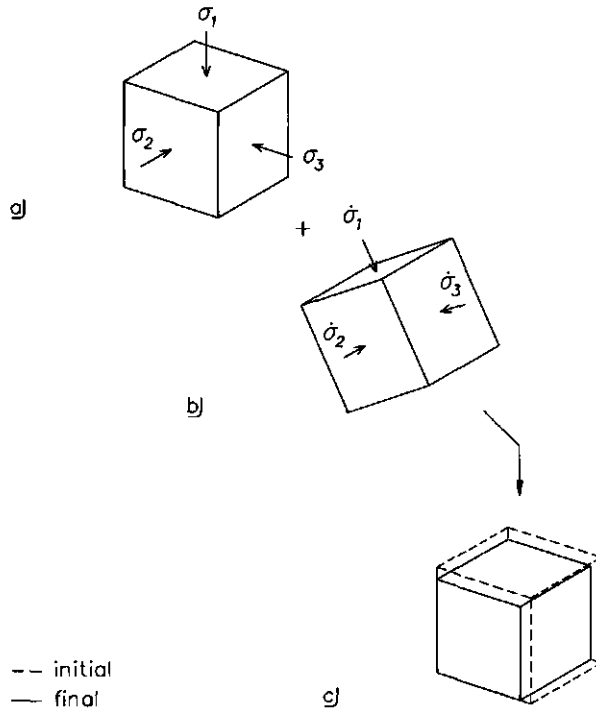
Figure 3.11 Three-dimensional reproduction of a loaded soil cube (a)
under the influence of principal stress increments (b) that
deforms plastically (c); $\dot{\varepsilon}_2^p = 0$ and $\psi < 0$.

3.1.5 Numerical examples

Finally, the strain increments for eight soils with different soil-model parameters are calculated. In these tables ψ is set to relative high value in comparison with the ψ-values of table 3.1 to show an obvious effect of the angle of dilatancy.

The materials in table 3.2 refer to dry, dense soils. Materials in table 3.3 refer to wet, dense and clayey soils, which are of great importance for soil-vehicle systems in agriculture.

	soil type				
	1	2	3	4	
$\dot{\sigma}_3$	-3.3333	-3.3333	-3.3333	-3.3333	[kN/m²]
υ	0.300	0.495	0.300	0.495	[-]
ψ	0	0	30	30	[°]
$\dot{\varepsilon}_1^e$	-0.0231	-0.0186	-0.0231	-0.0186	[-]
$\dot{\varepsilon}_2^e$	0.0103	0.0147	0.0103	0.0147	[-]
$\dot{\varepsilon}_3^e$	-0.0009	0.0036	-0.0009	0.0036	[-]
$\dot{\varepsilon}_1^p$	$\mu\begin{bmatrix}1\\0\\-1\end{bmatrix}$	$\mu\begin{bmatrix}1\\0\\-1\end{bmatrix}$	$\mu\begin{bmatrix}1\\0\\-3\end{bmatrix}$	$\mu\begin{bmatrix}1\\0\\-3\end{bmatrix}$	[-]
$\dot{\varepsilon}_2^p$					[-]
$\dot{\varepsilon}_3^p$					[-]

Table 3.2 Calculated elastic and plastic strain increments of soils, with an angle of internal friction of 30° and an elastic shear modulus G of 150 kN/m², subjected to a major principal stress increment $\dot{\sigma}_1$ of -10 kN/m².

	soil type				
	5	6	7	8	
$\dot{\sigma}_3$	-10	-10	-10	-10	[kN/m²]
υ	0.300	0.495	0.300	0.495	[-]
ψ	0	0	30	30	[°]
$\dot{\varepsilon}_1^e$	-0.0179	-0.0113	-0.0179	-0.0113	[-]
$\dot{\varepsilon}_2^e$	0.0154	0.0221	0.0154	0.0221	[-]
$\dot{\varepsilon}_3^e$	-0.0179	-0.0113	-0.0179	-0.0113	[-]
$\dot{\varepsilon}_1^p$	$\mu\begin{bmatrix}1\\0\\-1\end{bmatrix}$	$\mu\begin{bmatrix}1\\0\\-1\end{bmatrix}$	$\mu\begin{bmatrix}1\\0\\-3\end{bmatrix}$	$\mu\begin{bmatrix}1\\0\\-3\end{bmatrix}$	[-]
$\dot{\varepsilon}_2^p$					[-]
$\dot{\varepsilon}_3^p$					[-]

Table 3.3 Calculated elastic and plastic strain increments of frictionless soils, with an elastic shear modulus G of 150 kN/m², subjected to a major principal stress increment $\dot{\sigma}_1$ of -10 kN/m².

The calculation of soil type *8* is explained in detail to give a better understanding of the theory in this section.

Taking soil type *8* of table 3.3 as basic soil material and having a plane strain condition, the consistency equation 3.42, with respect to principal stresses, is written as

$$\dot{f} = \frac{\partial f}{\partial \sigma_1} \dot{\sigma}_1 + \frac{\partial f}{\partial \sigma_2} \dot{\sigma}_2 + \frac{\partial f}{\partial \sigma_3} \dot{\sigma}_3 = 0 \tag{3.56}$$

Knowing from equation 3.24

$$f = \tfrac{1}{2}(\sigma_3 - \sigma_1) + \tfrac{1}{2}(\sigma_3 + \sigma_1)\sin\varphi - c\,\cos\varphi$$

the consistency condition becomes

$$\dot{f} = -\tfrac{1}{2}(1 - \sin\varphi)\,\dot{\sigma}_1 + \tfrac{1}{2}(1 + \sin\varphi)\,\dot{\sigma}_3 = 0 \tag{3.57}$$

from which results $\dot{\sigma}_3 = -10$.

From equation 3.50 matrix D can be deduced

$$D = \frac{G}{\left(\frac{1}{2} - \upsilon\right)} \begin{bmatrix} 1-\upsilon & \upsilon & \upsilon \\ \upsilon & 1-\upsilon & \upsilon \\ \upsilon & \upsilon & 1-\upsilon \end{bmatrix} = \begin{bmatrix} 15150 & 14850 & 14850 \\ 14850 & 15150 & 14850 \\ 14850 & 14850 & 15150 \end{bmatrix}$$

Scalar d, column vector a and row vector b^T are calculated with equations 3.51 and 3.53

$$d = G\left(1 + \frac{\sin\varphi \sin\psi}{1-2\upsilon}\right) = 150$$

$$\underline{a} = \frac{G}{(1-2\upsilon)} \begin{bmatrix} -1+2\upsilon+\sin\psi \\ 2\upsilon\sin\psi \\ 1-2\upsilon+\sin\psi \end{bmatrix} = \begin{bmatrix} 7350 \\ 7425 \\ 7650 \end{bmatrix}$$

$$\underline{b}^T = \frac{G}{(1-2\upsilon)} \begin{bmatrix} -1+2\upsilon+\sin\varphi & 2\upsilon\sin\varphi & 1-2\upsilon+\sin\varphi \end{bmatrix} = \begin{bmatrix} -150 & 0 & 150 \end{bmatrix}$$

The final stress-strain relation is obtained by using equation 3.48

$$\underline{\dot{\sigma}} = \left[D - \frac{1}{d} \underline{a} \, \underline{b}^T \right] \underline{\dot{\varepsilon}}$$

from which results

$$\begin{bmatrix} -10 \\ 0 \\ -10 \end{bmatrix} = \begin{bmatrix} 22500 & 14850 & 7500 \\ 22275 & 15150 & 7425 \\ 22500 & 14850 & 7500 \end{bmatrix} \begin{bmatrix} \dot{\varepsilon}_1 \\ \dot{\varepsilon}_2 \\ \dot{\varepsilon}_3 \end{bmatrix}$$

The total strain increments are obtained through solving this system of equations. However, this system of equations is dependent, i.e. the determinant is zero. Therefore the solution is a line

$$\begin{bmatrix} \dot{\varepsilon}_1 \\ \dot{\varepsilon}_2 \\ \dot{\varepsilon}_3 \end{bmatrix} = \begin{bmatrix} -0.015013 \\ 0.022074 \\ 0 \end{bmatrix} + \eta \begin{bmatrix} -0.31623 \\ 0 \\ 0.94868 \end{bmatrix}$$

The elastic contribution of the total strain increments is obtained by using equation 3.3

$$\underline{\dot{\sigma}} = D \, \underline{\dot{\varepsilon}}^e$$

$$\begin{bmatrix} -10 \\ 0 \\ -10 \end{bmatrix} = \begin{bmatrix} 15150 & 14850 & 14850 \\ 14850 & 15150 & 14850 \\ 14850 & 14850 & 15150 \end{bmatrix} \begin{bmatrix} \dot{\varepsilon}_1^e \\ \dot{\varepsilon}_2^e \\ \dot{\varepsilon}_3^e \end{bmatrix}$$

$$\begin{bmatrix} \dot{\varepsilon}_1^e \\ \dot{\varepsilon}_2^e \\ \dot{\varepsilon}_3^e \end{bmatrix} = \begin{bmatrix} -0.011260 \\ 0.022074 \\ -0.011260 \end{bmatrix}$$

The plastic contribution is obtained by using equation 3.1

$$\underline{\dot{\varepsilon}}^p = \underline{\dot{\varepsilon}} - \underline{\dot{\varepsilon}}^e \tag{3.58}$$

from which follows

$$\begin{bmatrix} \dot{\varepsilon}_1^p \\ \dot{\varepsilon}_2^p \\ \dot{\varepsilon}_3^p \end{bmatrix} = \mu \begin{bmatrix} -1 \\ 0 \\ 3 \end{bmatrix}$$

It can be concluded from this completely elaborated calculation :
- the elastic incremental principal strain vector is not perpendicular to the yield function f
- with respect to the plastic incremental principal strain vector :
    - the direction of this vector is fixed, but the absolute size is yet undetermined
    - this vector stands perpendicular to the plastic potential function g
    - the intermediate plastic principal strain increment is and remains zero
    - $\dot{\varepsilon}_v^p = \dot{\varepsilon}_1^p + \dot{\varepsilon}_3^p \neq 0$ which fully agrees with $\psi \neq 0$.

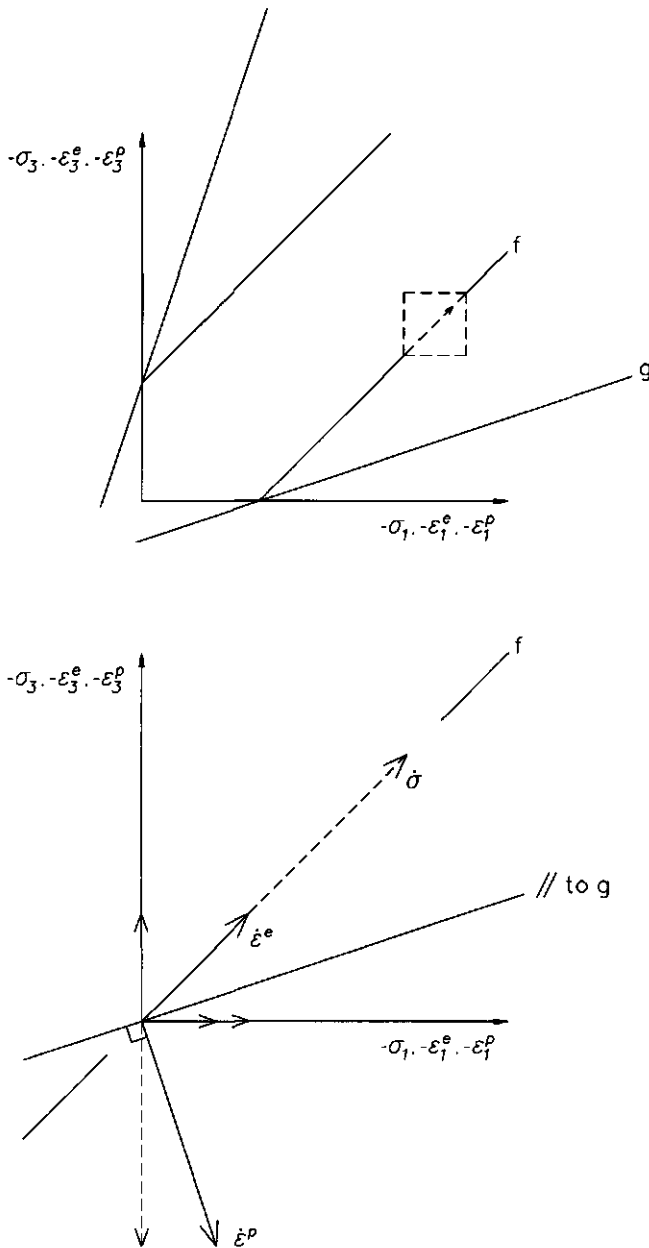A graphical representation of the results of the calculation is given in figure 3.12.

Figure 3.12 Graphical representation of elastic and plastic strain increments of soil type 8 of table 3.3; details of the part enclosed by dashed lines in the upper part are enlarged in the lower part.

3.2 Drucker-Prager

In this section two more yielding criteria are employed, namely Von Mises and Drucker-Prager. According to Owen & Hinton (1980), Von Mises and the described Tresca criteria closely approximate metal plasticity behaviour, whereas Drucker-Prager and the described Mohr-Coulomb criteria are applicable to concrete, rock and soil.

The shape of Tresca's yield surface in principal stress space is a hexagonal cylindrical prism (figure 3.4), which states that yielding begins when a certain maximum shear stress is reached. Von Mises states that yielding occurs when the second deviatoric stress invariant J_2' reaches a critical value. The second deviatoric stress invariant J_2' is composed of the first and the second stress invariant, J_1 and J_2 respectively, and is defined by

$$\begin{aligned} J_2' &= \tfrac{1}{3} J_1^2 - J_2 \\ &= \tfrac{1}{6} \left[\left(\sigma_1 - \sigma_2 \right)^2 + \left(\sigma_2 - \sigma_3 \right)^2 + \left(\sigma_3 - \sigma_1 \right)^2 \right] \end{aligned} \tag{3.58}$$

where

$$J_1 = \sigma_1 + \sigma_2 + \sigma_3 \tag{3.59}$$

$$J_2 = \sigma_1 \sigma_2 + \sigma_2 \sigma_3 + \sigma_3 \sigma_1 \tag{3.60}$$

The yielding function f according to Von Mises is represented by

$$f = J_2' - k^2 = 0 \tag{3.61}$$

where

k = material parameter

The geometrical interpretation of the Von Mises yield surface $f = 0$, when plotted in the principal stress space, will be a cylinder perpendicular to the π-plane (figure 3.13).
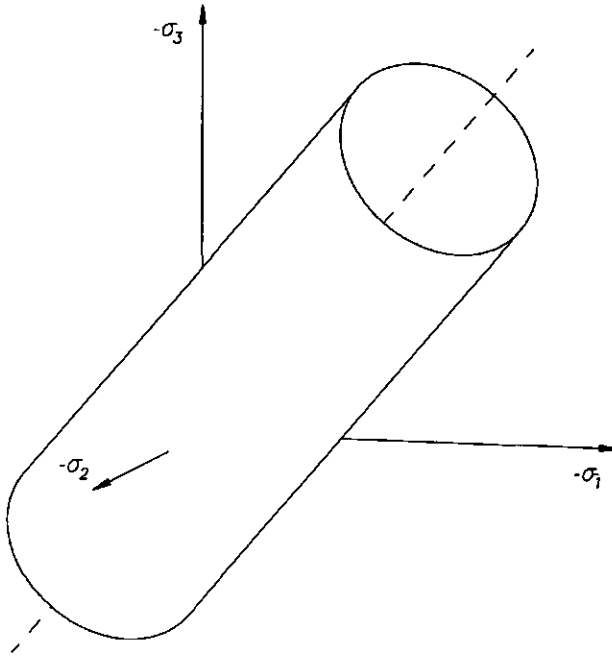
Figure 3.13   Von Mises yield surface in principal stress space.

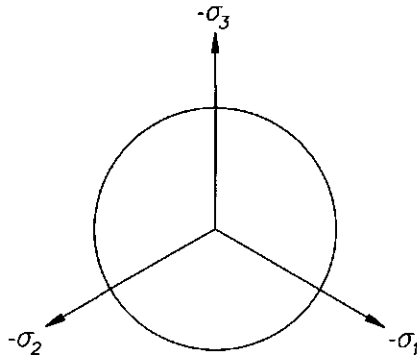Line of intersection of the Von Mises with the π-plane is a circle of radius $\sqrt{2}k$, figure 3.14.

Figure 3.14   Line of intersection of the Von Mises yield surface with the π-plane .

The Tresca yield locus is a hexagon with distances of $2c\sqrt{\frac{2}{3}}$ from origin to apex on the π-plane. The Von Mises and Tresca yield loci can be made to resemble each other very closely by selecting appropriate values of c and k. It is conventional to let the cylinder pass through the outer apices of the hexagon, i.e. by taking $k = c\sqrt{\frac{4}{3}}$ see figure 3.15. Then there is full agreement for a metal tension test or an unconfined compression test of soil; for both tests $\sigma_2 = \sigma_3 = 0$.
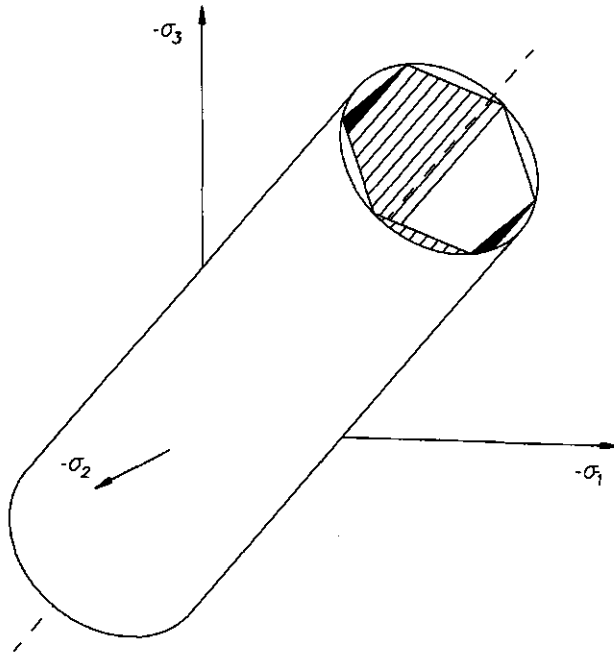

Figure 3.15   Fit of the Von Mises yield surface through the outer apices
of the Tresca yield surface in principal stress space.

The situation of figure 3.15 is also plotted from viewpoint of the space diagonal (figure 3.16) and with $\sigma_1 - \sigma_3$ and $\sigma_2 - \sigma_3$ as coordinate axes, figure 3.17.
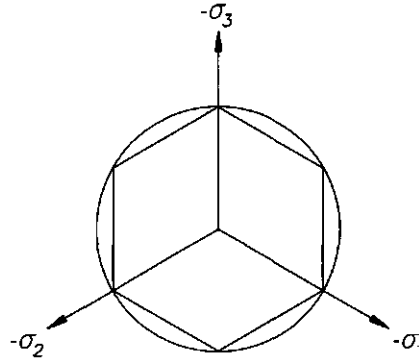
Figure 3.16 Lines of intersection of the Von Mises and the Tresca yield
surface with the π-plane.
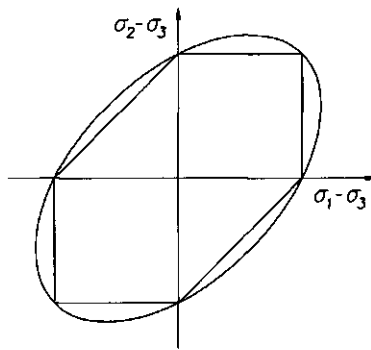
Figure 3.17 Lines of intersection of the Von Mises and the Tresca yield
surface with the ($\sigma_1 - \sigma_3$, $\sigma_2 - \sigma_3$)-plane.

However, soil failure, unlike metal yielding, is in some way a function of the hydrostatic
stress p

$$p = \tfrac{1}{3}\left(\sigma_1 + \sigma_2 + \sigma_3\right) \tag{3.62}$$

An approximation to the Mohr-Coulomb law was presented by Drucker-Prager as a
modification of the Von Mises yield criterion. An additional term in the original Von Mises
expression was introduced to take into account the influence of the first stress invariant J_1.
The Drucker-Prager yield function becomes (compressive stresses and strains are taken as
positive)

$$f = \sqrt{J_2{}'} - \alpha\left(J_1 + 3a\right) = 0 \tag{3.63}$$

where

$$\alpha = \text{coefficient related to the friction angle } \varphi$$
$$a = c \, / \tan \varphi \tag{3.64}$$

The Drucker-Prager yield surface has the shape of a circular cone, figure 3.18.
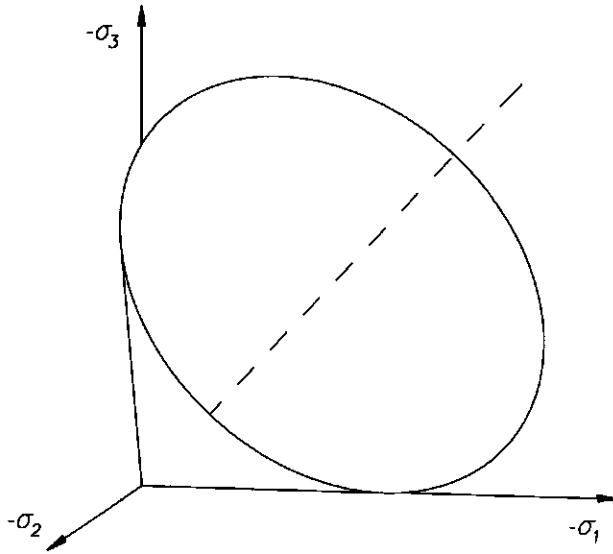
Figure 3.18 Drucker-Prager yield surface in principal stress space.

Lines of intersections of this yield surface onto arbitrary octahedral planes give concentric but not identical circles, figure 3.19.
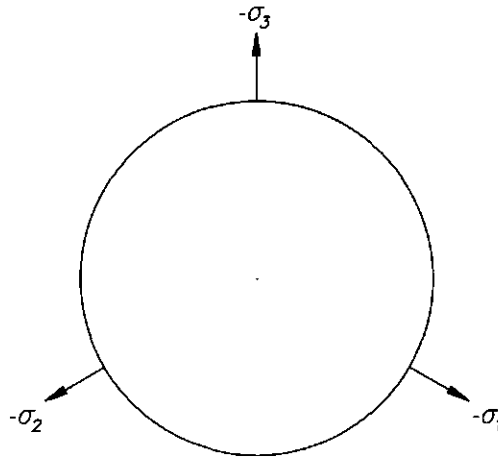
Figure 3.19 Line of intersection of the Drucker-Prager yield surface
with an arbitrary octahedral plane.

The plastic potential function g, which is used to determine the plastic flow during yielding, is defined by

$$g = \sqrt{J_2'} - \beta J_1 \qquad\qquad (3.65)$$

where

β = coefficient related to the dilatancy angle ψ

If β equals α of equation 3.63 an associated flow rule exists, i.e. the plastic strain increment vector is normal to the yield surface f.

For fitting the Drucker-Prager model to the Mohr-Coulomb model different relations can be used. From geometrical considerations of the two yield surfaces it is reasonable to let the Drucker-Prager yield surface coincide with the outer apices or the inner apices of the Mohr-Coulomb yield surface, a circumscribed cone or an inscribed cone respectively, figure 3.20.

Figure 3.20 The Drucker-Prager yield surface fits to the Mohr-Coulomb yield surface as a circumscribed cone and an inscribed cone.

Figure 3.21 Projection of the Mohr-Coulomb yield surface and the corresponding circumscribed and inscribed cone of Drucker-Prager onto the π-plane.

According to Owen & Hinton, 1980 and Song, 1990, the approximation of the circumscribed cone gives

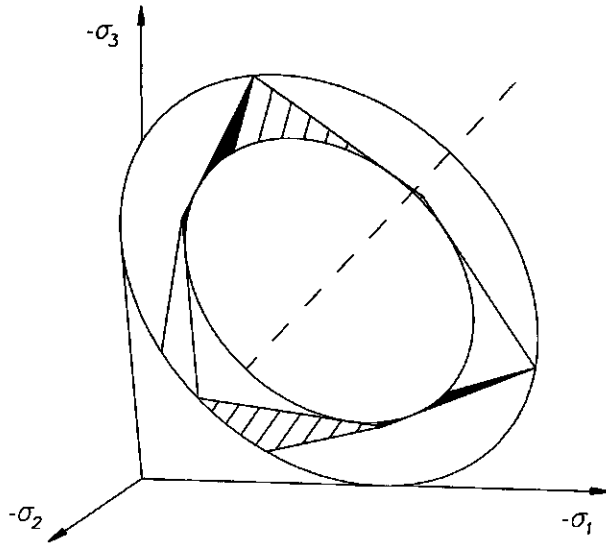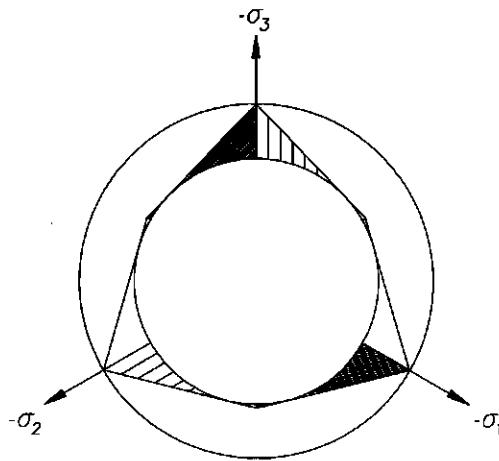$$\alpha = \frac{2 \sin \varphi}{\sqrt{3} \left(3 - \sin \varphi\right)} \tag{3.66}$$

For an approximation of the inscribed cone Owen & Hinton (1980) define

$$\alpha = \frac{2 \sin \varphi}{\sqrt{3} \left(3 + \sin \varphi\right)} \tag{3.67}$$

while Chen (1975) gives

$$\alpha = \frac{\tan \varphi}{\sqrt{9 + 12 \tan^2 \varphi}} \tag{3.68}$$

and Song (1990) deduces

$$\alpha = \frac{\sin \varphi}{\sqrt{9 + 3 \sin^2 \varphi}} \tag{3.69}$$

Equation 3.68 and 3.69 give the same α-values for any φ-value. Equation 3.67 gives higher α-values than equations 3.68 and 3.69; this discrepancy becomes smaller when φ increases. From figures 3.20 and 3.21 it is obvious that there is not a full agreement between the Mohr-Coulomb yield locus and the Drucker-Prager yield locus. In general, the relation between c and φ on one hand and a and α on the other depend on the value of σ_2 relative to σ_1 and σ_3. Only in the case of specific stress paths or properties there can be full or satisfactory agreement between the two models.

According to Song, equation 3.66 and 3.69 seem to be reasonable for friction angles less than $20°$; for higher friction angles the cross section of the Mohr-Coulomb hexagon will approach a triangle, then neither of the equations 3.66 and 3.69 appears to be reasonable. Song also deduced that when Mohr-Coulomb is written in a more general form the Mohr-Coulomb model can be expressed by the coefficients φ, α and β. Comparing these coefficients with those in the Drucker-Prager model, equations can be derived to determine the relation between φ, α and β. For instance, in the special case of a plane strain situation with a non-dilating material ($\psi = 0$; $\beta = 0$) the intermediate principal stress becomes

$$\sigma_2 = \tfrac{1}{2}\left(\sigma_1 + \sigma_3\right) \tag{3.70}$$

from which finally results

$$\alpha = \tfrac{1}{3}\sin\varphi \tag{3.71}$$

$$a = c\cos\varphi / 3\alpha \tag{3.72}$$

So, equation 3.72 equals equation 3.64. Therefore it can be concluded that the inscribed Drucker-Prager cone is suitable as an approximation of the Mohr-Coulomb model for plain strain conditions.

However, one must be keen on the fact that experimental data of true triaxial tests of Goldscheider, 1982, on one hand and hollow-cylinder tests of Kirkpatrick, 1957 and Wu et al., 1963, on the other ($\sigma_2 \neq \sigma_3$ prevails for all tests) approximate Mohr-Coulomb's yield surface more closely than Drucker-Prager's yield surface.

4 Soil-material interface and adherence

Nowadays, nearly all the machines in agriculture are equipped with wheels. Most of the wheels are fitted with pneumatic tyres. Solid steel wheels are used for depth control of tillage tools only and have a supplementary task. Driven steel wheels are used in two manners :
- puddle wheels; open iron construction of the wheels with iron grousers preparing paddy fields through their puddling effect
- cage wheels; the open iron construction of the wheels reduce compaction of the seed-bed during seedling operations.

Sometimes, in stead of wheels, agricultural practice uses iron sledges for depth control and/or to carry the weight of tillage tools. Viewed from that perspective the mouldboard of a plough may not be forgotten. Similarity in all the above-mentioned is the soil-material interface. For the sake of completeness the soil-plant material is mentioned, soil-sugar beet for example.

Therefore, it can be concluded that the interface between soil and material is playing a key role in agriculture. In this dissertation the soil-wheel interface is emphasised and will be discussed in this chapter.

4.1 Occurrence

Before making use of interface elements between plate and soil mass in the simulation calculations, the principles of soil-material interface and adherence will be treated in this chapter.
    In field traffic, tillage and laboratory experiments, boundary surfaces occur between soil bodies and other materials like steel and rubber and also between adjacent soil bodies. A small element of such surfaces may be considered as a boundary between two rigid bodies. Sometimes there is a relative movement in such a surface element, at other times not, but in general there is a stress acting across the surface element between the two bodies. The tangential component of that stress is the shear stress due to the friction of the surface element. This shear stress is fully developed if sufficient relative movement occurs. Sometimes, the relative movement is not such large and the shear stress has a relatively low value. Conversely, if a small shear stress is applied, a small relative movement will occur and rest will be restored. Application of a greater shear stress initiates a relative movement that continues.
Not fully developed shear stresses occur :
- in parts of contact surfaces of tires, wheels and rollers at low slip percentages
- where a so-called soil wedge adheres to the material surface; soil wedges may occur with tines, blades and shear elements (like track elements)
- in the soil-material interface, if a thin soil layer adheres to the material; this may occur at rough tool surfaces and in sticky soils.

Fully developed shear stresses can be expected :
- with tires, wheels and rollers at high slip percentages
- with sledges and relatively sharp cones
- at soil-soil interfaces in shearing devices
- in the contact surface of tools with small angles of approach under normal conditions.

For driven wheels shear stresses in the contact surface should be as high as possible to maximise pull. In other cases such as plough bodies, tines and sleds, low values of the shear stresses in the contact surface are desirable. Also in research activities low values are often desired. For instance for the bottom and top plates in tri-axial tests and unconfined compression tests and for the cylinders in uni-axial compression tests.

4.2 Fundamentals

Figure 4.1 shows a shear stress τ that is exerted by a material on a soil body (Koolen & Kuipers, 1983). Total stress S has a normal component σ_n. When there is significant relative movement in the interface, τ is fully developed. The shear stress τ for this case will be denoted by τ_s, where s is the abbreviation of sliding. It is assumed that the surface element is fixed to the soil.
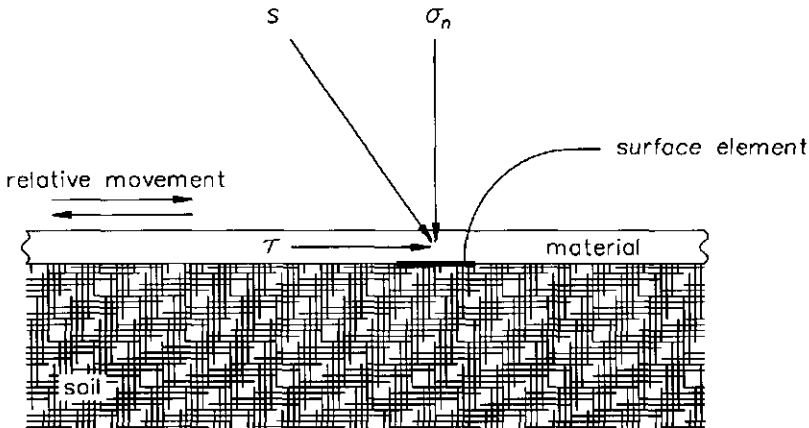
Figure 4.1   Stresses on a soil surface element sliding along a material.

Frictional properties for a boundary surface are generally measured by measuring τ_s at different values of σ_n. In general τ_s can be determined by :

$$\tau_s = \mu \, \sigma_n \qquad\qquad\qquad (4.1)$$

or more accurately by

$$\tau_x = a + \mu' \sigma_n \qquad (4.2)$$

where

μ = apparent coefficient of soil - metal friction

a = adhesion

μ' = true coefficient of soil - metal friction

In figure 4.2 soil element ABC slides along a material. The angle θ between the material surface and the plane on which σ_1 acts is given.

Figure 4.2 Graphically determined relationship between (σ_1, σ_3) and (τ, σ_n) on a sliding surface.

In plane AC equation 4.2 must hold, thus

$$\tau_x = a + \mu' \left(\sigma_n\right)_{AC} \qquad (4.3)$$

Normal stress σ_n and shear stress τ_s can be expressed as :

$$\sigma_n = \sigma_1 \cos^2 \theta + \sigma_3 \sin^2 \theta$$
$$\tau_x = (\sigma_1 - \sigma_3) \sin\theta \cos\theta \qquad (4.4)$$

and thus equation 4.2 for soil element ABC can be expressed as

$$\left(\sigma_1 - \sigma_3\right) \sin\theta\cos\theta = a + \mu' \left(\sigma_1 \cos^2\theta + \sigma_3 \sin^2\theta\right) \qquad (4.5)$$

The graphical representation using Mohr's circle is elucidating, figure 4.3.
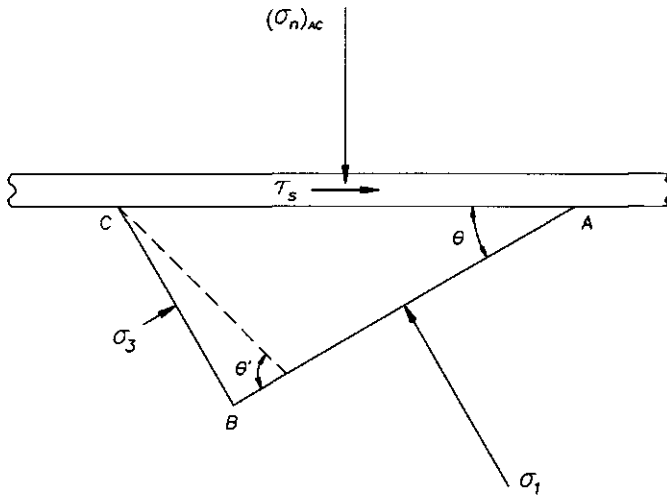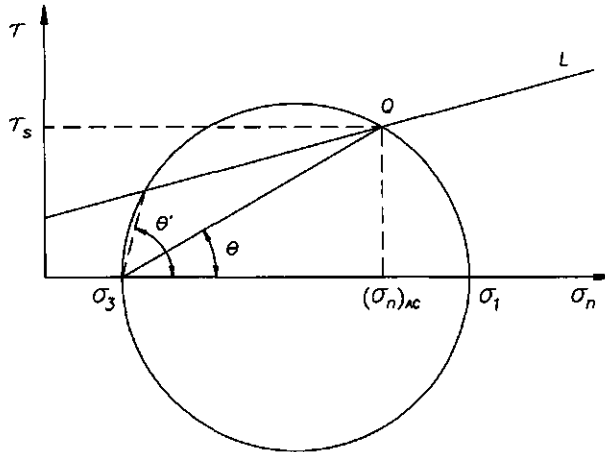

Figure 4.3 Graphically determined relationship between (σ_1, σ_3) and
(τ, σ) on a sliding surface.

Line L represents the sliding condition. This line is direction dependent and prevails only for the plane of sliding AC here. Suppose that point Q on L represents the state of stress in the plane of sliding AC. Then the line through Q at angle θ to the σ_n-axis yields σ_3 and the circle through σ_3 and Q with its centre on the σ_n-axis yields σ_1. Note that τ in the plane at angle θ' with the horizontal satisfies equation 4.2 as well. However, physically this equation is not valid for this plane, since it is not a soil-material interface. For planes at angles between θ and θ', the states of stress are represented by points above line L. Shear stresses in these planes may be much higher than the shear stress in the plane of sliding. Of course, high shear stresses can only exist if the soil is strong enough (Mohr's circle can never extend beyond the line of Coulomb's law). If, at fixed values of τ_s and σ_n in the plane of sliding, the angle θ between that plane and the plane perpendicular to σ_1 is different, other σ_1 and σ_3 values occur.

Adherence and wedge formation

Sometimes shear stresses in the soil-material interface are so great that sliding between the soil and the material not longer occurs. Instead, shear planes are formed within the soil body. Whether or not these alternative shear planes develop depends on the ratio between the resistance against sliding along the material and the soil internal strength. Sliding resistance is characterised by a and μ', soil internal strength by c and $\tan\varphi$. Two cases may be distinguished.

Case 1

Adherence of a thin soil layer of constant thickness as shown in figure 4.4.
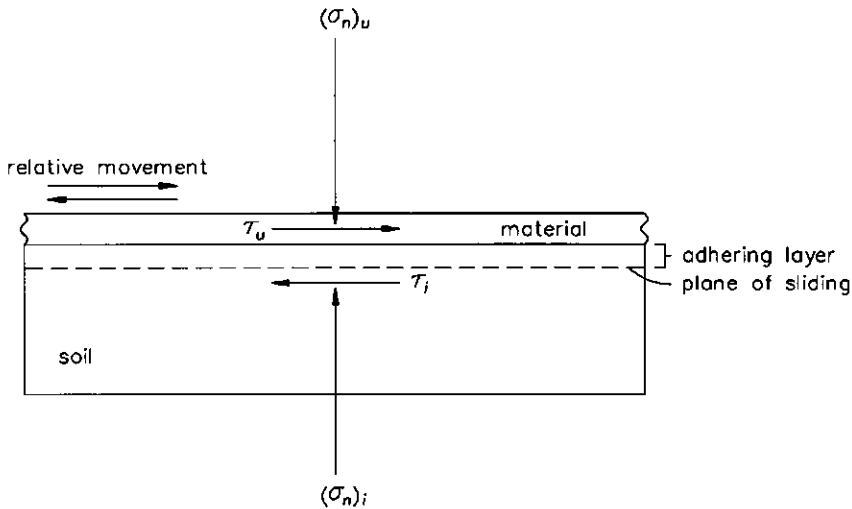

Figure 4.4 Conditions favouring soil adherence.

Equilibrium requires that

$$\begin{aligned}
(\sigma_n)_u &= (\sigma_n)_i \\
(\tau)_u &= (\tau)_i
\end{aligned}$$

(4.6)

There is no sliding along the material and, therefore,

$$(\tau)_u < a + \mu'(\sigma_n)_u$$

(4.7)

In the sliding (failure) plane, according to Coulomb prevails

$$(\tau)_i = c + (\sigma_n)_i \tan\varphi \tag{4.8}$$

These four equations can be combined to show that adherence occurs if

$$a + \mu' (\sigma_n)_u > c + (\sigma_n)_u \tan\varphi \tag{4.9}$$

or

$$\sigma_n < \frac{a - c}{\tan\varphi - \mu'} \tag{4.10}$$

Adherence can be predicted if a, μ', c, $\tan\varphi$ and σ_n are known. Scouring, sliding without adherence, is favoured by increasing σ_n. One may think of slatted mouldboards.

Case 2

Soil wedges resting against material surfaces of tines etc. that are immobilised temporarily (Fountaine & Payne, 1954). In contrast with case 1, this is a phenomenon that is reported frequently by agricultural practise. It has no significance in load-bearing processes.

Path dependency of instantaneous values of μ, a and μ'

Shear stresses just before movement between soil and material (static friction) are often different from those immediately after the start of movement (dynamic friction). For steel on dry sand Nichols (1931) found $\mu = \mu' = 0.26$ just before movement, and $\mu = \mu' = 0.23$ immediately after the start of movement.

Friction on the surface element in figure 4.5 may change with increasing length of sliding path and attain a constant value after a path length of one or more decimetres. With steel this change involves mostly an increase of μ, caused by changes in soil particle arrangement and in position and suction of soil water. In contrast, with rubber μ usually decreases, because the flexible rubber adjusts to surface irregularities and meets a smoother soil at a greater path length. In this way for steel μ may increase by e.g. 0.3 and for rubber it may decrease by e.g. 0.1 (Söhne, 1953).

The value of adhesion a seems to be especially sensitive to the highest value of σ_n that ever occurred on the surface element. A higher σ_n will give a closer contact. Söhne (1953) reported up to fivefold increases of a upon tenfold increases in highest σ_n.

The influence of sliding velocity

For wet soil and/or for speed variations over one or more orders of magnitude a speed dependency of μ should be taken into account. Increases of μ of 0.1 - 0.15 have been measured due to higher sliding speed (Vornkahl, 1967). It is likely that soil water viscosity plays a role in this.

Material aspects

Surface roughness has a large influence on friction. For a rusted steel surface, the coefficient of friction may be as high as $\tan\varphi$ (for unsaturated agricultural soils where φ varies between 25 and 45 degrees). If the rust is removed, friction will be considerably less but a high degree of surface polish will result in only a minor decrease. For a reasonably smooth, steel tool in an average, rather dry soil one may expect $\mu \approx \mu' \approx 0.25$ (Spoor, 1969).

Also the hardness of the material surface plays a role. Nichols (1931) measured for steel at low soil moisture contents and short sliding paths

$$\mu = \mu' = 0.37 - 0.00015\,H \tag{4.11}$$

where

$$H = \text{Brinell hardness}$$

H is about 650 for very hard tempered steel and about 125 for steel low in carbon. The influence of hardness was also discussed in the section on path dependency. Regarding the type of material one should mention that, on soil that is not too wet and for short sliding path lengths, μ is about 0.2 higher for rubber than for steel. For soil-soil friction it is usually assumed that $\mu' = \tan\varphi$.

Soil physical aspects

Soil moisture may strongly influence frictional behaviour. Roughly one may interpret the law of friction (equation 4.2)

$$\tau_s = a + \mu'\,\sigma_n \tag{4.11}$$

physically as follows, figure 4.5.
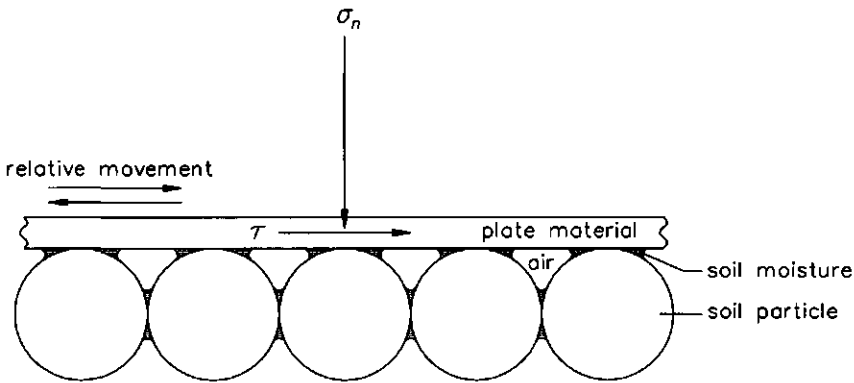
Figure 4.5 The role of soil water.

An external load on a plate induces a normal stress σ_n on the soil. This normal stress σ_n contributes to the effective stress between the solid part of the soil and the plate (effective stress is the sum of the normal components of the contact forces between the plate and the solids, divided by plate area A). There may be water between the plate and the soil particles. If this water is under suction it will provide an additional stress. This additional stress is called σ_w. Real total effective stress is then

$$\sigma_g = \sigma_w + \sigma_n \tag{4.12}$$

where g refers to grain. The friction between soil particles and plate follows the well-known law of friction

$$\tau = \sigma_g \, \upsilon \tag{4.13}$$

where

$$\upsilon = \text{coefficient of friction between the plate and single soil particles}$$

Combination of these two equations yields

$$\tau = \sigma_w \, \upsilon + \sigma_n \, \upsilon \tag{4.14}$$

A comparison of this equation with equation 4.2 shows that

$$\upsilon = \mu'$$
$$a = \sigma_w \, \upsilon \tag{4.15}$$

Additional stress σ_w due to soil water can be expressed as

$$\sigma_w = s\, A_{rel} \tag{4.16}$$

where

s = soil water suction

A_{rel} = wetted fraction of the plate area

The last two equations can be combined to

$$a = \upsilon\, s\, A_{rel} \tag{4.17}$$

Regarding this physical model the following remarks can be made :
- the occurrence of water between the plate and the soil particles requires good soil-plate contact; for this the duration of sliding, history of normal stress and soil structure are important factors
- soil water suction depends on moisture content, soil structure and soil type
- the wetted fraction of the plate area A_{rel} depends on the degree of contact, on soil moisture and on plate material
- the coefficient of friction between the plate and single soil particles υ is determined by surface roughness of the plate and by the mineral type and shape of the soil particles
- during the service life of a tool, the roughness of the soil-engaging surface is that of worn material; this roughness may be higher or lower than that of new material
- at higher moisture contents, soil water may act as a lubricant and lowers υ drastically; the moisture range where this occurs is known as the lubrication phase of soil friction (Nichols, 1931); in this range υ decreases with increasing moisture content
- at lower moisture contents water cannot be present between the soil particles and the plate; as a result τ will not depend strongly on moisture content and $a = 0$; this moisture range is called the dry phase
- at moisture contents between the dry phase and the lubrication phase, A_{rel} increases strongly with increasing moisture content and therefore τ also increases (adhesion phase)
- sliding velocity influences friction through soil water viscosity.

Finally, the mineral parts influence friction through type of mineral and packing density. For steel on dry sand friction was found to increase with packing density as a result of increased soil strength. Butterfield & Andrawes (1972) found $\mu = \mu' = 0.17$ for a soil at a porosity of 43.7 % and $\mu = \mu' = 0.28$ at a porosity of 35.7 %. Fine-textured soils have a higher coefficient of friction than coarse textured soils. For small sliding distances of steel on soils with low moisture contents Nichols (1931) found :

$$\begin{aligned}
\mu = \mu' &= 0.23 + 0.005\left(\% < 2\mu m\right) \qquad \text{if this \% } < 32 \\
\mu = \mu' &= 0.37 \qquad\qquad\qquad\qquad\quad \text{if this \% } \geq 32
\end{aligned} \tag{4.18}$$

5   Finite element program Plaxis

In this dissertation simulation calculations are made on basis of a finite element method. The finite element program Plaxis is finally selected.

First the concept of the finite element method is given. Next explanation is given of the standard and special finite elements in Plaxis, the interface elements.

5.1   Concept of the finite element method

The concept of the finite element method is discussed in several textbooks (for instance Zienkiewics, 1971). A brief explanation of the finite element method is given below according to Bonnier (1993).

It is stated that displacements and stresses are maintained in a limited number of points in a finite element calculation. By interpolation of the displacements from the nodes, the displacements can be calculated everywhere throughout the element. This interpolation is done by means of shape functions. The displacements within an element are determined solely by the nodes in that element. Depending on the number of nodes a certain degree of interpolation is possible. Because the displacements are known throughout, the strains at any point can be determined. The strains at one point are calculated from the derivatives of the displacements at that point as

$$\underline{\varepsilon} = L\,\underline{u} \tag{5.1}$$

where

$\underline{\varepsilon}$ is the strain vector, L is a differential operator matrix and $\underline{u}$ is the displacement vector at the point considered :

$$\underline{\varepsilon} = \begin{Bmatrix} \varepsilon_{xx} \\ \varepsilon_{yy} \\ \varepsilon_{zz} \\ \gamma_{xy} \end{Bmatrix}; \quad L = \begin{Bmatrix} \dfrac{\partial}{\partial x} & 0 & 0 \\ 0 & \dfrac{\partial}{\partial y} & 0 \\ 0 & 0 & \dfrac{\partial}{\partial z} \\ \dfrac{\partial}{\partial y} & \dfrac{\partial}{\partial x} & 0 \end{Bmatrix}; \quad \underline{u} = \begin{Bmatrix} u_x \\ u_y \\ u_z \end{Bmatrix} \tag{5.2}$$

These components can, by interpolation, be expressed in the displacements of the nodes in an element in the following way :

$$u_x = N_1 u_{x1} + N_2 u_{x2} + \ldots + N_n u_{xn} \tag{5.3}$$

where

u_{x1}, u_{x2}, ... $=$ displacement components of the nodes in an element

n $=$ number of nodes in an element

N_1, N_2, ... $=$ interpolation or shape functions

By interpolation according to equation 5.1 a continuous displacement field arises. By using the derivatives of the shape functions, by combining equations 5.1 and 5.3, the strains at one point can be calculated. There follows :

$$\underline{\varepsilon} = \underline{\underline{B}}\,\underline{a} \tag{5.4}$$

wherein

$\underline{\underline{B}}$ $=$ the so-called strain interpolation matrix

$\underline{a}$ $=$ the nodal displacement vector

In case of 15-noded elements strains are found till the third power, the so-called cubic strain elements.

By using the strains, the stresses can be determined. These stresses should be in equilibrium with external loads such as weight and boundary loads. Although the displacements, by the correct choice of shape functions, are also continuous beyond the element edges, this does not apply to the stresses. The equilibrium equations are

$$L^T \underline{\sigma} = -\underline{f} \tag{5.5}$$

where

$$L^T = \begin{Bmatrix} \dfrac{\partial}{\partial x} & 0 & \dfrac{\partial}{\partial y} \\ 0 & \dfrac{\partial}{\partial y} & \dfrac{\partial}{\partial y} \end{Bmatrix}; \quad \underline{\sigma} = \begin{Bmatrix} \sigma_{xx} \\ \sigma_{yy} \\ \sigma_{xy} \end{Bmatrix}; \quad \underline{f} = \begin{Bmatrix} f_x \\ f_y \end{Bmatrix} \tag{5.6}$$

in which f_x and f_y are body forces. Further, there still prevails $\sigma_{xy} = \sigma_{yx}$. At the boundaries the stresses should be in equilibrium with the present external load.

5.2   Finite elements

In order to carry out a finite element simulation calculation the problem has to be subdivided into triangular elements. The calculation refers to displacements and stresses. These two variables are maintained in a limited number of points. The basic finite element in Plaxis, the triangle, consists of 15 nodes and 12 Gaussian integration points, figure 5.1. The finite element calculations provide displacements at each individual node and stresses at each individual Gaussian integration point. This 15-noded triangle is suitable for both plane strain and axial symmetric calculations and performs very well for calculation of collapse loads as well as the prediction of failure mechanisms (Sloan & Randolph, 1982)
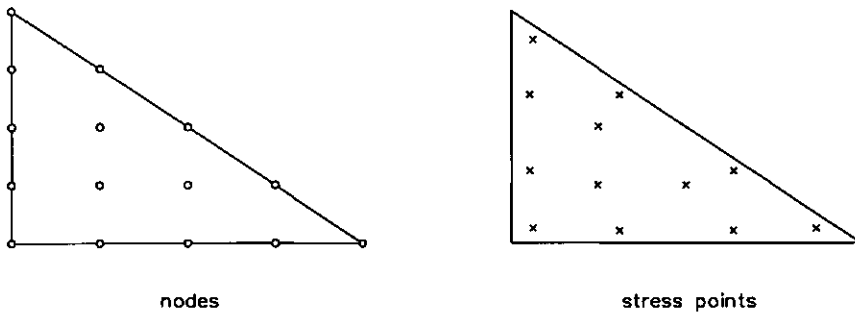
nodes   stress points

Figure 5.1   Location of nodes and stresspoints in a basic finite element in Plaxis.

5.3 Interface elements

To model soil-structure interaction, such as slipping and gapping, so-called interface elements can be used (Van Langen, 1991, Van Langen & Vermeer, 1991 and Vermeer, 1993). An interface element is a zero-thickness element with nodes on each side. The number of nodes depends on the connecting soil element. In this case 2 times 5 nodes are used. For visualisation purpose the nodes on opposite sides are shown as if the interface element has a finite thickness, figure 5.2.

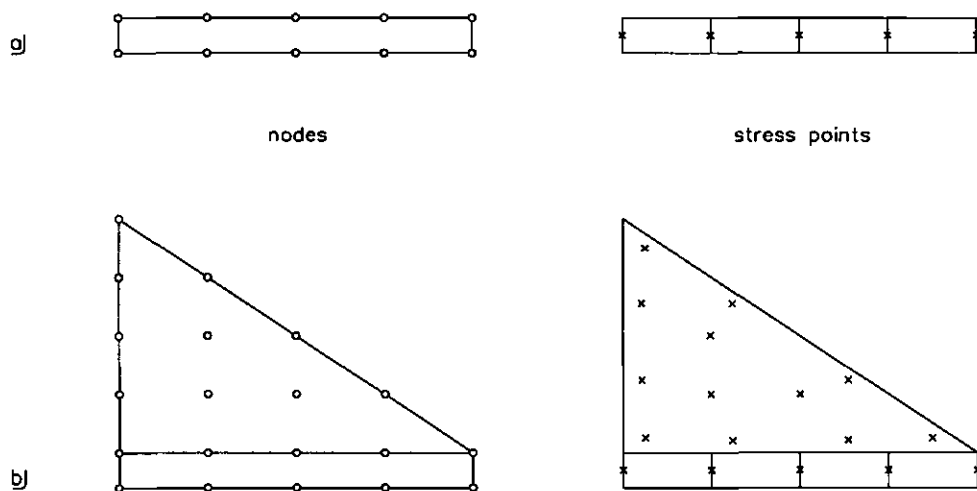nodes   stress points

Figure 5.2 Location of nodes and stresspoints in an interface element
(a), connected to a 15-noded triangular element (b).

Here it can be seen that the interface element has been presented as an element with a finite thickness of one tenth of the length of the interface element and consists of five pair of nodes and five stresspoints. The stresspoints are located at the position of each of the node pairs of the interface element. The behaviour of the interface element is described by an elasto-plastic Coulomb relation. Elastic behaviour of the interface element occurs in those cases where :

$$|\tau| < \sigma_n \tan\varphi_i + c_i \tag{5.7}$$

whereas plasticity occurs if

$$|\tau| = \sigma_n \tan\varphi_i + c_i \tag{5.8}$$

wherein

τ = shear stress acting in the interface

σ_n = normal stress acting in the interface

φ_i = angle of friction of the interface

c_i = cohesion of the interface

It should be remarked that only in the direction parallel to the interface element there will be checked on flow. This in contrast with soil elements where there is checked on flow in every direction. Practically this means that if the stress state in the interface element satisfies the flow criterion, flow may occur in the interface, in a direction parallel to that specific interface.

According to the Plaxis manual (Vermeer, 1993), elastic interface behaviour involves two phenomena :
- relative displacements normal to the interface called gapping
- relative movement parallel to the interface called slipping.

The magnitude of these displacements are :

$$\text{elastic gap displacement} = \frac{\sigma\, t_i}{K_i} \tag{5.9}$$

$$\text{elastic slip displacement} = \frac{\tau\, t_i}{G_i} \tag{5.10}$$

wherein

K_i = compression modulus of the interface

G_i = shear modulus of the interface

t_i = virtual thickness of the interface

Relation between the compression and shear moduli is given by

$$K_i = 2G_i\, \frac{1 - \upsilon_i}{1 - 2\upsilon_i} \tag{5.11}$$

wherein

υ_i = Poisson's ratio of the interface

In the used Plaxis finite element code υ_i is fixed at 0.45. To avoid numerical problems the material properties of the interface elements are linked to material properties of the soil by using a strength reduction factor R. The following rules are applied :

$$c_i = R\, c_{soil}$$
$$\tan \varphi_i = R\, \tan \varphi_{soil}$$
$$G_i = R^2\, G_{soil}$$
$$\upsilon_i = 0.45$$
$$\psi_i = 0$$

If R is set to unity the interface properties are the same as those within the associated data set. In the case R is set to a value of less than unity then the interface is weaker and more flexible than the associated soil.

The above is according to the manual. However, in the finite element code the coordinates of each node pair are identical which implies a zero thickness of the interface element. Each interface element assigned to it has a virtual thickness which is an imaginary dimension that is only used to obtain the material properties of the interface. Displacements in the interface perpendicular and parallel to the interface are related to normal and shear stresses in the interface through making use of a constant of proportionality. This constant of proportionality is given in the form of virtual thickness and strength parameters c, φ, G, υ and ψ. In this way mechanical properties of the soil elements and interface properties are tuned. With the use of interface elements extra normal and tangential displacements are allowed.

A graphical representation of the behaviour of the interface element is given in figure 5.3a. Here it can be seen that the coordinates of each node pair are identical which implies a zero thickness of the element.

Physical interpretation of the normal behaviour of the interface can be imagined by a spring with a normal stiffness K_n and two blocks fixed on plates which can shear to each other. However, movement on base of compression is disabled, see the enlarged blocks in figure 5.3b. Movement on the base of tension is allowed but restricted to a maximum value. Resistance against movement depends on the friction properties of the material layer (tensile strength T) between the plates of which the blocks are fixed. Thus, summarising it can be stated that there is, in the normal direction of the interface, elasto-plastic behaviour in one and elastic behaviour in the opposite direction.

Physical interpretation of the tangential behaviour of the interface can also be imagined by a spring with a shear stiffness K_s, figure 5.3a. Plasticity occurs if the shear stress between the two plates exceeds $\tau_{max} = c + \sigma_n \tan\varphi$. So, here elasto-plastic behaviour is allowed in two opposite tangential directions of the interface.

$\mathcal{T}_{max}$ K_S

$\delta = 0$

T

K_N

$\mathcal{T}_{max}$ = shear strength
K_S = shear/tangential stiffness
δ = virtual thickness
T = tensile strength
K_N = normal stiffness

a)

b)

σ_N σ_N
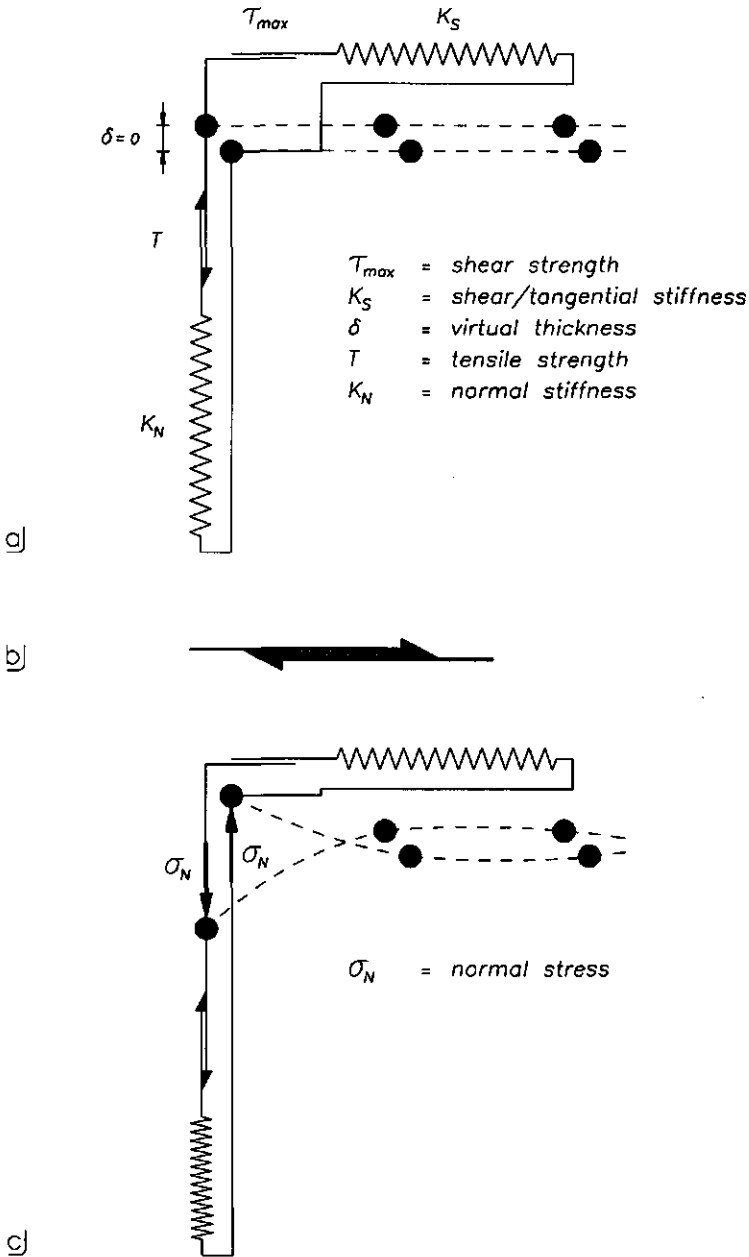
σ_N = normal stress

c)

Figure 5.3 Physical representation of the behaviour of an interface element (a), under the influence of a normal stress σ_n (c); details of plates and fixed blocks (b).

So, elastic displacements of the interface, normal and tangential, are proportional to σ and τ respectively (NB elastic displacement and not strain). On the other hand, the plastic behaviour in the tangential direction of the interface is subjected to the earlier described Mohr-Coulomb flow criterion. But the output of interface elements follows the interface presentation given in the manual. Consequence of this is that calculated and plotted displacements of interfaces sometimes are very surprising. For example, a displacement perpendicular to the interface can be much greater than the virtual thickness in a plot, suggesting a negative thickness of the element.

6   Derivation of agricultural soil model parameters for Plaxis

Simulation of soil behaviour in civil engineering is carried out by assuming that the soil beneath the ground water level consists of soil particles and water and above the phreatic line soil consists of soil particles only.

In agriculture, however, the area of interest is the first 0.5-1.0 m of soil beneath the surface level. Taking a close look at this layer it is obvious that besides soil particles and water, the soil also contains a varying amount of air. Even in the seasons autumn and winter where the conditions can be very wet sometimes, there is still an amount of pores in the soil filled with air. Therefore, values of soil model parameters suitable for simulating soil behaviour in case of civil engineering cannot be used one to one for simulation of soil behaviour of agricultural soils. In this chapter derivations of suitable agricultural soil model parameters for simulating agricultural soil behaviour are given.

Firstly, the soil model parameters of Mohr-Coulomb are treated. There is zoomed in at the elasticity modulus E and Poisson's ratio v because little is known about values for these parameters (Van den Akker et al., 1998).

Secondly, the elastic region of the Plaxis-Cap model is treated. The Plaxis-Cap model is a soil model enabling to describe soil compaction on the base of hardening. There is zoomed in at parameter C_p, a parameter related to the modified swelling index κ^* necessary in case of the Plaxis-Cap model (Vermeer, 1993). Again, because little is known about this parameter in case of agricultural soils (Van den Akker et al., 1998).

Finally, for the sake of completeness it should be noticed that total stresses are considered in this chapter unless it is stated explicitly that this is not the case.

6.1   Reference soil

In this dissertation point of departure for all the presented simulation calculations is a Wageningen moderately heavy river clay. In terms of the USDA-classification a silty clay loam (Dawidowski & Koolen, 1987). This soil is taken at a depth of 0.07-0.17 m beneath the ground level. Sampling took place in a field of mature sugar-beets in the autumn of 1985. Prior to this a large amount of field traffic had passed over the sampling sites for fertilising and spraying, but there were no signs that this traffic had caused severe damage to soil structure. At that time the ground water level was situated at 0.90 m beneath the ground level. Characteristics of the described reference soil are given in table 6.1.

agricultural reference soil		
sample weight	18.74	[kN/m^3]
pore volume	45	[%]
air filled pore volume	5	[%]
φ	0	[°]
c	81.82	[kN/m^2]
ψ	0	[°]

Table 6.1   Characteristics of the agricultural reference soil.

The volumetric strain behaviour of such a soil is mainly governed by Boyle's law applied to the entrapped air (Swinkels, 1982),

6.2   Mohr-Coulomb soil model parameters

Values of three out of five Mohr-Coulomb soil model parameters have been derived already. Derivation of values for the remaining two parameters, i.e. E and υ, is more complicated. Starting point is the measured stress-strain curve in an undrained or quick triaxial test, figure 6.1.
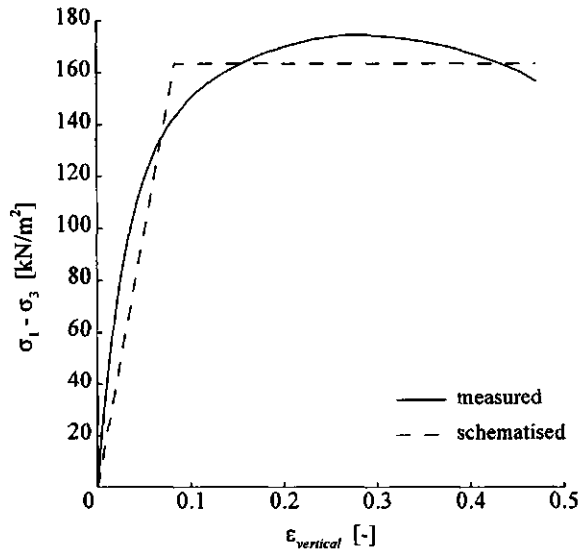

Figure 6.1   Stress - strain relation of the reference soil measured in an undrained triaxial test at a strain rate of 0.021 s^{-1} and schematised in an elastic and plastic part ($\sigma_3 = \sigma_2 = 200 \text{ kN/m}^2$).

Assumptions that have been made during interpretation of an undrained triaxial test of the reference soil are :
- soil particles and water are incompressible
- air is present as air pockets that are randomly distributed and stay enclosed in the sample during compression
- stability of the air-water mixture; instability occurs in those cases where the pressure is in the region beyond 500 kN/m^2 (Huizinga, 1969)
- the atmospheric pressure is fully transmitted through the whole soil sample without :
  - affecting soil matrix stresses
  - generation of extra shear stresses
- the exerted external pressure from the piston to the soil sample is fully transmitted through the whole sample
- the hydrostatic stress state implies the equality of all principal stresses ($\sigma_1 = \sigma_2 = \sigma_3$) and the hydrostatic stress equals there level; in case of the undrained triaxial test on the reference soil, $\sigma_1 \neq \sigma_2 = \sigma_3$; however the differences are very small and therefore the hydrostatic stress is approximately made equal to the mean sample stress

$$\sigma_{hydrostatic} = \sigma_{sample} = \frac{1}{3}\left(\sigma_1 + \sigma_2 + \sigma_3\right) \tag{6.1}$$

where total stresses are considered; therefore, from now on the term hydrostatic stress refers to equation 6.1 and agrees with the definition of Chen (1975).

Logically this means that the air pressure in the sample, σ_{air}, equals the total stress state in the sample at any time

$$\sigma_{sample} = \sigma_{air} \tag{6.2}$$

Before loading the triaxial test the total stress in the sample, the air pressure in the sample and the atmospheric pressure, $\sigma_{atmosphere}$, are identical

$$\sigma_{sample} = \sigma_{air} = \sigma_{atmosphere} = 101.325 \ \text{kN}/\text{m}^2 \tag{6.3}$$

During loading in the triaxial test with an external pressure from a piston, σ_{extern}, there prevails

$$\sigma_{sample} = \sigma_{air} = \sigma_{atmosphere} + \sigma_{extern} \tag{6.4}$$

wherein

$$\sigma_{extern} = \frac{1}{3}\left(\sigma_1 + \sigma_2 + \sigma_3\right) \tag{6.5}$$

The ideal gas law can be written as

$$\sigma_{air} \ V_{air} \ = \ \frac{M_{air}}{\omega_{air}} \ R \ T \tag{6.6}$$

wherein

σ_{air}	=	absolute air pressure, i.e. $\sigma_{atmosphere} + \sigma_{extern}$	[kN/m^2]
V_{air}	=	volume of air	[m^3]
M_{air}	=	mass of air	[kg]
ω_{air}	=	molecular mass of air	[kg/kmol]
R	=	universal (molar) gas constant (i.e. 8.34144)	[J/mol·K]
T	=	absolute temperature	[K]

The air in the soil sample can be considered as gas in a closed system with constant mass and temperature. Under these conditions the right-hand side of equation 6.6 is a constant and can be written as Boyle's law

$$\sigma_{air,1} \ V_{air,1} \ = \ \sigma_{air,2} \ V_{air,2} \ = \ \text{constant} \tag{6.7}$$

wherein

$\sigma_{air,1}$	=	absolute pressure of air at condition 1
$V_{air,1}$	=	volume of air at condition 1
$\sigma_{air,2}$	=	absolute pressure of air at condition 2
$V_{air,2}$	=	volume of air at condition 2

So, the change of volume of air is represented by

$$\Delta V_{air} \ = \ V_{air,\ initial} \ - \ \left(\frac{\text{constant}}{(\sigma_{atmosphere} + \sigma_{extern})} \right) \tag{6.8}$$

wherein

Δ	=	change of value of a specific quantity
$V_{air,\ initial}$	=	volume of air before testing

Soil particles and water are taken incompressible, thus

$$\Delta V_{air} \ = \ \Delta V_{sample} \tag{6.9}$$

In a triaxial test

$$\begin{aligned} \sigma_2 &= \sigma_3 \\ \varepsilon_2 &= \varepsilon_3 \end{aligned}$$
(6.10)

and relative volume change of the soil sample, ε_v , is described by

$$\varepsilon_v = \varepsilon_1 + 2\varepsilon_3 = \frac{\Delta V_{sample}}{V_{sample,\,initial}}$$

$$= \frac{V_{air,\,initial} - \left(\dfrac{constant}{\sigma_{atmosphere} + \frac{1}{3}(\sigma_1 + 2\,\sigma_3)} \right)}{V_{sample,\,initial}}$$
(6.11)

wherein

$$\varepsilon_v = \text{volumetric strain}$$
$$V_{sample,\,initial} = \text{volume of the soil sample before testing}$$

Equation 6.11 is used to approximate the relation between the air percentage, the hydrostatic stress and the volumetric strain for the elastic region of agricultural soils. In figure 6.2 the relation between the hydrostatic stress and the volumetric strain of the reference soil is plotted at different air percentages.
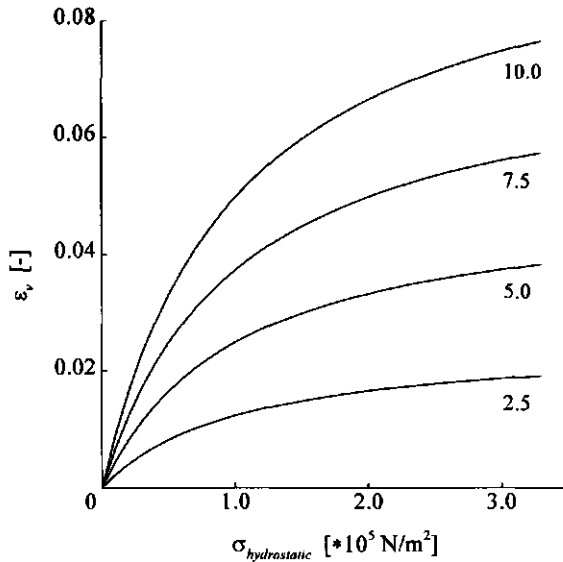
Figure 6.2   Theoretical hydrostatic stress - volumetric strain relation of
              the reference soil for the elastic region at four air
              percentages.

According to elasticity theory the relationship between the hydrostatic stress and the
volumetric strain is described by the bulk modulus K

$$\frac{1}{3}\left(\sigma_1 \, + \, \sigma_2 \, + \, \sigma_3\right) \, = \, K\left(\varepsilon_v\right) \tag{6.12}$$

wherein

$$K \, = \, \frac{E}{3\left(1 \, - \, 2\upsilon\right)} \tag{6.13}$$

$$\varepsilon_v \, = \, \varepsilon_1 \, + \varepsilon_2 \, + \varepsilon_3 \tag{6.14}$$

In case of a triaxial test equation 6.12 can be rewritten by

$$\varepsilon_1 \, + \, 2\varepsilon_3 \, = \, \frac{1}{3K}\left(\sigma_1 \, + \, 2\sigma_3\right) \tag{6.15}$$

However, the relation between the hydrostatic stress and the volumetric strain is linear for
equation 6.15 and non-linear in the case of equation 6.11. So, bulk modulus K can only be
approximated. Consider the experimental stress-strain curve of figure 6.1. This curve is

represented schematically by the dashed line in the same figure. It may be obvious that this schematised curve can be split up into an elastic and a plastic part. For different axial strains the corresponding hydrostatic stress can be calculated.

Taking the hydrostatic stress at the change from elastic to plastic state of the reference soil given in the schematised curve of figure 6.1 as point of departure. This hydrostatic stress together with the air percentage of 5 gives a certain volumetric strain according to equation 6.11. Bulkmodulus K can then be calculated with this volumetric strain in combination with the corresponding hydrostatic stress using equation 6.15, figure 6.3. This procedure to calculate K is followed because in this way the volumetric strains at the end of the elastic regions and at the beginning of the plastic regions are realistic, figure 6.1.
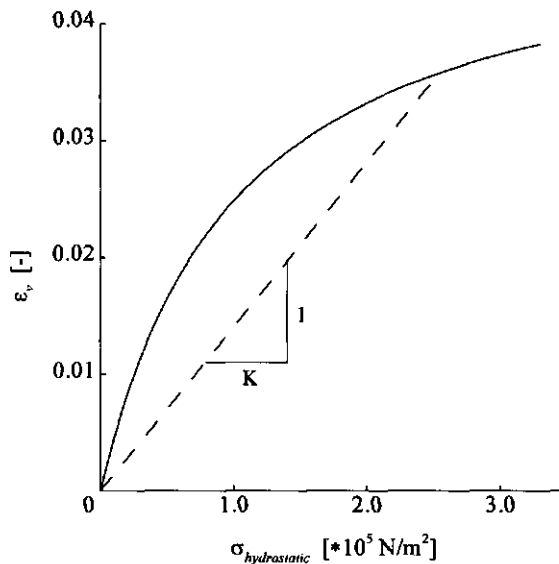

Figure 6.3   Hydrostatic stress - volumetric strain relation, calculated on the basis of Boyle's law applied to soil air and an approximation of K at the end of the elastic region of soil with 5 percentage air.

Conversion of the bulk modulus K into the elasticity parameters E and υ, required by the Plaxis finite element code, is described hereafter.

Parameters σ_1, σ_3 and ε_1 can be determined at the change from elastic to plastic state of the reference soil given in the schematised curve of figure 6.1. Parameter ε_3 is deduced from equation 6.15.

When the parameters τ_{xy}, G, γ_{xy} and ε_{xy} are given by

$$\tau_{xy} = G\gamma_{xy} \tag{6.16}$$

$$\tau_{xy} = \tfrac{1}{2}\left(\sigma_1 - \sigma_3\right) \tag{6.17}$$

$$G = \frac{E}{2\left(1+\upsilon\right)} \tag{6.18}$$

$$\gamma_{xy} = 2\,\varepsilon_{xy} \tag{6.19}$$

$$\varepsilon_{xy} = \tfrac{1}{2}\left(\varepsilon_1 - \varepsilon_3\right) \tag{6.20}$$

the shear modulus G can be rewritten as

$$G = \frac{\left(\sigma_1 - \sigma_3\right)}{2\left(\varepsilon_1 - \varepsilon_3\right)} \tag{6.21}$$

Equation 6.18 is rewritten by

$$\upsilon = \left(\frac{E}{2G}\right) - 1 \tag{6.22}$$

Substituting equation 6.22 into the general equation for linear elasticity (which can be deduced from equation 6.26)

$$\varepsilon_1 = \frac{1}{E}\left[\sigma_1 - \upsilon\left(\sigma_2 + \sigma_3\right)\right] \tag{6.23}$$

results in case of a triaxial test in

$$E = \frac{\sigma_1 + 2\sigma_3}{\left(\varepsilon_1 + \dfrac{\sigma_3}{G}\right)} \tag{6.24}$$

So, K gives ε_3 by equation 6.15, ε_3 gives G by equation 6.21, G gives E by equation 6.24 and E gives υ by equation 6.22.

Finally, two graphs are presented in which the air percentage is plotted against the calculated bulk modulus K, shear modulus G and the elasticity modulus E on the one hand and against the calculated Poisson's ratio υ on the other hand (figures 6.4 and 6.5). Base of these graphs is the stress state of the reference soil at the transition from elastic to plastic state in the schematised curve of figure 6.1.
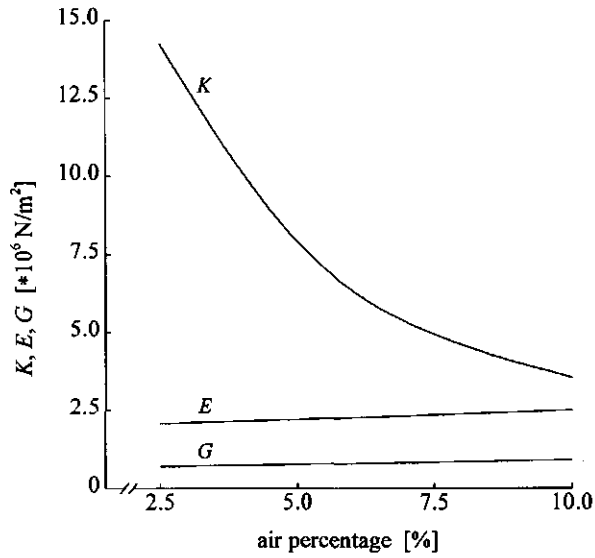
Figure 6.4 Theoretical air percentage - bulk modulus K, shear modulus G, elasticity modulus E relation of the reference soil.
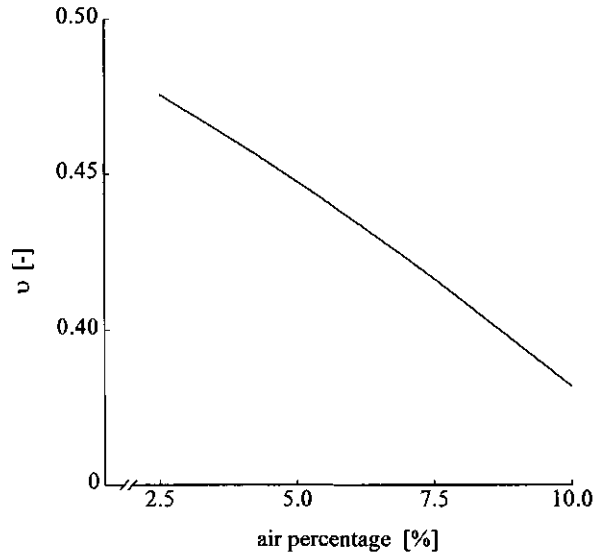

Figure 6.5 Theoretical air percentage - Poisson's ratio υ relation of the reference soil.

6.3 Plaxis-Cap soil model parameters

Observations of the treatment of loose agricultural soil induced by a passing tyre shows the observer that the soil partly rebounds after passing of the tyre. Physically this means that during loading of loose agricultural soil, the soil is compacted and soil air attains entrapped simultaneously. During leaving of the tyre the loading process turns into an unloading process. In this phase the soil is partly rebounding which is due to the fact of :
- elasticity of the soil skeleton
- expansion of soil air.
It is most likely that the largest part of the rebounding of the soil is due to the expansion of the entrapped soil air according to Boyle's law. Measurements of Perdok & Kroesbergen (1999) point also into that direction. This means that the above described behaviour is decisive for parameter C_p of the Plaxis-Cap model. Derivation of suitable values for C_p in case of the reference agricultural soil is given in the following sections.

6.3.1 Elastic region

For convenience the generalised form of Hooke's law, the elastic stress-strain behaviour of an ideal isotropic soil material, is given below completely

$$
\begin{bmatrix} \dot{\sigma}_{xx} \\ \dot{\sigma}_{yy} \\ \dot{\sigma}_{zz} \\ \dot{\sigma}_{xy} \\ \dot{\sigma}_{yz} \\ \dot{\sigma}_{zx} \end{bmatrix} = \frac{E}{(1-2\upsilon)(1+\upsilon)} \begin{bmatrix} 1-\upsilon & \upsilon & \upsilon & 0 & 0 & 0 \\ \upsilon & 1-\upsilon & \upsilon & 0 & 0 & 0 \\ \upsilon & \upsilon & 1-\upsilon & 0 & 0 & 0 \\ 0 & 0 & 0 & \frac{1}{2}-\upsilon & 0 & 0 \\ 0 & 0 & 0 & 0 & \frac{1}{2}-\upsilon & 0 \\ 0 & 0 & 0 & 0 & 0 & \frac{1}{2}-\upsilon \end{bmatrix} \begin{bmatrix} \dot{\varepsilon}^e_{xx} \\ \dot{\varepsilon}^e_{yy} \\ \dot{\varepsilon}^e_{zz} \\ \dot{\varepsilon}^e_{xy} \\ \dot{\varepsilon}^e_{yz} \\ \dot{\varepsilon}^e_{zx} \end{bmatrix} \quad (6.25)
$$

where E and υ are the Young's modulus and the Poisson's ratio appropriate for changes of stresses. The values of E and υ are assumed to remain constant over small increments of stresses and strains, as the soil material is assumed to be linear elastic. Rearranging and rewriting equation 6.25 in terms of principal stresses and principal strains gives

$$
\begin{bmatrix} \dot{\varepsilon}^e_1 \\ \dot{\varepsilon}^e_2 \\ \dot{\varepsilon}^e_3 \end{bmatrix} = \frac{1}{E} \begin{bmatrix} 1 & -\upsilon & -\upsilon \\ -\upsilon & 1 & -\upsilon \\ -\upsilon & -\upsilon & 1 \end{bmatrix} \begin{bmatrix} \dot{\sigma}_1 \\ \dot{\sigma}_2 \\ \dot{\sigma}_3 \end{bmatrix} \quad (6.26)
$$

For the special case of axial symmetry, see equation 6.10, the following equations are deduced from equation 6.26

$$\dot{\varepsilon}_1 = \left(\dot{\sigma}_1 - 2\upsilon\dot{\sigma}_3\right)/E$$
$$\dot{\varepsilon}_2 = \dot{\varepsilon}_3 = \left((1-\upsilon)\,\dot{\sigma}_3 - \upsilon\dot{\sigma}_1\right)/E \tag{6.27}$$

In case of the one dimensional compression test horizontal strains will remain zero ($\dot{\varepsilon}_2 = \dot{\varepsilon}_3 = 0$) and equation 6.27*b* becomes

$$\dot{\sigma}_3 = \frac{\upsilon}{(1-\upsilon)}\dot{\sigma}_1 \tag{6.28}$$

Substituting equation 6.28 into equation 6.27*a* gives

$$\dot{\varepsilon}_1 = \frac{1}{E}\left(1 - \frac{2\upsilon^2}{1-\upsilon}\right)\dot{\sigma}_1 \tag{6.29}$$

Combining equation 6.29 with equation 6.18 gives

$$\dot{\varepsilon}_1 = \frac{1}{G}\left(\frac{\frac{1}{2}-\upsilon}{1-\upsilon}\right)\dot{\sigma}_1 \tag{6.30}$$

A well-known one-dimensional compression test is the so-called one-dimensional consolidation test. When the test induces an unloading phase, this phase is considered to be elastic. This curve part is followed again during reloading. A typical graph for this consolidation test is a semi-log relation between effective stress σ_1 and the relative settlement ε_1, figure 6.6.
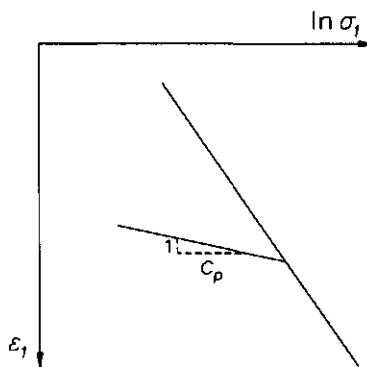

Figure 6.6 Schematised semi-log graph of σ_1, ε_1-relation of a one-dimensional consolidation test.

Essentially, the elastic curve part is linear which means that $\dot{\varepsilon}_1$ is proportional to the $\ln \sigma_1$-increment implying that $\dot{\varepsilon}_1$ is proportional to $\dot{\sigma}_1/\sigma_1$. According to Huizinga (1969) this proportionality is described by

$$\dot{\varepsilon}_1 = \frac{1}{C_p \sigma_1} \dot{\sigma}_1 \tag{6.31}$$

wherein

$$C_p = \text{swelling index}$$

Comparing equation 6.30 with equation 6.31 shows that the term $\dfrac{1}{G}\left(\dfrac{\frac{1}{2}-\upsilon}{1-\upsilon}\right)$ equals $\dfrac{1}{C_p \sigma_1}$.

This means that the elastic relation between $\dot{\varepsilon}_1$ and $\dot{\sigma}_1$ has become stress-dependent. Every soil has its specific C_p, thus the term $(1/C_p \sigma_1)$ can be calculated for each stress level of the soil to be considered. The Poisson's ratio υ in equation 6.30 is taken constant over a loading cycle. Combining equation 6.30 with equation 6.31 gives the possibility to calculate, for every stress level of a particular soil, the shear modulus G which the Plaxis code requires as input for the elastic region of the Plaxis-Cap model.

The second elastic soil model parameter of the Plaxis-Cap model is the already used Poisson's ratio υ. The value of this soil model parameter, on base of effective stress, is greater for loading processes than for unloading processes. To simulate loading as well as unloading and reloading processes satisfactorily, υ must range between 0.1 and 0.2 according to Vermeer (1992, 1993).

6.3.2 Determination of parameter C_p

The elastic parameter C_p of the Plaxis-Cap model can be derived from the unloading part of a drained, one dimensional compression test. Assuming the soil consists of soil particles and water only, civil engineering approach, the relation between the incremental strain and the incremental stress is given by

$$\delta \varepsilon = \frac{1}{C_p} \frac{\delta \sigma}{\sigma} \tag{6.32}$$

Integration gives

$$\varepsilon - \varepsilon_0 = \frac{1}{C_p} \ln \frac{\sigma}{\sigma_0} \tag{6.33}$$

wherein

$\varepsilon_0, \ \sigma_0 \ = \ $ integration constants

Equation 6.33 gives a straight line through the origin in a semi-log graph with tangent modulus $1/C_p$, figure 6.7. In practice, a semi-log graph of σ / σ_0 against $\varepsilon - \varepsilon_0$ shows that the relation between $\ln(\sigma / \sigma_0)$ and $\varepsilon - \varepsilon_0$ is not always ideal, i.e. straight. Therefore, some difficulties arise in deriving a correct C_p-value from plotted measured values. Especially the initial part of the semi-log curve may not be straight. Therefore, a C_p-value that is derived by curve fitting will depend on the σ_0-value.
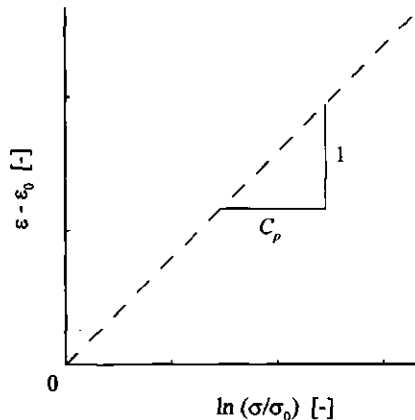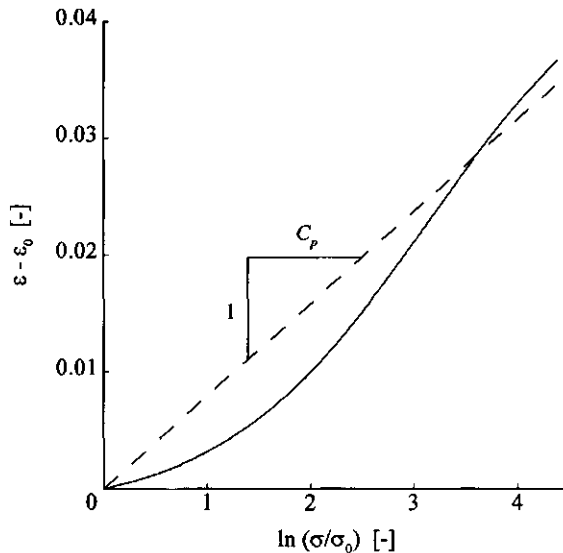

Figure 6.7 Idealised semi-log graph of stress - strain relation of the unloading part of a drained one-dimensional compression test.

In agriculture, the wet, dense and clayey soils behave as undrained material upon loading (Chancellor & Vomocil, 1985). Not having taken into account the air component in civil engineering and the absolute necessity of accounting for soil air in agricultural engineering is an important difference within the scope of the elasticity parameter C_p. So, the known C_p-values, derived from drained test of saturated soils, are not suitable for simulation of agricultural soils.

Therefore, simulation calculations were made to obtain realistic C_p-values, for agricultural soils. From measurements it is known that elasticity of agricultural soils is mainly due to enclosed air (Swinkels, 1982 and Perdok & Kroesbergen, 1999). It is also known that enclosed air throughout the whole sample is subjected to some pressure (Stroosnijder & Koorevaar, 1972).

With this in mind, a one-dimensional undrained compression test is simulated. For the sake of clarity, this implies that all stresses and parameters refer to total stresses. The simulated soil is the already mentioned reference soil of section 6.1. Assumptions that have been made in case of an undrained triaxial test prevail also in case of an undrained one-dimensional compression test with the exception of $\varepsilon_2 = \varepsilon_3 \neq 0$. Now $\varepsilon_2 = \varepsilon_3 = 0$ prevails. The simulations are made at air percentages ranging from 1 to 10 combined with two K_0-levels. Usually, the coefficient of lateral earth pressure K_0 represents the ratio between the effective horizontal initial and effective vertical initial stresses. However, in the context of this chapter K_0 represents the ratio between the total horizontal initial and total vertical initial stresses :

$$K_0 = \frac{\sigma_{horizontal}}{\sigma_{vertical}} \tag{6.34}$$

Using the elastic stress-strain relations, the relation between K_0 and Poisson's ratio υ is given by

$$K_0 = \frac{\upsilon}{1-\upsilon} \tag{6.35}$$

According to Klay (1975), K_0 varies from 0.8 to 0.9 in wet clayey material. Therefore, calculations are made at the lower K_0 limit of 0.8 and the upper K_0 limit of 0.9 with corresponding υ-values 0.44 and 0.47 respectively.

Derivation of the volume change of a soil sample in an undrained one-dimensional compression test is nearly similar to the volume change of a soil sample in an undrained triaxial test given in section 6.2. However, equation 6.34 is used now and the following relation can be deduced

$$\sigma_2 = \sigma_3 = K_0 \sigma_1 \tag{6.36}$$

Substituting equation 6.36 into equation 6.11 finally results into the following volume change relation of a soil sample in an undrained one-dimensional compression test

$$\varepsilon_1 = \frac{\Delta V_{sample}}{V_{sample,\,initial}}$$

$$= \frac{V_{air,\,initial} - \left(\dfrac{constant}{\sigma_{atmosphere} + \frac{1}{3}\sigma_1 \left(1 + 2K_0\right)} \right)}{V_{sample,\,initial}} \qquad (6.37)$$

On the base of equation 6.37 soil model parameter C_p can be derived. First of all a σ_0-value must be chosen from which a corresponding ε_0 is calculated. Subsequently, series of pairs of the quantities $\ln(\sigma/\sigma_0)$ and $\varepsilon - \varepsilon_0$ for a defined range ($\sigma_i/\sigma_0 \geq 1$) are calculated and plotted. The tangent modulus of a fitted straight line through the origin corresponds to $1/C_p$, figure 6.8.

Figure 6.8 Semi-log graph of stress - strain relation of the unloading part of an undrained one-dimensional compression test, calculated on the base of equation 6.37 and approximated by a straight line.

A specific problem in determining a C_p-value is the dependency of C_p on chosen σ_0-level. Therefore, a realistic σ_0 must be chosen. The soil layer to be considered is located directly beneath the ground level and has a thickness of 0.50 m with a sample weight of about 20 kN/m³. At the average depth of 0.25 m this corresponds with a σ_0 of 5.0 kN/m².

This initial air pressure of 5.0 kN/m^2 is a quite realistic value in view of the measurements of Stroosnijder & Koorevaar (1972). They measured an initial air pressure range of clay of 0 to 8.0 kN/m^2. Graphical reproduction of calculation results whereby soil model parameter C_p is calculated at air percentages ranging from 1 to 10 combined with two K_0-levels, 0.8 and 0.9, are presented in figure 6.9.
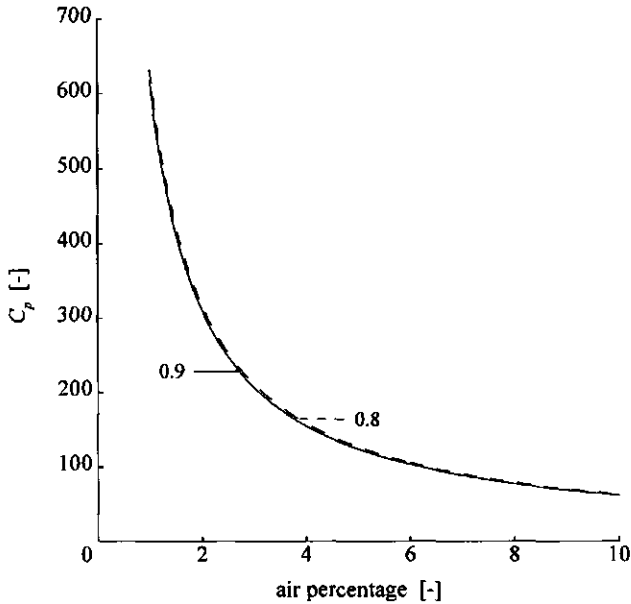

Figure 6.9 Relation between air percentage and C_p for $K_0 = 0.8$ and $K_0 = 0.9$ ($\sigma_0 = 5.0$ kN/m^2).

From figure 6.9 can be concluded that the influence of K_0 on C_p is negligible. On the other hand the level of C_p is strongly related to the air percentage.

Finally, the Boyle-curve of figure 6.8, which is based on equation 6.37 and from which soil model parameter C_p is derived, and the curve that is predicted by the estimated C_p using equation 6.33 are presented in figure 6.10 under the conditions of a K_0 of 0.8, an air percentage of 5 % and a σ_0 of 5.0 kN/m^2.
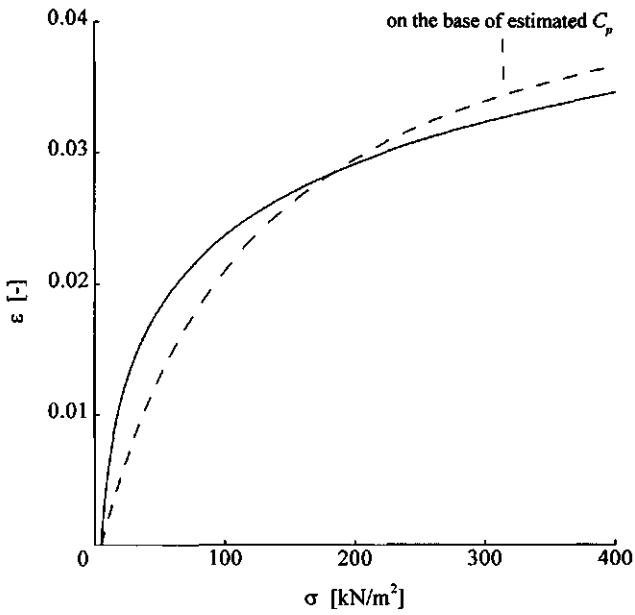
Figure 6.10 Stress - strain relation according to equation 6.37 and according to equation 6.33 on the base of an estimated C_p.

7   Extended Plaxis version and Trestana

Before presenting the analysis results for a specific case, the used extended Plaxis version and treatment and stress analysis program Trestana will be examined.

7.1   Extended Plaxis version

In the standard Plaxis program (version 5.3, chapter 5) displacements and strains are calculated for the nodes and stresses for the stresspoints. These output results can be shown per node or stresspoint for each calculation step for only a limited number of points if desired. For carrying out detailed analyses of treatment and stress paths, the standard Plaxis program is extended with an extra output module which was especially made by the Plaxis-team. This module labels all the stresspoints of the entire finite element mesh with a number and its coordinates and writes for each triangular element the calculation results of every step of all stresspoints within that element, 12 in this case, together with the specific label to one ascii-output file. So, such files could be obtained for each triangular element of the finite element mesh.

For example, the results of one particular step of one particular stresspoint of one ascii-output file of a particular triangular finite element of the reference case are :

- incremental displacements	$\dot{U}_x$, $\dot{U}_y$
- incremental strains	$\dot{\varepsilon}_{xx}$, $\dot{\varepsilon}_{yy}$, $\dot{\gamma}_{xy}$
- incremental rigid body rotation	$\dot{\omega}_{xy}$
- stresses	σ_{xx}, σ_{yy}, σ_{xy}, σ_{zz}.

7.2   Treatment and stress analysis program Trestana

To analyse output data generated by the extended Plaxis 5.3 version and to handle thoroughly the large amount of involved data in the order of 10 Mb for a single simulation calculation, the treatment and stress analysis program Trestana has been written. The structure of the program is presented in the scheme of figure 7.1. The figure is followed by more detailed explanation of the calculation procedure for quantities mentioned in the box 'determination of' as presented in the figure. Detailed information of the newly-defined composite quantities, so-called kneading numbers, and the graphical output part of Trestana is presented at relevant places in this dissertation.
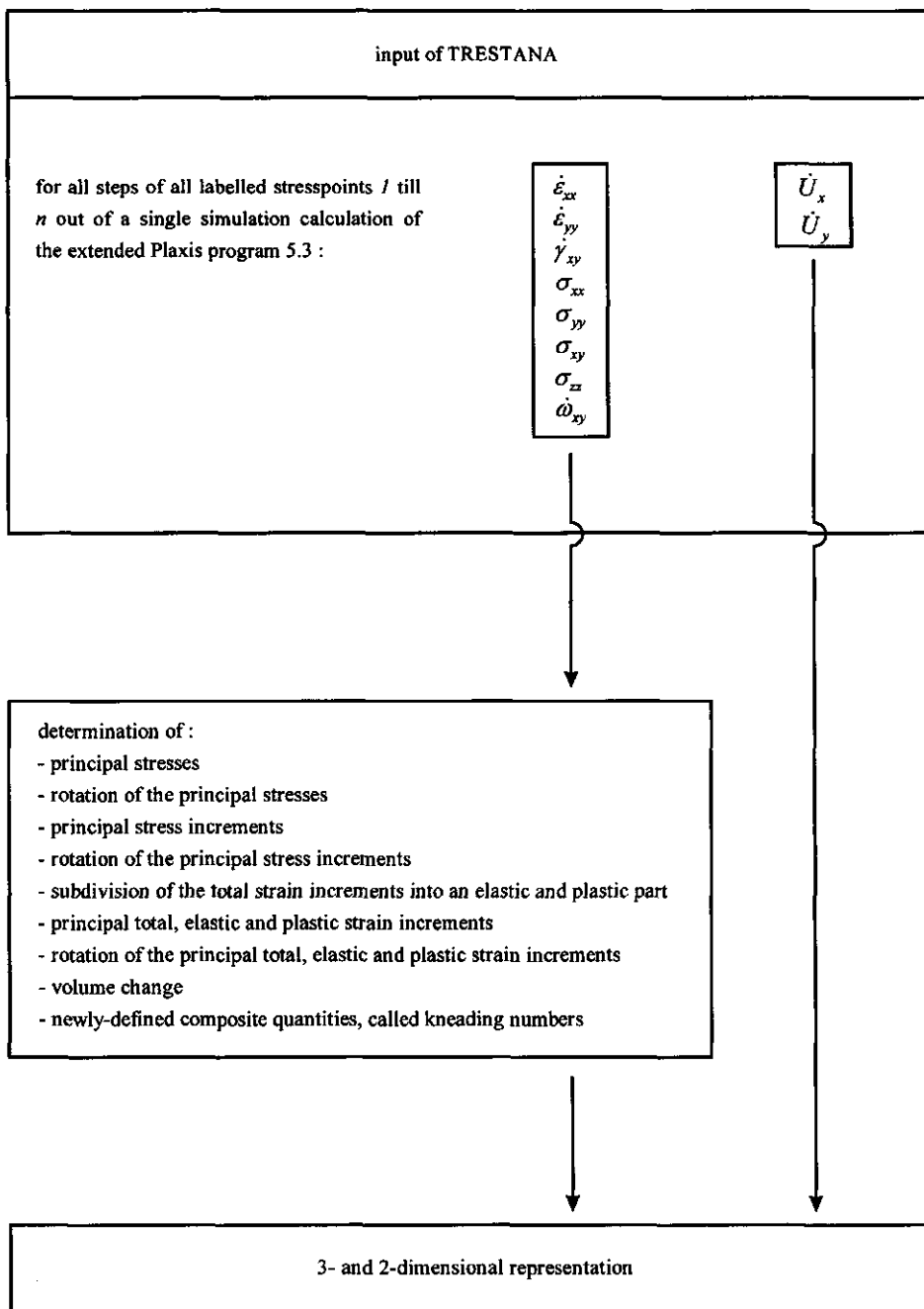
input of TRESTANA

for all steps of all labelled stresspoints l till
n out of a single simulation calculation of
the extended Plaxis program 5.3 :

$$\dot{\varepsilon}_{xx}$$
$$\dot{\varepsilon}_{yy}$$
$$\dot{\gamma}_{xy}$$
$$\sigma_{xx}$$
$$\sigma_{yy}$$
$$\sigma_{xy}$$
$$\sigma_{zz}$$
$$\dot{\omega}_{xy}$$

$$\dot{U}_x$$
$$\dot{U}_y$$

determination of :
- principal stresses
- rotation of the principal stresses
- principal stress increments
- rotation of the principal stress increments
- subdivision of the total strain increments into an elastic and plastic part
- principal total, elastic and plastic strain increments
- rotation of the principal total, elastic and plastic strain increments
- volume change
- newly-defined composite quantities, called kneading numbers

3- and 2-dimensional representation

Figure 7.1 Structure of the treatment and stress analysis program Trestana.

Principal stresses

Derivation of principal stresses implies finding eigenvalues with corresponding eigenvectors of a specific stress matrix. The eigenvalue problem is to determine the non-trivial solutions of the equation

$$A x = \lambda x \tag{7.1}$$

wherein

A = n-by-n matrix
x = length n column vector
λ = scalar

In case of stresses in a plane strain situation, matrix A is described by

$$A = \begin{bmatrix} \sigma_{xx} & \sigma_{xy} & 0 \\ \sigma_{xy} & \sigma_{yy} & 0 \\ 0 & 0 & \sigma_{zz} \end{bmatrix} \tag{7.2}$$

After a couple of matrix transformations, the desired eigenvalues and eigenvectors can be deduced from the solved equation

$$A X = X D \tag{7.3}$$

wherein

D = diagonal matrix whose values represent the eigenvalues
X = matrix whose columns represent the eigenvectors

The eigenvectors are scaled so that the norm of each vector is 1.

Rotation of the principal stresses

Rotation of a principal stress is reduced to the determination of the rotation between two vectors, which is described hereafter. Distinction is made between the non-corrected and corrected determination of the rotation between two vectors.

Non-corrected determination of the rotation between two vectors

Let A_{t-1} be a vector A at time t-1 and A_t the vector A at time t, with or without changes in length in comparison to time t-1. The change of the direction of vector A in one time step is the rotation of vector A. The amount of rotation of vector A_{t-1} to vector A_t is derived from the well-known relation

$$\cos \alpha = \frac{A_{t-1} \cdot A_t}{|A_{t-1}||A_t|} \tag{7.4}$$

For determination of the direction of the rotation of the vector, the procedure hereafter is followed. Vector A_{t-1} and vector A_t are normalised at unit length, which is denoted by A_{t-1}^* and A_t^* respectively

$$A_{t-1}^* = \begin{bmatrix} p \\ q \end{bmatrix}$$
$$A_t^* = \begin{bmatrix} r \\ s \end{bmatrix} \tag{7.5}$$

and presented in figure 7.2.
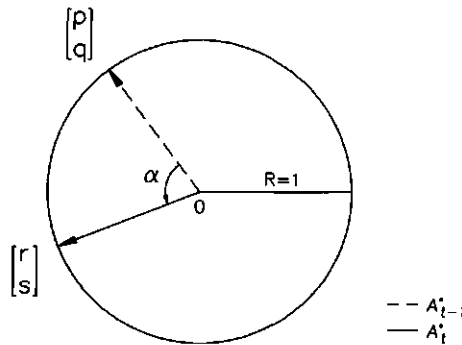
Figure 7.2   Vector A_{t-1}^* and A_t^*.

Afterwards, the vectors A^*_{t-1} and A^*_t are rotated round the origin simultaneously in such a way that vector A^*_{t-1} finally equals vector $[1 \ 0]^T$. Algebraically this means that

$$[R]\left[A^*_{t-1}\right] = \begin{bmatrix} 1 \\ 0 \end{bmatrix} \tag{7.6}$$

where matrix R is the rotation matrix and is of the form

$$\begin{bmatrix} a & b \\ -b & a \end{bmatrix} \tag{7.7}$$

Combining equations 7.5, 7.6 and 7.7 results into

$$\begin{aligned} a &= p \\ b &= q \end{aligned} \tag{7.8}$$

and rotation matrix R is known.

Rotation of vector $[r \ s]^T$ in a way similar to vector $[p \ q]^T$ gives vector $[u \ v]^T$:

$$\begin{bmatrix} p & q \\ -q & p \end{bmatrix}\begin{bmatrix} r \\ s \end{bmatrix} = \begin{bmatrix} u \\ v \end{bmatrix} \tag{7.9}$$

So,

$v < 0$ clockwise rotation

$\left.\begin{aligned} v &= 0 \\ u &= 0 \end{aligned}\right\}$ no rotation

$\left.\begin{aligned} v &= 0 \\ u &= -1 \end{aligned}\right\}$ rotation of 180 degrees

$v > 0$ anticlockwise rotation

According to the described procedure of determination of the rotation between two vectors the magnitude of the rotation interval is $\langle -180, 180]$ degrees.

Corrected determination of the rotation between two vectors

Determination of the rotation between two vectors with the earlier-described non-corrected approach means that the rotation lies in the interval of $\langle-180, 180]$ degrees. However, if vectors are eigenvectors and the rotation between these eigenvectors must be determined, a special situation arises which leads to a different approach. Characteristic of an eigenvector is the fact that the vector that arises through adding up or subtracting 180 degrees to that specific vector is also an eigenvector. Therefore it is always possible to correct the calculated rotation between two eigenvectors in such a way that the rotation finally lies in the interval [-90, 90] degrees through making use of the property of adding up or subtracting 180 degrees to the eigenvector at time t, if necessary. The so obtained rotation between two eigenvectors is denoted in this dissertation by corrected rotation.

Principal stress increments and rotation of the principal stress increments

Stress increments are determined by subtracting stresses at time t-1 from stresses at time t. Determination of the principal stress increments and the rotation of the principal stress increments are carried out in a way similar to the stresses.

Subdivision of total strain increments into an elastic and plastic part

For simulation of the reference case in Plaxis the Mohr-Coulomb model is used, which means that Hooke's law is used to calculate the elastic relation between stress and strain increments (equation 6.25). For a plain strain situation prevails

$$\dot{\varepsilon}_{zz}^{e} = \dot{\varepsilon}_{yz}^{e} = \dot{\varepsilon}_{zx}^{e} = 0 \qquad (7.10)$$

from which results

$$\dot{\sigma}_{zz} = \upsilon\left(\dot{\sigma}_{xx} + \dot{\sigma}_{yy}\right) \qquad (7.11)$$

Substituting equations 7.10 and 7.11 into equation 6.25 finally gives

$$
\begin{aligned}
\dot{\varepsilon}_{xx}^{e} &= \frac{1}{E}\left(\left(1 - \upsilon^{2}\right)\dot{\sigma}_{xx} - \upsilon\left(1 + \upsilon\right)\dot{\sigma}_{yy}\right) \\
\dot{\varepsilon}_{yy}^{e} &= \frac{1}{E}\left(\left(1 - \upsilon^{2}\right)\dot{\sigma}_{yy} - \upsilon\left(1 + \upsilon\right)\dot{\sigma}_{xx}\right) \\
\dot{\varepsilon}_{xy}^{e} &= \frac{1}{E}\left(1 + \upsilon\right)\dot{\sigma}_{xy}
\end{aligned}
\qquad (7.12)
$$

Both the stress and strain increments are known from the Plaxis output. So, the plastic strain increment part can be deduced according to equation 3.1.

Principal total, elastic and plastic strain increments

Derivation of principal total, elastic and plastic strain increments is carried out in a way similar to the determination of the principal stresses

However, in case of total strain increments also another procedure can be followed to determine the principal total strain increments. In this case there is sought alliance with the theory of homogeneous strain described in chapter 2 and the homogeneous strain analysis described by Tijink et al. (1988). This other procedure also gives the possibility to verify the results obtained by the first mentioned procedure. Moreover, subdividing the overall treatment of a parallelepiped into a deformational and rotational part gains an insight to the treatment analyses, especially in the rigid body rotations, which is therefore given hereafter.

A parallelepiped in a 2-dimensional orthogonal coordinate system can be described by a 2-by-2 matrix B, under condition that one angular point coincides with the origin of the system. The columns of B (Be^1 and Be^2) are the parallelepiped edges that meet in the origin ($e^1 = [1 \ 0]^T$, $e^2 = [0 \ 1]^T$).
Consider two soil cubes, one before treatment represented algebraically by B_i and one after treatment represented by B_f. Defining an overall treatment matrix T

$$B_f = T B_i \tag{7.13}$$

Matrix T is found by solving the matrix equation

$$B_f^T = B_i^T T^T \tag{7.14}$$

using Gaussian elimination.

With a polar decomposition matrix T can be expressed in both $T = R S$ and $T = V R$, where S represents the right stretch matrix and V the left stretch matrix. In both cases R represents the rotation. If deformations are infinitesimal, $S \approx V$ (Hunter, 1983) and for decomposition of matrix T there is selected $T = R S$. Furthermore, matrix S is called the matrix of deformation. From linear algebra it is known that every matrix $A(m,n)$ can be written as

$$A = U D V^T \tag{7.15}$$

with

$$U^T U = V^T V = I_n \tag{7.16}$$

Matrix D is a diagonal matrix with, on its diagonal, the so-called singular values of A, which satisfy $\delta_1 \geq \delta_2 \geq \ ... \ \delta_n \geq 0$.
If a singular value decomposition is carried out for matrix T (Golub & van Loan, 1989), then

$$T = U D V^T = \left(U V^T \right)\left(V D V^T \right) \tag{7.17}$$

wherein

$$U V^T = \text{rotation matrix } R$$
$$V D V^T = \text{deformation matrix } S$$

Characteristics of the obtained matrices are :
- columns of V are eigenvalues of S
- δ_1 and δ_2 are eigenvalues of S
- eigenvector directions of S are principal directions
- matrix $R = \begin{bmatrix} \cos \alpha & -\sin \alpha \\ \sin \alpha & \cos \alpha \end{bmatrix}$, in which α is the rigid body rotation of the parallelepiped.

However, it must be stated that the rigid body rotation can also be determined in a more direct way with the help of the earlier described u and v of chapter 2. The rigid body rotation ω_{xy} then becomes (equation 2.37)

$$\omega_{xy} = 0.5 \left(\frac{\partial v}{\partial x} - \frac{\partial u}{\partial y} \right)$$

Because u and v are known inside the Plaxis program it is logical that the rigid body rotation is determined on base of above described equation.

Rotation of the principal total, elastic and plastic strains

Determination of the rotation of the principal total, elastic and plastic strains is carried out in a way similar to the stresses.

Volume change

In case of a plane strain situation $\dot{\varepsilon}_{zz} = 0$ and the volume change increment is determined by

$$\Delta V = \dot{\varepsilon}_{xx} + \dot{\varepsilon}_{yy} \qquad\qquad (7.18)$$

8 Evaluation of Plaxis and Trestana results for a reference case

In this chapter a basic soil-load system, a reference case (section 8.1), is presented including the matching initial conditions, loading type, boundary conditions and specific Plaxis finite element input. Afterwards, on the base of results of the extended Plaxis version with the presented reference case, a detailed treatment and stress analysis is given based on the treatment and stress analysis program Trestana (section 8.2).

To avoid losing all track of situation, this relative long and complex chapter is preceded by definitions of frequently used terms together with a global subdivision of section 8.2.

In the treatment and stress analysis program Trestana distinction is made between direct and derived quantities and whether the quantities are verifiable or not. Meaning of the terms direct, derived and verifiable is given below :

direct   : Plaxis results are transmitted one to one through Trestana and only presented from another viewpoint sometimes
derived   : Plaxis results calculated by Trestana from direct quantities; they include well-know quantities, for example principal stresses and strains, or newly-defined composite quantities called kneading numbers
verifiable   : results/quantities can be compared with literature and/or measurements.

Subdivision of Plaxis and the treatment and stress analysis program Trestana are carried out according to the following arrangement :

8.2.1   verifiable direct quantities   : - displacement field
                                                                  - trajectories
                                                                  - pressure-sinkage relationship
                                                                  - vertical stress distribution underneath and beside a strip
                                                                  - stress distribution at the bottom, wall and in the plane of symmetry
                                                                  - consequences of numerical noise
                                                                     - linearity of principal stress increments
                                                                     - linearity of $\dot{\sigma}_{xx}$, $\dot{\sigma}_{yy}$ and $\dot{\sigma}_{xy}$
                                                                     - general case
                                                                     - discretization

8.2.2   further important direct quantities   : - directions of the principal stresses
                                                                  - plastic points
                                                                  - stresses σ_{xx}, σ_{yy}, σ_{xy} and σ_{zz} and choice of graphical representation
                                                                  - coping with data scatter near strip

8.2.3   verifiable derived quantity   : - volume change

8.2.4   further important derived quantities : - rigid body rotation
                                              - principal stresses σ_1, σ_2 and σ_3
                                              - rotation of the eigenvector of principal stress σ_1
                                              - $\Sigma \dot{\varepsilon}_{xx}$, $\Sigma \dot{\varepsilon}_{yy}$, $\Sigma \dot{\varepsilon}_{xy}$
                                              - $\Sigma \dot{\varepsilon}_1$, $\Sigma \dot{\varepsilon}_3$
                                              - intermediate stress coefficient b
                                              - rotation of the eigenvector of principal strain increment $\dot{\varepsilon}_1$
                                              - composite quantities, called kneading numbers.

Needed theories to explain analysis results are given at relevant places in this dissertation.

8.1   Reference case

For the choice of the reference case there is sought alliance with measurements of a tyre impression in agricultural fields (Tijink et al., 1988) and laboratory measurements of controlled distortion of agricultural soils (Dawidowski et al., 1990). Therefore, the simulation calculation is carried out as an impression of a strip with a rough contact surface into the middle of a soil bin (figure 8.1a). The impression of the strip into the soil is 10 percent of the initial height i.e. 0.03 m and is modelled as a prescribed displacement. Furthermore, the case is plane strain modelled with triangular finite elements in Plaxis. Element nodes that represent the bottom of the soil bin are fixed in both the vertical and horizontal direction. Element nodes representing the raised edge of the soil bin are fixed in horizontal direction and can move freely in vertical direction. The same prevails for element nodes at the underside of the rough strip. Because of the presence of symmetry in this case, only one half of the mesh is considered. Logically this means that in the plane of symmetry the element nodes can only move vertically, figure 8.1b.

(a)

(b)

B = 0.075 m

4B

6B

axis of symmetry
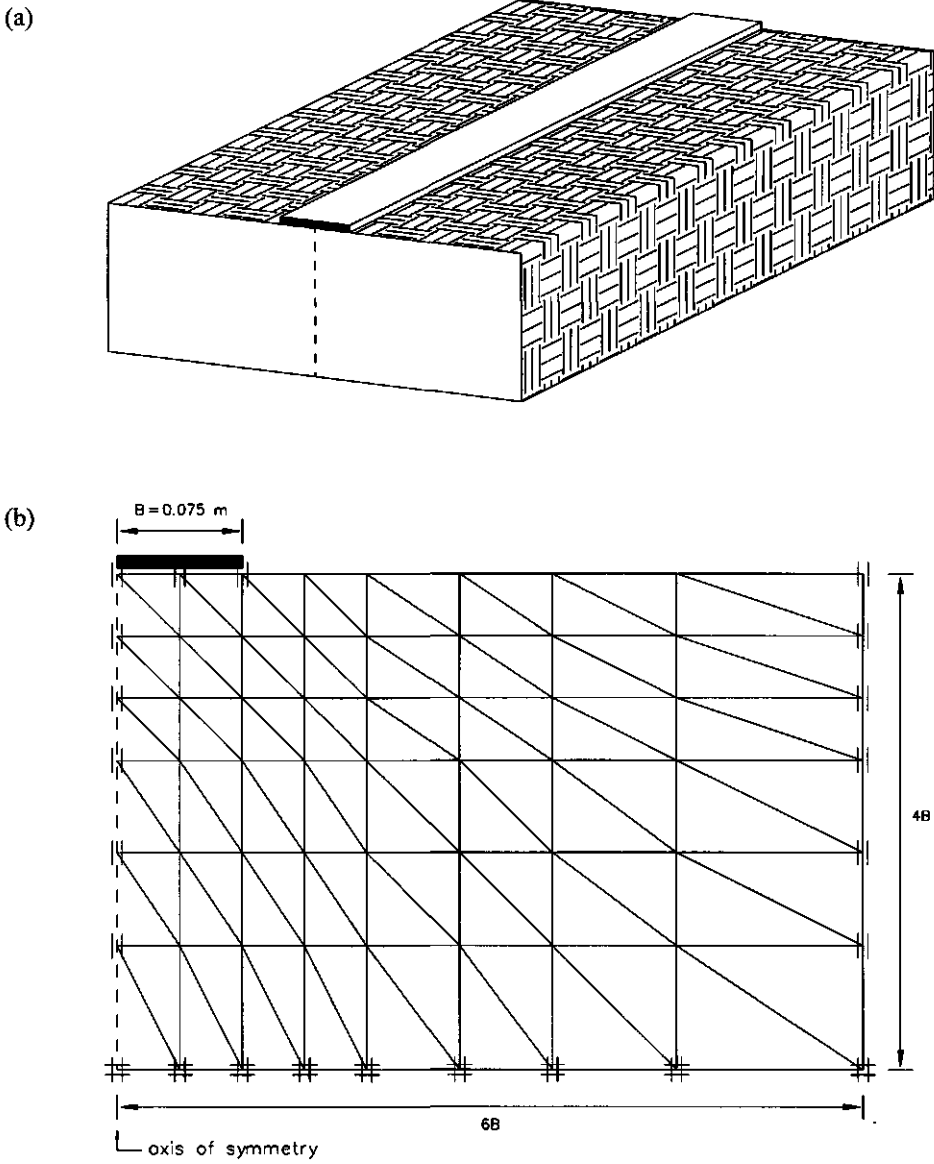
Figure 8.1 Schematisation of soil mass with strip (a) and finite
element modelling of the soil mass with strip (b).

The simulated material is the already described reference soil of section 6.1. One of the characteristics of this soil condition is the presence of a yield stress. The yield stress is independent of the stress level and amount of strain but dependent of the strain rate (El-Domiaty & Chancellor, 1970 and Dawidowski et al., 1990). However, strain rate dependency is ignored here. Other characteristics are :
-   absence of internal friction
-   although the soil is considered saturated, there is still some small amount of entrapped air present in the soil
-   during quick loading air and water stay enclosed in the soil; the water is incompressible and the air will be compressed; needed values of the soil model parameters E and υ are the derived values from chapter 6
-   pore space and density, after triaxial tests, are unaffected by loading (Dawidowski & Koolen, 1987 and Dawidowski et al., 1990) implying that there was non-zero elastic volume strain but no plastic volume strain and plastic hardening.

In view of these characteristics there is chosen to simulate the reference soil behaviour with a conventional Mohr-Coulomb model.

Due to the fact that the soil is loaded with a tyre, associated with high-loading speed, means that the soil behaviour is undrained. The derived Poisson's ratio υ in case of the reference soil is 0.45, chapter 6. However, for undrained material behaviour Plaxis does not accept Poisson's ratios greater than 0.35 and a discrepancy arises. However, if simulations are carried out drained the value of Poisson's ratio υ of 0.45 is not an input problem in Plaxis and the calculated stresses are the total stresses. This is in line with agricultural soil mechanics, Koolen & Kuipers (1983).

The simulation calculations are carried out using the updated mesh analysis because sometimes the local deformations are relatively large.

There are 33 steps needed to simulate the impression of the plate of 10 percent of the initial height of the modelled soil mass. Because the displacement of the strip per step is not equal on the one hand and there will be referred a couple of times to different steps with respect to corresponding strip displacements on the other, table 8.1 is given.

step number	strip impression [m]	strip impression in proportion to the initial modelled soil height [%]
0	0.000e+00	0.000e+00
1	5.238e-05	1.746e-02
2	1.572e-04	5.239e-02
3	3.666e-04	1.222e-01
4	7.860e-04	2.620e-01
5	1.624e-03	5.414e-01
6	3.300e-03	1.100e-00
7	4.977e-03	1.659e-00
8	6.654e-03	2.218e-00
9	8.331e-03	2.777e-00
10	1.001e-02	3.336e-00
11	1.169e-02	3.895e-00
12	1.252e-02	4.174e-00
13	1.336e-02	4.453e-00
14	1.420e-02	4.733e-00
15	1.504e-02	5.012e-00
16	1.588e-02	5.292e-00
17	1.671e-02	5.571e-00
18	1.755e-02	5.851e-00
19	1.839e-02	6.130e-00
20	1.923e-02	6.409e-00
21	2.007e-02	6.689e-00
22	2.090e-02	6.968e-00
23	2.174e-02	7.248e-00
24	2.258e-02	7.527e-00
25	2.342e-02	7.807e-00
26	2.426e-02	8.086e-00
27	2.510e-02	8.365e-00
28	2.594e-02	8.645e-00
29	2.677e-02	8.924e-00
30	2.761e-02	9.204e-00
31	2.845e-02	9.483e-00
32	2.929e-02	9.763e-00
33	3.000e-02	1.000e+01

Table 8.1 Relation finite element steps - strip impression of the reference case.

8.2   Evaluation of Plaxis and Trestana results

8.2.1   Verifiable direct quantities

Displacement field

Figures 8.2 and 8.3 represent the deformed mesh and the displacement field, respectively, corresponding to an impression of the strip of 10 percent of the initial height. In figure 8.2 the grid exists of lines connecting all the final coordinates of the nodes. This has been done in such a way that, for the initial condition, a rectangular grid has been obtained. It should be remarked that the dashed lines in the outermost regions in this and coming figures represent the initial mesh. In the displacement field of figure 8.3 the direction and the amount of displacement of each node during the impression is given by a straight arrow connecting initial and final coordinate of each node. The arrow configuration is proportional to the displacement.

scale   [m]

0   2.5   5   [•10⁻²]
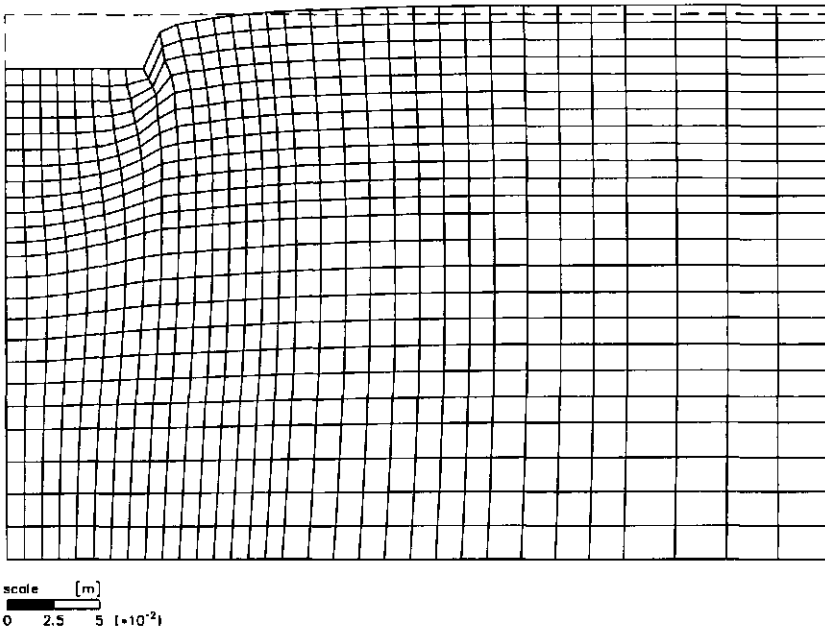
Figure 8.2   Deformed mesh at an impression of the strip of 10 percent
(step 33).
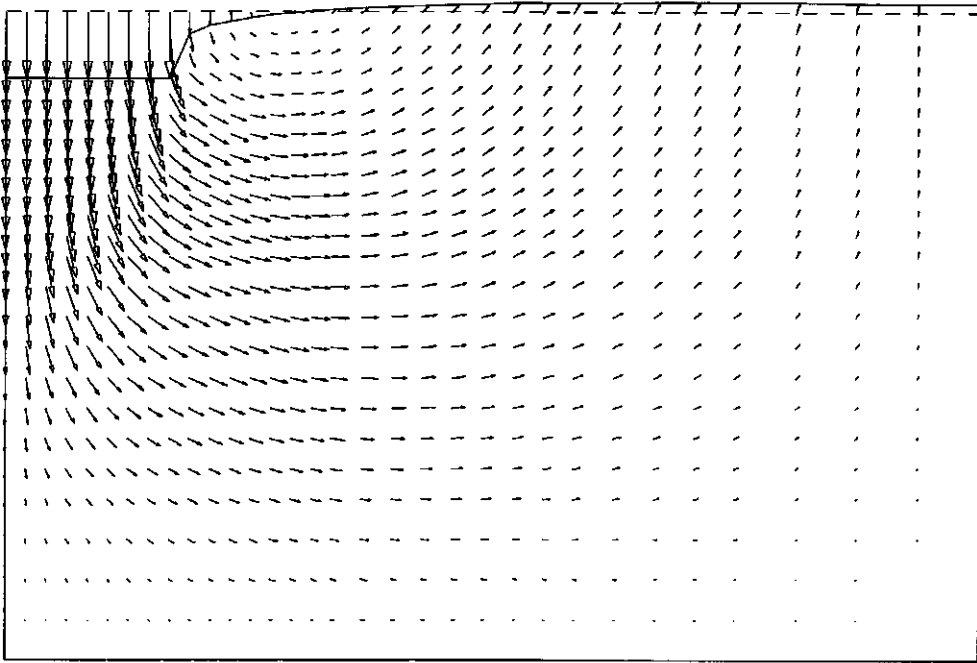
Figure 8.3 Displacement field at an impression of the strip of 10 percent (step 33).

Clearly visible in these figures is the fact that the soil has moved upwards at the vertical edge of the bin far away from the strip. The obtained deformed mesh together with the above described fact agree very well with measurements of Söhne (1953), Gill & Van den Berg (1967) and Chancellor & Upadhyaya (1994).

Trajectories

Figure 8.4 represents trajectories of the nodes of the strip impression, which also fit well with measurements of Chancellor & Schmidt (1962), who used an x-ray technique, and Gill & Van den Berg (1967). The latter used a glass-sided box technique. By this technique the soil particles scrape a fine layer of aluminium from the glass so that the continuous movements of the particles in contact with the glass are recorded.

It should be remarked that at the end of each trajectory an arrow point of equal size is placed. The direction of the arrow represents the direction of the last displacement increment of the trajectory. This explains the somewhat strange looking directions of the arrows at the end of the trajectories near the edge of the strip.
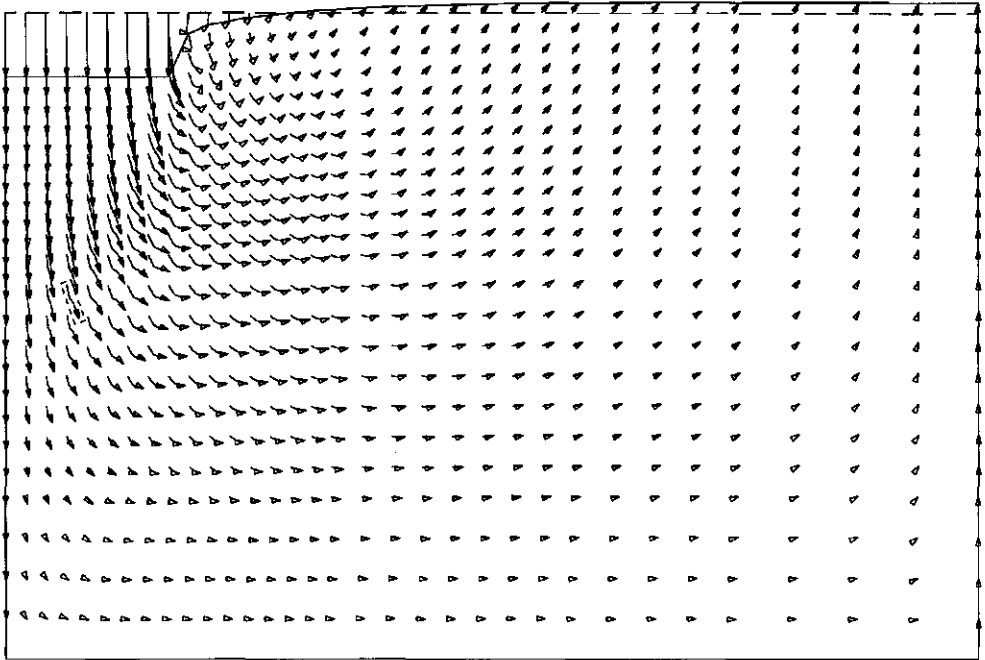
Figure 8.4   Trajectory field corresponding to an impression of the strip
of 10 percent.

However, some trajectories of figure 8.4 show deviations from measurements of Chancellor &
Schmidt (1962) and Gill & Van den Berg (1967). These deviating trajectories show a (sharp)
bend. One of these trajectories, which is framed by a dashed line in figure 8.4 and is located at
approximately the middle of the height of the modelled soil mass near the axis of symmetry,
is enlarged and represented in figure 8.5.
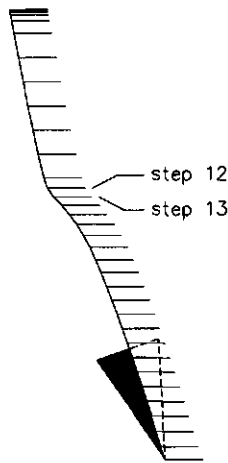
Figure 8.5 Enlargement of the framed trajectory of figure 8.4.

In step 12 the largest bending of the specific trajectory can be detected. This is due to the fact that in this step the soil behaviour in the neighbouring soil mass, i.c. stress point 65, switches from elastic to plastic. This can be seen in figure 8.6 where point 13, which indicates the end of step 12, lies on the yielding envelope. Note that this 2-dimensional yielding envelope is derived from a 3-dimensional yielding envelope with a similar shape as presented in figure 3.4.
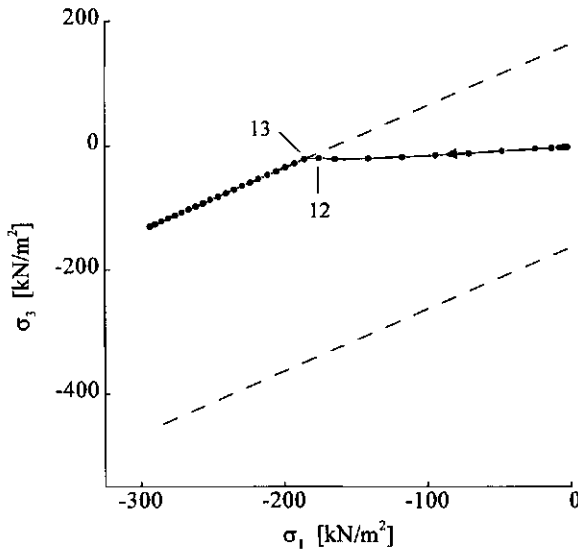
Figure 8.6 Stress path of stress point 65 with corresponding yield envelope in σ_1, σ_3-space.

Pressure-sinkage relationship

Over the years there is written a lot about pressure-sinkage relationships, e.g. in relation to bearing capacity problems in civil engineering. Many results do not consider the compressibility of soils and require much further development before they can be applied successfully to field soils (Wills, 1966). The most widely known and accepted pressure-sinkage prediction equation for field soils is, Bekker (1956)

$$p = k z^n \tag{8.1}$$

where

p = pressure on the strip
z = plate sinkage
n = property of the soil
k = parameter dependent on soil and strip geometry

Thus, according to this equation pressure-sinkage data should reduce to a linear function when plotted on logarithmic axes. Especially in the lower sinkage range there is experimental evidence that data deviate from the given equation (Sela & Ehrlich, 1971, Wills, 1966 and Houtman, 1977). The pressure-sinkage graph, figure 8.7, that was calculated from Plaxis output of the reference case also deviates from equation 8.1.
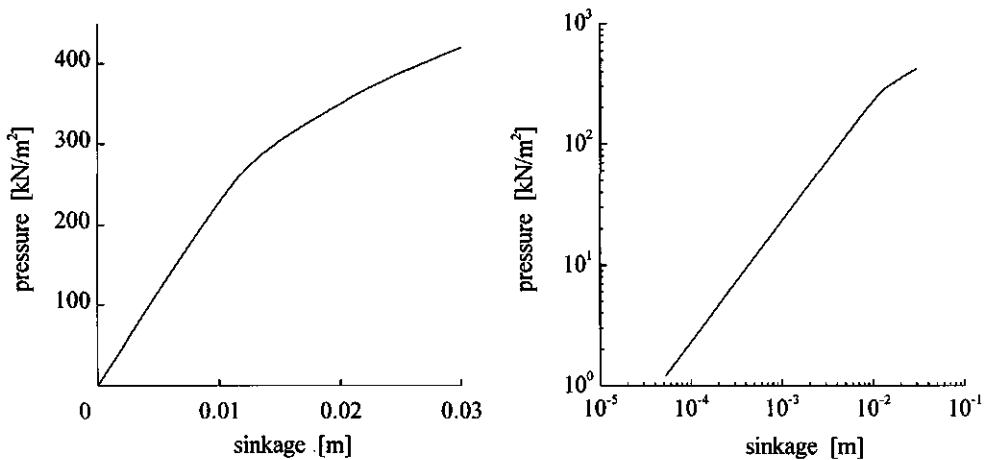
Figure 8.7 Pressure-sinkage curve of the reference case on linear-linear (a) and log-log scale (b).

Vertical stress distribution underneath and beside a strip

In this dissertation the analytical solution (elastic) of a pressure distribution underneath a rigid strip of Timoshenko & Goodier (1951) is used to verify the numerical results. The pressure distribution is given by :

$$q = \frac{p}{\pi \sqrt{a^2 - x^2}}$$

(8.2)

where

q = pressure underneath the strip at distance x
p = force on the strip per unit of length
a = distance from the plane of symmetry to the edge of the strip
x = distance from the plane of symmetry

Figure 8.8 gives both the analytical and numerical results for pressure distribution underneath the strip of step 6 of the reference case, which is the last step before plasticity occurs in the soil material. It can be concluded that the numerical results agree well with the given analytical solution.
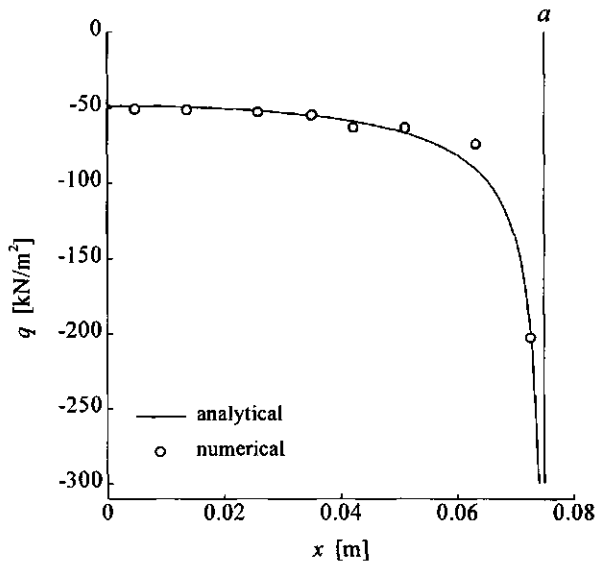
Figure 8.8 Analytical, according to equation 8.2, and numerical stresses underneath a rigid strip.

It should be remarked that in literature no unique solutions can be found in the case of the plastic region. Söhne (1951) gives a possible pressure distribution underneath a rigid strip where the largest pressure under the centre of the strip occurs. However, this is not proven by experimental results. Romp (1970) and Perdijk (1971) showed experimental results of rigid strip impressions in clay. The results give no rise to systematic and clear conclusions with respect to the pressure distribution underneath the rigid strip, although the distribution tends to the presence of the largest pressure under the edge of the strip. The representation of the numerical results of the reference case of the vertical pressure underneath the strip and in the upper layer beside the strip is shown in figure 8.9.
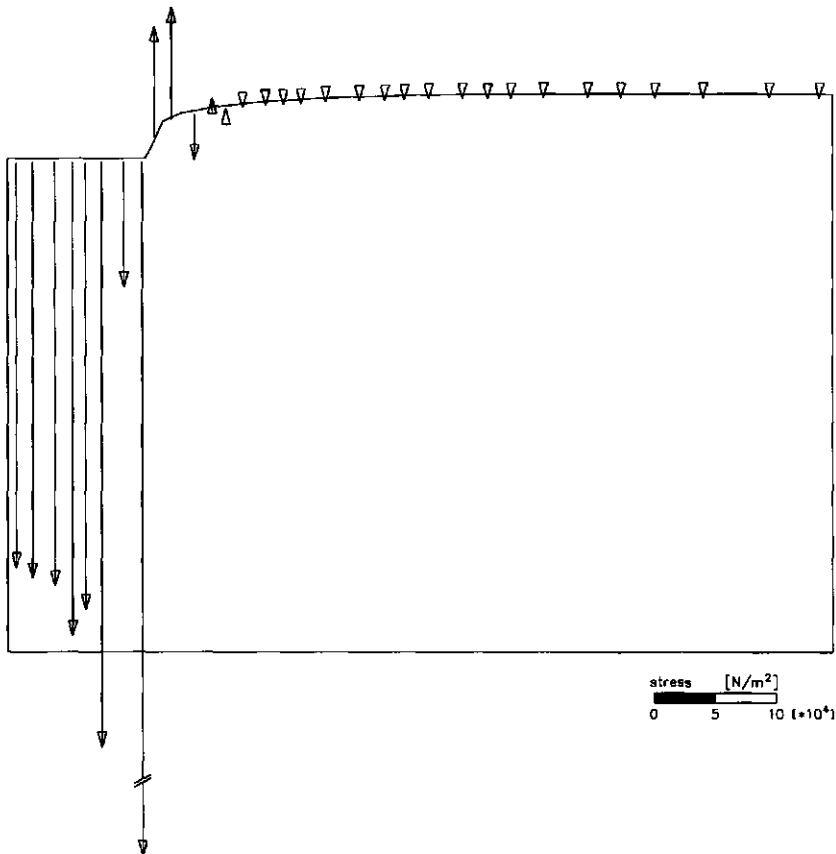
Figure 8.9   Vertical pressure distribution of the toplayer underneath and beside the strip at an impression of the strip of 10 percent (step 33).

Stress distribution at the bottom, wall and in the plane of symmetry

In figure 8.10 the vertical pressure distribution on the bottom of the soil bin is represented on the basis of numerical results. This distribution agrees well with measurements of Muys (1968).

stress   [N/m²]

0   5   10 [•10⁴]
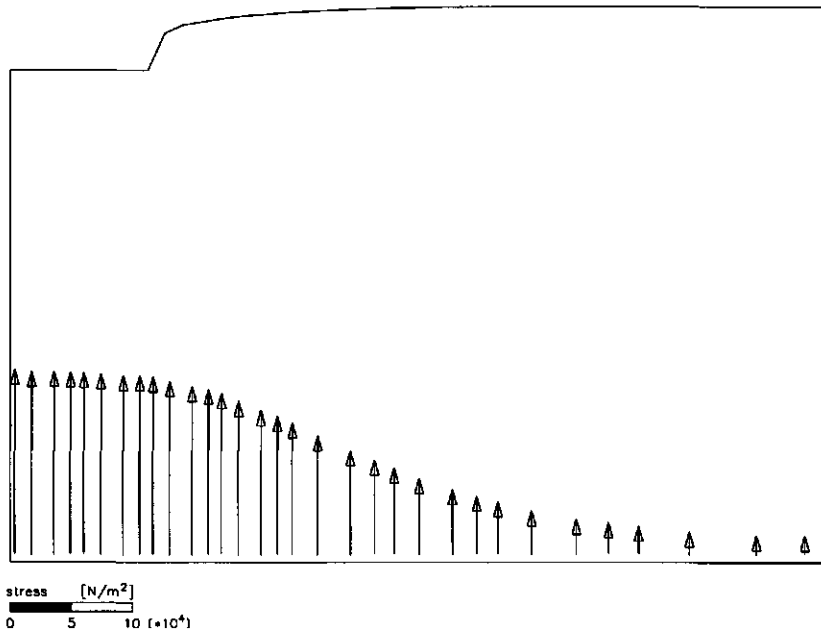
Figure 8.10 Vertical pressure distribution at the bottom of the soil bin
at an impression of the soil strip of 10 percent (step 33).

The horizontal pressures at the wall and in the plane of symmetry of the soil bin, both corresponding to an impression of the strip of 10 percent, are given in figure 8.11. In comparison to the pressure distribution on the wall of the soil bin, the pressure distribution in the plane of symmetry is distributed less uniformly. Near the lower part of the plane of symmetry the effect of the bottom on the pressure distribution is clearly visible.
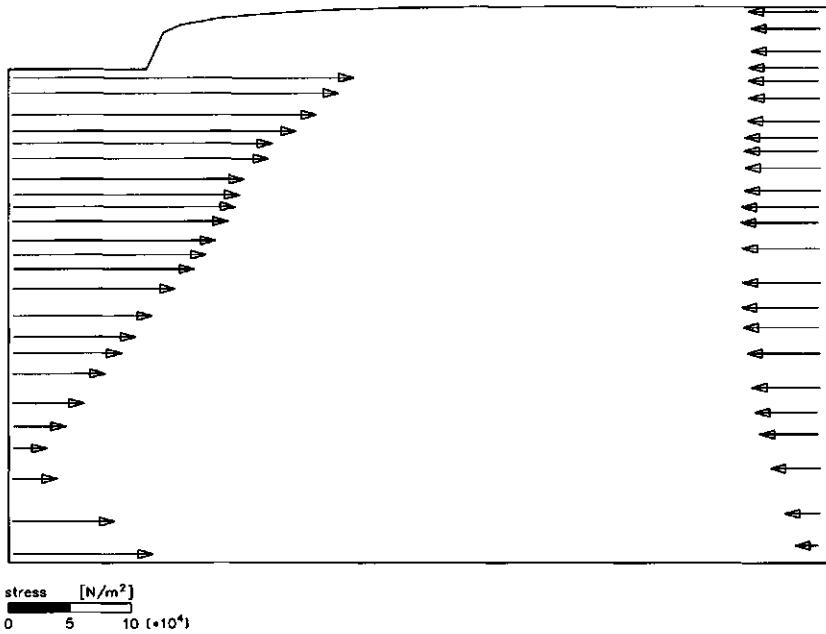
Figure 8.11   Horizontal pressure distribution at the wall and in the plane
              of symmetry of the soil bin at an impression of the soil
              strip of 10 percent (step 33).

Also the shear stresses at the wall and the plane of symmetry of the soil bin are plotted in a way similar to figure 8.11. In the Plaxis calculations the wall of the soil bin was taken as perfectly smooth, which implies that there should not be shear stresses present at the wall. The numerical output, figure 8.12, slightly deviates from this model input. In a real case there is always a little friction between the soil and the wall. This results, in rigid strip experiments where the wall of the bin is not fixed to the bin bottom, in a vertical upwards moving wall during the experiment (Perdijk, 1971 and Söhne, 1953). In the plane of symmetry the shear stresses should theoretically be zero. Here also the Plaxis output slightly deviates. Consequences of calculated finite shear stresses where this is theoretically unlogical are described in the next section 'Consequences of numerical noise'.

upwards   downwards   downwards   upwards

stress   [N/m²]

0   1   2 (•10³)
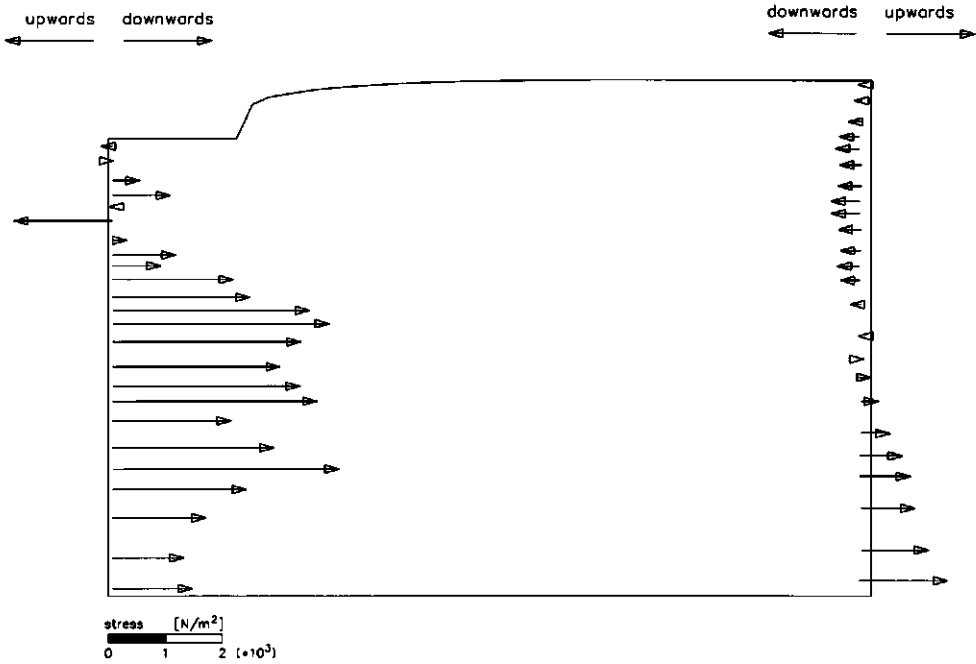
Figure 8.12   Shear stresses exerted by the vertical boundaries on the
              modelled soil mass at an impression of the soil strip of 10
              percent (step 33).

Consequences of numerical noise

Each stress situation of a soil element can be visualised with the help of the circles of Mohr, which is shown in chapter 3. In such a graph the major and minor principal stresses are derived from σ_{xx}, σ_{yy} and σ_{xy}, figure 8.13.
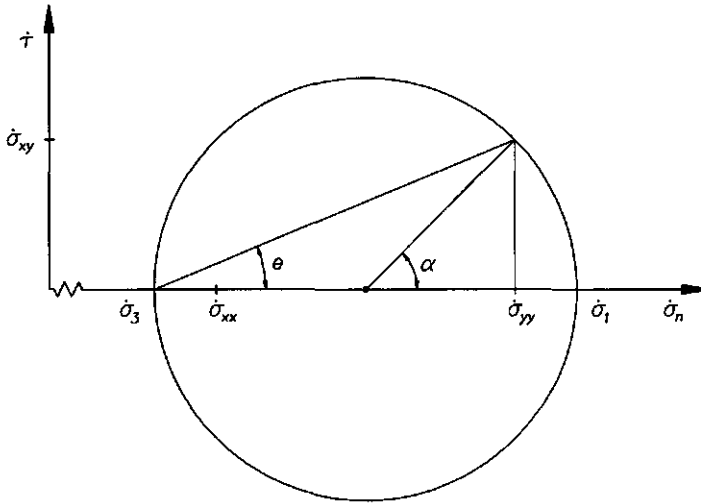
Figure 8.13 Representation of an arbitrary stress increment state with
the help of the stress circle of Mohr.

The angle α represents twice the angle θ which is the angle between the y-component of the Cartesian xy-coordinate system and the eigenvector of the major principal stress increment $\dot{\sigma}_1$, figure 8.14.
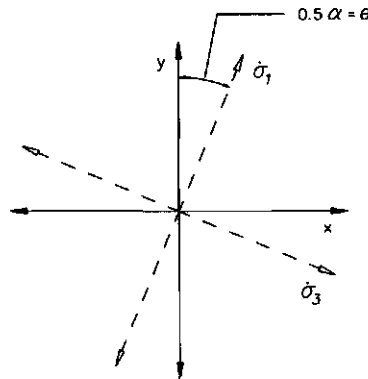
Figure 8.14 Representation of the angle α and θ of the stress circle of
Mohr.

If in two successive stress increment situations angle α changes, than apparently there is a rotation of the eigenvector of the major principal stress increment, implying that the lines between the origin and the $\dot{\sigma}_{yy}, \dot{\sigma}_{xy}$-coordinates (figure 8.13) of the stress circle of Mohr for each stress increment state do not remain parallel to each other.

Taking into account an arbitrary soil element of a loading process. A possible development of the stress increments of the process is presented with the help of the circles of Mohr in figure 8.15.
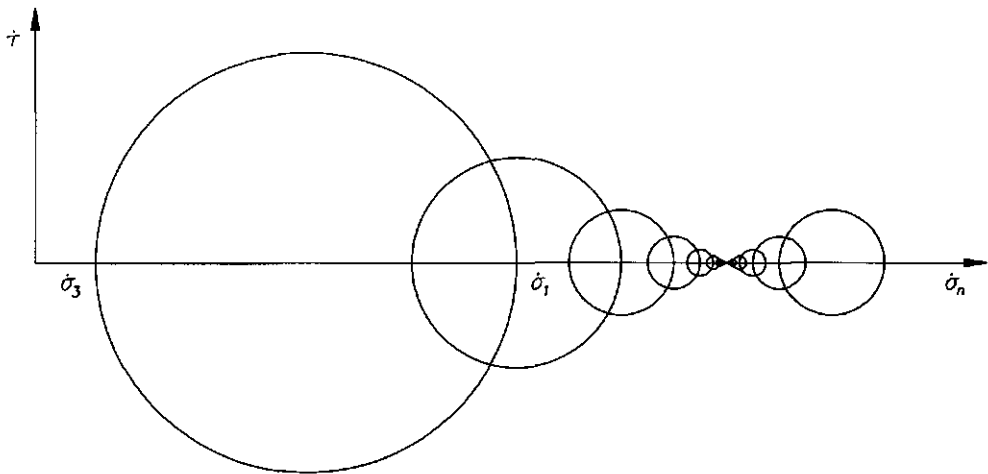
Figure 8.15 Stress increment development of a soil element during loading in $\dot{\tau}, \dot{\sigma}_n$-space.

The increase of the stress increments goes simultaneously with a decrease of the difference of the principal stress increments. This decrease of the stress increment difference means a degeneration of the circle of Mohr to a point, which represents a special situation in which necessarily the four stress increments $\dot{\sigma}_1$, $\dot{\sigma}_3$, $\dot{\sigma}_{xx}$ and $\dot{\sigma}_{yy}$ equal each other in the absence of the $\dot{\sigma}_{xy}$ component. After that point increasing stress increments combined with an increase of difference of the principal stress increments mean a regeneration of a point to a real circle of Mohr.

Linearity of principal stress increments

Consider a soil element with principal stress increments $\dot{\sigma}_a$ and $\dot{\sigma}_b$ as presented in figure 8.16*a*, implying there is no shear stress increment active.

a)

b)   step number
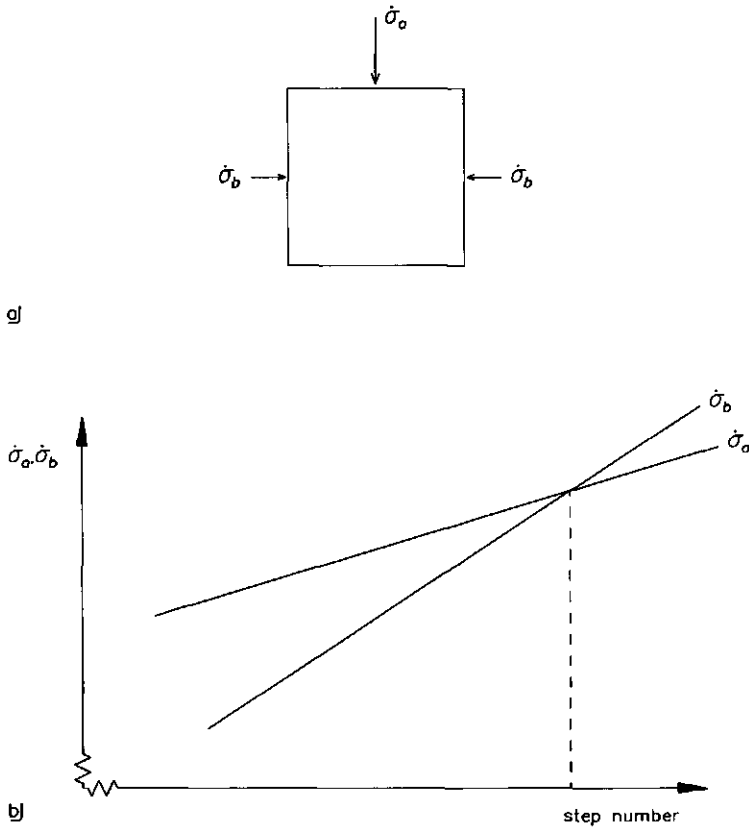
Figure 8.16 Principal stress increment situation of a soil cube (a),
development of the principal stress increments (b).

The development of the principal stress increments is presented in figure 8.16*b*. In this particular situation the eigenvector of the major principal stress increment turns over from the *y*-direction to the *x*-direction in the interval just before and directly after the crossing of $\dot{\sigma}_a$ and $\dot{\sigma}_b$. This turn over of the eigenvector of the major principal stress increment is exactly 90 degrees.

Linearity of $\dot{\sigma}_{xx}$, $\dot{\sigma}_{yy}$ and $\dot{\sigma}_{xy}$

In a stress situation with a linear development of $\dot{\sigma}_{xx}$, $\dot{\sigma}_{yy}$ and $\dot{\sigma}_{xy}$, the lines between the origin and the $\dot{\sigma}_{yy}, \dot{\sigma}_{xy}$-coordinates of the stress circle of Mohr remain parallel to each other which implies no rotation of the eigenvector of the major principal stress increment at all, step $n-3$ and $n-1$ of figure 8.17.
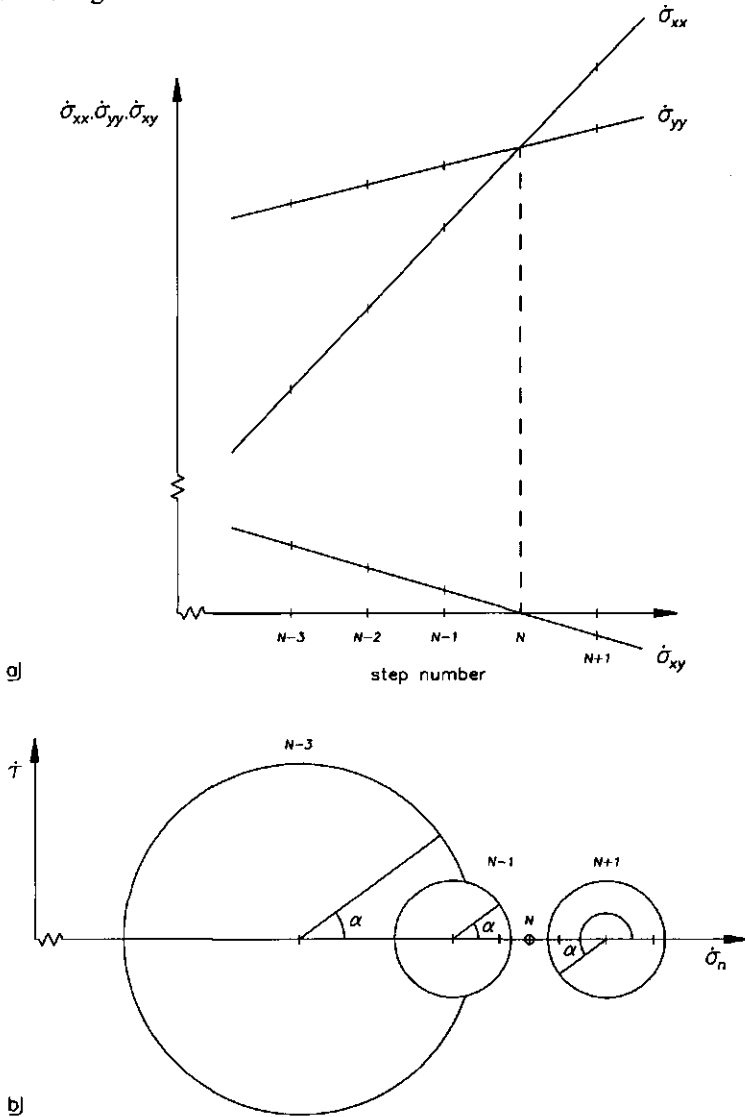
Figure 8.17 Linear development of $\dot{\sigma}_{xx}$, $\dot{\sigma}_{yy}$ and $\dot{\sigma}_{xy}$ (a) with corresponding circles of Mohr (b).

For the steps $n-1$, n and $n+1$ the stress increments $\dot{\sigma}_{yy}$ and $\dot{\sigma}_{xx}$ cross each other associated with a simultaneous crossing of the x-axis by $\dot{\sigma}_{xy}$. Also in this case the lines between the origin and the $\dot{\sigma}_{yy}, \dot{\sigma}_{xy}$-coordinates of the stress circle of Mohr remain parallel to each other. However the line of step $n-1$ with corresponding angle α has turned over 180 degrees with respect to step $n+1$, which means a turn over of the eigenvector of the major principal stress increment of 90 degrees. Putting the circles $n-1$, n and $n+1$ on top of each other with point n as centre, the turn over of the eigenvector of the major principal stress increment of 90 degrees can be shown directly with the help of angle θ, figure 8.18.
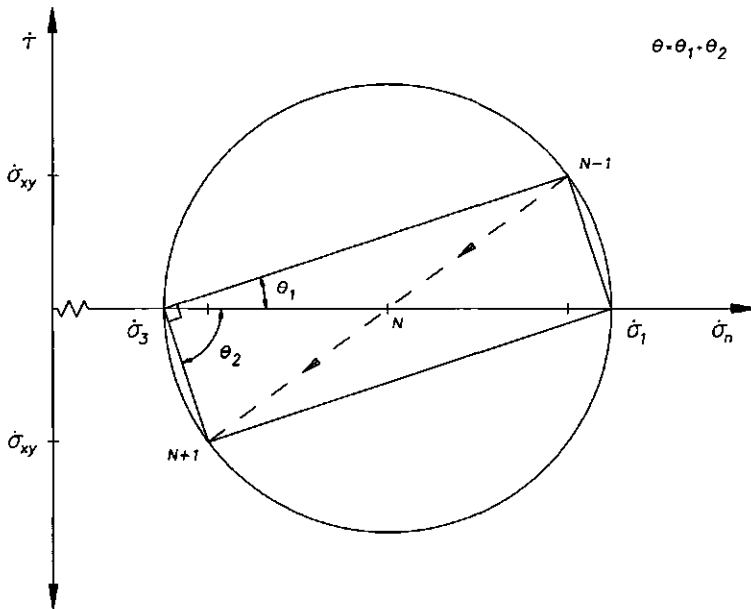
Figure 8.18 Representation of angle θ with respect to a linear development of $\dot{\sigma}_{xx}$, $\dot{\sigma}_{yy}$ and $\dot{\sigma}_{xy}$.

General case

The development of stress increments of a soil element of a loading process with the help of the circles of Mohr in $\dot{\tau}, \dot{\sigma}_n$-space has already been represented in figure 8.15. A possible corresponding simultaneous development of the stress increments $\dot{\sigma}_{xx}$, $\dot{\sigma}_{yy}$ and $\dot{\sigma}_{xy}$ against steps of time in the interval just before and directly after the degeneration to a point of the circle of Mohr is given in figure 8.19.
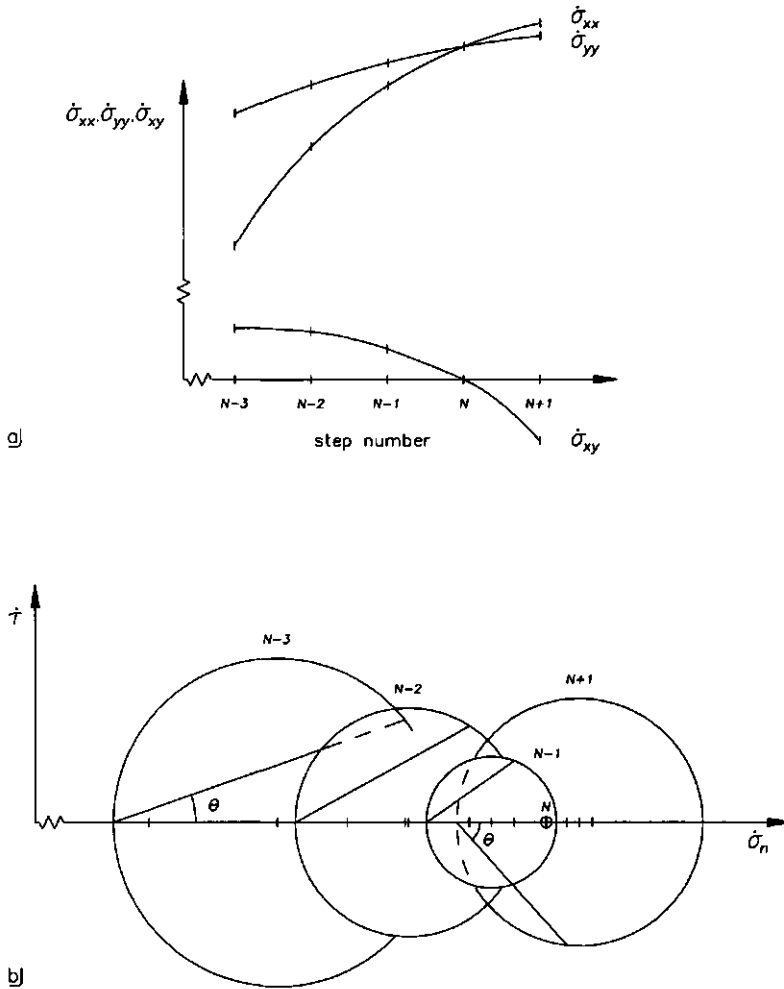
Figure 8.19 Development of $\dot{\sigma}_{xx}$, $\dot{\sigma}_{yy}$ and $\dot{\sigma}_{xy}$ (a) with corresponding circles of Mohr (b) in general case.

Between step $n-3$ and $n-1$ only a rotation of the eigenvector of the major principal stress increment occurs. Between steps $n-1$, n and $n+1$ the occurred rotation of the eigenvector of the major principal stress increment can be split up into a turn over of 90 degrees, presented by the dashed line of figure 8.20, and a pure rotation of the eigenvector of the major principal stress increment, presented by the angle β.
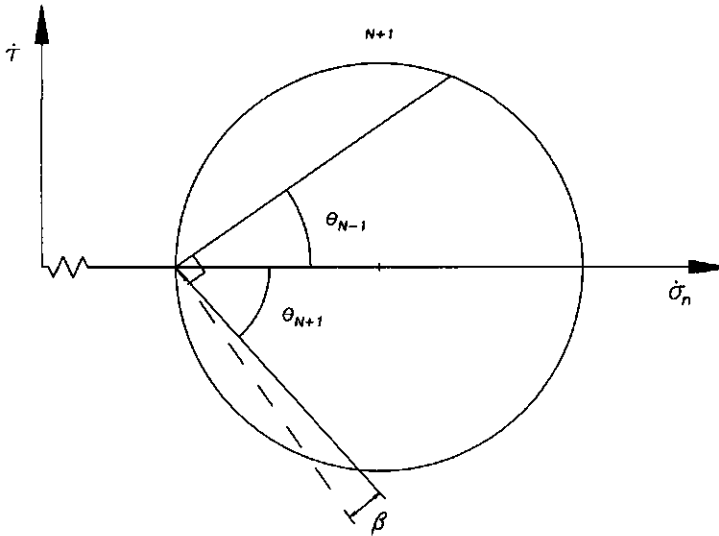
Figure 8.20 Division of a rotation of the eigenvector of the major
            principal stress increment in a turn over of 90 degrees and
            a pure rotation.

Discretization

A calculation with a finite element program is in fact a simulation of a certain process which
is discretized. If the output of $\dot\sigma_{xx}$, $\dot\sigma_{yy}$ and $\dot\sigma_{xy}$ is correctly calculated than the rotation of the
eigenvector of the major principal stress increment can also be calculated correctly, being
independent of the used step size.

Possible source of trouble is numerical 'noise' in the finite element output, concerning $\dot\sigma_{xx}$,
$\dot\sigma_{yy}$ and $\dot\sigma_{xy}$. Through this noise it is possible that during the crossing or touching of $\dot\sigma_{xx}$ and
$\dot\sigma_{yy}$, $\dot\sigma_{xy}$ does not cross or touch the x-axis. Taking for example figure 8.21. Basis for figure
8.21 is figure 8.17, with the difference that the $\dot\sigma_{xy}$-line is translated vertically upwards (*a*)
and downwards (*c*), which implies that the crossing of the x-axis through the $\dot\sigma_{xy}$-line does not
occur simultaneously with the crossing of $\dot\sigma_{xx}$ and $\dot\sigma_{yy}$.
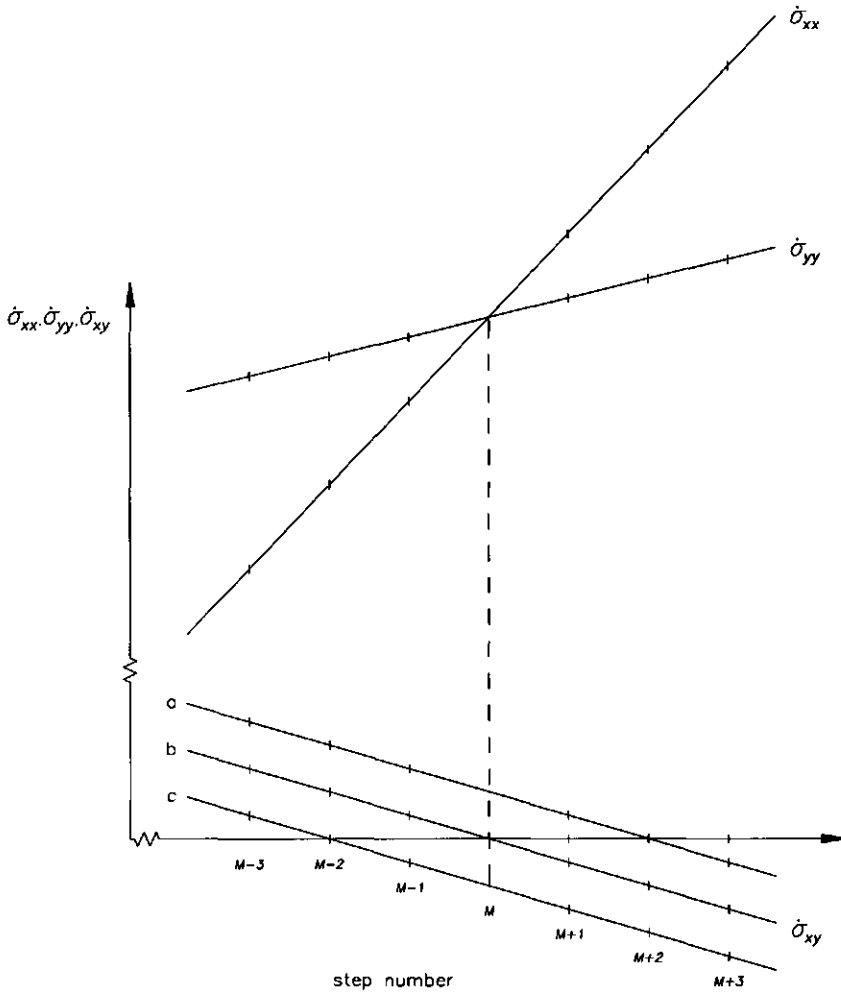
Figure 8.21 Linear development of $\dot{\sigma}_{xx}$, $\dot{\sigma}_{yy}$ and $\dot{\sigma}_{xy}$ whereby the $\dot{\sigma}_{xy}$ -
line is translated vertically upwards and downwards.

From figure 8.17 it is known that the rotation of the eigenvector of the major principal stress increment is a turn over and was exactly 90 degrees in the interval one step before and one step directly after the crossing of $\dot{\sigma}_{xx}$ and $\dot{\sigma}_{yy}$. In the case of figure 8.21 this is not the case for situation a and c. Only when the interval of step numbers around the crossing of $\dot{\sigma}_{xx}$ and $\dot{\sigma}_{yy}$ is sufficiently enlarged, by extrapolating the lines, the rotation of the eigenvector of the major principal stress increment approximates the turn over of 90 degrees, figure 8.22. From this figure can also be seen that the rotation of the eigenvector of the major principal stress increment in the case of situation b is not reached in one step. This is due to the fact that there arises a situation at step m in which $\dot{\sigma}_{xx}$ and $\dot{\sigma}_{yy}$ equal each other in the absence of $\dot{\sigma}_{xy}$. In

such a situation the stress increments are the principal stress increments and the corresponding eigenvectors are $[1 \ 0]^T$ and $[0 \ 1]^T$.
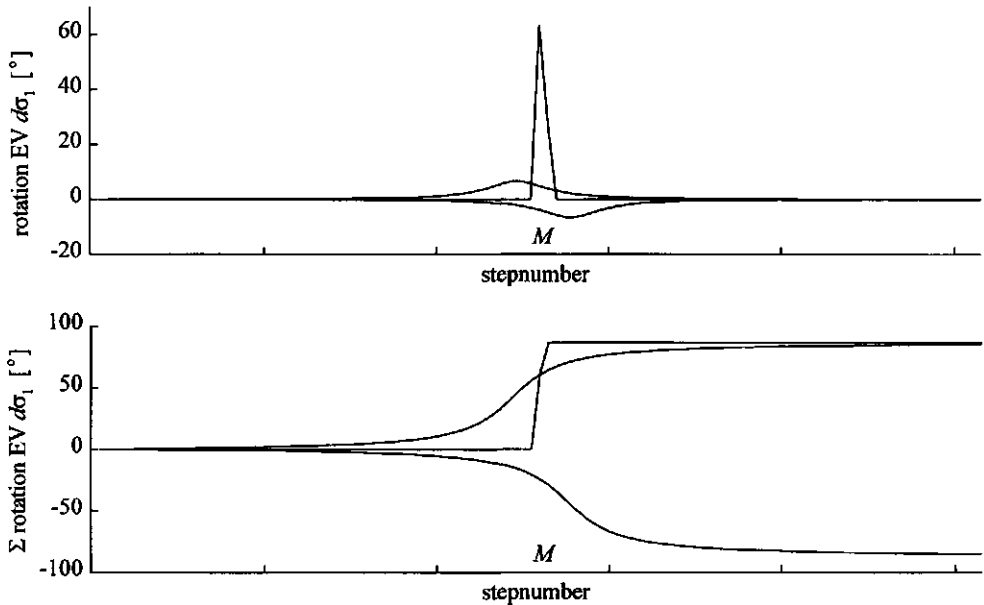
Figure 8.22 Limits of the rotation of the eigenvector of the major
principal stress increment, on base of figure 8.21.

It is worthwhile to mention that, with preservation of the development of the different stress increment curves, changing the absolute size of difference between the $\dot{\sigma}_{xx}$ and $\dot{\sigma}_{yy}$ curves on the one hand and the $\dot{\sigma}_{xy}$ on the other, leaves the rotation of the major principal stress increment unaffected.

8.2.2 Further important direct quantities

Directions of the principal stresses

Before the impression of the strip into the soil is simulated, an initial stress field is generated on basis of the K_0-procedure. This initial principal stress field is given in figure 8.23. For each triangular finite element of the mesh, three internal principal stresses are shown with the help of crosses. The length of each line represents the magnitude of the principal stress and the direction indicates the principal direction. Tensile stresses are indicated by an arrow.
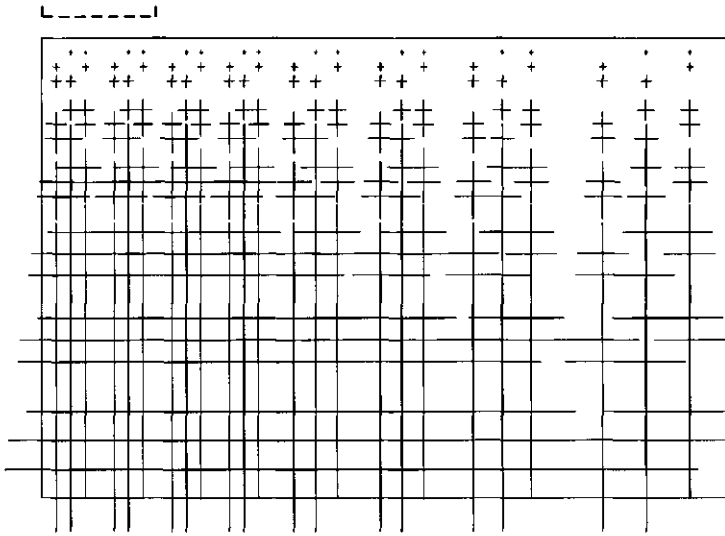
Figure 8.23 Initial principal stress field (step 0; max principal stress -5.55e+03 N/m²).

It can be seen that the total stress field at any step is therefore an interaction of the stress field, which is the direct result of the strip impression, and the initial stress field. Figure 8.24 gives the principal stress field of step 1, which corresponds to an impression of the strip of 0.0175 percent of the initial height of the soil bin.
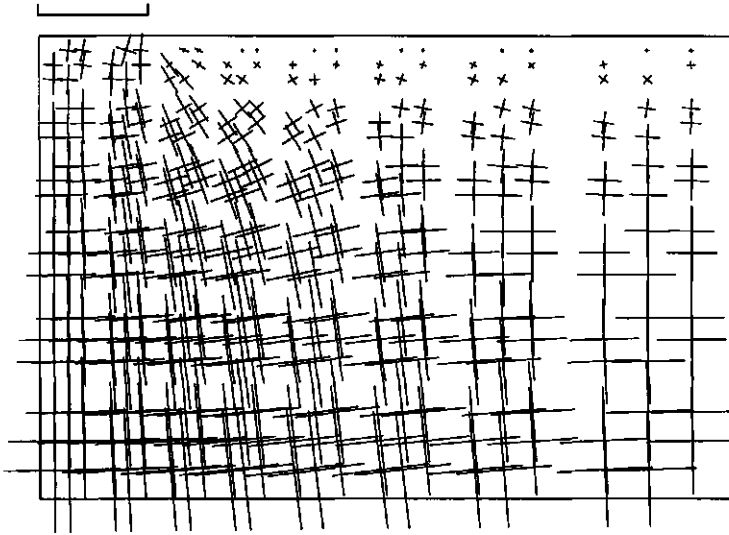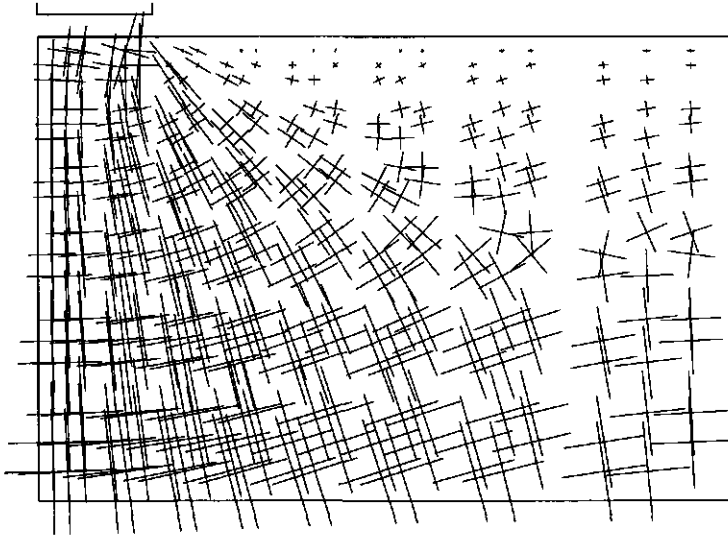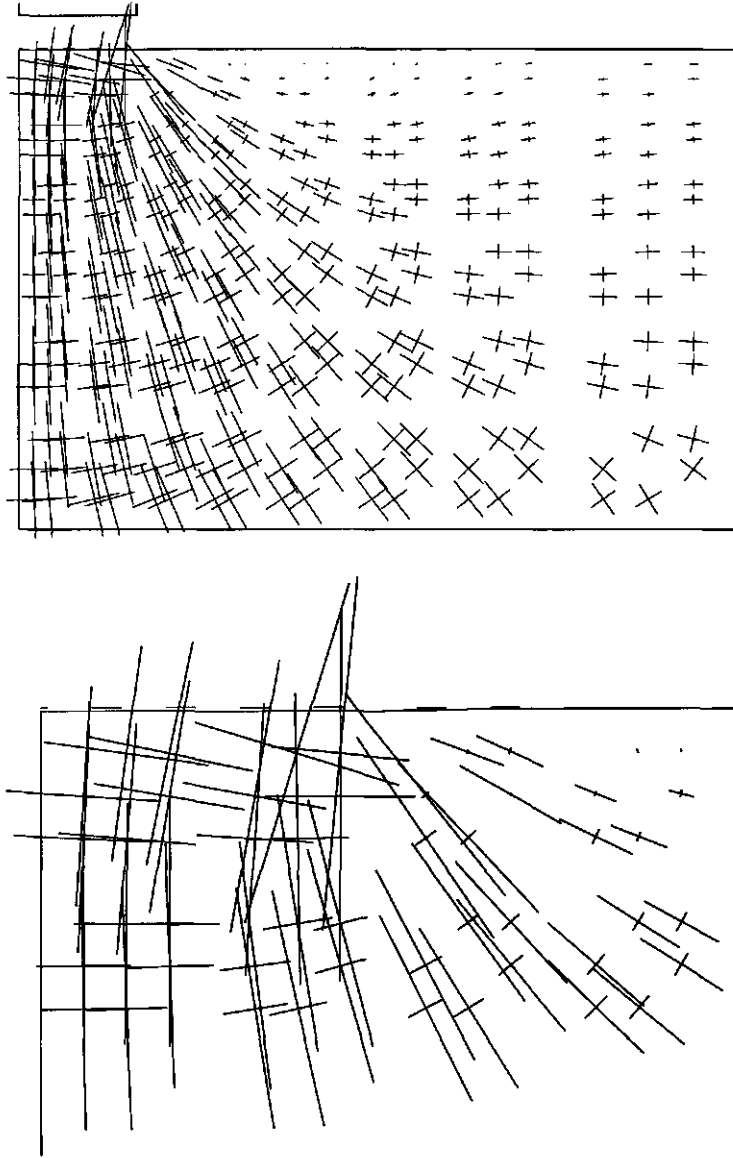
Figure 8.24 Effective principal stress field at an impression of the strip
            of 0.0175 percent (step 1; max principal stress -6.02e+03
            N/m^2).

Presentation of the stresses at the interface of strip-soil is given at figure 8.25. Presentation of
the normal, shear and principal stresses acting on a soil element, located at the region of the
closed and hatched arrow of figure 8.25, is given at figure 8.26.
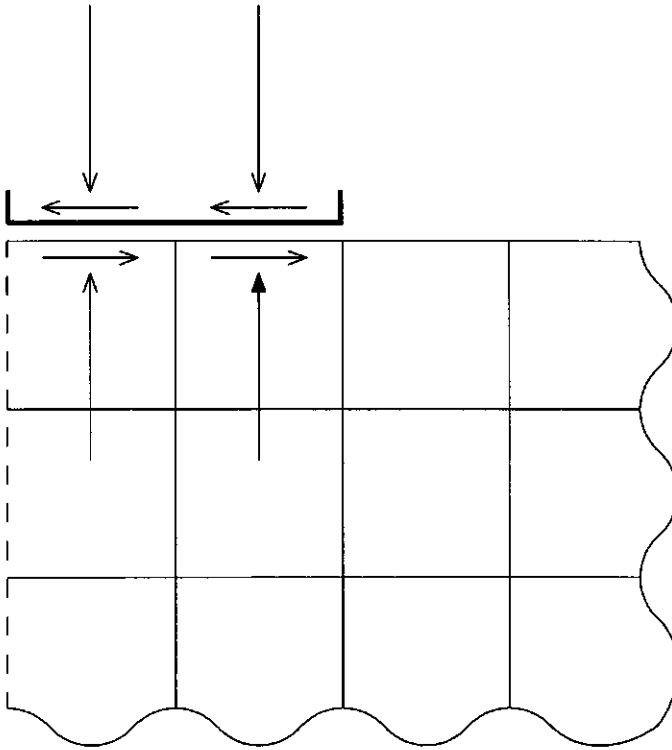
Figure 8.25 Stresses acting at the interface strip-soil.
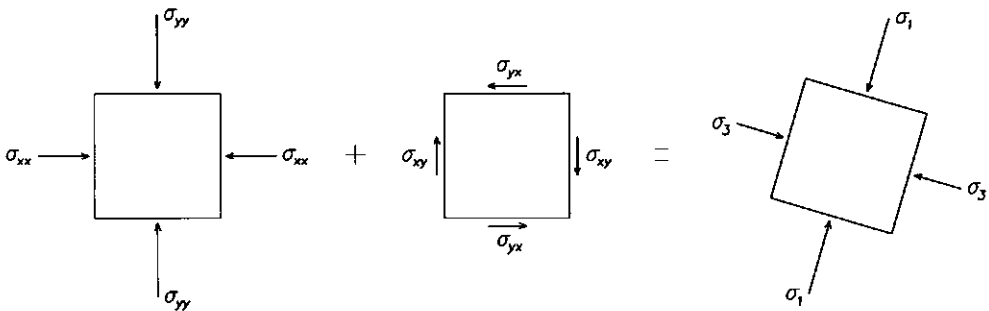
Figure 8.26 Composition of the principal stresses at the region of the
closed and hatched arrow of figure 8.25.

Generally, by a rigid strip impression the tendency of squeezing soil material just beneath the
strip increases when going from the plane of symmetry to the edge of the strip. This may (at

least partly) explain why the shear stress increases from the axis of symmetry to the edge of the strip. This increase may explain the observed increasing clockwise rotation of the principal stresses underneath the strip of figure 8.24 when going from left to right.

Where the principal stresses are nearly equal, the directions of the principal stresses seem to be more or less arbitrary, figure 8.27. This agrees with the fact that for equal principal stresses each direction is, theoretically, a principal direction.
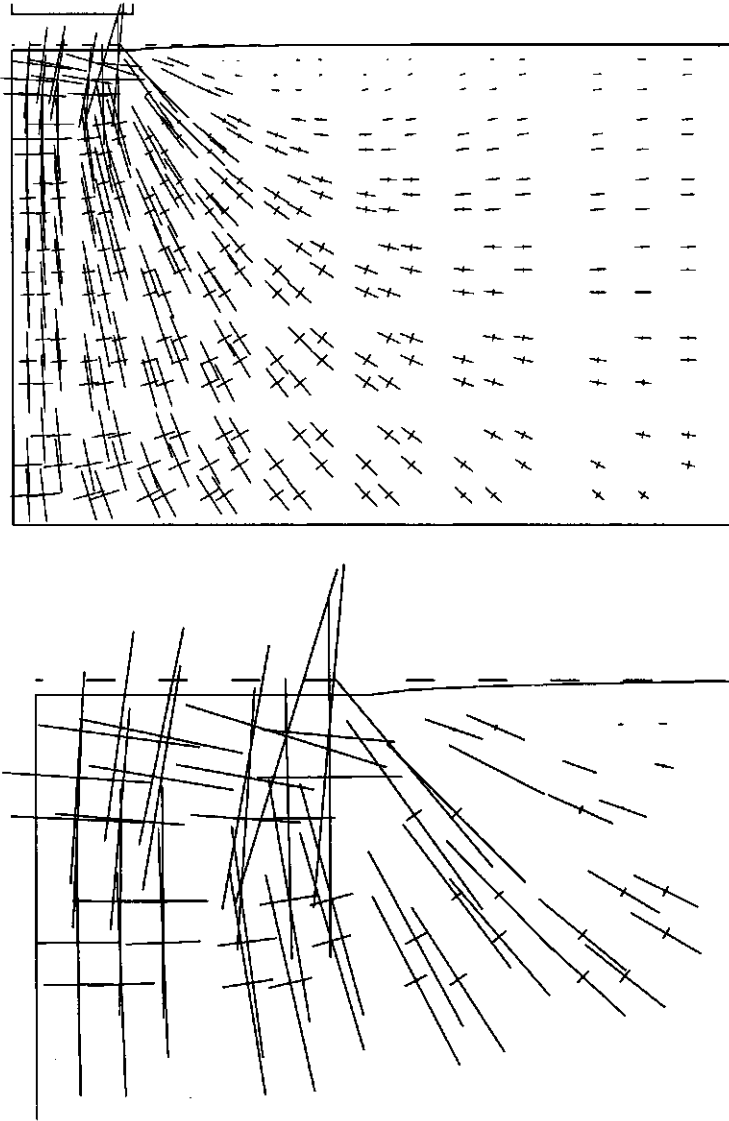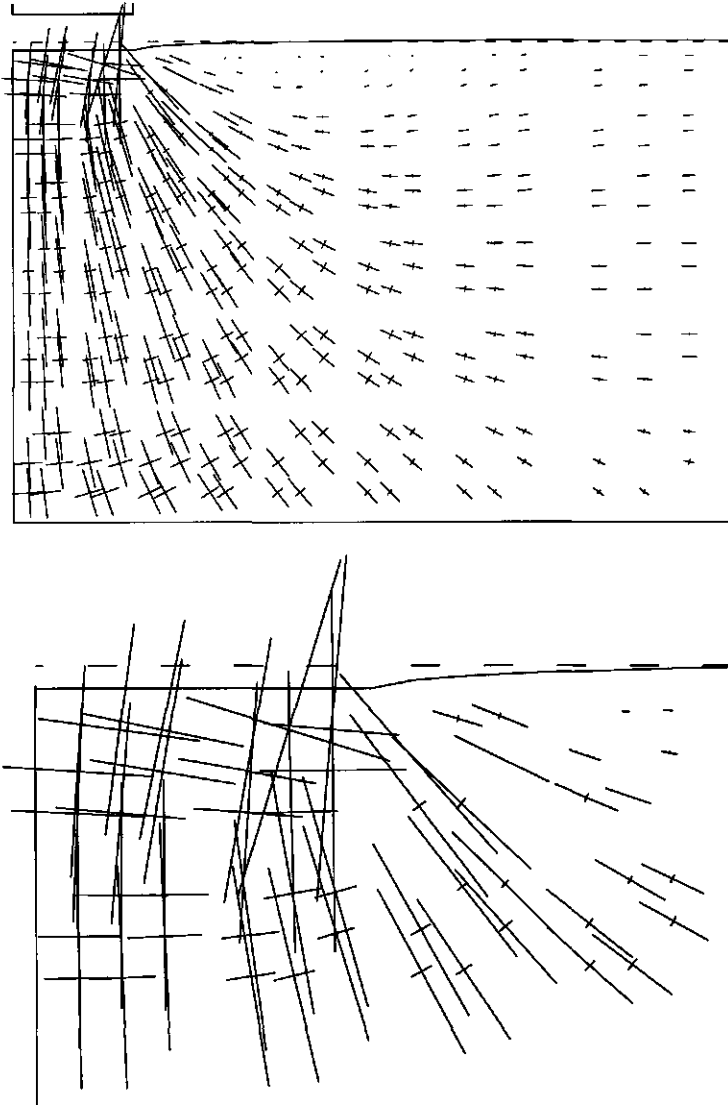

Figure 8.27 Effective principal stress field at an impression of the strip of 0.052 percent (step 2; max principal stress -9.67e+03 N/m^2).

By further impression of a strip into the soil, the major principal stress just beneath the strip is the largest in comparison to the region further downwards (Chancellor & Schmidt, 1962 and Chancellor et al., 1962). In the case of step 4, corresponding to an impression of the strip of 0.262 percent, the observed phenomenon in the region directly underneath the strip is opposite to the above written, figure 8.28.

Figure 8.28 Effective principal stress field underneath the strip at an
impression of the strip of 0.262 percent (step 4; max
principal stress -4.85e+04 N/m^2).

The major principal stress in the region just beneath the edge of the strip is theoretically
greater than the major principal stress at the same horizontal level but situated more in the

direction of the axis of symmetry. In the case of step 6, corresponding to an impression of the strip of 1.10 percent, the observed is opposite to the earlier written, figure 8.29.
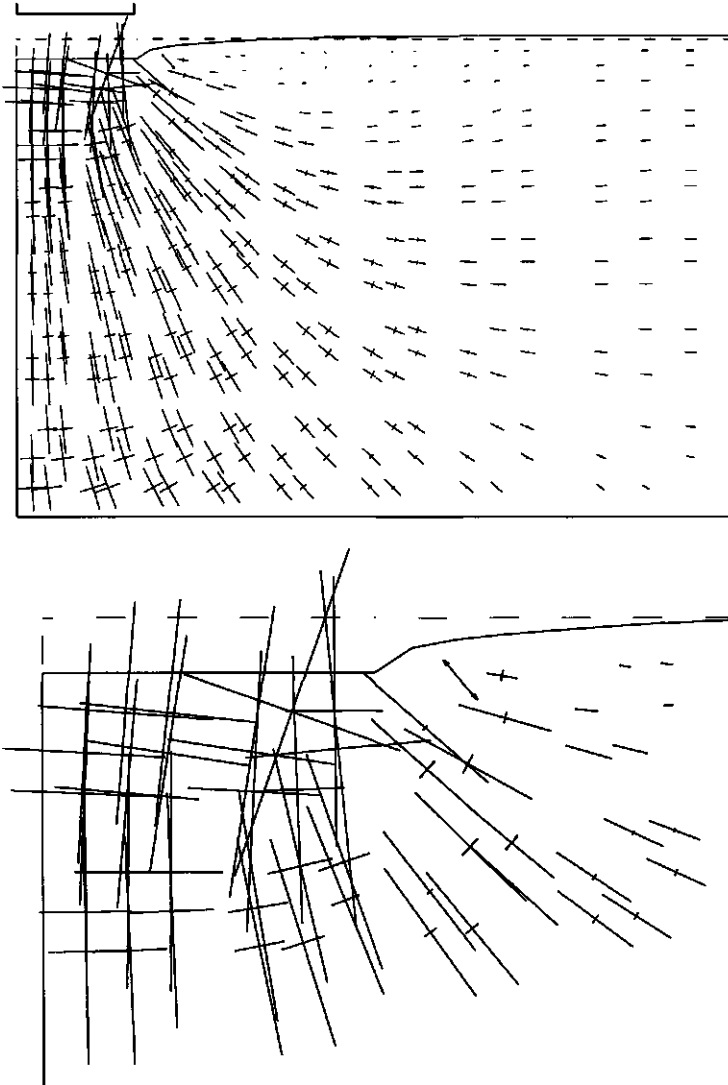

Figure 8.29 Effective principal stress field at an impression of the strip of 1.10 percent (step 6; max principal stress -2.08e+05 N/m^2).

The first plastic point occurs just near the edge of the strip at an impression of the strip of 1.66 percent (step 7), figure 8.30. It can be seen that in this region the absolute sizes of the major principal stresses become great and simultaneously the minor principal stresses are minimising, which means that stress points in this region are situated closely to the yielding envelope.
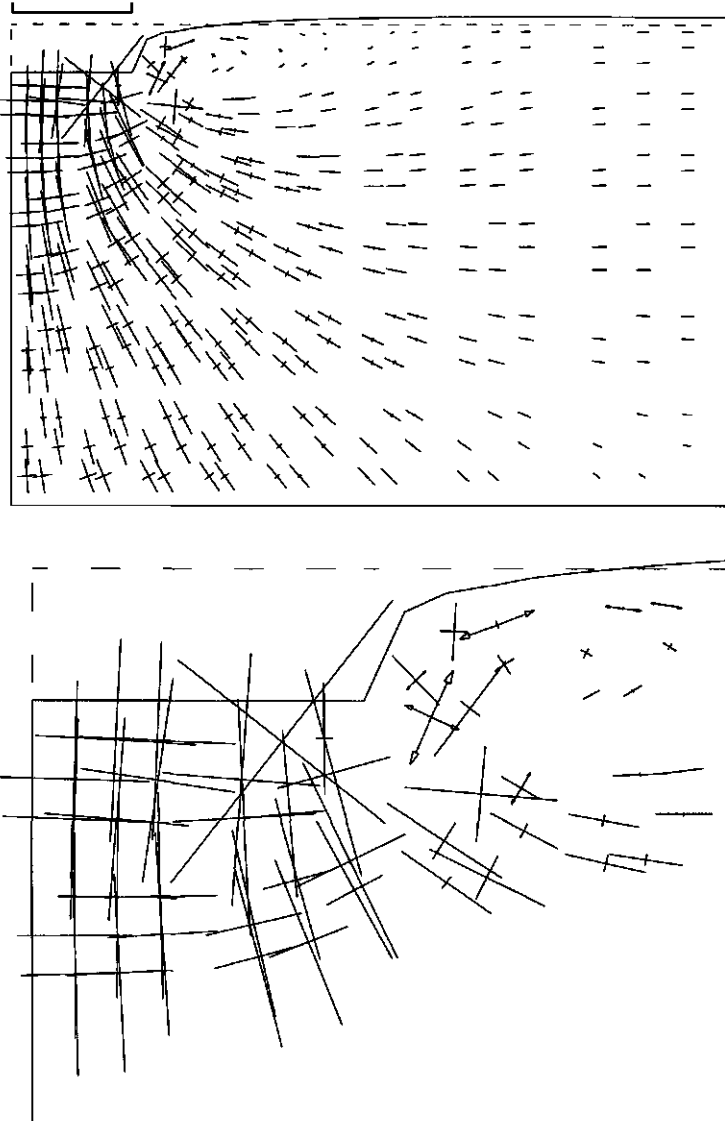

Figure 8.30 Effective principal stress field at an impression of the strip of 1.66 percent (step 7; max principal stress -3.21e+05 N/m²).

At an impression of the strip of 4.17 percent (step 12) the location of the first principal
stresses, being tensile stresses, are visible, figure 8.31 (tensile stresses are indicated by an
arrow). The place of the tensile stresses is not unlogical, because it is just this region where
cracks appear in practice.

Figure 8.31 Effective principal stress field at an impression of the strip
            of 4.17 percent (step 12; max principal stress -7.02e+05
            N/m²).

Finally the stress field at an impression of the strip of 10 percent is given, figure 8.32. What catches the eye the most in this figure is the excessive large major principal stress and its direction. Existence of local areas where the stresses are highly irregular and seem inimitable are often implying that the displacements in this area are also inimitable.

Figure 8.32 Effective principal stress field at an impression of the strip of 10 percent (step 33; max principal stress -1,32e+06 N/m^2).

Plastic points

Plastic points in the used finite element method are stress points, which soil behaviour is plastic instead of elastic in the presented step. In figure 8.33 the location of the first plastic point of the reference case is presented, which corresponds to an impression of the strip of 1.66 percent, step 7.

□   Plastic Mohr-Coulomb point
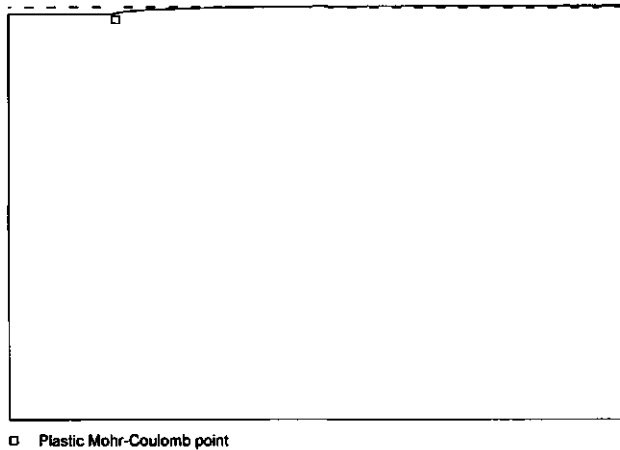
Figure 8.33 First plastic point at an impression of the strip of 1.66 percent (step 7).

Figure 8.34 presents the plastic region at an impression of the strip of 10 percent, step 33.

□   Plastic Mohr-Coulomb point
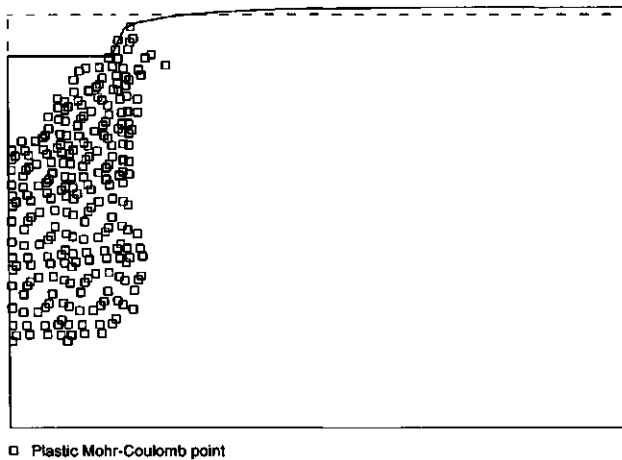
Figure 8.34 Plastic points at an impression of the strip of 10 percent (step 33).

Stresses σ_{xx}, σ_{yy}, σ_{xy} and σ_{zz} and choice of graphical representation

As a result of the location of the stresspoints in one triangular element of the mesh, the stresspoints of the complete initial mesh are irregularly spaced, i.e. not equidistant. This irregularity of the stresspoints becomes greater in those cases where deformed meshes are considered. On that account, for analysing of data it is more and more useful to create three-dimensional plots with the mesh, initial or deformed, as ground surface and a specific quantity as height. In this dissertation this is done in two ways, namely with the inverse distance method and a so-called real one-to-one procedure.

Differences between these presentations will be shown on basis of the deformed mesh as ground surface and σ_{yy} and σ_{xy} as quantity in the z-direction. Plots of σ_{xx} and σ_{zz} will not be presented in this part, because these plots are similar to the shape of the surface of σ_{yy}.

With the inverse distance method irregularly-spaced data of the ground surface, i.e. x and y coordinates of the mesh, are interpolated to a regularly-spaced grid of data. All points on the grid are interpolated values. Thus, the grid may not follow the original data exactly, but the surface will be a representation of the interpolated data. The used method to generate a gridded surface of the regularly-spaced nodes from the irregularly-spaced data is the inverse distance method. The z-value at each node is calculated using the following relations

$$z = \sum_{i=1}^{n} \left[\frac{\left(z_i / d_i^w \right)}{\sum_{i=1}^{n} \left(1 / d_i^w \right)} \right] \tag{8.3}$$

$$d_i = \sqrt{\left(x_i - x \right)^2 + \left(y_i - y \right)^2}$$

wherein

z	=	value of the node being calculated
n	=	number of original data points
z_i	=	an original data point
d_i	=	distance to the point
w	=	weight factor
x_i, y_i	=	location of the original data point
x, y	=	location of the current node

All original data points, z_1 till z_n, are taken into account in the calculation of each grid node's z-value. The influence of an original data point on the current node decreases with its distance d_i from the node. In addition, a weighting power w is applied to the distance. The higher the weight, the more rapidly this influence decreases with distance.

In this dissertation the number of gridlines in the x and y direction, which gives control over the density of the grid and the number of interpolated nodes, are taken in such a way that a square centimetre grid arises. In combination with quantity σ_{yy} this gives figure 8.35.
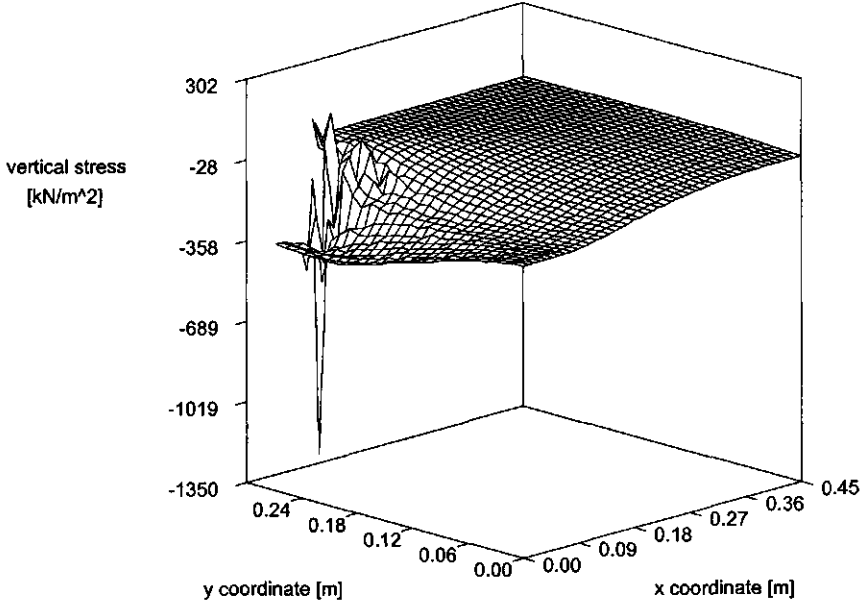

Figure 8.35 Three-dimensional plot of σ_{yy} against the deformed mesh at an impression of the strip of 10 percent (step 33; inverse distance method; $w = 5$).

In case of the real three-dimensional representation of a quantity, it is necessary to go back to the basic triangle of the used finite element code with its corresponding stresspoints, figure 8.36.
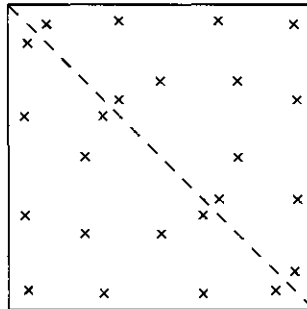
Figure 8.36 Two basic triangles with corresponding stresspoints.

To generate a complete three-dimensional surface, stresspoints must be connected to obtain elementary surfaces and these surfaces on their turn must be connected to each other to generate the total three-dimensional surface. To realise the above described there are a couple of manners. However, in this dissertation there is chosen to construct as much as possible small elementary quadrilaterals in the mesh in such a way that the boundary between the quadrilaterals, consisting of two basis triangles, can be distinguished. To put the latter mentioned quadrilaterals together there are also quadrilaterals used. Where this is impossible there is fallen back on triangles, figure 8.37.
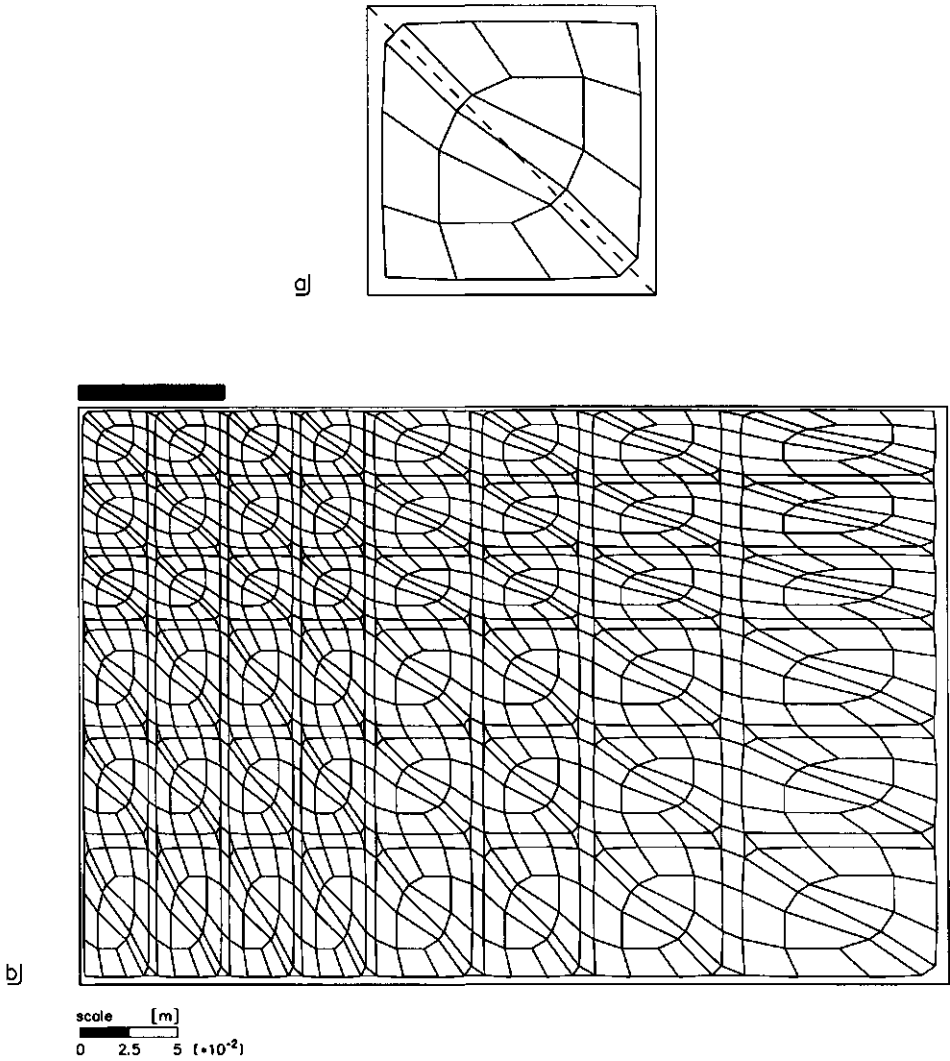
Figure 8.37 Construction of quadrilaterals in two basic triangles (a) and
in the total initial mesh of the reference case (b).

Because the deformed mesh subdivided into quadrilaterals, corresponding to 10 percent strip impression, is of great importance in the coming three-dimensional figures, this deformed mesh is given in figure 8.38.
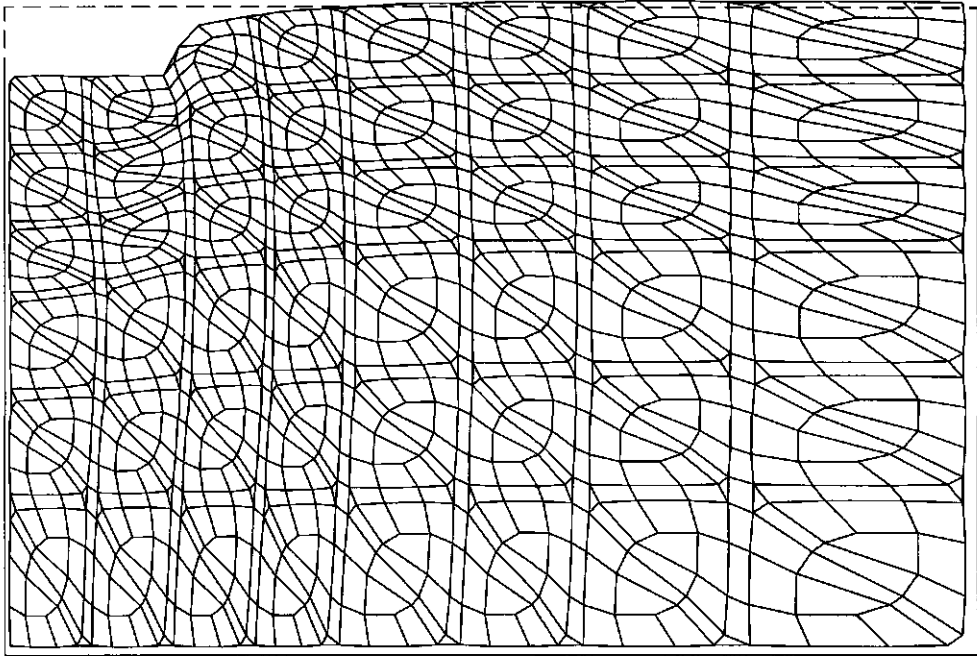
scale   [m]

0   2.5   5 [*10⁻²]

Figure 8.38 Deformed mesh subdivided into quadrilaterals at an
impression of the strip of 10 percent (step 33).

Combining the deformed mesh at 10 percent impression of the strip (step 33) as ground
surface, with subdivision of the mesh into quadrilaterals in a way similar to the figures 8.37
and 8.38, and σ_{yy} as z-coordinate, the three-dimensional plot of figure 8.39 can be
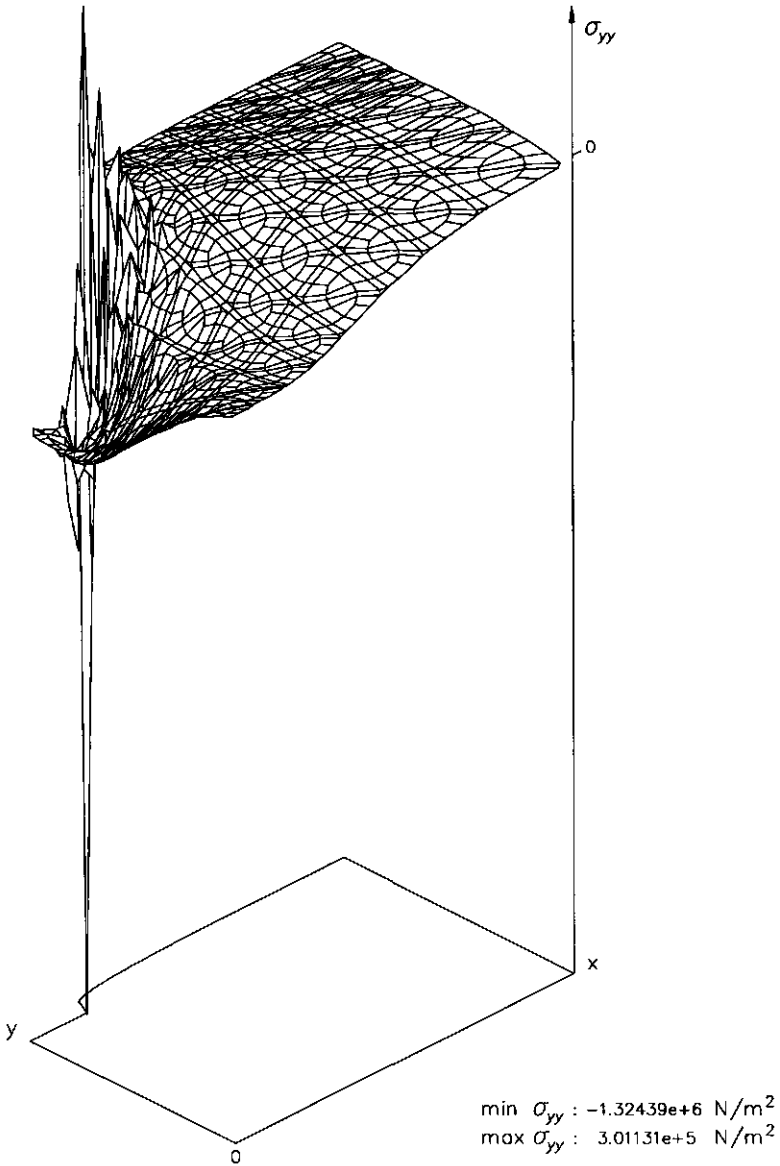constructed.

Figure 8.39 Three-dimensional plot of σ_{yy} on basis of subdivision of
the deformed mesh into quadrilaterals at an impression of
the strip of 10 percent (step 33).

The fact that with the used finite element code triangles are the basic elements, subdivision of the mesh into triangles would be most straightforward, see figure 8.40.
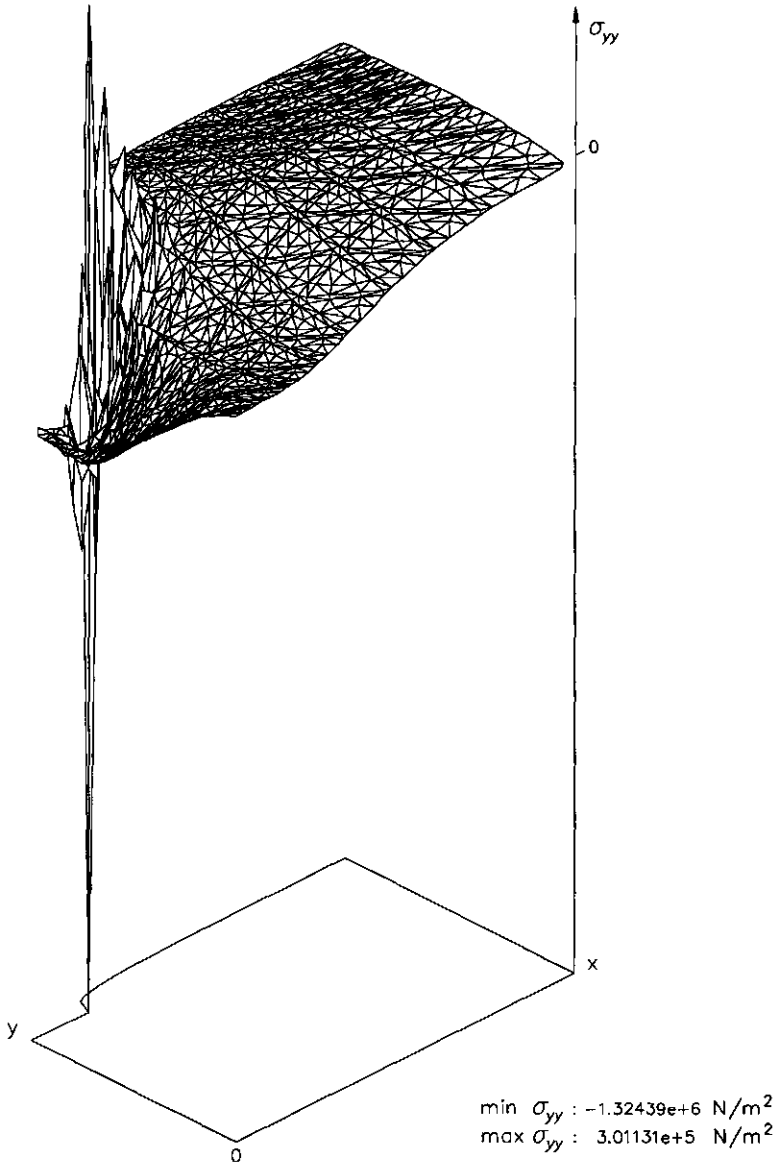
Figure 8.40   Three-dimensional plot of σ_{yy} on basis of subdivision of
the deformed mesh into triangles at an impression of the
strip of 10 percent (step 33).

Although the figures 8.39 and 8.40 contain the same information, the first mentioned figure
gives a less busy impression which makes it easier to interpret the plot. Therefore, there is

chosen for the subdivision into quadrilaterals of the mesh to generate three-dimensional plots with one-to-one representation of finite element results in this dissertation.

Advantage of the real one-to-one procedure is that all the data are represented exactly, without occurrence of additional noise through interpolating procedures. Disadvantage can sometimes be that there is no information available, through extrapolating, of the considered quantity at the edges of the mesh.
There are deviations in the interpolated values of the inverse distance method and the original data of the real one-to-one procedure. Comparison of the interpolated values and the real data is difficult through their different locations. To get an impression of the deviations, the interpolated values of σ_{yy} at the axis of symmetry and the finite element results of σ_{yy} of stresspoints lying as close as possible to the axis of symmetry are both given in figure 8.41.
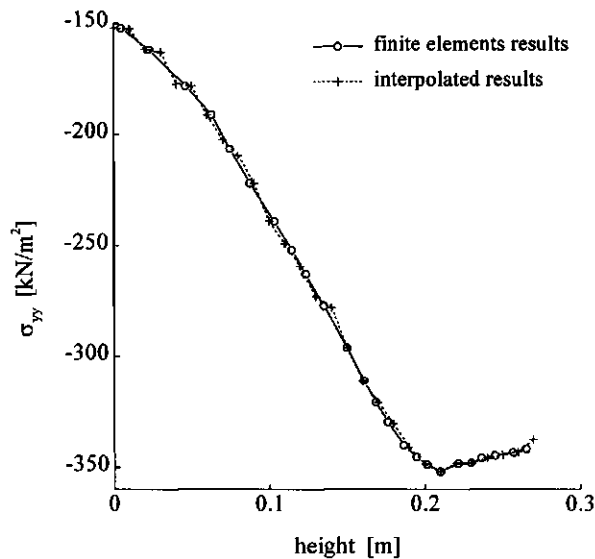

Figure 8.41   Finite element results of σ_{yy} near the axis of symmetry and interpolated results of σ_{yy} at the axis of symmetry at an impression of the strip of 10 percent (step 33).

In the figures 8.42 and 8.43 σ_{xy} is plotted against the deformed mesh at 10 percent impression of the strip on basis of the interpolated values, inverse distance method, and the original data, respectively.
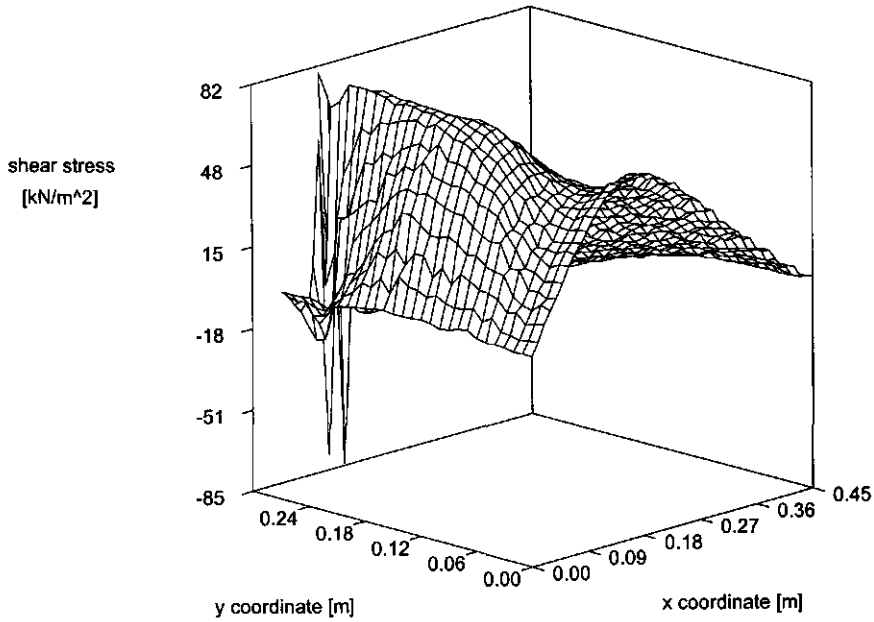
Figure 8.42   Three-dimensional plot of σ_{xy} against the deformed mesh at an impression of the strip of 10 percent (step 33; inverse distance method; $w = 5$).

min σ_{xy} : $-7.9431e+4$ N/m^2
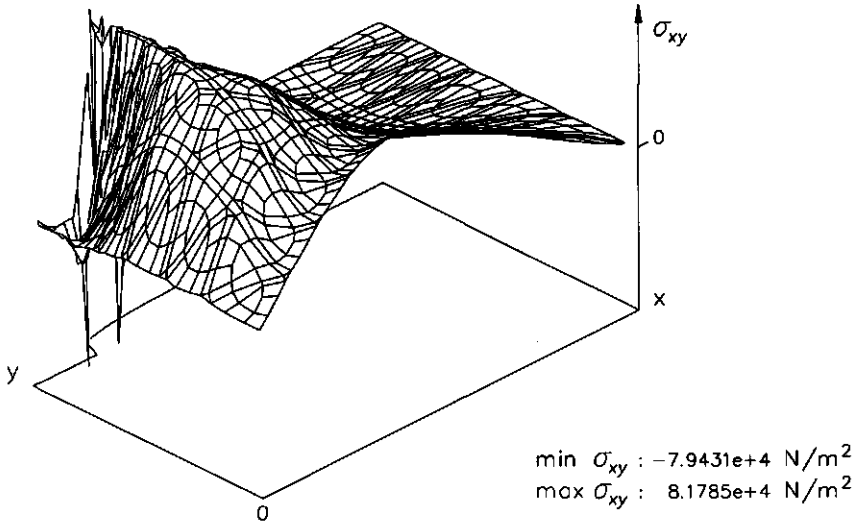max σ_{xy} : $8.1785e+4$ N/m^2

Figure 8.43   Three-dimensional plot of σ_{xy} on basis of subdivision of the deformed mesh into quadrilaterals at an impression of the strip of 10 percent (step 33).

The interpolated values at and original data near the axis of symmetry are represented in the following figure.
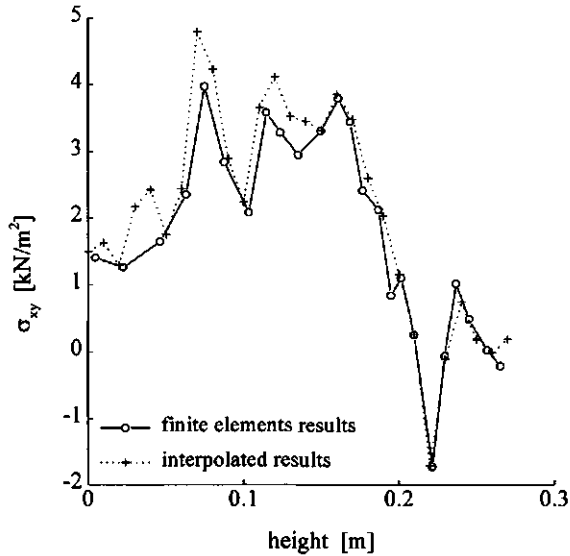

Figure 8.44   Finite element results of σ_{xy} near the axis of symmetry and interpolated results of σ_{xy} at the axis of symmetry at an impression of the strip of 10 percent (step 33).

From the latest seven figures it can be concluded that the inverse distance method can be a useful tool to represent irregular spaced data. However, attention should be given in those regions where the variation of the considered specific quantity is large.
The choice of making use of the inverse distance method or the one-to-one method to present data in three dimensions depends on which form of presentation is most satisfactory for the object in view.

It should be remarked that in the case of σ_{yy} (and of σ_{xx} and σ_{zz}) the development of the quantity just beneath and besides the plate is very irregular, i.e. very spiky. This phenomenon is manifested to a lesser extend in the case of quantity σ_{xy}.

Coping with data scatter near strip

To come to a useful definition of composite quantities several basic components from which the composite quantities would be composed, for instance σ_{xx}, σ_{yy}, σ_{xy} and σ_{zz}, must have a more or less smooth development.
Therefore, at this stage alternatives are described to come to a smoother development of interesting quantities, if possible. The alternatives refer to the boundary condition how to simulate the strip impression into the soil.

Alternatives are :
1 prescribed displacement of nodes of the strip with free movement in the x-direction
2 prescribed displacement of nodes of the strip in combination with the use of interface elements
3 prescribed tractions of nodes of the strip with free movement in the x-direction
4 prescribed tractions of nodes of the strip whereby no movement in the x-direction is allowed.

Thus, the different boundary conditions of all the alternatives refer to nodes which in the case of the reference case endure a prescribed displacement to simulate a strip impression with a rough bottom side. These nodes are presented in figure 8.45 and denoted by A till I. In the more detailed description of the alternatives there will be referred to this figure.
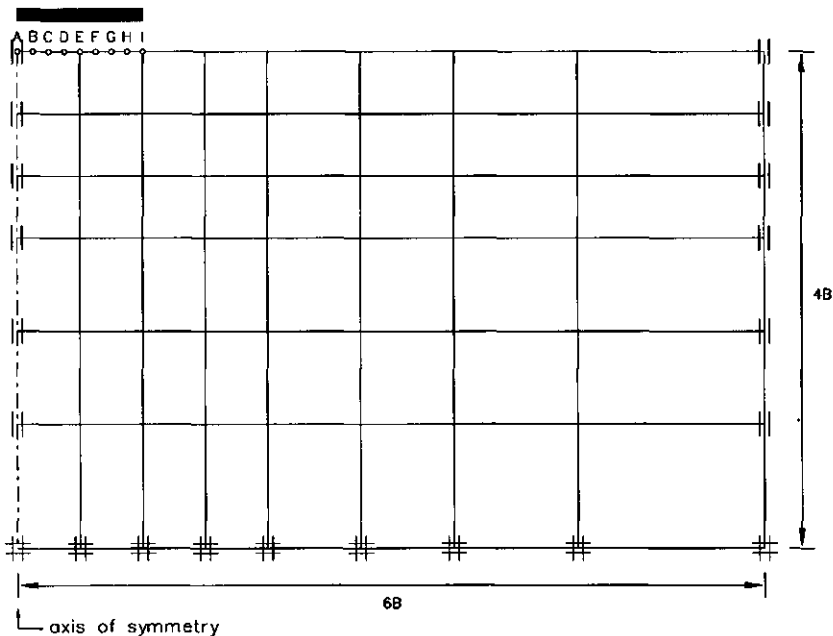

Figure 8.45 Mesh with specific nodes.

From figure 8.45 it can be seen that in case of all the given alternatives nothing has changed in the geometry of the modelled soil mass.

In the earlier described sequence of alternatives output results will be given. From each case plots will be given, surrounded with corresponding remarks, of :
- the deformed mesh in the region near the simulated strip impression
- the vertical pressure distribution of the upper layer of the bin
- σ_{yy} against the deformed mesh.
At the end some conclusions will be given.

Alternative 1

During the simulated strip impression, where nodes A till I endure a prescribed vertical displacement downwards of 10 percent of the initial height of the soil bin, the nodes B till I can move freely in the x-direction. Consequence is that node I initially lying beneath the edge of the strip, has shifted to the right relative to the strip. This is indicated by an arrow in figure 8.46. The vertical stress distribution of the upper layer of the bin and the three-dimensional plot of σ_{yy} against the deformed mesh at an impression of the strip of 10 percent are given in the figures 8.47 and 8.48.
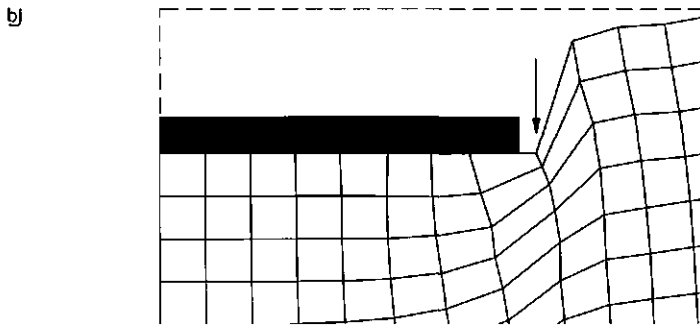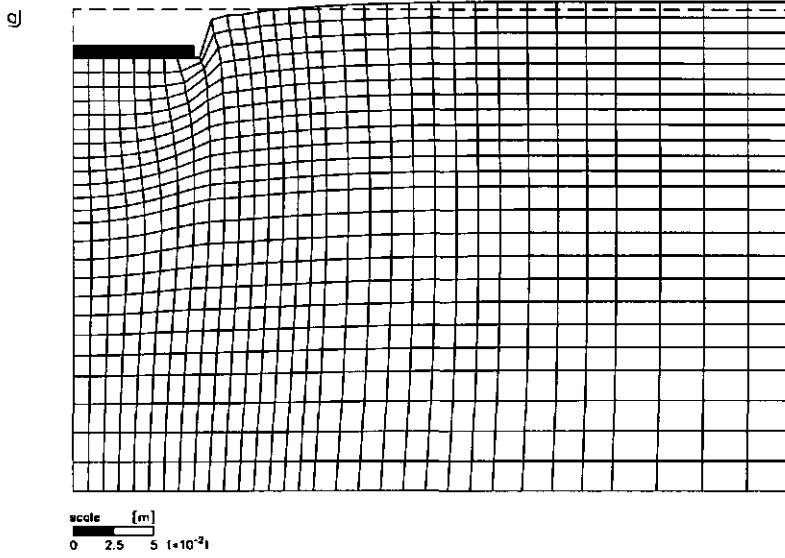
a)

b)

Figure 8.46 Deformed mesh at an impression of the strip of 10 percent
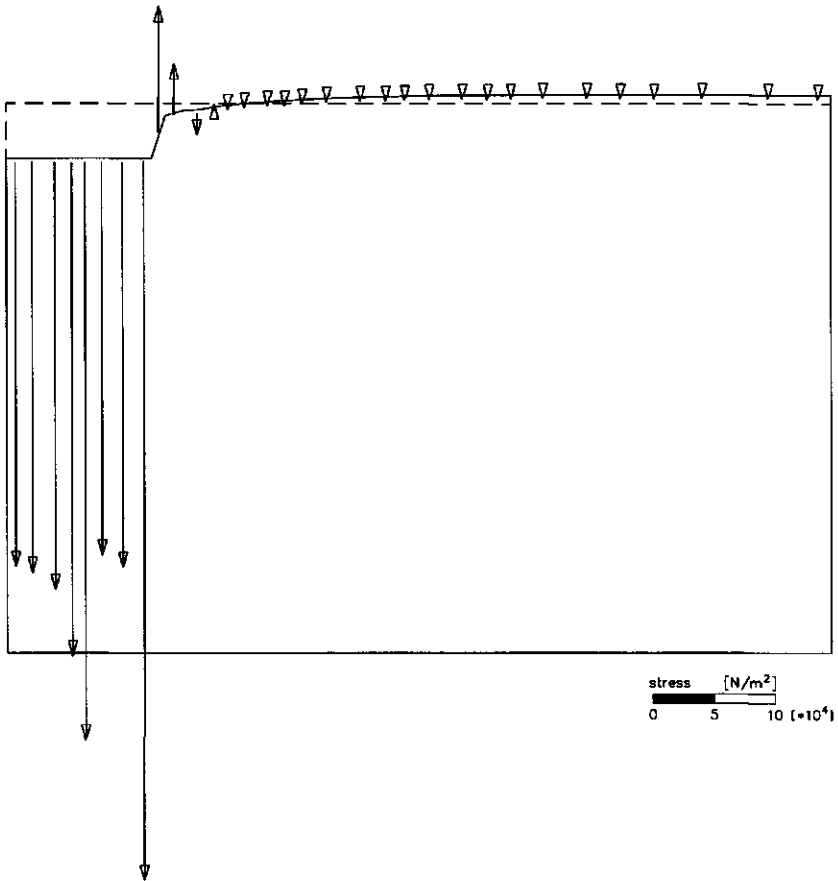   (a), enlarged (b).

Figure 8.47   Vertical pressure distribution of the upper layer of the bin
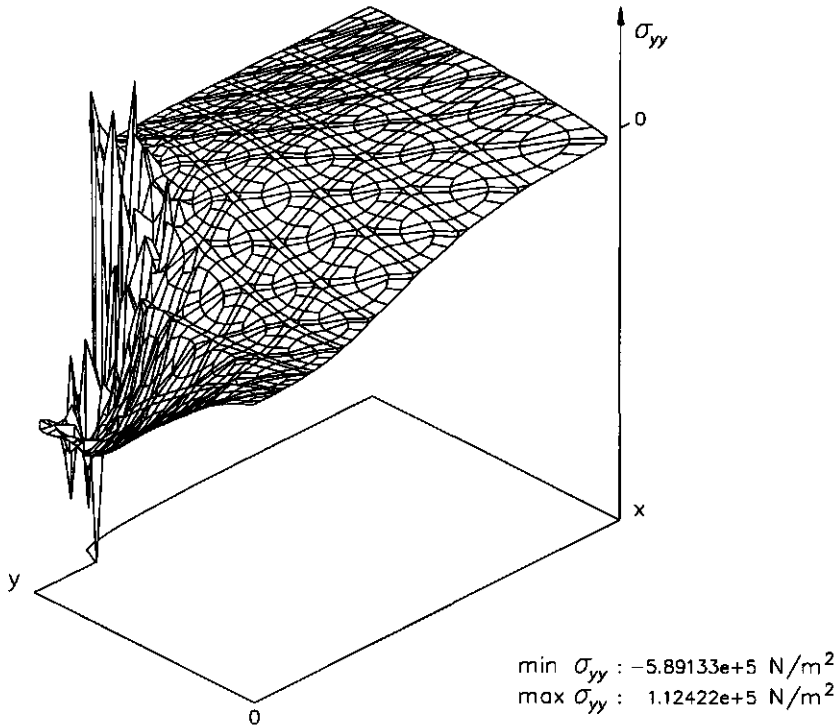at an impression of the strip of 10 percent.

min σ_{yy} : $-5.89133e+5$ N/m^2
max σ_{yy} : $1.12422e+5$ N/m^2

Figure 8.48 Three-dimensional plot of σ_{yy} against the deformed mesh
at an impression of the strip of 10 percent.

Alternative 2

In this alternative interface elements are used to model the interaction between the strip and soil. This means in this case that the two horizontal interface elements are used from which the node pairs are lying at the locations of the nodes A till E and E till I respectively. Each node of a node pair endures the same prescribed vertical displacement downwards, which simulates the strip impression. This alternative simulation calculation is calculated in the case strength reduction factor R is set to 1 and 0.1, respectively.

_R = 1_

In this case the strip impression is simulated with a plate with a rough bottom side. This
means specifically that the soil in connection with the strip is fixed to the strip, adhering layer,
but in the soil just beneath the fixed soil slip can exist with a shearing resistance equal to the
cohesion of the soil. Incidentally in this simulation calculation the fixed values of υ and ψ of
the interface exactly are the same as the υ and ψ of the soil mass. This implies that all the
interface and soil properties are identical so that the effect of using interface elements clearly
can be distinguished. Figure 8.49 represents the deformed mesh at an impression of the strip
of 9.55 percent. In the Plaxis output the deformed interface is presented by the nodes that
exhibited slip (in this case the nodes that are at the imaginary underside of the interface).
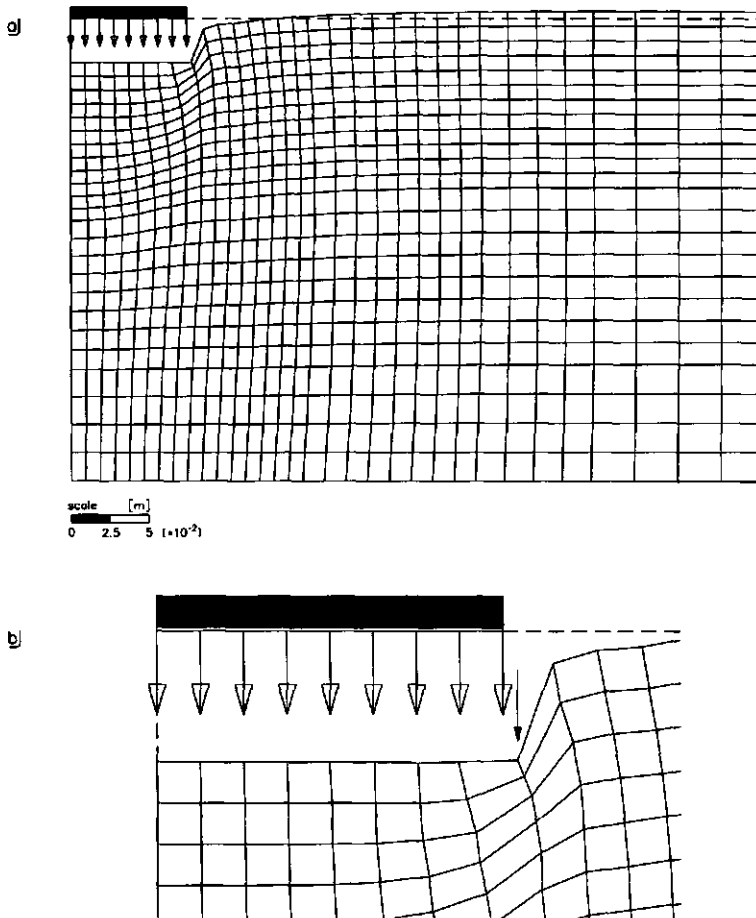
Figure 8.49 Deformed mesh at an impression of the strip of 9.55
percent (a), interface visible in enlarged section (b).

From the enlarged figure of the region near the strip the effect of occurrence of slip in the interface can be detected. The node initially lying beneath the edge of the strip, indicated by a closed arrow in the figure, has shifted to the right relative to the strip. In figure 8.50 the vertical pressure distribution of the upper layer of the bin is presented. The three-dimensional plot of σ_{yy} against the deformed mesh at an impression of the strip of 10 percent is given in figure 8.51.
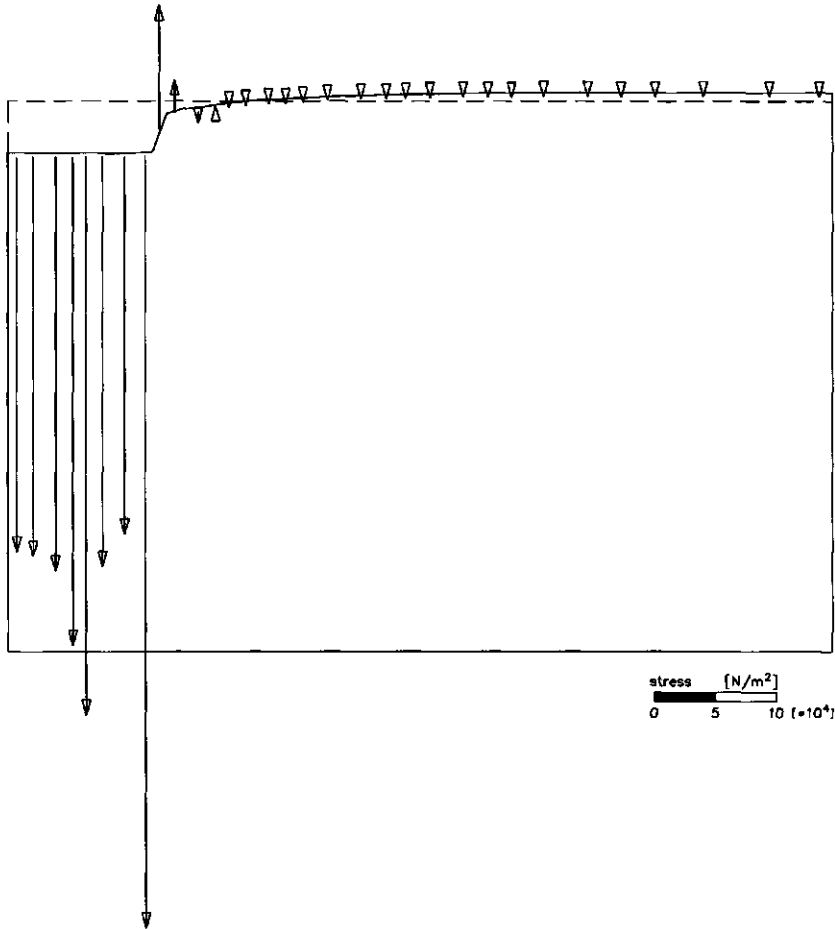

Figure 8.50 Vertical pressure distribution of the upper layer of the bin
at an impression of the plate of 9.55 percent.

$$\text{min } \sigma_{yy} : -6.32519e+5 \text{ N/m}^2$$
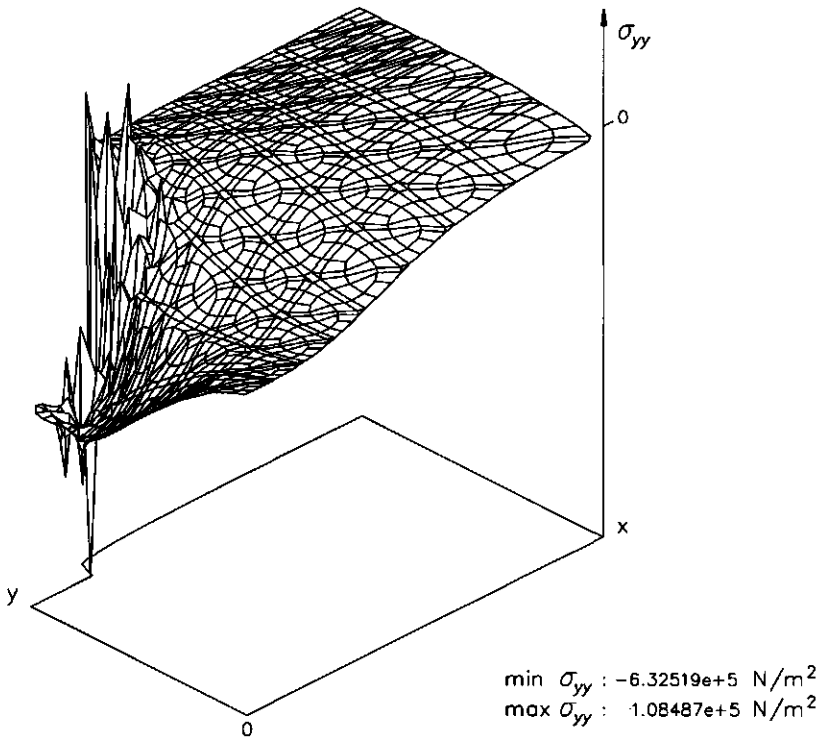$$\text{max } \sigma_{yy} : \ 1.08487e+5 \text{ N/m}^2$$

Figure 8.51 Three-dimensional plot of σ_{yy} against the deformed mesh
at an impression of the strip of 9.55 percent.

$R = 0.1$

A strength reduction factor R of 0.1 simulates a more or less adhesionless behaviour of the strip-soil interface. Here also the existence of slip of the interface nodes can clearly be distinguished, figure 8.52. The vertical stress distribution of the upper layer of the bin and the three-dimensional plot of σ_{yy} against the deformed mesh at an impression of the strip of 10 percent are given in the figures 8.53 and 8.54.

Figure 8.52 Deformed mesh at an impression of the strip of 10 percent.

stress   [N/m²]
0   5   10 [*10⁴]

Figure 8.53 Vertical pressure distribution of the upper layer of the bin
at an impression of the strip of 10 percent.

σ_{yy}

min σ_{yy} : $-3.87000e+5$ N/m^2
max σ_{yy} : $7.72520e+4$ N/m^2

Figure 8.54 Three-dimensional plot of σ_{yy} against the deformed mesh
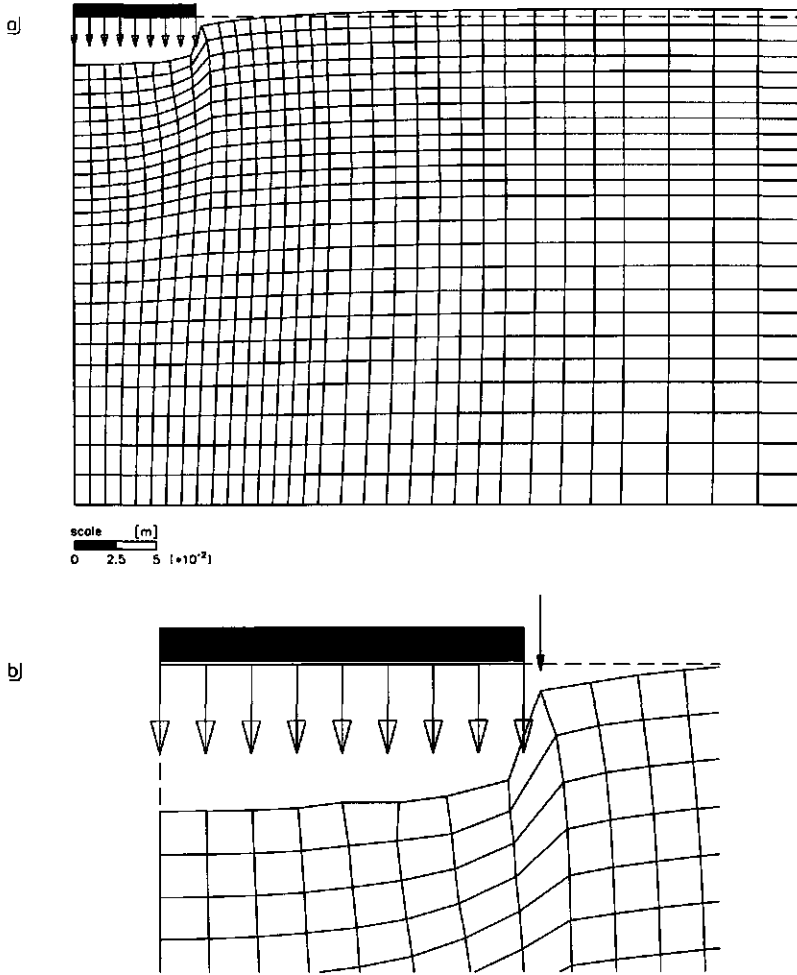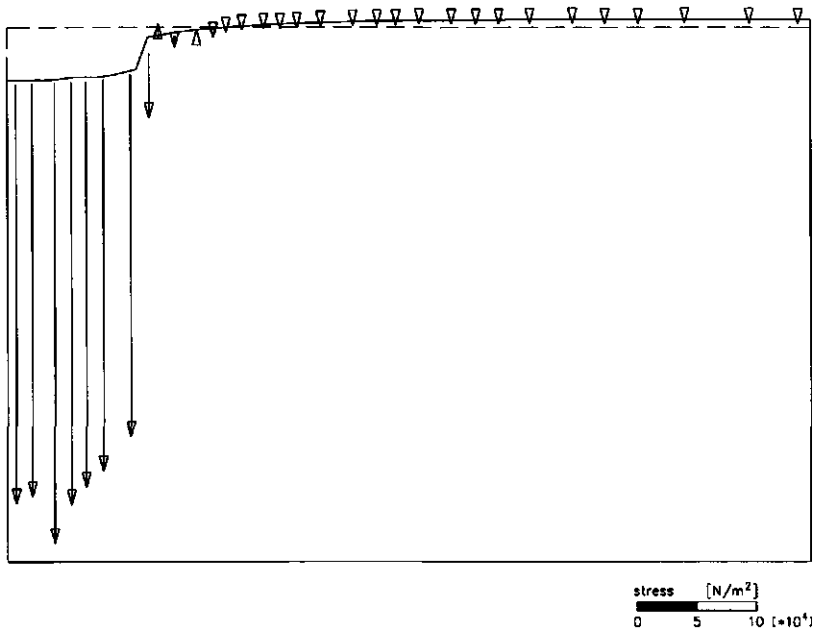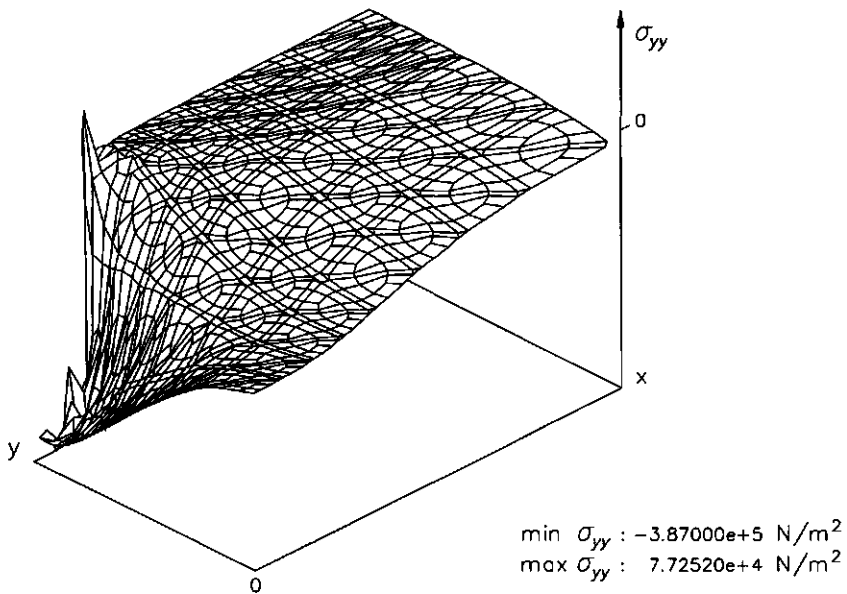at an impression of the strip of 10 percent.

From the last two figures can be concluded that the effect of the use of interfaces results in a less spikyness of the stresses. The fact that the bottom side of the strip and the toplayer of the soil, which initially coincide, coincide no more after the loading process is a complicating factor. In the case of $R = 0.1$ it looks as if the soil near the strip has flown upwards, which is not the case. Analysing what has happened is given below.

Properties of the used interface elements are :
- absence of plastic volumetric strain
- plastic flow is parallel to the interface
- presence of elastic volumetric strain
- elastic volumetric strain can occur in both horizontal and vertical direction.

Through the choice of a low value of strength reduction factor R the interface possesses a low stiffness ($G_i = R^2 G_{soil}$). A low value of G_i corresponds with a low K_i ($K_i = 2G_i (1 - v_i / 1 - 2v_i)$).
Thus, by a given stress and a small value of R the elastic gap displacement becomes tall ($\sigma t_i / K_i$). The fact that the normal stresses in the interface not remain equal in size results in a non-straightness of the interface through different elastic gap displacements. Through the occurrence of plastic flow this phenomenon is strengthening.

Alternative 3

In this alternative prescribed tractions, stresses on boundaries, are used, figure 8.55. At the nodes A till I a prescribed vertical traction downwards is applied of the amount of the pressure that was needed in simulation of the reference case to achieve a strip impression of 10 percent, namely -4.1947e+05 N/m^2. Nodes B till I can move freely in the x-direction. However, the soil body collapsed at the traction value of -3.1390e+05 N/m^2 on the strip and therefore output results refer to this traction value.

Figure 8.55 Deformed mesh at a traction value of -3.1390e+05 N/m^2
on the strip (a), enlarged (b).

The vertical stress distribution of the upper layer of the bin and the three-dimensional plot of σ_{yy} against the deformed mesh at an impression of the strip of 10 percent are given in the figures 8.56 and 8.57.

Figure 8.56 Vertical pressure distribution of the upper layer of the bin
at a traction value of -3.1390e+05 N/m^2 on the strip.

min σ_{yy} : −4.60682e+5 N/m^2
max σ_{yy} : 4.14350e+4 N/m^2

Figure 8.57 Three-dimensional plot of σ_{yy} against the deformed mesh
at a traction value of -3.1390e+05 N/m^2 on the strip.

Alternative 4

Also in this alternative prescribed vertical tractions downwards are used for the nodes A till I of -4.1947e+05 N/m^2, figure 8.58. However, restrictions are made in the horizontal movement of the nodes. None of the nodes A till I can move freely in the x-direction during the loading process.
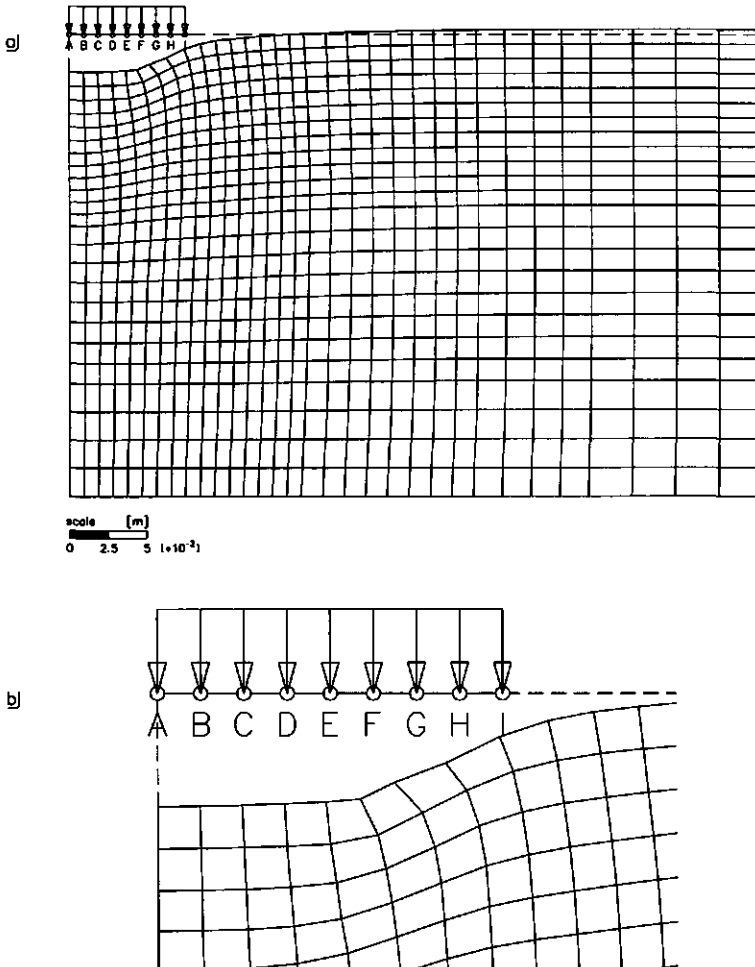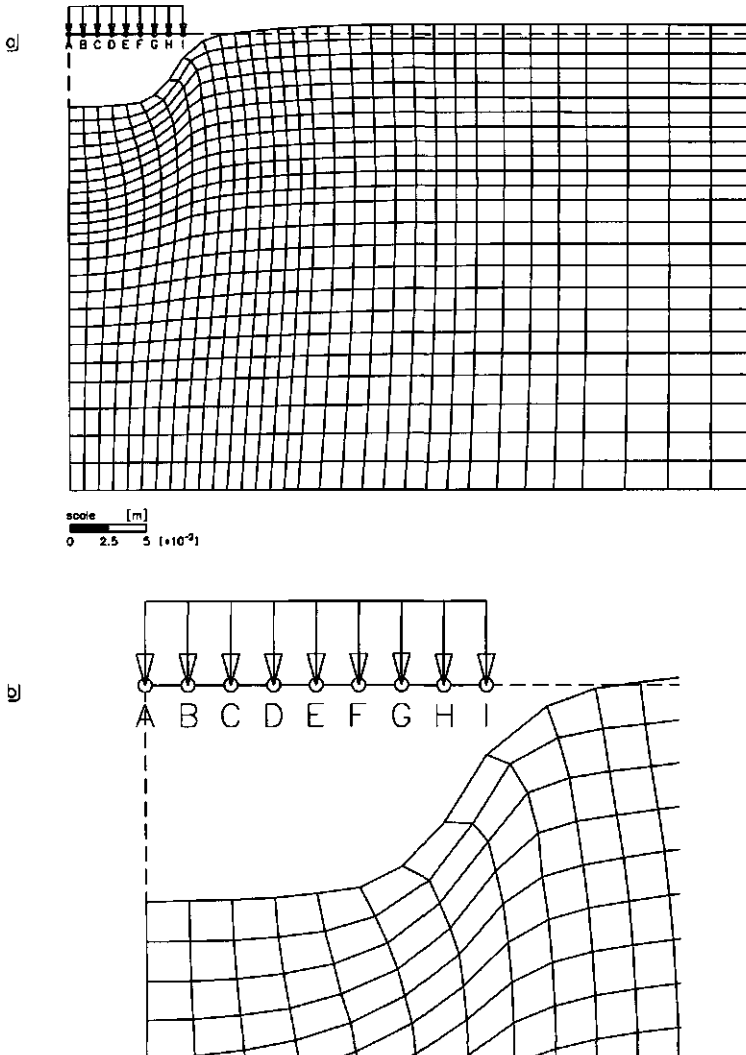

Figure 8.58 Deformed mesh at a traction value of -4.1947e+05 N/m^2
on the strip (a), enlarged (b).

The vertical stress distribution of the upper layer of the bin and the three-dimensional plot of σ_{yy} against the deformed mesh at an impression of the strip of 10 percent are given in the figures 8.59 and 8.60.
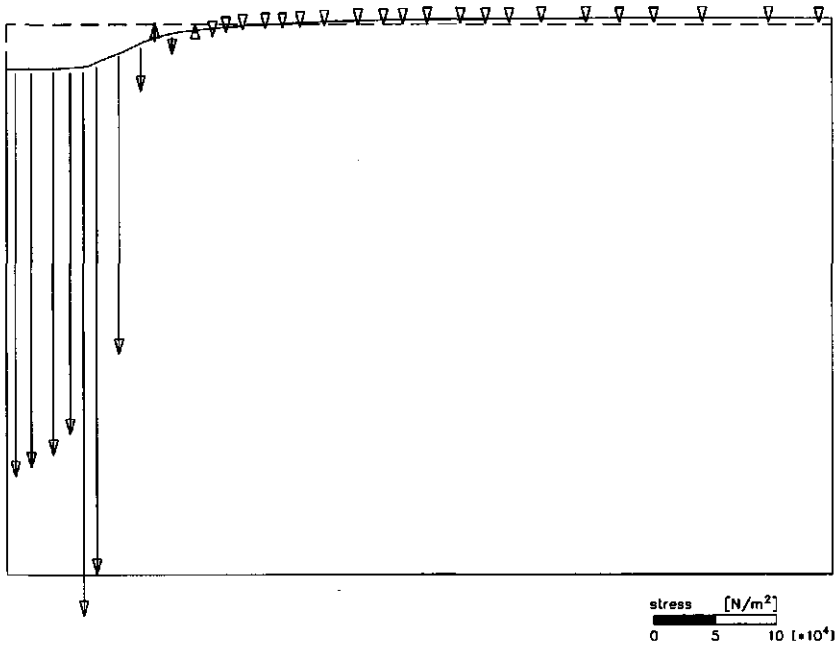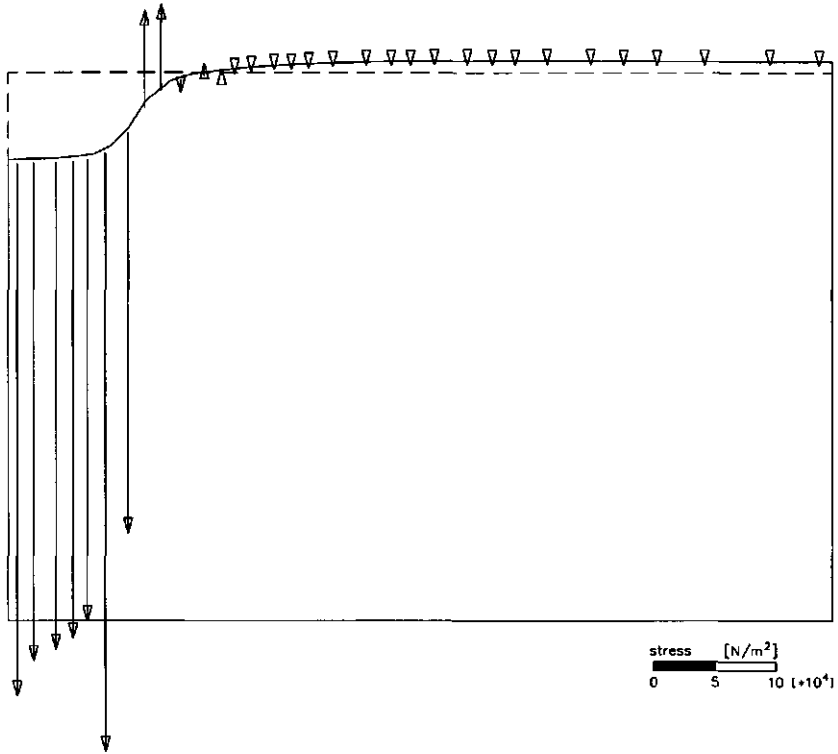

Figure 8.59 Vertical pressure distribution of the upper layer of the bin
at a traction value of -4.1947e+05 N/m^2 on the strip

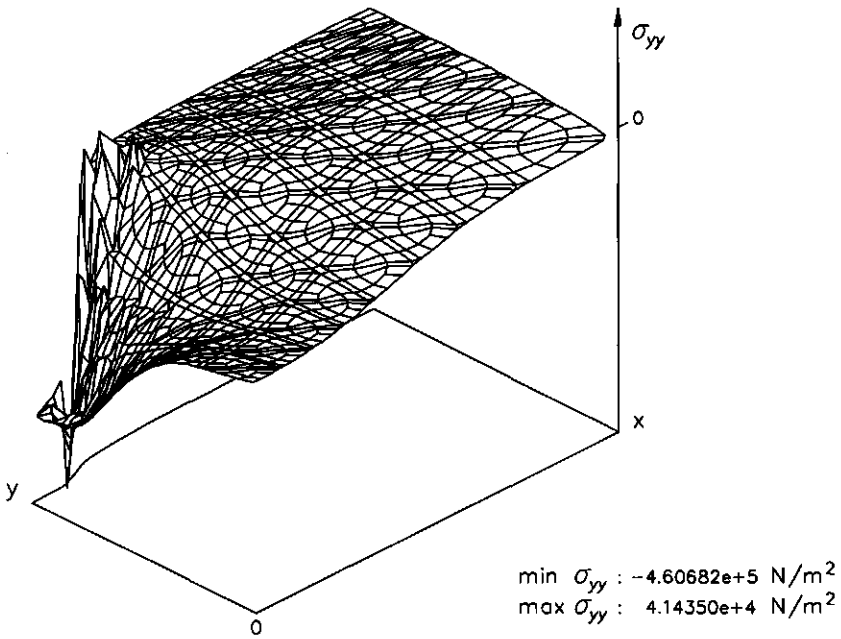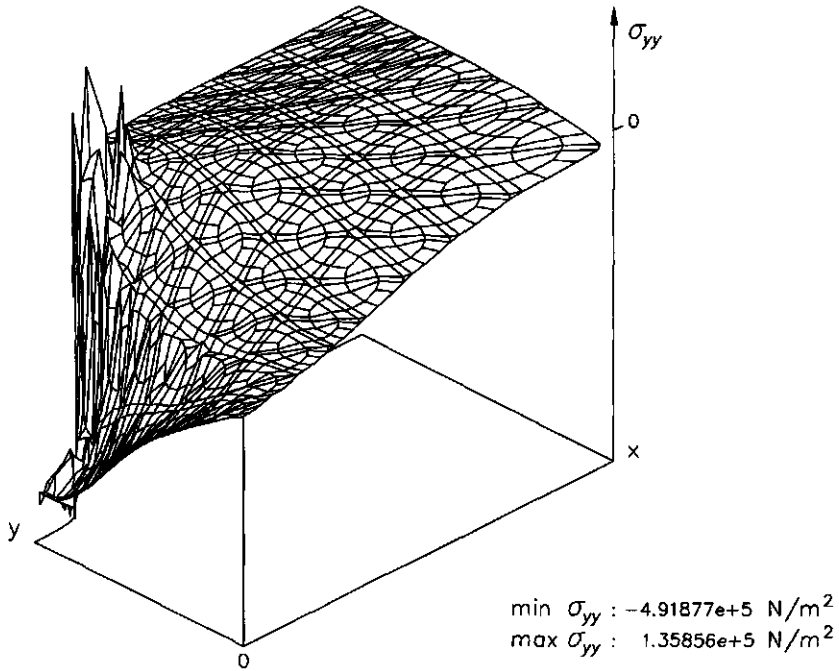Figure 8.60 Three-dimensional plot of σ_{yy} against the deformed mesh
at a traction value of -4.1947e+05 N/m^2.

Conclusions

All the alternatives give a smoother distribution of quantity σ_{yy} against the deformed mesh compared to the original reference case. However, those regions of the reference case where the spikyness is the greatest, these regions can also be detected in case of all the alternatives, although the spikyness is of a smaller order.

8.2.3 Verifiable derived quantity

Volume change

Of special interest is the plastic volume change. In the set of parameters of the reference soil dilatancy angle ψ is zero, which includes that there is no plastic volume change allowed. Therefore, the sum of plastic volume change increments is a measure of accuracy of a done simulation calculation. In figure 8.61 the sum of the plastic volume increments over all the steps between 10 and 0 percent strip impression is plotted against the deformed mesh at an impression of the strip of 10 percent (step 33).

$$\min \ \textstyle\sum \dot{\varepsilon}_v^p : -8.88926e-5$$
$$\max \ \textstyle\sum \dot{\varepsilon}_v^p : \ \ 9.89621e-3$$

Figure 8.61 Three-dimensional plot of the sum of plastic volume increments over all steps between 10 and 0 percent strip impression against the deformed mesh at an impression of the strip of 10 percent (step 33).

The positive peak value in the figure corresponds with deviation, i.c. increase, of the initial pore space of about 1 percent. In agriculture literature, the change in pore space is expressed usually in terms of percentage pore volume change. In this case the described increase of the initial pore space of 1 percent corresponds for a soil with initial pore space of 0.45 percent with an increase of the percentage pore volume space of 0.54 percent.
The fact that for most of the surface the deviation slightly differs from 1 percent, it can be concluded that the accuracy of the done simulation calculation is ample sufficient.

8.2.4 Further important derived quantities

Rigid body rotation

In figure 8.62 the development of the sum of the rigid body rotation over all steps between 10 and 0 percent strip impression of the reference case is shown.

min Σ rigid body rotation : -2.37762 $^\circ$
max Σ rigid body rotation : $8.08300e-1$ $^\circ$

Figure 8.62 Three-dimensional plot of the sum of the rigid body rotation over all steps between 10 and 0 percent strip impression against the deformed mesh at an impression of the strip of 10 percent (step 33).

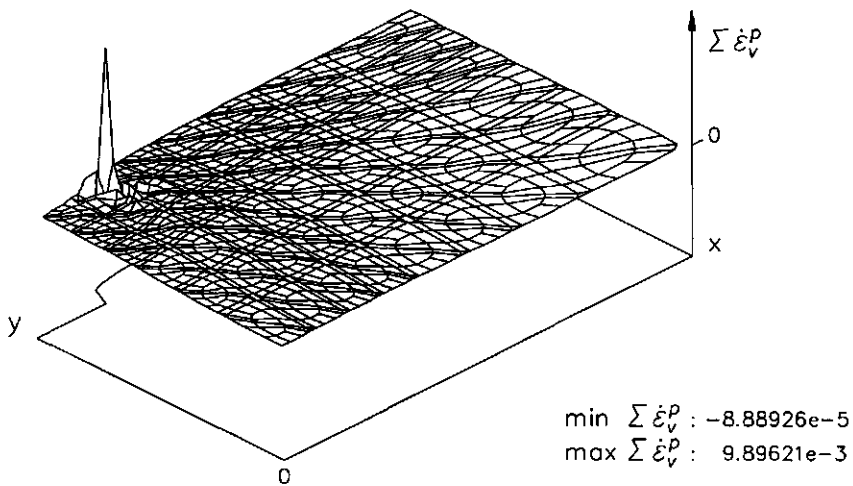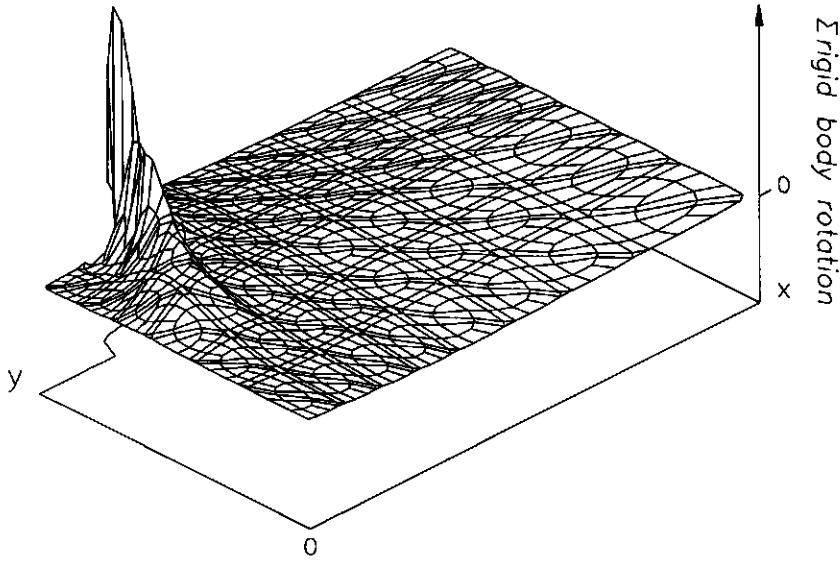*Principal stresses σ_1, σ_2 and σ_3*

In figure 8.63 the three-dimensional plot of σ_1 at 10 percent strip impression against the deformed mesh at an impression of the strip of 10 percent is given. The shape of this surface plot equals more or less the surface plot of σ_{yy} at the same boundary conditions (figure 8.39). Exception is the region just right of the strip. In this region σ_{yy} has low negative values, whereas σ_1 has positive values. This is due to the fact that in this region horizontally orientated tensile stresses exist in proportion to relatively small vertically orientated compressive stresses.

min σ_1 : $-1.32461e+6$ N/m^2
max σ_1 : $1.88126e+5$ N/m^2
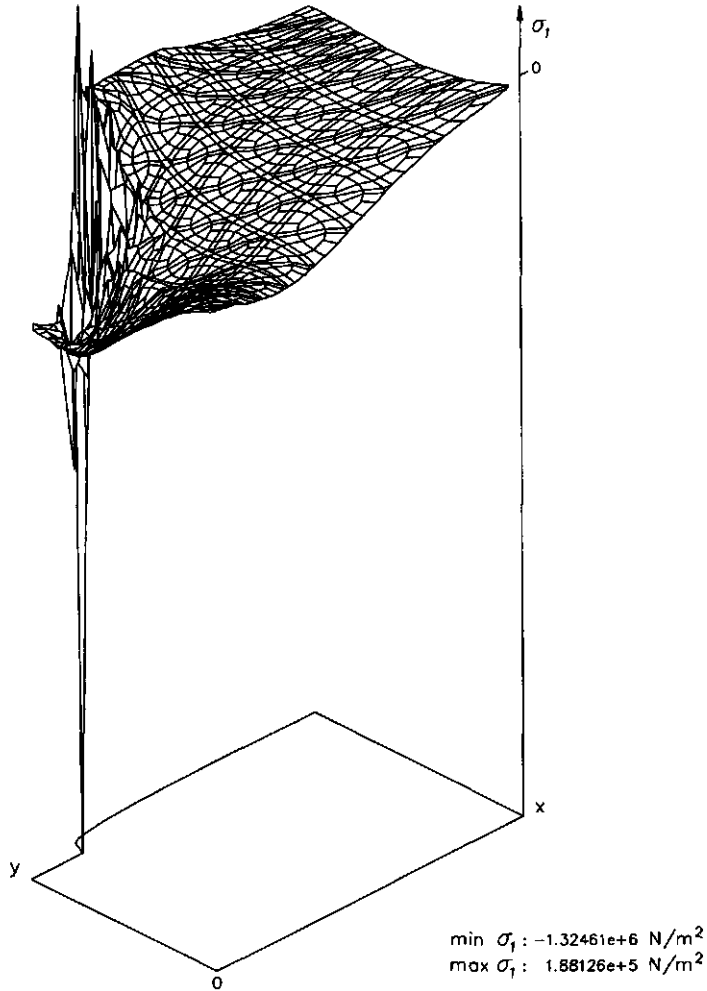
Figure 8.63   Three-dimensional plot of σ_1 at 10 percent strip impression against the deformed mesh at an impression of the strip of 10 percent (step 33).

For the sake of completeness, the three-dimensional plots of σ_2 and σ_3 at 10 percent strip impression against the deformed mesh at an impression of the strip of 10 percent (step 33) are given in figure 8.64 and 8.65.

min σ_2: $-1.16097e+6$ N/m^2
max σ_2: $2.42951e+5$ N/m^2
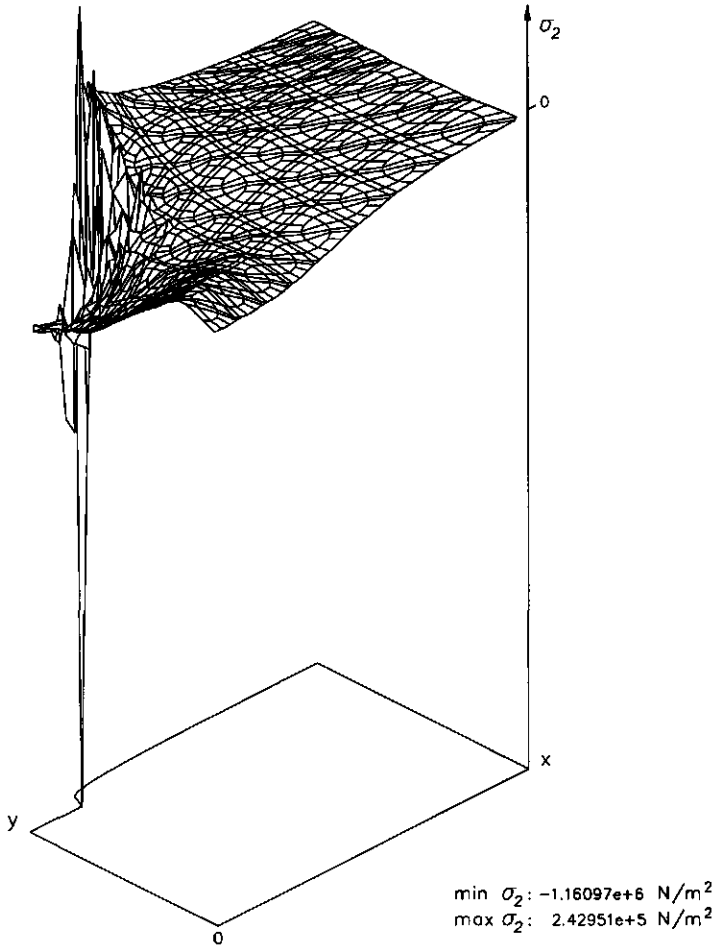
Figure 8.64   Three-dimensional plot of σ_2 at 10 percent strip impression
against the deformed mesh at an impression of the strip of
10 percent (step 33).
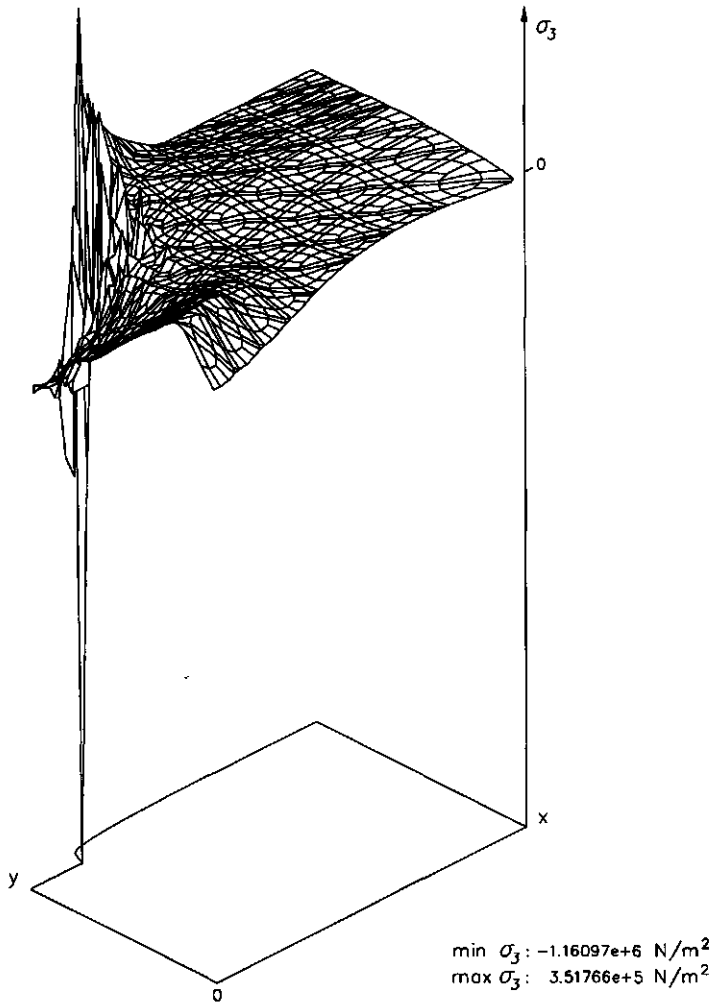
Figure 8.65   Three-dimensional plot of σ_3 at 10 percent strip impression
              against the deformed mesh at an impression of the strip of
              10 percent (step 33).

Rotation of the eigenvector of principal stress σ_1

Plot of the corrected rotation, according to section 7.2, of the eigenvector of σ_1 between 10 percent strip impression (step 33) and the initial stress field (step 0) against the deformed mesh at an impression of the strip of 10 percent (step 33) is given in figure 8.66a.

min *cor rot ev* σ_1 : $-8.99770\mathrm{e}{+1}$ °
max *cor rot ev* σ_1 : $8.99967\mathrm{e}{+1}$ °

bJ

Figure 8.66   Three-dimensional plot, at two different viewpoints, of the
corrected rotation of the eigenvector of σ_1 between 10 and
0 percent strip impression against the deformed mesh at an
impression of the strip of 10 percent (step 33).

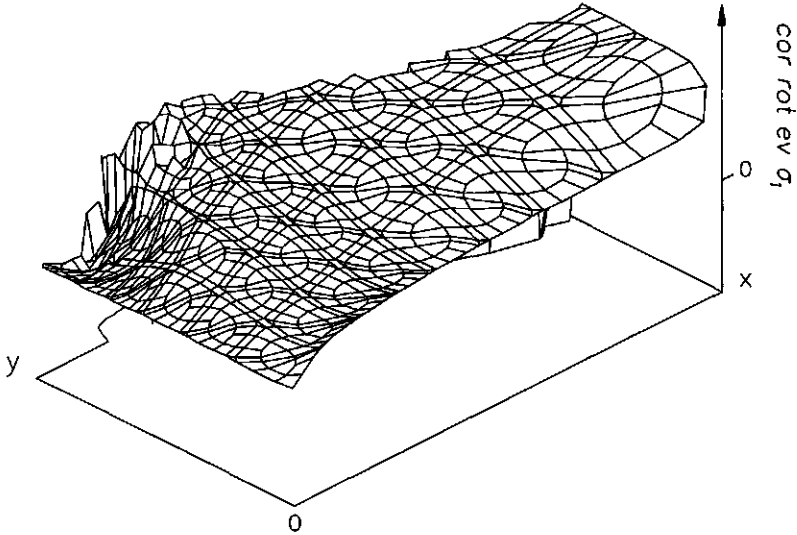Essentially figure 8.66a is an another type of representation of rotation of σ_1-vectors
compared to the initial positions of the σ_1-vectors given in figure 8.32. However, there is an
important difference between these two types of figures. In figure 8.32 the position of the
principal stresses in the xy-plane after 10 percent strip impression, from which the rotation of
the principal stresses can be derived, are given of 3 of the 12 existing stresspoints per basic
finite element triangle, whereas in figure 8.66 the numeric value of the rotation of the major
principal stress between 10 and 0 percent strip impression is represented for each stresspoint.

What is attracting attention in figure 8.66a is the abrupt break off of the continuous
surface. To make this better visible, figure 8.66a is represented from another viewpoint in
figure 8.66b. From this latter viewpoint it seems that there has been a translation of a part of
the surface of about 180 degrees downwards, which causes the valley in the surface.

Corresponding to figure 8.66 is figure 8.67 where the sum of the corrected rotation of the
eigenvector of σ_1 over all the steps of each stresspoint between 10 and 0 percent strip
impression is plotted against the deformed mesh at an impression of the strip of 10 percent
(step 33).

$$\min \ \Sigma \ cor \ rot \ ev \ \sigma_1 : \ -8.99430e+1 \ ^\circ$$
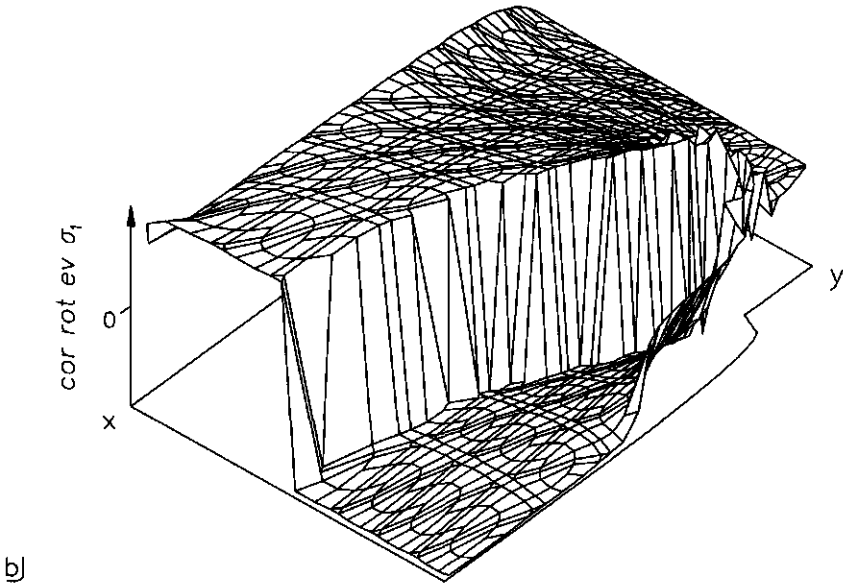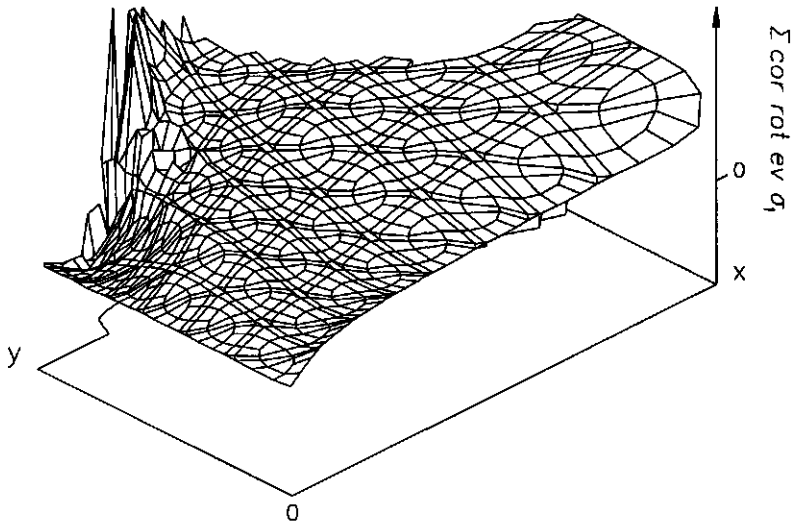$$\max \ \Sigma \ cor \ rot \ ev \ \sigma_1 : \ \ \ 1.76930e+2 \ ^\circ$$

a)
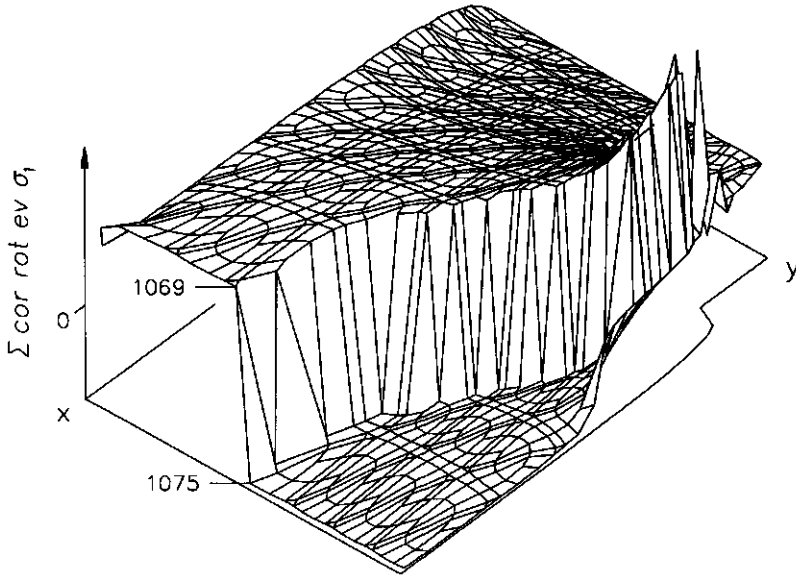
b)

Figure 8.67   Three-dimensional plot, at two different viewpoints, of the sum of the corrected rotation of the eigenvector of σ_1 over all steps between 10 and 0 percent strip impression against the deformed mesh at an impression of the strip of 10 percent (step 33).

The overall look of figure 8.67 is the same as for figure 8.66. Discrepancy between the figures is present in the region near the strip. Higher values of the sum of the corrected rotation of the eigenvector of σ_1 over all the steps, in comparison to the corrected rotation of the eigenvector of σ_1 only between the initial step and the last step by the same final strip impression, means that the rotation of σ_1-vector during all the steps has not been continuously in one and the same direction.

Also in this figure a valley region can be detected in a way similar as for figure 8.66. Therefore, it is useful at this stage to take a closer look at the observed phenomenon. For that reason there will be zoomed in at the stresspoints 1069 and 1075, indicated in figure 8.67*b*. These stresspoints are lying beside one another but differ from each other in the calculated value of the sum of the corrected rotation of the eigenvector of the major principal stress σ_1.
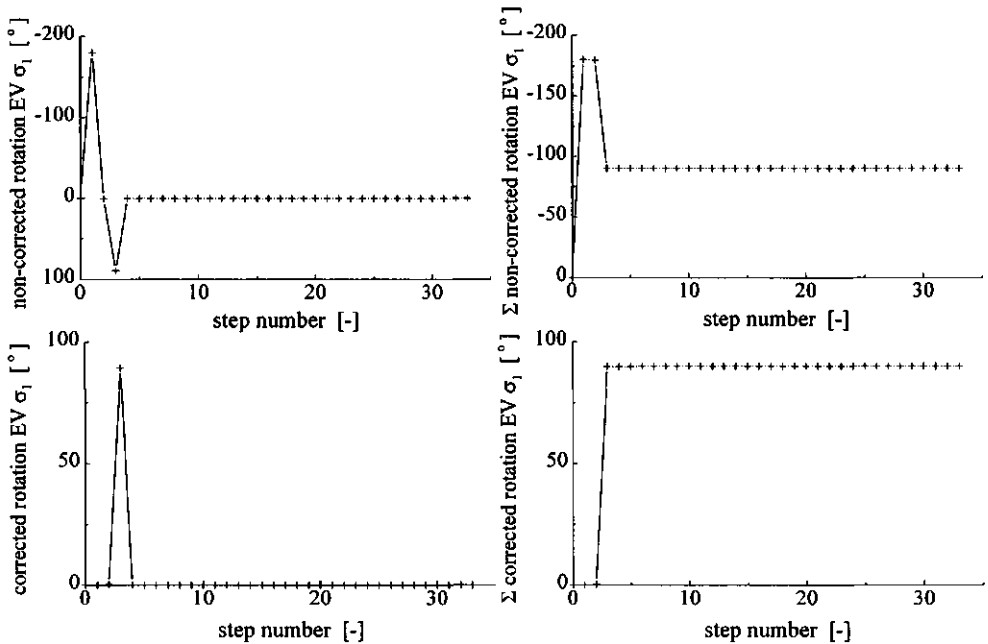
Figure 8.68 Plots of non-corrected and corrected rotation, inclusive cumulation, of the eigenvector of the major principal stress σ_1 against the step number of stresspoint 1069.
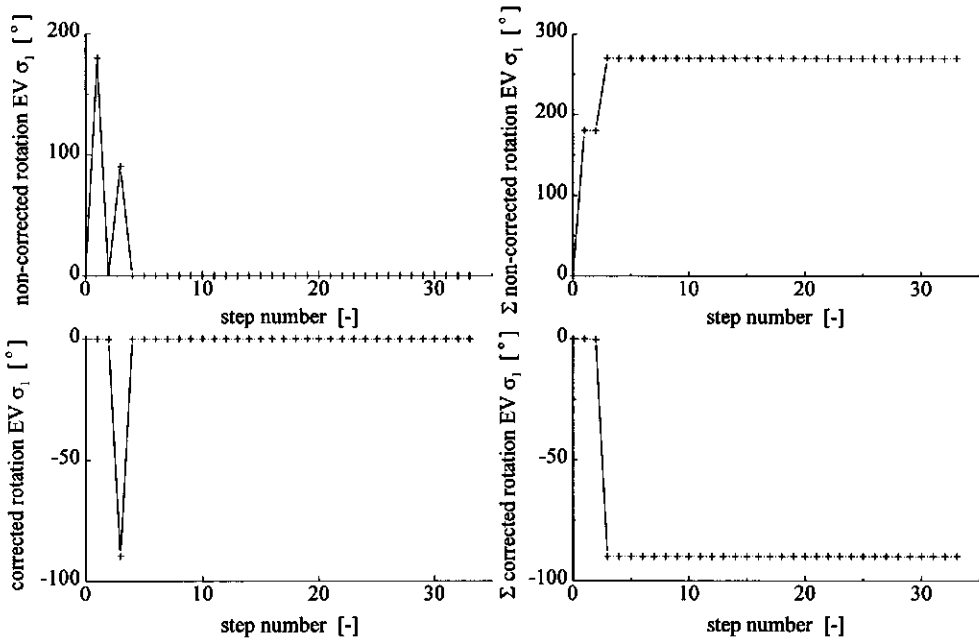
Figure 8.69 Plots of non-corrected and corrected rotation, inclusive cumulation, of the eigenvector of the major principal stress σ_1 against the step number of stresspoint 1075.

Figures 8.68 and 8.69 represent the development of the non-corrected and corrected rotation of the eigenvector of the major principal stress σ_1 against the number of steps of the stresspoints 1069 and 1075. From these figures it is obvious that the steps who are playing a role of interest are the steps 0 till 3. Just in the third step the difference in rotation of about 180 degrees between the stresspoints occurs and remains during further impression of the plate.

To get grip on the observed phenomenon till step 3, the numerical values of σ_{xx}, σ_{yy}, σ_{xy}, σ_1, direction of σ_1, non-corrected and corrected rotation of σ_1-vector are given for both stresspoints in tables 8.2 and 8.3. In addition to these tables the positions of σ_1 for the considered steps of both stresspoints are represented visually in figure 8.70.

stresspoint 1069				
step number	σ_{xx}	σ_{yy}	σ_{xy}	σ_1
0	−2.4840814e+03	−3.0293676e+03	0.0000000e+00	−3.0293676e+03
1	−2.6180945e+03	−3.0131585e+03	2.1766854e−01	−3.0131586e+03
2	−2.8860574e+03	−2.9806430e+03	6.4868453e−01	−2.9806474e+03
3	−3.4216870e+03	−2.9151700e+03	1.4934284e+00	−3.4216914e+03
step number	eigenvector corresponding to σ_1		non-corrected rotation σ_1	corrected rotation σ_1
0	0.0000000e+00	1.0000000e+00	0.0000000e+00	0.0000000e+00
1	5.5097007e−04	−9.9999985e−01	−1.7996843e+02	3.1568261e−02
2	6.8576905e−03	−9.9997649e−01	3.6135154e−01	3.6135154e−01
3	9.9999565e−01	−2.9483886e−03	8.9438150e+01	8.9438150e+01

Table 8.2 Output results of stresspoint 1069.

stresspoint 1075				
step number	σ_{xx}	σ_{yy}	σ_{xy}	σ_1
0	−2.2789466e+03	−2.7792032e+03	0.0000000e+00	−2.7792032e+03
1	−2.4132735e+03	−2.7628665e+03	−8.1791220e−02	−2.7628665e+03
2	−2.6818429e+03	−2.7300907e+03	−2.4917296e−01	−2.7300920e+03
3	−3.2186388e+03	−2.6641272e+03	−6.0016558e−01	−3.2186394e+03
step number	eigenvector corresponding to σ_1		non-corrected rotation σ_1	corrected rotation σ_1
0	0.0000000e+00	1.0000000e+00	0.0000000e+00	0.0000000e+00
1	−2.3396124e−04	−9.9999997e−01	1.7998660e+02	−1.3404992e−02
2	−5.1642353e−03	−9.9998667e−01	−2.8248521e−01	−2.8248521e−01
3	9.9999941e−01	1.0823300e−03	9.0357903e+01	−8.9642097e+02

Table 8.3 Output results of stresspoint 1075.

stresspoint 1069
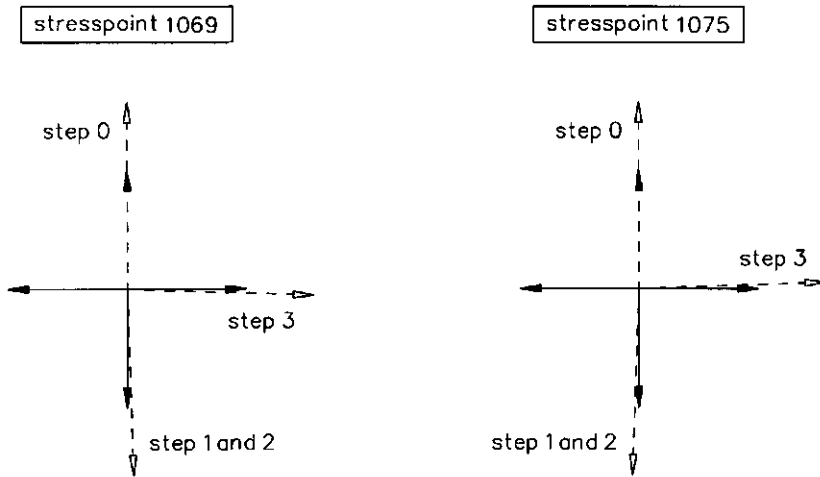
stresspoint 1075

Figure 8.70 Direction of the eigenvector of σ_1 of steps 0 till 3 of stresspoints 1069 and 1075.

According to section 'Determination of the rotation between two vectors' the results of the non-corrected rotation of σ_1-vector are straight forward. With the help of the correction that the rotation between two vectors, corresponding to two following steps, must lie in the interval [-90, 90] degrees, the calculated corrected rotations of σ_1-vector also agree with the earlier-described section.

In prospective of constructing composite quantities, the rotation of the eigenvector of σ_1 plays an important role possibly. However, the results of both the non-corrected as well as the corrected rotation of the eigenvector of σ_1 are not totally satisfying.

In order to get rid of the difference in corrected rotation of the eigenvector σ_1 between two neighbouring points in one step of almost 180 degrees, the absolute value of the calculated corrected rotation of the eigenvector of σ_1 of each step is taken and added up. Result of this procedure is presented in figure 8.71.

$\min \ \Sigma \, abs \ cor \ rot \ ev \ \sigma_1 : 7.78893e{-}1 \ ^{\circ}$
$\max \ \Sigma \, abs \ cor \ rot \ ev \ \sigma_1 : 1.87853e{+}2 \ ^{\circ}$

a)

b)
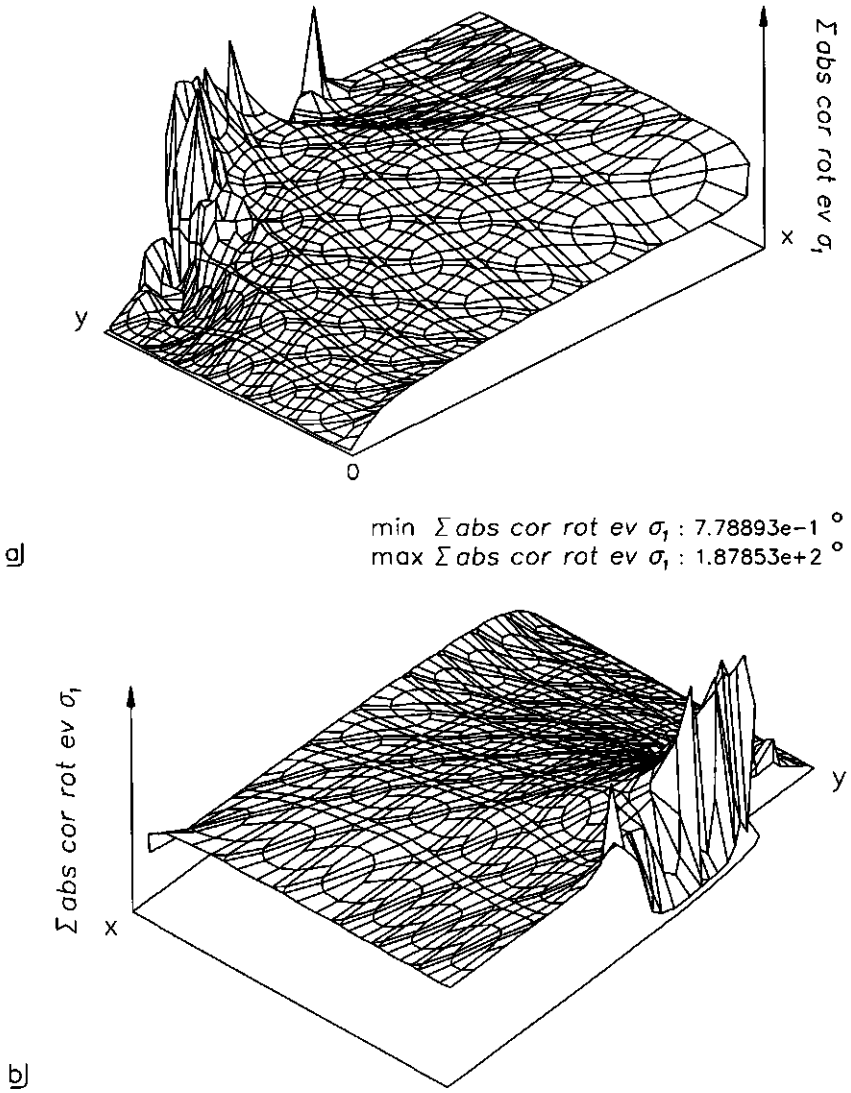
Figure 8.71 Three-dimensional plot, at two different viewpoints, of the
sum of the absolute corrected rotation of the eigenvector of
σ_1 over all steps between 10 and 0 percent strip impression
against the deformed mesh at an impression of the strip of
10 percent (step 33).

Quantities $\Sigma\dot\varepsilon_{xx}$, $\Sigma\dot\varepsilon_{yy}$, $\Sigma\dot\varepsilon_{xy}$, $\Sigma\dot\varepsilon_1$ and $\Sigma\dot\varepsilon_3$

In the following figures 8.72 till 8.77, three-dimensional plots of the summation over all the steps between 10 and 0 percent strip impression of the reference case in case of 5 elementary quantities, $\Sigma\dot\varepsilon_{xx}$, $\Sigma\dot\varepsilon_{yy}$, $\Sigma\dot\varepsilon_{xy}$, $\Sigma\dot\varepsilon_1$ and $\Sigma\dot\varepsilon_3$, and the intermediate stress coefficient b are given.

$$\min \ \Sigma\dot\varepsilon_{xx} \ : \ -2.11843e{-}1$$
$$\max \ \Sigma\dot\varepsilon_{xx} \ : \ \ \ 3.82457e{-}1$$

Figure 8.72 Three-dimensional plot of $\Sigma\dot\varepsilon_{xx}$ over all steps between 10 and 0 percent strip impression against the deformed mesh at an impression of the strip of 10 percent (step 33)

$$\sum \dot{\varepsilon}_{yy}$$

min $\sum \dot{\varepsilon}_{yy}$: $-4.41973e-1$
max $\sum \dot{\varepsilon}_{yy}$: $2.47914e-1$
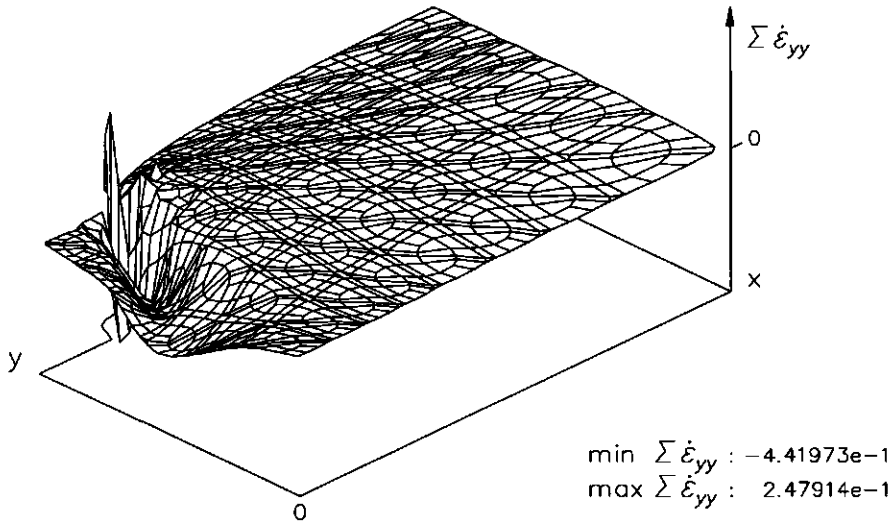
Figure 8.73 Three-dimensional plot of $\sum \dot{\varepsilon}_{yy}$ over all steps between 10 and 0 percent strip impression against the deformed mesh at an impression of the strip of 10 percent (step 33)

$$\sum \dot{\varepsilon}_{xy}$$

min $\sum \dot{\varepsilon}_{xy}$: $-2.56980e-1$
max $\sum \dot{\varepsilon}_{xy}$: 2.26658

Figure 8.74 Three-dimensional plot of $\sum \dot{\varepsilon}_{xy}$ over all steps between 10 and 0 percent strip impression against the deformed mesh at an impression of the strip of 10 percent (step 33)

$$\min \ \Sigma \dot{\varepsilon}_1 : -1.15890$$
$$\max \ \Sigma \dot{\varepsilon}_1 : -2.88472e-3$$

Figure 8.75 Three-dimensional plot of $\Sigma \dot{\varepsilon}_1$ over all steps between 10 and 0 percent strip impression against the deformed mesh at an impression of the strip of 10 percent (step 33)

$$\min \ \Sigma \dot{\varepsilon}_3 : 1.04085e-4$$
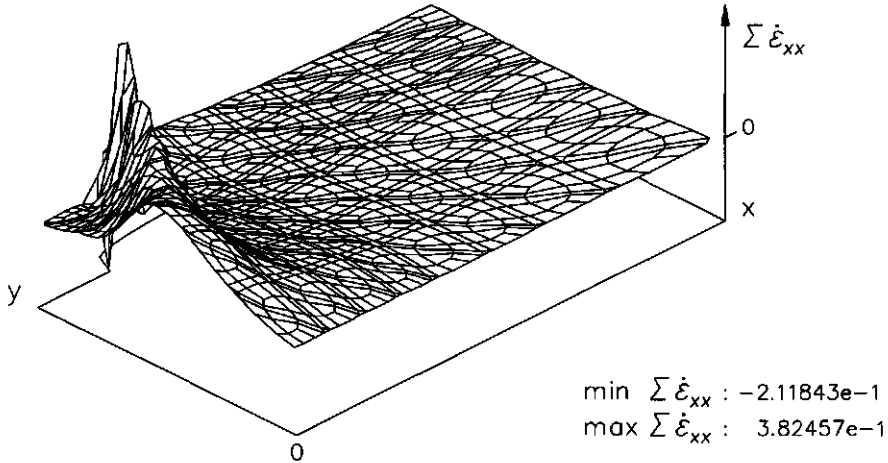$$\max \ \Sigma \dot{\varepsilon}_3 : 1.19497$$
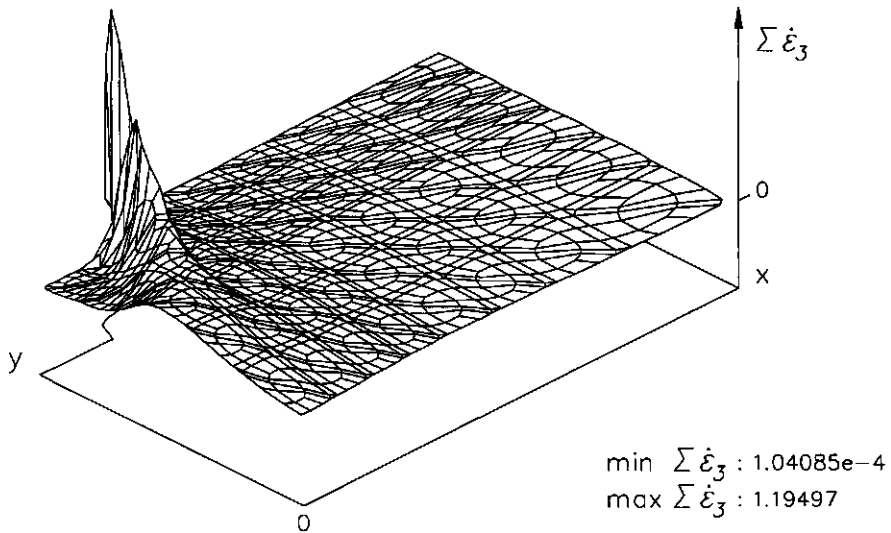
Figure 8.76 Three-dimensional plot of $\Sigma \dot{\varepsilon}_3$ over all steps between 10 and 0 percent strip impression against the deformed mesh at an impression of the strip of 10 percent (step 33)
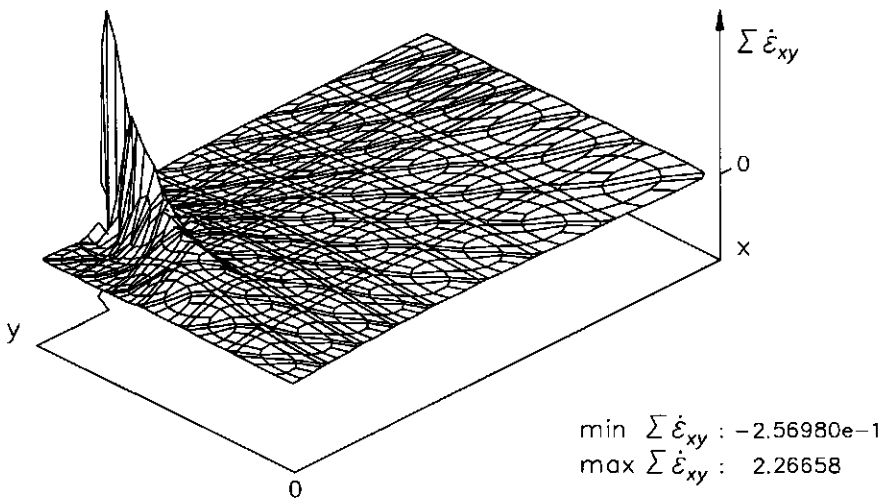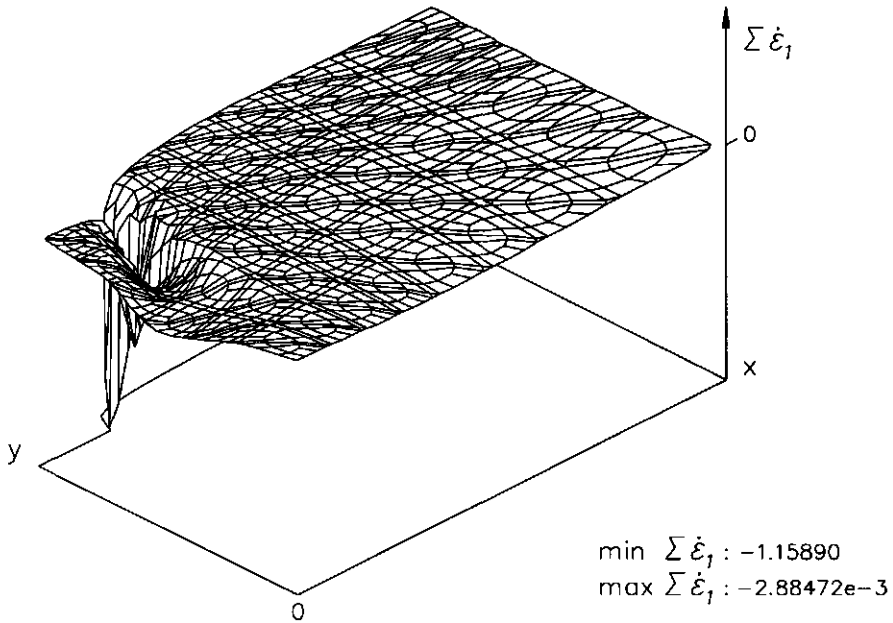
Intermediate stress coefficient b

In figure 8.77 the three-dimensional plot of coefficient b of step 33, corresponding to an impression of the strip of 10 percent (step 33), against the deformed mesh at an impression of the strip of 10 percent is given. This because intermediate stress coefficient b appears regularly in literature in relation to the rotation of σ_1 (for example Yoshimine et al., 1998). The intermediate stress coefficient b is defined as

$$b = \frac{\left(\sigma_2 - \sigma_3\right)}{\left(\sigma_1 - \sigma_3\right)} \tag{8.4}$$

In a certain sense coefficient b represents the influence of the intermediate principal stress σ_2. In the case $b = 0$ both smallest principal stresses, σ_2 and σ_3, equal each other. This situation takes place in a standard triaxial test. In the case $b = 1$ the two larger principal stresses, σ_1 and σ_2, equal each other. This takes place in a triaxial extension test where a pull force to the piston is exerted. Other values of coefficient b can not be adjusted for a tiaxial apparatus. Practically, in case of the considered plane strain situation, coefficient b ranges from 0 till 1. Special case is the situation where coefficient b equals 0.5. Then $\sigma_2 = 0.5 \left(\sigma_1 + \sigma\right)$.

min b : 9.3472e-8
max b : 6.8758e-1
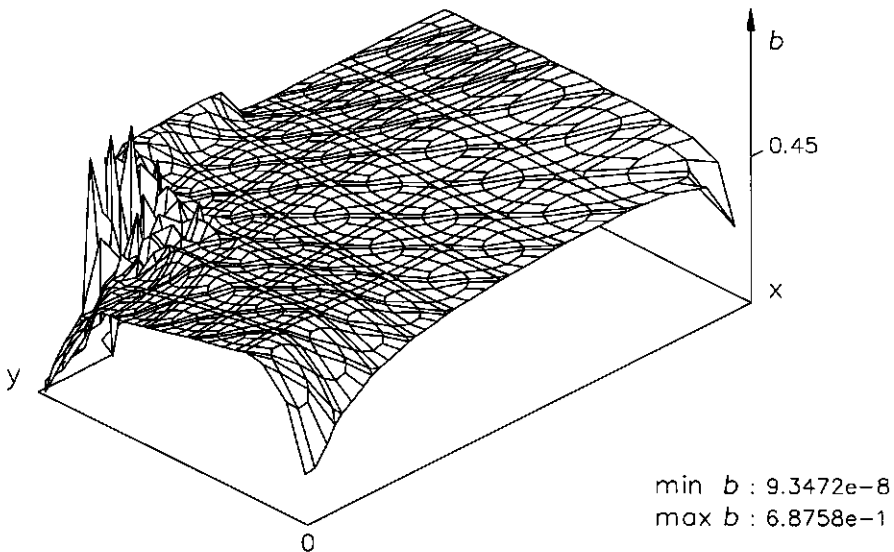
Figure 8.77 Three-dimensional plot of coefficient b at 10 percent strip
impression against the deformed mesh at an impression of
the strip of 10 percent (step 33).

Rotation of the eigenvector of the major total principal strain increment $\dot{\varepsilon}_1$

In figure 8.78, where the sum of the corrected rotation of the eigenvector of the total major principal strain increment $\dot{\varepsilon}_1$ over all steps between 10 and 0 percent strip impression is plotted against the deformed mesh corresponding to an impression of the strip of 10 percent (step 33) of the reference case, two peak values near the axis of symmetry can be detected. The peak with the negative value belongs to stresspoint 103. The existence of non-zero values in the plane of symmetry of the sum of the corrected rotation of the eigenvector of the total major principal strain increment is theoretically unlogical. Therefore there will be zoomed at the peak of stresspoint 103 in detail, followed by a discussion after some theoretical remarks.

$$\min \ \Sigma cor \ rot \ ev \ \dot{\varepsilon}_1 : -8.19840e+1 \ ^\circ$$
$$\max \ \Sigma cor \ rot \ ev \ \dot{\varepsilon}_1 : \ \ \ 1.77393e+2 \ ^\circ$$
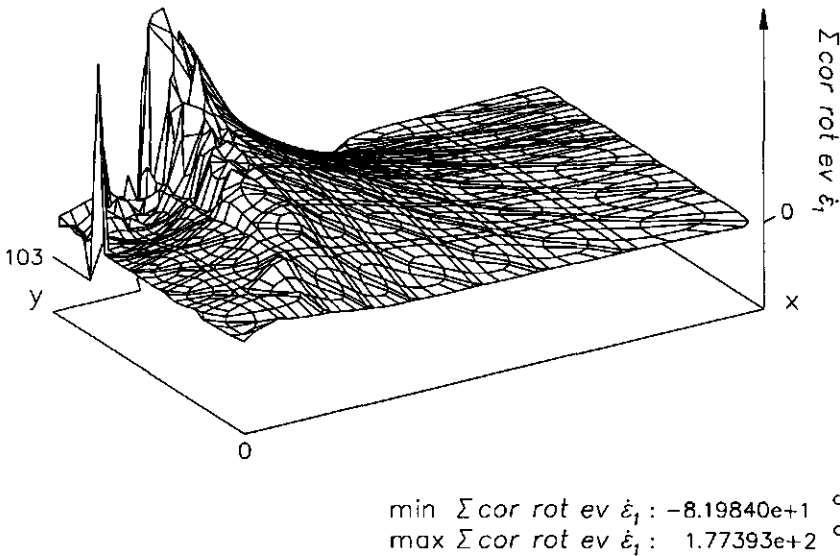
Figure 8.78   Three-dimensional plot of the sum of the corrected rotation of the eigenvector of the total major principal strain increment $\dot{\varepsilon}_1$ over all steps between 10 and 0 percent strip impression against the deformed mesh at an impression of the strip of 10 percent (step 33).

Theory

Dealing with a plane strain situation (in which no plastic volume strain is allowed, $\psi = 0$), and no plastic shear strain occurs, figure 8.79,
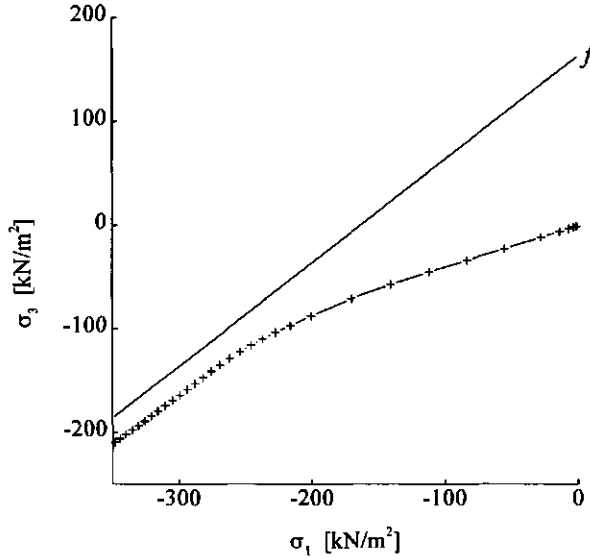
Figure 8.79 Graph of stress path of stresspoint 103 and yield line f in σ_1, σ_3-space.

the following set of elastic equations prevails

$$\dot{\varepsilon}_{xx} = \frac{1}{E}\left(\left(1 - v^2\right)\dot{\sigma}_{xx} - \left(v + v^2\right)\dot{\sigma}_{yy}\right)$$

$$\dot{\varepsilon}_{yy} = \frac{1}{E}\left(\left(1 - v^2\right)\dot{\sigma}_{yy} - \left(v + v^2\right)\dot{\sigma}_{xx}\right) \tag{8.5}$$

$$\dot{\varepsilon}_{xy} = \frac{1}{E}\left(1 + v\right)\dot{\sigma}_{xy}$$

With respect to principal directions equation 8.5 becomes :

$$\dot{\varepsilon}_1 = \frac{1}{E}\left(\left(1 - v^2\right)\dot{\sigma}_1 - \left(v + v^2\right)\dot{\sigma}_3\right)$$
$$\dot{\varepsilon}_3 = \frac{1}{E}\left(\left(1 - v^2\right)\dot{\sigma}_3 - \left(v + v^2\right)\dot{\sigma}_1\right) \tag{8.6}$$

In the elastic region $\dot{\sigma}_{ij}$ gives the directions of the incremental stresses and incremental strains. Presentation of the equations 8.5 and 8.6 as a derived quantity $\dot{\varepsilon}_{xx}/\dot{\varepsilon}_{yy}$ as a function of $\dot{\sigma}_{xx}/\dot{\sigma}_{yy}$ is given at figure 8.80.
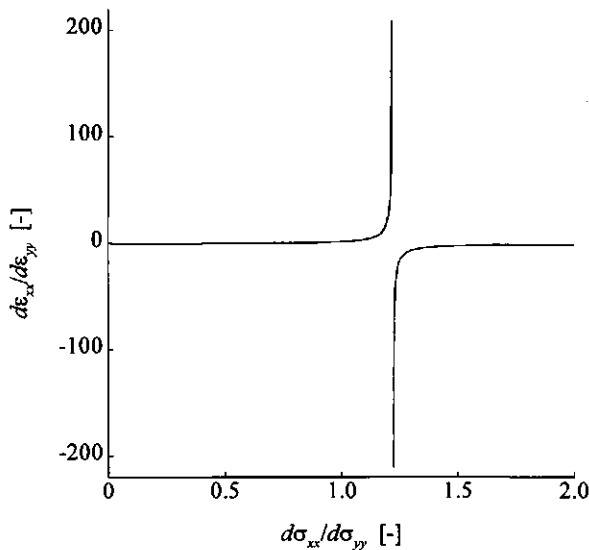
Figure 8.80 Graph of $\dot{\varepsilon}_{xx}/\dot{\varepsilon}_{yy} = f(\dot{\sigma}_{xx}/\dot{\sigma}_{yy})$;
($E = -3.1390e+06$ N/m^2 and $v = 0.45$).

In the cases of the peak values near the axis of symmetry of figure 8.78, $\dot{\sigma}_{xx}/\dot{\sigma}_{yy}$ is varying in the range 0.3-1.05. Plot of this input range of $\dot{\sigma}_{xx}/\dot{\sigma}_{yy}$ against $\dot{\varepsilon}_{xx}/\dot{\varepsilon}_{yy}$ gives figure 8.81.
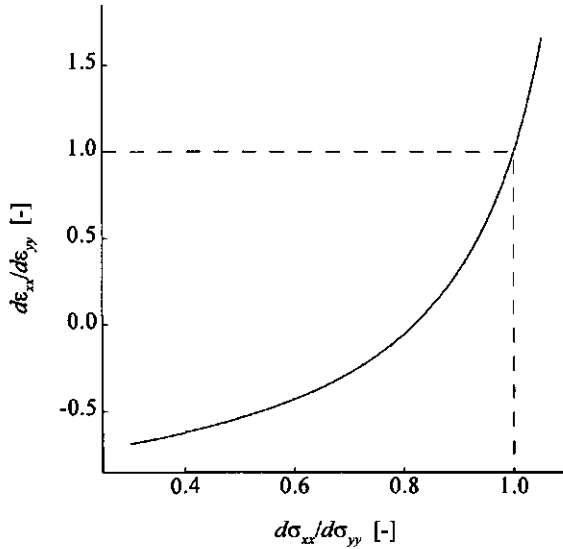
Figure 8.81 Enlarged part of $\dfrac{\dot{\varepsilon}_{xx}}{\dot{\varepsilon}_{yy}} = f\left(\dfrac{\dot{\sigma}_{xx}}{\dot{\sigma}_{yy}}\right)$.

Thus, in cases where $\dot{\sigma}_{xx}$ is the smallest stress increment $\dot{\varepsilon}_{xx}$ is also the smallest strain increment. This means that the eigenvector of the major principal stress increment $\dot{\sigma}_1$ as well as the eigenvector of the major principal strain increment $\dot{\varepsilon}_1$ are located in same regions of the space in figure 8.82.
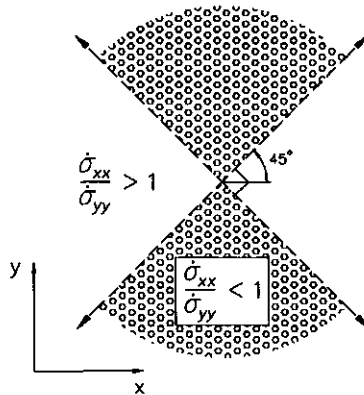
Figure 8.82 Orientation of the eigenvectors of the major principal stress increment $\dot{\sigma}_1$ and the major principal strain increment $\dot{\varepsilon}_1$ in the xy-plane in the case of $\dot{\sigma}_{xx}/\dot{\sigma}_{yy} < 1$, hatched area, and $\dot{\sigma}_{xx}/\dot{\sigma}_{yy} > 1$, blank area.

Discussion of stresspoint 103

There is zoomed in at the negative peak near the axis of symmetry in figure 8.78, stresspoint 103. The corresponding graphs of the stresses and the sum of the corrected rotation of the eigenvector of the major principal stress σ_1 are presented in figure 8.83, the graphs of the stress increments $\dot{\sigma}$ and the sum of the corrected rotation of the eigenvector of the major principal stress increments $\dot{\sigma_1}$ in figure 8.84.
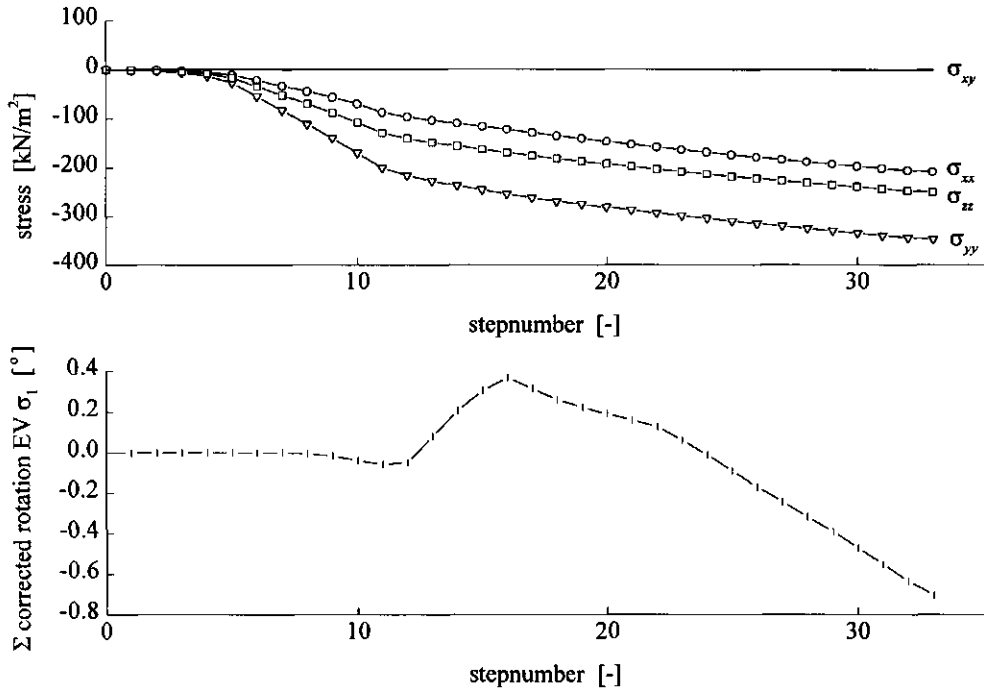
Figure 8.83   Graphs of stresses σ_{xx}, σ_{yy}, σ_{xy} and σ_{zz} and sum of the corrected rotation of the eigenvector of σ_1 against the step number.
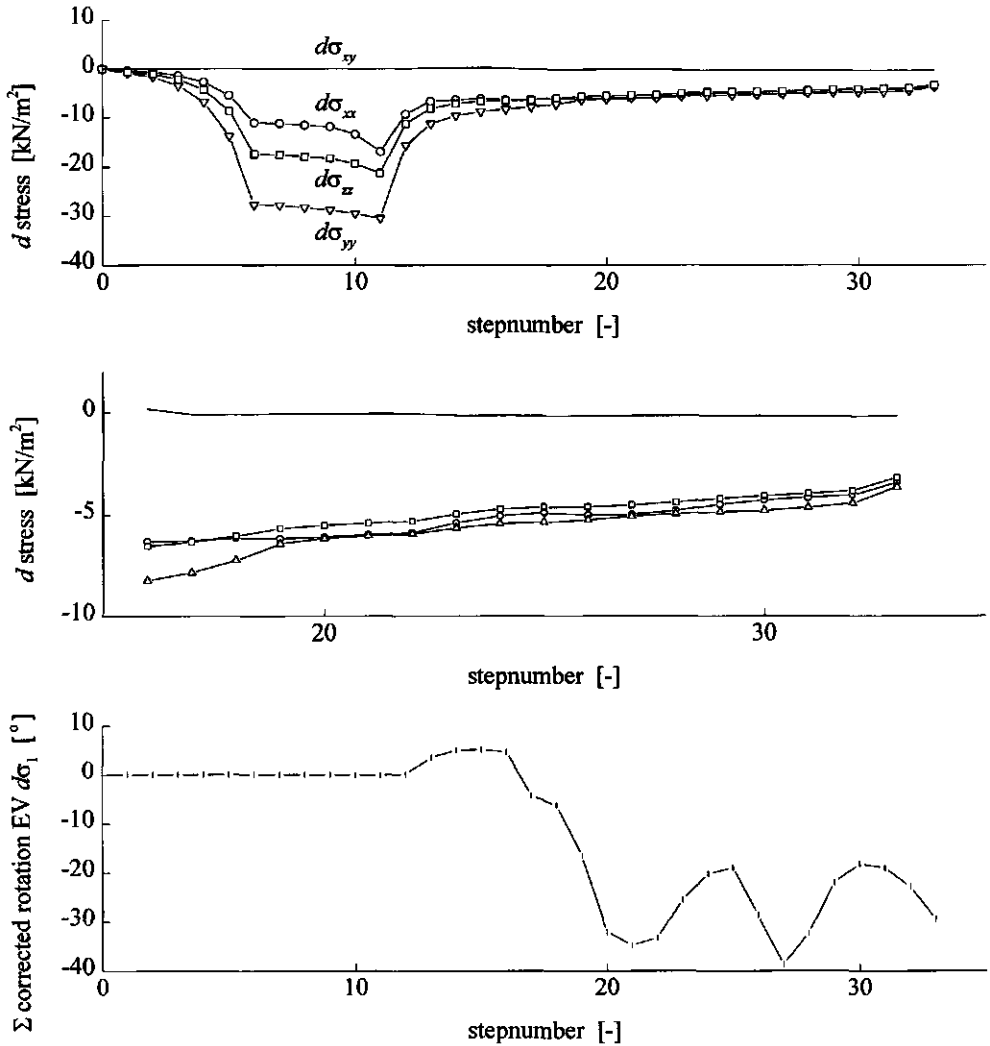
Figure 8.84 Graphs of stress increments $\dot{\sigma}$ (a), enlarged (b) and sum of
            the corrected rotation of the eigenvector of $\dot{\sigma}_1$ (c) against
            the step number.

The most negative stress increments are pointing for each step in the y-direction. Therefore, on the base of figure 8.81, plotting the total strain increments $\dot{\varepsilon}$ against the step number, a graph is expected where the total strain increments in the y-direction are smaller than the total strain increments in the x-direction for each step.
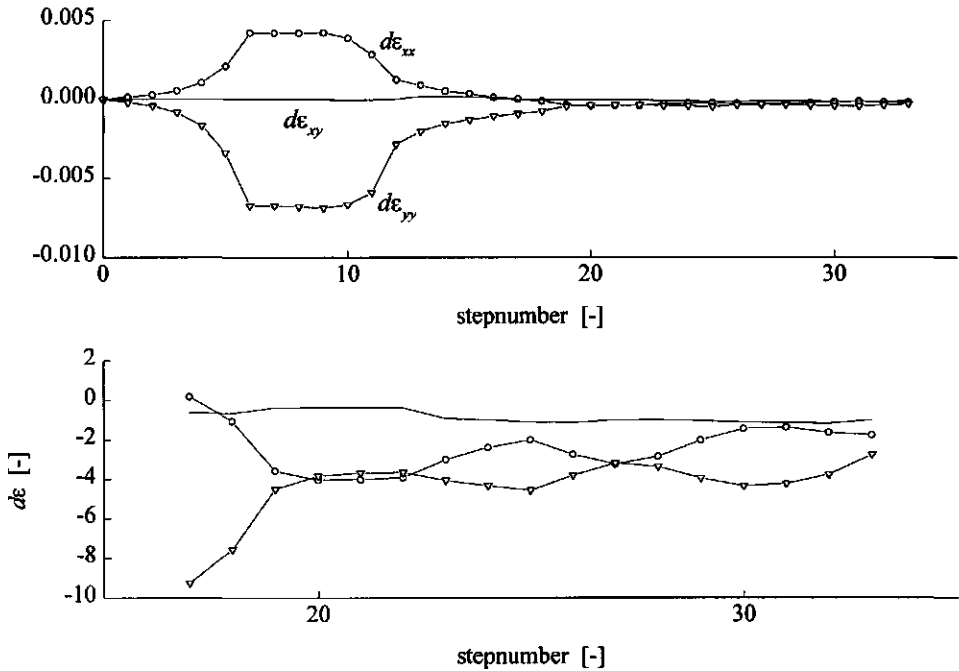
Figure 8.85 Graph of the total strain increment $\dot{\varepsilon}$ (a), enlarged (b) against the step number.

However, the results in figure 8.85 disagree for a few steps with what is expected on basis of the stress increments.

Causes of the negative peak value of stresspoint 103

Probable cause of the negative peak value of the sum of the rotation of the major total principal strain increment of stresspoint 103 is the fact that there has occurred a more or less hydrostatic stress increment situation in three or two dimensions on basis of the principal stress increments.

A hydrostatic stress increment situation in three dimensions may lead to a continuous switch of the direction of the major principal stress increment in the xy-plane and/or between the xy-plane and the z-direction. The same prevails for the direction of the major principal strain increment because the major principal strain increments are derived directly from the principal stress increments.

In a hydrostatic stress increment situation in two dimensions it is only interesting when the major and intermediate principal stress increments equal each other.

In the case of stresspoint 103 a certain three dimensional hydrostatic stress increment situation is reached after step 17 (figure 8.84). Till step 17 there is a tolerable difference between the three stress increments $\dot{\sigma}_{yy}$, $\dot{\sigma}_{zz}$ and $\dot{\sigma}_{xx}$. However in step 17 $\dot{\sigma}_{xx}$ and $\dot{\sigma}_{zz}$ come close together, whereas in step 18 the roles of $\dot{\sigma}_{xx}$ and $\dot{\sigma}_{zz}$ are changed and $\dot{\sigma}_{xx}$ becomes the intermediate stress increment and $\dot{\sigma}_{zz}$ the largest stress increment. In principal stress increment space this means that there must be a turn over of the eigenvector of the minor principal stress increment of the xy-plane into the z-direction and of the eigenvector of the intermediate principal stress increment of the z-direction into the xy-plane between step 17 and 18, figure 8.86. The turn over of the eigenvector of the minor principle stress increment of the xy-plane into the z-direction can be conceived as the beginning of a hydrostatic stress increment situation in this case.
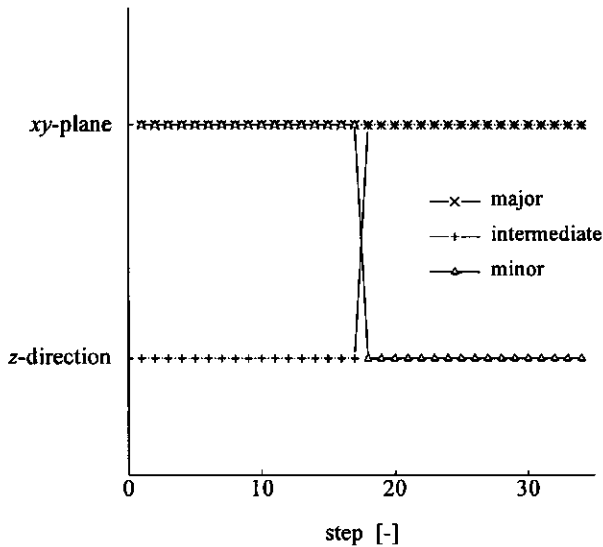
Figure 8.86   Graph of turn over of eigenvectors of principal stress
              increments.

From step 17 the hydrostatic stress increment situation remains, with this difference that $\dot{\sigma}_{yy}$, and $\dot{\sigma}_{xx}$ come sometimes very closely to each other, for example step 20 and 21, however in the absence of switch of roles in order of priority between $\dot{\sigma}_{yy}$ and $\dot{\sigma}_{xx}$.

First effect of the hydrostatic stress increment situation is the fact that the rotation of the eigenvector of the major principal stress increments starts to fluctuate, figure 8.84, which is probably due to the fact of the lower accuracy of the calculated stress increments in such a hydrostatic stress increment situation. That there arises a certain inaccuracy in the calculated stress increments can be derived most simply from the development of the shear stress. Near the axis of symmetry the shear stress should have a constant value near zero. The calculated shear stress shows a fluctuating shear stress, figure 8.87.
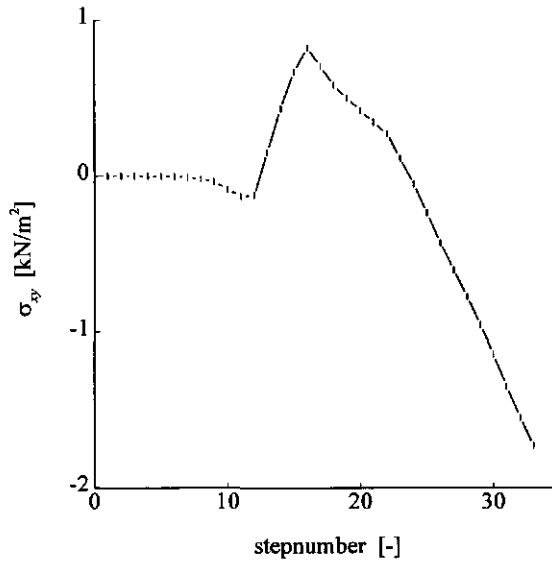
Figure 8.87 Graph of shear stress against the step number.

Effect of a fluctuating shear stress increment on the rotation of the eigenvector of the major principal stress increment at a constant $\dot{\sigma}_{xx}$, $\dot{\sigma}_{yy}$ and $\dot{\sigma}_{zz}$ is given at figure 8.88. In this graph the values of $\dot{\sigma}_{xx}$, $\dot{\sigma}_{yy}$ and $\dot{\sigma}_{zz}$ of step 16 are taken as the values of $\dot{\sigma}_{xx}$, $\dot{\sigma}_{yy}$ and $\dot{\sigma}_{zz}$ for each step of this graph, while $\dot{\sigma}_{xy}$ is fluctuating as for stresspoint 103, figure 8.84a.
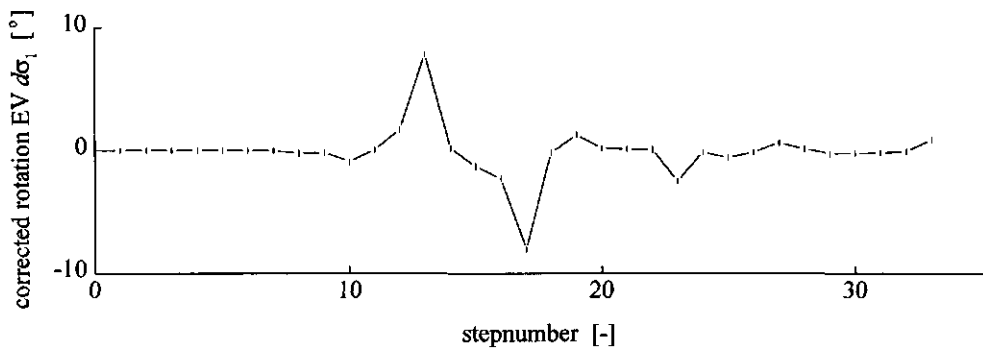
Figure 8.88 Graph of the rotation of the eigenvector of the major principle stress increment $\dot{\sigma}_1$ against the step number by a changing shear stress increment $\dot{\sigma}_{xy}$.

Second effect is the fluctuation of the rotation of the eigenvector of the principal strain increments. The fluctuation of the rotations of the eigenvector of the principal strain increments, figure 8.89, is expected to be the same as the fluctuations of the rotations of the

eigenvector of the principal stress increments, figure 8.84, because it is an elastic calculation. Although, the shape of the fluctuation of the rotations of the eigenvector of the major principal strain increments is more or less the same as the fluctuation of the rotations of the eigenvector of the major principal stress increments, the magnitude is different.
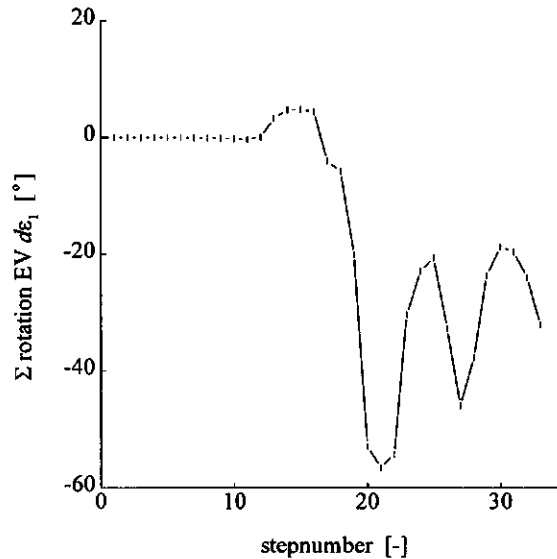
Figure 8.89 Graph of sum of the corrected rotation of the eigenvector of the major total principal strain increment $\dot{\varepsilon}_1$ against the step number.

Probably this is due to the fact that the calculated strain quantities of the nodes can not be interpolated precisely to the stresspoints.

Resuming it must be emphasised that when a certain hydrostatic stress increment situation occurs, the rotations of the eigenvector of the major principal stress increments and the major principal strain increments start to fluctuate which leads to the result that the peak value of the sum of the rotations of the eigenvector of the major principal strain increment $\dot{\varepsilon}_1$ becomes strongly arbitrarily and depends on the step number. For instance, when figure 8.78 would have been made for step 21, the sum of the rotation of the major total principal strain increments $\dot{\varepsilon}_1$ for stresspoint 103 would have been -57 degrees.

Composite quantities, called kneading numbers

Subjecting soil to loading processes and/or prescribed displacements finally results into a change of micro-factors of the soil. By micro-factors is meant the amount and distribution of water, solid parts or bounds (not arising from the soil water) between these solid parts in the soil. Derivatives of the micro-factors are the so-called soil qualities. Soil qualities are understood to mean properties like :
- coefficient of oxygen diffusion
- coefficient of water permeability
- moisture characteristic
- root penetration resistance
- coefficient of heat conductivity.

Seeds and plants react almost immediately on changes of soil qualities. However, changes of single quantities, i.c stress and strain, do not uniquely explain the changes of soil qualities one to one (Dawidowski et al., 1990, Lerink, 1990 and Steinbusch, 1993).

A parallel to the above-mentioned can be found in the case of trying to explain the cause of compaction of agricultural soils. By soil compaction, the state of compactness of the soil increases under the influence of a certain treatment, for instance a loading process caused by a tyre. Research led to the conclusion that single quantities, in this case the largest principal stresses and stress invariants, did not lead to unique relations with measured soil compaction.

Back to the loading process with the prescribed displacement of the strip of the reference soil treated in this thesis. In view of conclusions of Dawidowski et al., 1990, Lerink, 1990 and Steinbusch, 1993, that changes of single quantities do not uniquely explain the changes of soil qualities one to one, composite quantities are presented in this section. Composite quantities can be constructed of principal stresses, principal stress increments, principal strains, principal strain increments, the rotation of the principal directions of these quantities and the rigid body rotation. From now on the composite quantities are called kneading numbers, because the whole treatment process under the strip of the reference soil can be imagined by kneading of clay for instance. Furthermore, by constructing kneading numbers one must keep in mind that these values should be defined in such a way that the changes of these kneading numbers reasonably correlate with the changes of soil qualities. Unfortunately, the correlation between the kneading numbers and soil qualities is beyond the scope of these dissertation.

Basic of constructing kneading numbers is trying to imagine what is happening in an infinitesimal soil cube somewhere under the strip of the reference case. The term kneading represents the process that principal directions of stresses and strains in the material under consideration rotate in time, simultaneously with a possible change of shape and/or volume. Final purpose for the future is to describe the kneading process with the help of kneading numbers. At this stage and within the scope of this thesis, some items are presented which can serve as building blocks for the construction of kneading numbers. Simultaneously, there are also given some literature statements which refer to a specific building block for the construction of kneading numbers.

Building blocks :
- rigid body rotation
  - according to chapter 2 a treatment of an infinitesimal soil cube can be split up in four elemental reactions; one of these reactions is the rigid body rotation which can change during different steps of the strip impression
  - particle rotation, on average, takes place in parallel with the corresponding macroscopic rotation in the continuum sense; in other words, the mean particle rotation is not independent of the macroscopic rotation, in case of dense granular materials (Oda & Kazama, 1998)
- principal strain increments and corresponding principal directions
  - during the impression of the strip into the soil, the principle strain increments can be calculated; moreover, the directions of the eigenvectors of these strain increments change most of the time during the impression of the strip
  - there is a stress path dependency of strain (Matsuoka et al., 1989)
  - continuous rotation of the principal axis of strain means that a material direction is periodically loaded and unloaded; this fact enables easier changes in the structure of granular material and implies a general tendency for compaction (Joer et al., 1998)
- principal stresses and corresponding principal directions
  - the influence of stress rotation gives a faster degradation of the clay structure; the natural response to loading depends on the orientation of the principal stresses during strain (Hicher & Taghzouti, 1995 and Hicher & Lade, 1987)
  - settlement and lateral displacement under a strip are significantly influenced by principal stress rotation (Matsuoka et al., 1989)
  - if the stress state circles a couple of times along a Mohr's stress circle, rather large plastic strains are observed under the principal stress rotation with constant principal stresses (Matsuoka et al., 1990)
  - in cyclic tests, the influence of stress rotation in torsion shear tests was clearly evident in the faster degradation of the clay structure resulting in larger pore pressures and greater strains than in tests without stress rotation (Hicher & Lade, 1987)
  - for any density of sand, a larger α-value (a larger inclination of σ_1 from the vertical) and a larger intermediate principal stress coefficient b generated greater pore water pressure (Yoshimine et al., 1998).

Taking into account the above items means that kneading numbers are a composition of single quantities, quantities that are described, in great detail sometimes, in this chapter. Measurements give raise to the idea that a change of soil qualities in wet clayey material occurs under the influence of relatively high principal stresses (Lerink, 1990, and Steinbusch, 1993).

Therefore, taking the earlier-mentioned into consideration, a set of possible kneading numbers is presented, with increasing complexity :
- $\Sigma\,(\sigma_1 \cdot \dot{\varepsilon}_1)$
- $\Sigma\,(\sigma_1 \cdot |$ corrected rotation of the eigenvector of $\sigma_1 \,| \cdot \dot{\varepsilon}_1)$
- $\Sigma\,(\dot{\sigma}_1 \cdot |$ corrected rotation of the eigenvector of $\dot{\sigma}_1 \,| \cdot \dot{\varepsilon}_1)$
- $\Sigma\,($corrected rotation of the eigenvector of $\dot{\varepsilon}_1$ − rigid body rotation$)$
- $\Sigma\,(\sigma_1 \cdot ($corrected rotation of the eigenvector of $\dot{\varepsilon}_1$ − rigid body rotation$))$

$\underline{\Sigma\,(\sigma_1 \cdot \dot{\varepsilon}_1)}$

The given kneading number in figure 8.90 is based on σ_1, figure 8.63, and $\dot{\varepsilon}_1$, figure 8.75. It must be stated that the peak in this figure is primarily due to the plastic principal stress increment $\dot{\varepsilon}_1^p$.
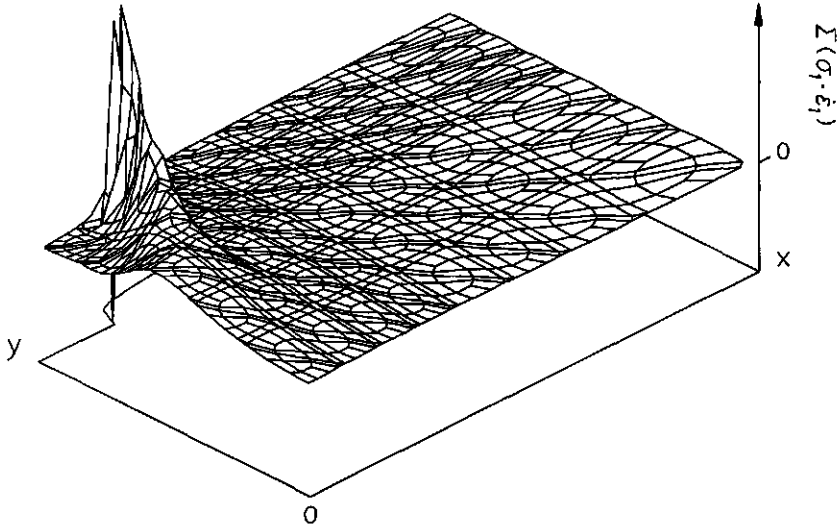
$$\min\ \Sigma\,(\sigma_1 \cdot \dot{\varepsilon}_1) : -1.33179e+5\ \ N/m^2$$
$$\max\ \Sigma\,(\sigma_1 \cdot \dot{\varepsilon}_1) : \ \ 2.55593e+5\ \ N/m^2$$

Figure 8.90   Three-dimensional plot of $\Sigma\,(\sigma_1 \cdot \dot{\varepsilon}_1)$ over all steps between 10 and 0 percent strip impression against the deformed mesh at an impression of the strip of 10 percent (step 33).

$\underline{\Sigma\,(\sigma_1\cdot|\,\text{cor rot EV }\sigma_1\,|\cdot\dot\varepsilon_1)}$

Extension of the kneading number $\Sigma\,(\sigma_1\cdot\dot\varepsilon_1)$, figure 8.90, with the absolute corrected rotation of the eigenvector of σ_1 gives the kneading number $\Sigma\,(\sigma_1\cdot|\,\text{cor rot EV }\sigma_1\,|\cdot\dot\varepsilon_1)$, which is given in figure 8.91.
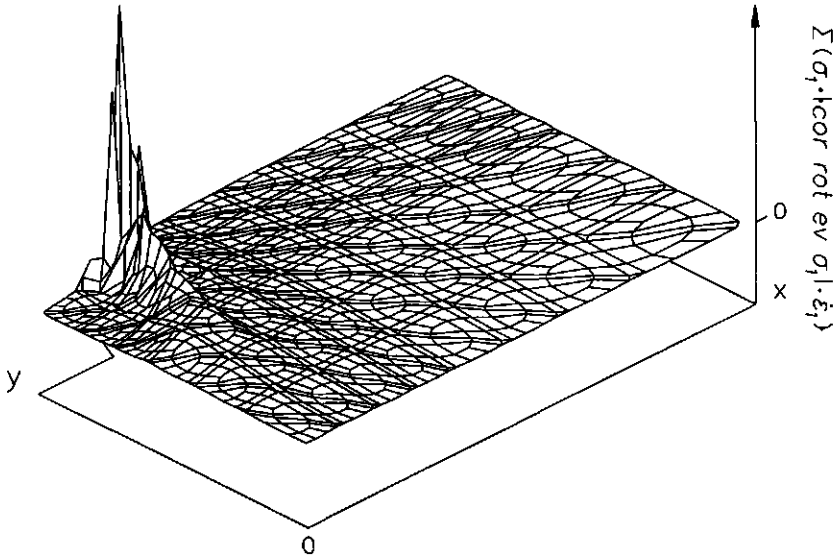
$$\min\ \Sigma(\sigma_1\cdot|cor\ rot\ ev\ \sigma_1|\cdot\dot\varepsilon_1):\ -9.39256e+1\ ^\circ\,N/m^2$$
$$\max\ \Sigma(\sigma_1\cdot|cor\ rot\ ev\ \sigma_1|\cdot\dot\varepsilon_1):\ \ \ 3.54016e+5\ ^\circ\,N/m^2$$

Figure 8.91 Three-dimensional plot of $\Sigma\,(\sigma_1\cdot|\,\text{cor rot EV }\sigma_1\,|\cdot\dot\varepsilon_1)$ over all steps between 10 and 0 percent strip impression against the deformed mesh at an impression of the strip of 10 percent (step 33).

$$\Sigma \, (\dot{\sigma}_1 \cdot | \text{cor rot EV } \dot{\sigma}_1 \, | \cdot \dot{\varepsilon}_1 \,)$$

This kneading number contains the same information as the kneading number $\Sigma \, (\sigma_1 \cdot | \text{cor rot EV } \sigma_1 \, | \cdot \dot{\varepsilon}_1 \,)$, but presented at a different way. Difference is that all the components of the kneading number are based on increments now, figure 8.92.

Comparing the kneading number $\Sigma \, (\sigma_1 \cdot | \text{cor rot EV } \sigma_1 \, | \cdot \dot{\varepsilon}_1 \,)$ and the kneading number $\Sigma \, (\dot{\sigma}_1 \cdot | \text{cor rot EV } \dot{\sigma}_1 \, | \cdot \dot{\varepsilon}_1 \,)$ shows that the peak region near the edge of the strip can be detected in both figures. What is attracting attention in case of kneading number $\Sigma \, (\dot{\sigma}_1 \cdot | \text{cor rot EV } \dot{\sigma}_1 \, | \cdot \dot{\varepsilon}_1 \,)$ are the number of peaks near the axis of symmetry which do not exist in case of kneading number $\Sigma \, (\sigma_1 \cdot | \text{cor rot EV } \sigma_1 \, | \cdot \dot{\varepsilon}_1 \,)$. Peaks near the axis of symmetry where also found by quantity $\Sigma \, (\text{cor rot EV } \dot{\varepsilon}_1 \,)$. Aspects of the theoretical discussion there, i.c. the hydrostatic stress increment situation, can usefully be applied to explain parts of the peaks near the axis of symmetry in case of the kneading number $\Sigma \, (\dot{\sigma}_1 \cdot | \text{cor rot EV } \dot{\sigma}_1 \, | \cdot \dot{\varepsilon}_1 \,)$.
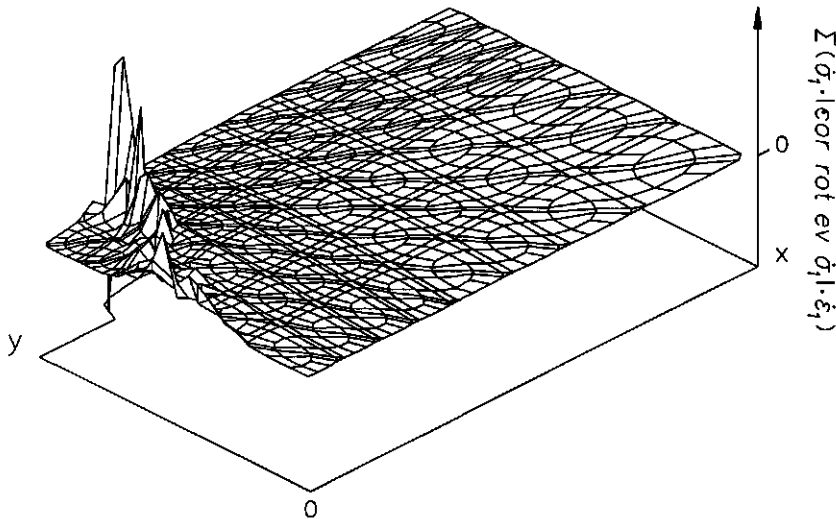
$$\min \; \Sigma(\dot{\sigma}_1 \cdot | \text{cor rot ev } \dot{\sigma}_1 | \cdot \dot{\varepsilon}_1) : \; -7.61810e+4 \;\; ^\circ \, N/m^2$$
$$\max \; \Sigma(\dot{\sigma}_1 \cdot | \text{cor rot ev } \dot{\sigma}_1 | \cdot \dot{\varepsilon}_1) : \;\;\; 1.05589e+5 \;\; ^\circ \, N/m^2$$

Figure 8.92   Three-dimensional plot of $\Sigma \, (\dot{\sigma}_1 \cdot | \text{cor rot EV } \dot{\sigma}_1 \, | \cdot \dot{\varepsilon}_1 \,)$ over all steps between 10 and 0 percent strip impression against the deformed mesh at an impression of the strip of 10 percent (step 33).

$\underline{\Sigma \text{ (cor rot EV } \dot{\varepsilon}_1 - \text{rigid body rotation)}}$

This kneading number is given because a cubical soil element can endure a difference in rotation of the eigenvector of $\dot{\varepsilon}_1$ on the one hand and a rigid body rotation on the other, figure 8.93. Importance of this kneading number will increase in those cases where the rigid body rotation is relatively large in comparison to the corrected rotation of the eigenvector of $\dot{\varepsilon}_1$.
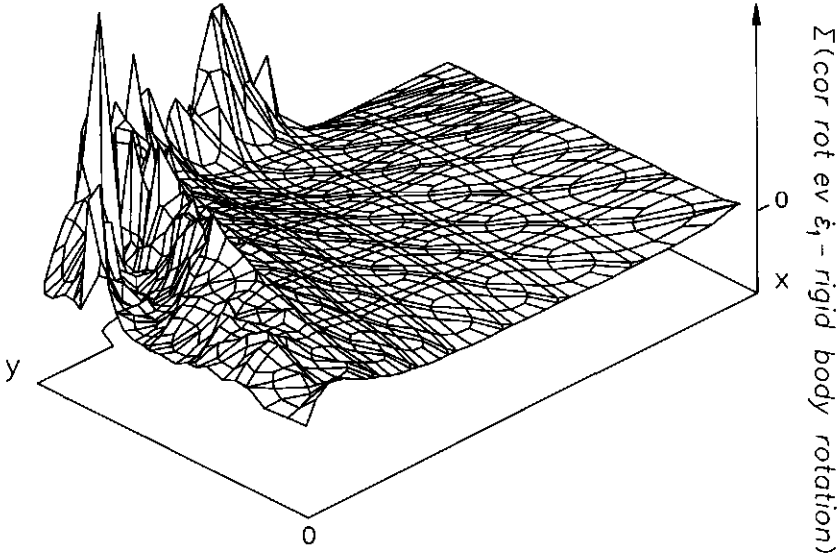
min $\Sigma(cor\ rot\ ev\ \dot{\varepsilon}_1 - rigid\ body\ rotation)$: 3.86080e-2 $^\circ$
max $\Sigma(cor\ rot\ ev\ \dot{\varepsilon}_1 - rigid\ body\ rotation)$: 3.68256e+2 $^\circ$

Figure 8.93   Three-dimensional plot of Σ (cor rot EV $\dot{\varepsilon}_1$ – rigid body rotation) over all steps between 10 and 0 percent strip impression against the deformed mesh at an impression of the strip of 10 percent (step 33).

$\Sigma\,(\sigma_1 \cdot (\text{cor rot EV }\dot{\varepsilon}_1 - \text{rigid body rotation}))$

This kneading number is an extension of the given kneading number $\Sigma\,(\text{cor rot EV }\dot{\varepsilon}_1 - \text{rigid body rotation})$, figure 8.93, with the quantity σ_1, figure 8.63. The former gives a spiky view in the region under the strip and besides the strip. The latter gives a reasonable smooth view of the development of σ_1, except in the direct neighbourhood of the strip. Figure kneed5 that is based on the development of above-mentioned quantities, gives some unexpected results, namely an overall view of the development of kneading number $\Sigma\,(\sigma_1 \cdot (\text{cor rot EV }\dot{\varepsilon}_1 - \text{rigid body rotation}))$ which is reasonable smooth in the absence of the spiky region beside the strip. Thus, here is shown that combination of two quantities with a spiky development, not necessarily means that the arising quantity has also a spiky development.
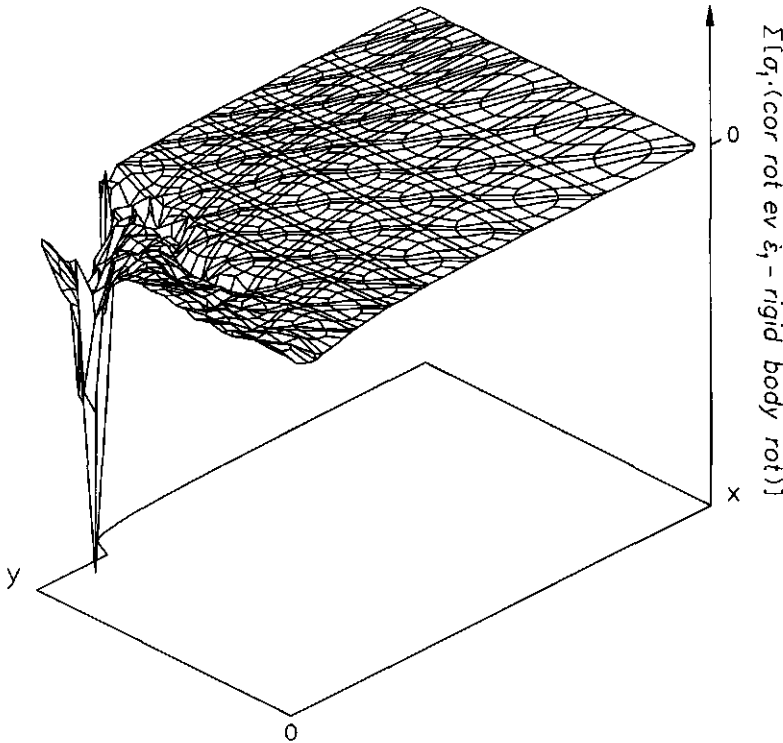
min $\Sigma[\sigma_1 \cdot (cor\ rot\ ev\ \dot{\varepsilon}_1 - rigid\ body\ rot)]$: $-1.30594e{+}8$ $^{\circ}$ N/m^2
max $\Sigma[\sigma_1 \cdot (cor\ rot\ ev\ \dot{\varepsilon}_1 - rigid\ body\ rot)]$: $7.56283e{+}6$ $^{\circ}$ N/m^2

Figure 8.94   Three-dimensional plot of $\Sigma\,(\sigma_1 \cdot (\text{cor rot EV }\dot{\varepsilon}_1 - \text{rigid body rotation}))$ over all steps between 10 and 0 percent strip impression against the deformed mesh at an impression of the strip of 10 percent (step 33).

From all the given figures of single quantities in this chapter it can be concluded that specific regions can be detected where the spikyness of a quantity is the greatest. Complicating is the fact that the spiky regions differ between different single quantities. The same prevails for the composite quantities, the kneading numbers. In the best case, the region(s) of spikyness of the kneading number coincide with earlier-found region(s) of spikyness of single and composite quantities. In the worst case the region(s) of spikyness of those quantities do not cover each other.

This all gives raise to the concept of defining at least two domains. One domain where the quantities, single or composite, will be considered and can be useful to expand knowledge about kneading of the soil. In the remaining domain(s), the quantities can only be presented or omitted.

So, it depends on the case and the quantity under consideration of that specific case, how useful domains look like. The fact that in this dissertation only one reference case is treated with several quantities and associated specific domain subdivisions, means that a general subdivision of the (deformed) mesh into useful domains cannot be given.

9 Discussion and conclusions

In this dissertation the agricultural tyre-soil interaction is simplified and simulated as an impression of a strip into the soil. Simulation calculations are carried out on base of the finite element program Plaxis, using the elastic-perfectly-plastic Mohr-Coulomb model. This model is preferred above a more sophisticated cap-hardening model because in this dissertation is primarily focussed on treatment and stress analysis.

Characteristic of a wet moderately heavy river clay is the presence of an amount of entrapped air. Derivation of values for the soil model parameters E and υ is given in detail in case of the above-mentioned soil, because little is known about values of these parameters (Van den Akker, 1998). Also a detailed derivation is given of the soil model parameter C_p, which is related to the elastic region of the Plaxis-Cap model, because theoretical derivation of values for this specific parameter gives difficulties in common research practice. By derivation of values for the soil model parameters, little concern is given to the accuracy of the values, because in practice it is more important to be able to derive values of soil model parameters that play a main role, than concerning about accuracy of values of all required parameters.

A severe challenge of the developed treatment and stress analysis program Trestana, is how to carefully handle the large amount of generated data without loosing information through the use of smoothing procedures. Characteristic of Trestana is that a specific quantity is represented as height against the deformed mesh as ground surface. Representation of quantities is possible to and from all possible directions. Disadvantage of the program is the fact that it takes a reasonable amount of time to make it suitable for other geometry's than used in the reference case. Furthermore, visualisation of a specific quantity as height against a deformed mesh, is strong when using automatic mesh generation procedures of the finite element program. On the other hand, interpretation of the visualisation can be improved conceivably, if, together with the three-dimensional surface, iso-lines are presented at the ground surface.

Soil-tyre interaction is playing a key role in agriculture. Modelling this interaction with a finite element program shows that this still remains complicated. Progress can be made with other boundary conditions in combination with the use of interface elements. However, development of the investigated quantities in the neighbourhood of the end of the strip shows still an undesirable spikyness.

The most important region of interest in agriculture is the region under the tyre. So, the proposed subdivision of the calculated output into domains of different importance, is useful. For the most important domain of the given reference case, i.e. the whole cross-section excluded the region near the end of the strip, building blocks for constructing so-called kneading numbers are given. Rotations of principal directions are possibly key controlling factors in case of kneading. The presented summation of the absolute corrected rotation of the eigenvector corresponding to σ_1 seems suitable. In case of the sum of the corrected rotation of the eigenvector corresponding to $\dot{\varepsilon}_1$, one must be aware of the occurrence of incremental hydrostatic stress situations in combination with a fluctuating shear stress near the axis of symmetry. A possible cause of this discrepancy is the fact that displacements, which are

calculated in the nodes, are interpolated at the stresspoints. However, the location of the nodes and stresspoints is not identical. Decreasing this noise might be reached by refining the mesh with more finite elements. In that case the locations of the nodes and stresspoints better coincide. This increases the importance of the sum of the corrected rotation of the eigenvector corresponding to ε_1 as building block.

Presentation of building blocks to construct kneading numbers on base of composite quantities, give raise to the idea of expanding possibilities of this concept. Although single quantities are relatively spiky, a composite quantity can be constructed with a reasonable smooth development. This indicates that progress can be made in the search for useful kneading numbers.

Although it should be stated here that it is still a long way from predicting the change of soil qualities on base of theoretically kneading numbers. Visualisation of quantities in cross-section, theoretical explanation of rarities and careful constructing composite quantities are only a starting point in the attempt to gain more insight in the process of kneading of agricultural soil. The next step should be the investigation, generation and analysis of kneading numbers, conceivably on base of alternative soil models, followed by considering these numbers in relation to soil qualities determined at relevant locations of soil loading processes.

Finally, it is not unlikely that parts of the presented building blocks for the pursued kneading process can also serve for getting grip on the so-called smear effect, e.g. during drainage and pipe laying activities in agricultural and civil engineering.

Sign convention and notation

A rectangular Cartesian coordinate system is used. Tensile stresses, tensile strains and anticlockwise rotation are taken as positive, figure A.1.
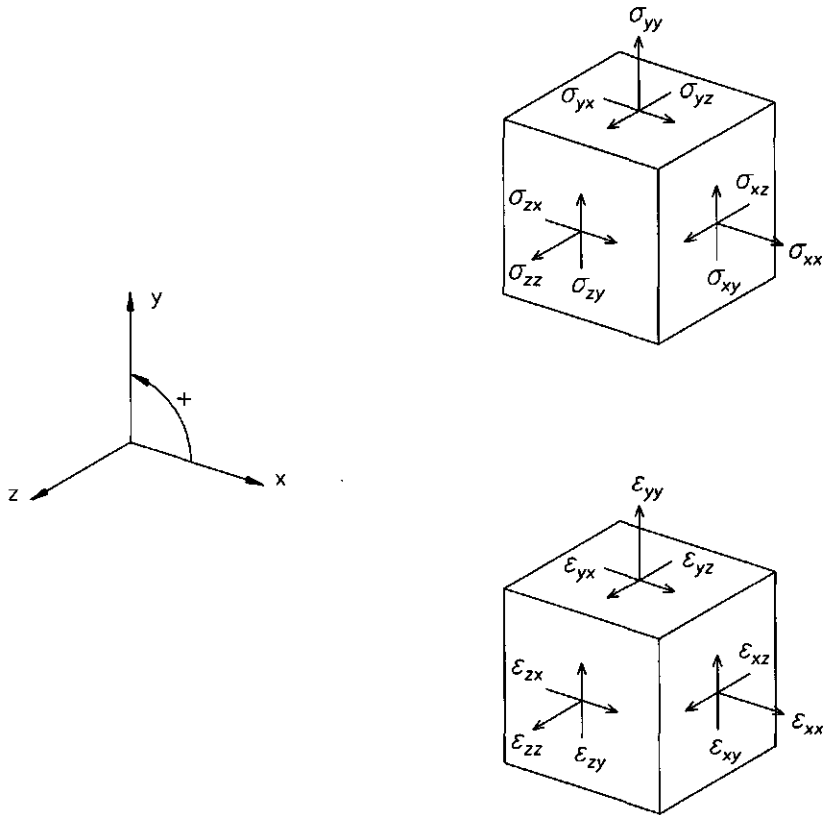
Figure A1 Positive coordinate system and sign convention for
rotation, stresses and strains.

A single underscore is used to identify a column vector. A dot above a symbol or the letter d written in italics (d) in front of the symbol indicates that it all took place in a small time step, e.g. time-derivative (rate) of a particular quantity. For example a stress increment : $\dot{\sigma}$ or $d\sigma$.

A global list of symbols is not included because several symbols have more than one meaning. Instead, symbols are defined when they first appear.

References

- J.J.H. van den Akker, J. Avidsson and R. Horn (eds.), 1998. Experiences with the impact and prevention of subsoil compaction in the European community. Part 1 and 2. Proceedings of the first workshop of the concerted action on subsoil compaction, 28-30 may, 1998, Wageningen, The Netherlands, pp. 278
- Atkinson, J.H. and P.L. Bransby, 1978. The mechanics of soils. McGraw-Hill, London, pp. 373
- Bekker, M.G., 1956. Theory of land locomotion. Ann Arbor : University of MichiganPress, pp. 520
- Bonnier, P.G, 1993. Testing, modelling and numerical analysis of the mechanical behaviour of bituminous concrete. Dissertation, Delft University of Technology, pp. 162
- Butterfield, R. and K.Z. Andrawes, 1972. On the angles of friction between sand and plane surfaces. J. of Terramechanics 8(4) : 15-23
- Chancellor, W.J. and R.H. Schmidt, 1962. Soil deformation beneath surface loads
- Chancellor, W.J., R.H. Schmidt and W. Söhne, 1962. Laboratory measurement of soil compaction and plastic flow. Transactions of the ASAE, 235-239
- Chancellor, W.J. and S.K. Upadhyaya. Effects of stability mechanisms during triaxial tests of cylindrical soil samples on stress ratio vs. strain ratio relations. Transactions of the ASAE, pp. 240-249
- Chancellor, W.J. and J.A Vomocil, 1985. Stress and energy characteristics of agricultural soils during deformation and failure. Int. Conference on Soil Dynamics. Procedings Vol 2, Auburn, Alabama. June, 1985, pp. 225-240
- Chen, W.F., 1975. Limited analysis and soil plasticity. Elsevier, Amsterdam, pp. 638
- Dawidowski, J.B. and A.J. Koolen, 1987. Changes in soil water suction, conductivity and dry strenght during deformation of wet undisturbed samples. Soil & Tillage Research, 9 : 169-180
- Dawidowski, J.B., P. Lerink and A.J. Koolen, 1990. Controlled distortion of soil samples with reference to soil physical effects. In : Soil and Tillage Research, Vol. 17 (1990), pp. 15-30
- El-Domiaty, A.M. and W.J. Chancellor, 1970. Stress-strain characteristics of a saturated clay soil at various rates of strain. Transactions of the ASAE, pp. 685-689
- Fountaine, E.R. and P.C.J. Payne, 1954. Causes of non-scouring in soil working implements. 5th Int Cong Soil Sci Trans, Leopoldville, vol 2, pp. 35-45
- Ford, H., 1963. Advanced mechanics of materials. Longmans, Green and Co LTD, London, pp. 672
- Fung, Y.C., 1965. Foundations of solid mechanics. Prentice-Hall, Inc., New Jersey, pp. 525
- Gill, w.R. and G.E.Van den Berg, 1967. Soil dynamics in tillage and traction
- Goldscheider, R., 1982. True triaxial tests on dense sand. In : Results of the International Workshop on Constititive Relations for Soils / Grenoble / 6-8 September, pp. 11-54
- Golub, G.H and C.F. van Loan, 1989. Matrix computations. Johns Hopkins University, Baltimore, pp. 642

- Hicher P.Y and P.V. Lade, 1987. Rotation of principal directions in K_0-consolidated clay. In : Journal of geotechnical engineering, Vol. 113, No. 7, pp 774-788
- Hicher, P.Y. and A. Taghzouti, 1995. 3D cyclic behavior of saturated clay. Earthquake Geotechnical Engineering, pp. 271-276, Balkema
- Houtman, H.J., 1977. Trafficability of agricultural soil. Unpublished MSc. thesis, WAU Wageningen, pp. 48 (in dutch)
- Huizinga, T.K.,1969. Grondmechanica. Elsevier, Amsterdam, pp 291 (in dutch)
- Hunter, S.C. 1983. Mechanics of continuous media. Ellis Horwood Ltd. New York, pp. 640
- Joer, H.A., J. Lanier and M. Fahey, 1998. Deformation of granular materials due to rotation of principal axes. In : Géotechnique, Vol. 48, No. 5, pp. 605-619
- Kirckpatrick, W.M., 1957. The condition of failure of sands. In : Proc. Intern. Conf. Soil Mech. And Found. Eng., vol. 1
- Klay, M.C., 1975. The significance of pore pressures in soil, with respect to strenght. MSc. thesis, WAU Wageningen, pp. 49 (in dutch)
- Koolen, A.J. and H. Kuipers, 1983. Agricultural soil mechanics. Springer-Verlag, Berlin, pp. 241
- Langen, H. van, 1991. Numerical analysis of soil-structure interaction. Dissertation, Delft University of Technology, pp. 142
- Langen, H. van and P.A. Vermeer, 1991. Interface elements for singular plasticity points. Int. J. for Numerical and Analytical Methods in Geomechanics, Vol. 15 : pp. 301-315
- Lebert, M., N. Burger and R. Horn, 1987. Welche Bedeutung kommt der Aggregatstabilität während des Schervorganges zu?. Mitteilungen der Deutschen Bodenkundlichen Gesellschaft, 53 : 427-432
- Lerink, P., 1990. Technical note : The kneading distortion apparatus, 1990. In : Soil and Tillage Research, Vol. 17 (1990), pp. 173-179
- Matsuoka, H. Y. Suzuki and T. Murata, 1989. A constitutive model for soils evaluating principal stress rotation and its application to finite element analysis. In : Numerical models in geomechanics. NUMOG 3. Proceedings of the 3rd international symposium held at Niagara Falls, Canada, 8-11 May 1989, 155-162, Elsevier Science Publishers LTD
- Matsuoka, H. Y. Suzuki and T. Murata, 1990. A constitutive model for soils evaluating principal stress rotation and its application to some deformation problems. In : Soils and Foundations, Vol. 30, No. 1, pp. 142-154
- Muijs, C, 1968. Pressure distribution under plates. MSc. thesis, WAU Wageningen, pp. 24 (in dutch)
- Nichols, M.L., 1931. The dynamic properties of soil II. Soil and metal friction. Agricultural engineering 12 : 259-264
- Oda, M and H. Kazama, 1998. In : Géotechnique, Vol. 48, No. 4, pp. 465-481
- Owen, D.R.J. and E. Hinton, 1980. Finite elements in plasticity. Pineridge, Swansea, pp. 594
- Perdijk, E, 1971. Pressure distribution under plates and the flowing of soil. MSc. thesis, WAU Wageningen, pp. 45 (in dutch)

- Perdok, U.D. and B. Kroesbergen, 1999. Cone index as a function of soil moisture and pore volume. In : Proc. 13th Int. Conf. of the ISTVS, Vol. 1, Munich, Germany, Sept. 14-17, 1999, pp. 5-12
- Romp, G.J., 1970. Pressure distribution in the contact surface of the plate-soil. MSc. thesis, WAU Wageningen, pp. 33 (in dutch)
- Sela, A.D. and I.R. Ehrlich, 1971. Load support capability of flat plates of various shapes in soils. Automotive engineering congress, Detroit, Michigan
- Sloan, S.W. and M.F. Randolph, 1982. Numerical prediction of collapse loads using finite element methods. Int. J. for Numerical and Analytical Methods in Geomechanics, Vol. 6, pp. 47-63
- Song, E.X., 1990. Elasto-plastic consolidation under steady and cyclic loading. Ph.D. thesis, Delft university of technology, Delft, pp. 145
- Söhne, W, 1951. Das mechanische Verhalten des Ackerbodens bei Belastungen, unter rollenden Rädern sowie bei der Bodenbearbeitung. Grundlagen der Landtechnik, Heft 1, 1951, pp. 87-94
- Söhne, W, 1953. Druckverteilung im Boden und Bodenverformung unter Schlepperreifen. Grundlagen der Landtechnik, 5 : 49-63
- Söhne, W., 1953. Reibung und Kohäsion bei Ackerbodens. Grundlagen der Landtechnik, Heft 5 : 64-80
- Spoor, G., 1969. Design of soil engaging implements. Farm Machine Design Eng. Sept
- Steinbusch, M.J.H.R., 1993. From tyre to plant, WAU Wageningen, pp. 187 (in dutch)
- Stroosnijder, L. and P. Koorevaar, 1972. Air pressure within soil aggregates during quick wetting and subsequent "explosion". 1: Preliminary experimental results. Med. Fac. Landbouwwet. Rijksuniversiteit, Gent 37(3) : 1095-1106
- Swinkels, H.J.M., 1982. Soil air during loading. Msc. thesis, WAU Wageningen, pp. 47 (in dutch)
- Tijink, F.G.J., P. Lerink and A.J. Koolen, 1988. Summation of shear deformation in stream tubes in soil under a moving tyre. Soil & tillage research, 12 : 323-345
- Timoshenko, S. and J.N. Goodier, 1951. Theory of elasticity. McGraw-Hill, London, pp. 506
- Vermeer, P.A., 1992. Plaxis Gebruikersbijeenkomst, 8 oktober 1992. Utrecht, pp. 9 (in dutch)
- Vermeer, P.A., 1993. Plaxis manual, version 5x, Balkema , Rotterdam
- Vermeer, P.A., 1990. The Mohr-Coulomb model. Delft, pp. 19 (in dutch)
- Vermeer, P.A. and R. de Borst, 1984. Non-associated plasticity for soils, concrete and rock. Heron 29 (3), Delft, pp. 64
- Vornkahl, W., 1967. Dynamik gezogener Bodenwerkzeuge im Modellversuch. Fortsch Ber VDI-Z Reihe14, 7
- Wills, B.M.D., 1966. The load sinkage equation in theory and practice. Proceedings 2nd international conference ISTVS, Quebec, pp. 199-246
- Wu, T.H., A.K. Loh and L.E. Malvern, 1963. Study of failure of envelope of soils. In : J. Soil Mech. And Found. Div. Soc. Civil Engrs.

- Yoshimine M. K. Ishihara and W. Vargas, 1998. Effects of principal stress direction and intermediate principal stress on undrained shear behaviour of sand. In : Soils and Foundations, Vol. 38, No. 3, pp. 179-188
- Zienkiewics, O.C., 1971. The finite element method in engineering science, McGraw-Hill, London, pp. 285

Summary

During vehicular traffic on agricultural soils, the soil is subjected to a loading process which finally results into a change of micro-factors of the soil. By micro-factors is meant the amount and distribution of water, solid parts or bounds, not arising from the soil water, between these solid parts in the soil. Derivatives of the micro-factors are the so-called soil qualities. Soil qualities are understood to mean properties like coefficient of oxygen diffusion and water permeability, moisture characteristic, root penetration resistance and the coefficient of heat conductivity.

Seeds and plants need a specific set of values of these soil qualities to grow properly. Seeds and plants react immediately on the slightest change of one of the values of the soil qualities. Therefore there will be searched at relations between loading processes of the agricultural soil and the effect on the change of soil qualities, to create the possibility of predicting the change of soil qualities on base of an expected loading process of the soil under consideration.

In this dissertation the loading process of the soil is simulated through an impression of a strip into the soil with the help of a finite element method. Before simulations are presented, description is given of :
- stress and strain theories with respect to a cubical soil body
- the elastic-perfectly-plastic Mohr-Coulomb model
- soil-material interface
- finite and interface elements of the used finite element program Plaxis.

After that the derivation of soil model parameters for the finite element program Plaxis is given in case of a presented reference soil, a wet moderately heavy river clay with an entrapped air percentage of 5 %. Beside soil model parameters of the Mohr-Coulomb model, attention is given to soil model parameters of the elastic region of the Plaxis-Cap model.

A reference soil-load system is presented with corresponding finite element input. For handling the large amount of finite element output results, the stress and strain analysis program Trestana is developed and described. Characteristic of the program is that three-dimensional plots of quantities can be presented against the deformed mesh as ground surface, without loosing information through the use of smoothing procedures.

Subsequently, single and composite quantities are presented which can serve as building blocks for constructing of so-called kneading numbers of soil. This all in view of the idea that changes of kneading numbers reasonably correlate with the changes in soil qualities.

Finally, general considerations on the treated dissertation subjects and recommendations for future research are given.

Samenvatting

Gedurende rijden over land wordt de grond onderworpen aan een belastingsproces. Dit proces resulteert uiteindelijk in een verandering van de microfactoren van de grond. Onder microfactoren wordt verstaan de hoeveelheid en verdeling van water, vaste delen of bindingen tussen de vaste delen in de grond.

Afgeleide van de microfactoren zijn de zogenaamde bodemkwaliteiten. Onder bodem-kwaliteiten vallen eigenschappen als zuurstofdiffusie, waterdoorlatendheid, vochtkarakteris-tiek, wortelindringweerstand en warmtegeleiding.

Zaden en planten hebben voor een goede ontwikkeling en groei een specifieke set aan bodemkwaliteiten nodig. Op de kleinste bodemkwaliteitsverandering reageren zaden en planten direct. Om deze reden wordt er gezocht naar relaties tussen belastingsprocessen van landbouwgrond en de daarmee gepaard gaande veranderingen van bodemkwaliteiten. Uiteindelijke doel is, om te voorspellen welke bodemkwaliteitsverandering zal optreden op basis van een te verwachten belastingsproces voor een bepaalde grond.

In deze dissertatie wordt het belastingsproces gesimuleerd door met behulp van de eindige elementen methode een star stempel in de grond te drukken. Voordat de simulaties worden gepresenteerd is er ingegaan op :
- spannings- en deformatie theorieën met betrekking tot een kubisch grond lichaam
- het elastisch-plastische Mohr-Coulomb model
- de grond-materiaal interface
- eindige en interface elementen van het gebruikte eindige elementen pakket Plaxis.

Afleiding van waarden voor grondmodelparameters voor het eindige elementen pakket Plaxis is gegeven voor een referentiegrond, een natte middel-zware rivierklei met een ingesloten luchtpercentage van 5 %. Naast waarden voor grondmodelparameters van het Mohr-Coulomb model is er ingegaan op waarden voor grondmodelparameters van het elastische gebied van het Plaxis-Cap model.

Een referentie grond-belastingssysteem is gepresenteerd met bijbehorende eindige elementen invoer. Voor verwerken van de grote hoeveelheden eindige elementen uitkomsten is er een spannings- en deformatieanalyse programma, Trestana, ontwikkeld en beschreven. Kenmerkend voor dit programma is dat er drie-dimensionale afbeeldingen kunnen worden gegenereerd waarbij een specifieke grootheid wordt uitgezet tegen een gedeformeerd raster als grondvlak, zonder extra ruis door het gebruik van interpolatieprocedures.

Vervolgens zijn enkele en samengestelde grootheden gepresenteerd welke dienst kunnen doen als bouwstenen voor de constructie van de zogenaamde kneedgetallen van grond. Dit alles in het licht van het idee dat kneedgetallen zullen correleren met bodemkwaliteiten.

Tenslotte zijn er conclusies getrokken uit behandelde dissertatie-onderwerpen en aanbe-velingen gegeven voor toekomstig onderzoek.

Nawoord

Dit is een goede plaats in de dissertatie om terug te kijken hoe het allemaal is begonnen en hoe een en ander vervolgens verder is verlopen.

Aanleiding voor de promotie-studie is een afstudeervak geweest bij de vakgroep Grondbewerking bij de toenmalige Landbouwuniversiteit in '91. Het afstudeervak betrof het bestuderen van de vervorming van een vertikale wortelholte door een vertikale belasting aan de hand van een eindige elementen methode. Via de Technische Universiteit Eindhoven ben ik in contact gekomen met het Nederlandse eindige elementen pakket Plaxis. Voor uitvoering van het afstudeervak met Plaxis kwam ik terecht bij de provincie Gelderland, afdeling Waterkering. Door naast uitvoering van het afstudeervak mee te draaien met de dagelijkse gang van zaken van deze afdeling is de interesse ontstaan in de civiele techniek en met name de geotechniek. Dit werd bespoedigd door contacten met het Plaxis-team, welke toendertijd onderdeel uitmaakte van het Geotechnisch Laboratorium van de Faculteit der Civiele Techniek van de Technische Universiteit Delft. Daar uit het afstudeervak bleek dat het gebruik van het eindige elementen pakket Plaxis veel potenties bood voor toepassing in de landbouw-grondmechanica kon er vervolgens een promotie-studie gestart worden met de voor u liggende dissertatie als resultaat. Deze studie startte op een cijfermatig mooie datum, namelijk 11-11-1991 bij de vakgroep Grondbewerking aan de Landbouwuniversiteit. Plaats van de promotie-studie was het robuuste en karakteristieke gebouw aan de Diedenweg 20. Op de begane grond was het laboratorium waar tijdens het koffie zetten altijd even werd binnengevallen. Deze momenten waren altijd zeer waardevol omdat nu het door mij een verdieping hoger uitgevoerde theoretische werk in de juiste context konden worden geplaatst, wanneer weerbarstige waardebepalingen voor grondmodelparameters werden uitgevoerd en uitgelegd door Jos Kroesbergen. Eenmaal, na de gezellige koffiepauzes, teruggekomen te zijn op de kamer op de eerste verdieping kon er in alle rust worden nagegaan of door de waarde van de vijftiende decimaal achter de komma de rotatie van een infinitesimaal grondparallellepipedum de rotatie nu rechts- of linksom optrad. Geweldig was dat. Zeker als je uit het raam tegen die mooie fraaie boom keek waar dan een boomklever olijk zowel links- als rechtsom roteerde voor de speurtocht naar voedsel, zich niet bewust zijnde dat dit wel eens te maken kon hebben met de grootte van de vijftiende decimaal. Heel relativerend. Relativerend voor alles was ook de filosofie die 's avonds werd opgepakt in die periode. Deze ongecompliceerde periode was voorbij toen de promotie-studie part-time werd voortgezet en er part-time bij de Dienst Weg- en Waterbouwkunde van Rijkswaterstaat te Delft werd gewerkt vanaf september '94.

Ruim een jaar later kwam er een duidelijk keerpunt in mijn leven, namelijk het auto-ongeluk op de Grebbeberg op 15 november '95. Een inschattingsfout met wat later bleek nare gevolgen. Zomaar ineens hang je tussen de bomen van het Utrechts Landschap. Op het eerste gezicht alleen een grote snee op het voorhoofd, dus dat valt wel mee ... Het verdere verhaal begint met dat ik op de avond van die bewuste dag dingen heb opgeruimd die tot heden ten dage nooit zijn teruggevonden. Waarschijnlijk opgeborgen in de kliko. In de weken daarna zit de hele nekpartij vast en denk je bij jezelf, hoe schrijf je dat ook alweer in het Nederlands en hoe zeg en schrijf je dat in het Engels. Kortom, whiplash-achtige verschijnselen. De

buitenwacht is het waarschijnlijk niet opgevallen, maar vertrouw me, je wordt er toch lichtelijk onzeker van als je bijvoorbeeld niet meer weet of er in de woorden mogelijk, eigenlijk, gezamenlijk of namelijk nu wel of niet de letter n moet staan. Het is me pijnlijk duidelijk geworden dat een mens niet gebouwd is om een zijdelingse aanrijding van 80 km/uur te incasseren, zelfs niet met gebleken, zelf-ingebouwde, crash-bestendige stoelen met voldoende hoge hoofdsteunen in een oerdegelijke Mitsubishi Colt. De daarop volgende periode tot maart '96, tijdstip einde promotie-studie, is er dan ook één geweest van rust. Na deze periode is de betrekking bij de Dienst Weg- en Waterbouwkunde full-time geworden. Om het voor mezelf enigszins overzichtelijk te houden en verder te herstellen is er bewust voor gekozen om activiteiten met betrekking tot de dissertatie op te schorten. Gelukkig bleek dat in mijn hoofd langzaam de vroegere verbindingen zich weer begonnen te herstellen en dat het schrijven in het Nederlands en het schrijven en spreken in het Engels tergend langzaam beter ging. Ervaring leert dat een jaar niets is bij dit soort processen. But I'm back on track en ben er blij om dat het uiteindelijk toch goed is afgelopen. Eind '98 kon de dissertatie dan ook weer worden opgepakt en worden afgemaakt.

Nu is dan ook het mooie moment gekomen dat ik mensen mag bedanken die op enigerwijze aan deze dissertatie hebben bijgedragen.

Udo Perdok, jij creëerde de voorzieningen die nodig waren voor het uitvoeren van deze promotie-studie. Je vroeg vaak naar de reikwijdte van het onderwerp of aanverwant gesnor (blijft een leuke term trouwens). Ik ben me er van bewust dat ik je wel eens op het verkeerde been zette door systematisch eerst alle beperkingen van het een en ander op te noemen en daarna de rest. Gesprekken werden hierdoor snel erg lang, maar gelukkig kwam dat ook door het feit dat je interesse zich niet alleen beperkte tot de promotie-studie. Heel plezierig. Een onuitwisbare indruk heb je achtergelaten in Mugge(n)beet. Moesten we maar eens herhalen.

Jos Koolen, elke dag kwam ik 'even' bij je binnen. Aanvankelijk met veel vragen over theorieën, later met eigen werk ter becommentariëring. Je hebt altijd de tijd genomen om er met me over te discussiëren en hoe met het een en ander wetenschappelijk om te gaan. Achteraf gezien denk ik dat je wel eens bijna gek moet zijn geworden van de vele drie-dimensionale afbeeldingen die ik je heb gepresenteerd naar aanleiding van één eindige elementen simulatie. Je hebt het niet laten blijken en samen met mij gezocht naar wat echt nodig was en wat overdone was. Bedankt daarvoor.

Dirk Kurstjens, je was de enige jonge collega die in hetzelfde schuitje zat. Wandelend door het prachtige Arboretum moesten de gesprekken naast onkruid en grond wel over andere, hogere zaken gaan. Terug in Diedenweg 20 samen Acad'en. Ieder onze eigen capaciteiten in de strijd gooiend, is er altijd wat moois en bruikbaars ontstaan. Voor herhaling vatbaar.

Albert Boers en de mannen van AIV onder leiding van Ed Olrichs, jullie inbreng en faciliteiten bij het drukklaar maken van de dissertatie heb ik gewaardeerd.

Tom Dingjan, Paul van Espelo en Geerten Lenters, jullie creativiteit met betrekking tot de omslag maakte het maken ervan tot een verademing.

Frans Boone, Willem Hoogmoed, Jan Kouwenhoven, Jos Kroesbergen, Piet Looijen en Corrie Seves, jullie maakten de koffiepauzes, barbecues en uitstapjes compleet en gezellig.

Het Plaxis-team, jullie waren altijd bereid vragen te beantwoorden en problemen op te lossen. Paul Bonnier, jou wil ik speciaal bedanken omdat ik tijdens het afstuderen al zaken met jullie programma probeerde uit te rekenen waar het programma toen nog niet echt tegen bestand was. Gelukkig wist jij slimme alternatieven. Van jouw alternatieven heb ik tijdens de promotie-studie en later in mijn werk nog vaker gebruik mogen maken. Bedankt daarvoor.

Tammo Vegter, zomaar ineens stelde jij belangeloos aan mij tijd ter beschikking om de dissertatie af te ronden. Dit was net dat duwtje dat nodig was het een en ander weer structureel en met voldoende diepgang op de rails te zetten. Bijzonder dank daarvoor.

Aart van den Berg, Suresh Bharatsingh, Arjan Grashuis, Hans Grootveld, Sander Jonker, Tom Piepers en Arjan Venmans, toen ik tijd kreeg voor afronding van de dissertatie, verdeelden jullie het van mij overblijvende werk zonder moeilijkheden over jullie schouders. Als dat geen collegialiteit is. Speciaal woord voor mijn kamergenoot Aart. Naast het feit dat container-duiken erg goed past binnen het kader van hergebruik van materialen en goed is voor het milieu, is het geestverruimend en geeft het een goede sfeer. Nadeel is dat ze je thuis al weer zien aankomen met die 'rotzooi'. Wat kun je daar nou weer mee ? Uit eigen onderzoek is gebleken dat dit laatste als sneeuw voor de zon verdwijnt indien bij het thuisfront iets kapot gaat, hetgeen vervolgens precies gerepareerd kan worden met het door jou jaren in depot gehouden, niet meer verkrijgbare onderdeel, wat bovendien ook nog eens gevonden is. Vergeet niet, dan ben je dé man.

Eefke de Graaf, dat je nog aan me dacht voordat de diverse kubussen jouw toneel zouden verlaten via de kliko. Je had waarschijnlijk nooit durven dromen dat één van jouw kubussen opgewaardeerd zou worden door je neef met als eindbestemming de meest zichtbare plaats van zijn dissertatie.

Berry Peelen, jou bedank ik voor je nooit aflatende gastvrijheid en behulpzaamheid met betrekking tot onderhoud en reparatie van m'n wagenpark. We hebben onder andere een gezamenlijke interesse voor de techniek van auto's. Jouw auto-technische ervaring gaat echter veel verder en daar heb ik veel van geleerd. Ik zal nooit die sleutelpartij aan de Lancer vergeten tot diep in de nacht bij -16 °C, waarbij ik geen gevoel meer in de vingers en tenen had en mijn neus ook raar begon aan te voelen, terwijl jij het alleen wel wat fris vond.

Gerline, de laatste alinea is voor jou. Samen hebben we eind '91 besloten dat ik de promotie-studie zou starten. Dat er een aantal vervelende en tijdrovende zaken ons pad zouden kruisen, was met de beste wil van de wereld niet te voorzien. Maar we zijn er goed doorheen gekomen. Je vond het wel eens moeilijk dat je me niet kon helpen. Aan de ene kant was dit waar, aan de andere kant ook weer niet. Mede dankzij jouw steun, loyaliteit en zorgzaamheid is deze dissertatie tot stand gekomen. Daarom is het heel mooi dat deze dag, door een punt te zetten achter het dissertatie-gesnor, een nog specialere schittering krijgt wat betreft onze verdere gezamenlijke toekomst. Een toekomst die hopelijk minder complex wordt met eindelijk meer tijd voor elkaar.

Curriculum vitae

Naam	Albert Sarris Barneveld
Geboren	28 maart 1966 te Hattem

sept. 1978 - juli 1983   Chr. Scholengemeenschap De Heertganck te Heerde
Afgesloten met Havo-diploma

juli 1983 - juli 1987   Chr. Hogere Landbouwschool te Dronten
Afgesloten met diploma van landbouwkundig ingenieur
Afstudeerrichting   : Zoötechniek
Specialisatie   : Landbouwtechniek
Afstudeerproject   : Ammoniak-emissie-arme toedieningsme-
thoden van mest in de landbouw

juli 1987 - aug. 1988   Militaire dienst

sept. 1988 - aug. 1991   Landbouwuniversiteit Wageningen
Afgesloten met diploma (cum laude) van landbouwtechnisch ingenieur
Studierichting   : Landbouwtechniek
Afstudeerrichtingen : - Grondbewerking
Vervorming van een vertikale wortelholte benaderd met de eindige elementen methode
- Wiskunde
Praktische functietheorie, speciale func-
ties en continuümmechanica

nov. 1991 - sept. 1994   Assistent-In-Opleiding aan de Landbouwuniversiteit Wageningen, vakgroep Grondbewerking

sept. 1994 - mrt. 1996   Part-time Assistent-In-Opleiding aan de Landbouwuniversiteit Wageningen, vakgroep Grondbewerking
Part-time werkzaam bij Rijkswaterstaat, Dienst Weg- en Waterbouwkunde, hoofdafdeling Waterbouw, afdeling Geo-
techniek als wetenschappelijk medewerker m.b.t modellerings-
onderzoek van kruipgedrag van grond en stabiliteit van dijken

mrt. 1996 - mei 1997   Full-time werkzaam bij Rijkswaterstaat, Dienst Weg- en Waterbouwkunde, hoofdafdeling Waterbouw, afdeling Geotechniek als wetenschappelijk medewerker m.b.t modellerings-onderzoek van en experimenteel onderzoek naar kruipgedrag van grond en effecten van kruip op tunnelbouw

mei 1997 - tot heden   Werkzaam bij Rijkswaterstaat, Dienst Weg- en Waterbouwkunde, hoofdafdeling Infrastructuur, afdeling Realisatie en Onderhoud Infrastructuur, sectie Geotechniek en Wegfunderingen als projectleider m.b.t expertsysteem bouwmethoden onderbouw wegen en aanvulling geotechnische ontwerphandboeken wegenbouw; naast geotechnische advisering strekken de activiteiten zich uit tot de projecten economisch afweegmodel wegenbouw en wegen naar de toekomst